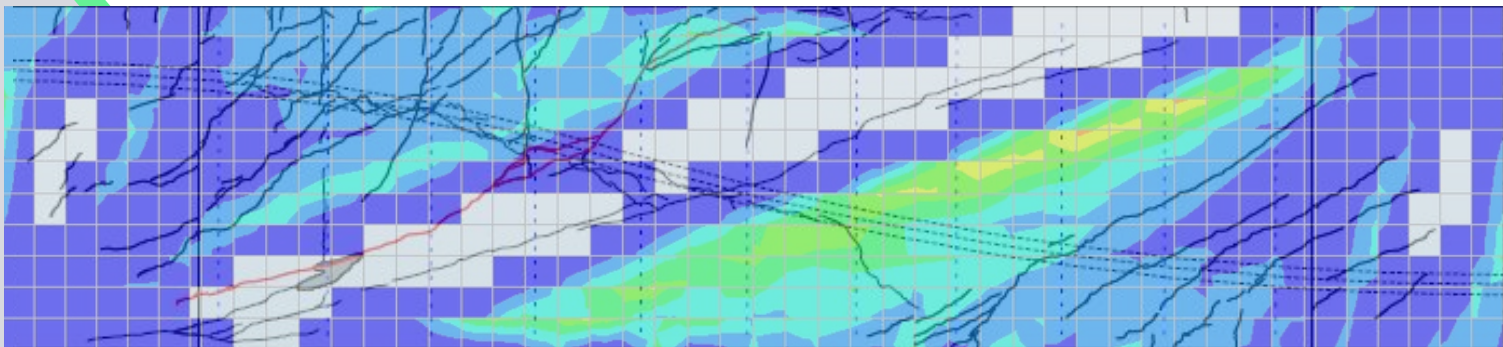


Investigation of the influence of open straight-legged stirrups on the shear resistance of concrete beams

Nonlinear Finite Element Analysis



Investigation of the influence of open straight-legged stirrups on the shear resistance of concrete beams

Master thesis submitted to Delft University of Technology
in partial fulfilment of the requirements for the degree of

MASTER OF SCIENCE

in Civil Engineering (Structural Engineering)
Faculty of Civil Engineering and Geosciences

by

M.J. (Robin) Streng

Student number: 4696794

To be defended in public on Wednesday March 15, 2023 at 11:30 AM

Graduation committee

Chairperson	: Prof. dr. ir. M.A.N. Hendriks, Section of Concrete Structures
First Supervisor	: Dr. R. Esposito, Section of Applied Mechanics
Second Supervisor	: Dr. ir. Y. Yang, Section of Concrete Structures
External Supervisor	: Dr. ir. M.A. Roosen, Rijkswaterstaat and TU Delft
External Supervisor	: Ir. B. van den Broek, Rijkswaterstaat

An electronic version of this thesis is available at <http://repository.tudelft.nl/>

Preface

This thesis concludes my master Civil Engineering with the track Structural Engineering at the TU Delft. Over the last 5.5 years, I have learned a lot about multiple aspects of civil engineering, of which I especially liked calculating various components of structures and playing with the software that was provided during my study. For the last year, I have been working on this thesis at Rijkswaterstaat, which was very challenging and where I learned a lot.

This thesis consists of an investigation of the influence of open straight-legged stirrups in concrete beams subjected to shear with the use of nonlinear finite element analyses. The reason for this topic is a problem with the reassessment of existing bridges containing these incorrectly detailed stirrups that are managed by Rijkswaterstaat. For everyone interested in the shear behaviour of reinforced concrete beams and the finite element modelling of such beams, this thesis might provide new insights.

I would like to thank my graduation committee for their academic guidance and feedback, and especially Bart van den Broek and Marco Roosen for motivating me and leading me in the right direction. I also want to thank the people of the Afdeling Bruggen en Viaducten at Rijkswaterstaat and in particular Lidewij van Wagenveld for arranging everything I needed to finalise my thesis. I am grateful for the support from my family and friends. I want to thank my grandparents for providing a silent place to work, enjoyable coffee breaks and tasty lunches. Last but not least, a special thanks to Hannah for your loving support, you helped me where you could and were always able to cheer me up when I needed it.

*Robin Streng
Lopik, March 2023*

Abstract

Nowadays, Rijkswaterstaat reassesses many older concrete bridges to guarantee their structural safety under the influence of increased traffic loads and stricter standards. Many of these concrete bridges contain open straight-legged stirrups, which are not allowed to take into account for the calculations of the shear resistance according to current standards. This often results in theoretical insufficient shear capacity and critical damage to structures, but this is not observed in reality. This indicates that the open straight-legged stirrups probably do contribute to the shear resistance, where an accurate assessment of this contribution could prevent unnecessary and costly structural safety measures. However, very few shear tests with relevant cross-sectional dimensions are performed and documented in literature, especially tests containing open straight-legged stirrups.

The application of Nonlinear Finite Element Analysis (NLFEA) is a useful tool to evaluate and understand the behaviour of structures, but provisions for the implementation of open straight-legged stirrups in concrete structures are lacking. Thus, the goal of this research is to provide a finite element modelling strategy that is able to accurately describe the behaviour of concrete beams with open straight-legged stirrups subjected to shear. The research focusses on describing the behaviour of rectangular concrete beams with open and closed straight-legged stirrups with finite element models using DIANA 10.5 [1].

Schramm [2] has performed multiple shear tests on prestressed concrete beams with several no longer permitted stirrups, including open straight-legged stirrups. He found that open straight-legged stirrups can significantly contribute to the transfer of shear forces [2]. The relevance of the rectangular test beams for comparison with box-girders is validated in this thesis, where the stress distributions in a linear elastic rectangular and box-girder cross-section due to axial forces, bending moments, shear forces and torsion are compared.

In the interest of providing a suitable solution strategy, Schramm's test beams with closed and open straight-legged stirrups are reproduced with 3-dimensional nonlinear finite element models based on the recommendations of the RTD1016-1 [3], where the influence of various modelling considerations is investigated. The concrete is modelled with a smeared total strain-based crack model with the Hordijk tensioning and parabolic compression relations, including confinement and lateral cracking effects. Reinforcements are modelled as embedded truss elements with the Von-Mises plasticity model. To describe the accurate anchorage behaviour of the open straight-legged stirrups, the interaction between the surrounding concrete and the stirrups is described with the Shima bond-slip relation. The finite element model is first calibrated with a beam with closed stirrups, where modelling clamped restraints with supports on both sides of the beam result in a too-stiff response. By allowing a little rotational freedom in the form of boundary springs, the stiffness of the beam is manipulated without changing the overall load-bearing behaviour.

Various solution strategies are defined where multiple parameters are investigated. The models with closed stirrups include an investigation of the influence of full Newton Raphson and secant iteration scheme and the mesh size. The models with open straight-legged stirrups include a further calibration of the model, where the influence of the fixed and rotating crack orientation, the fully bonded and bond-slip interface between the concrete and reinforcements and the full Newton Raphson and secant iteration scheme is investigated.

From the finite element results, it follows that a rotating crack model and the full Newton-Raphson iteration scheme based on the recommendations from the RTD1016-1 [3] in combination with the boundary springs are able to predict the realistic shear behaviour of beams with closed stirrups. However, the ultimate shear load is very mesh dependent, where a larger shear resistance is found for smaller element sizes, where especially the contribution of the compression zone seems to be very susceptible to the element size. Also, it follows that the used bond-slip relation for open straight-legged stirrups leads to incorrect crack patterns, where a different failure mode than expected is predicted for all solution strategies. The chosen iteration scheme is also very influential, where a full Newton-Raphson scheme combined with the bond-slip relation for the stirrups leads to failure due to delamination of the concrete cover and the secant scheme consistently results in significant overpredictions of the shear resistance, underpredictions of the stirrup contributions and failure due to horizontal cracks through the middle of the beam. Within this study, no suitable solution strategy is found that is able to explain the behaviour of open straight-legged stirrups in concrete beams subjected to shear. The anchorage of the open ends is defined with a bond-slip relation, but the inclusion of such relation for open straight-legged stirrups results in incorrect failure modes.

For further research, it is recommended to investigate the nonlinear finite element behaviour of beams with fully bonded stirrups with reduced lengths at the open ends. Also, it is recommended to further validate the substructure technique used for Schramm's experiments [2] due to considerably lower stiffnesses than found in reference tests or perform a different experimental study consisting of beams with open straight-legged stirrups with a different test setup. Finally, it is recommended that the mesh dependency for beams with relatively large heights is further investigated, especially focussing on the susceptibility of the shear contribution of the compression zone.

Table of contents

Preface	III
Abstract	V
List of figures	IX
List of tables	XIV
List of symbols	XV
1 Introduction	1
1.1 Background and motivation	1
1.2 Scope, research questions and methodology	5
1.3 Thesis outline	5
2 Shear behaviour of RC beams	7
2.1 Shear in an uncracked concrete beam	7
2.2 Shear resistance of a cracked concrete beam without stirrups	9
2.3 Shear resistance of a cracked concrete beam with closed stirrups	14
2.4 Bond behaviour between concrete and reinforcement	18
2.5 Summary of shear load transfer mechanisms	24
3 Finite element modelling of RC beams	25
3.1 Kinematic relations	25
3.2 Constitutive relations	28
3.3 Equilibrium conditions	36
4 Experimental benchmark: Schramm [2]	41
4.1 Comparison between rectangular and box-girder cross-sections	41
4.2 Schramm's research [2]	48
5 Finite element modelling approach	58
5.1 Finite element model	58
5.2 Description of part 1: RC beams with closed stirrups	68
5.3 Description of part 2: RC beams with open straight-legged stirrups	69
5.4 Judgement of the results	73
6 Finite element results	75
6.1 Part 1: RC beams with closed stirrups	75
6.2 Part 2.1: RC beams with open straight-legged stirrups, Calibration	86
7 Discussion of the results	98
7.1 Contribution per load-bearing mechanism	98
7.2 Validation of the bond-slip relation	104
7.3 The consistent failure mode and overprediction of the secant iteration scheme	105

7.4 Investigation of the bond behaviour of open straight-legged stirrups	105
7.5 Influence of element size	108
8 Conclusions and recommendations	109
8.1 Conclusions	109
8.2 Recommendations.....	111
9 References.....	112
Appendix A Schramm’s experiments [2]: properties and results	115
A.1 Geometrical and material properties	115
A.2 Results.....	116
Appendix B Verification of the finite element model	122
B.1 Boundary conditions: boundary springs vs. supports.....	122
B.2 Stiffness of the steel plates	124
B.3 The interface between steel plates and concrete beam	126
Appendix C Convergence plots	128
C.1 Group 1	128
C.2 Group 2	131

List of figures

Figure 1.1: The Rooyensteijnse brug [5]	1
Figure 1.2: Half of the cross-section of the Rooyensteijnse brug at the third support from the left [6] ..	1
Figure 1.3: Strut-and-tie model for shear in concrete beams [9]	2
Figure 1.4: Correct detailing of stirrups [8].....	2
Figure 1.5: Incorrect detailing of stirrups [5].....	2
Figure 1.6: Existing effective length $l_{bd,aanw}$ in the compression zone for open stirrups [10]	3
Figure 1.7: Incorrectly detailed stirrup types [2]	4
Figure 1.8: Relevant tested cross-sections [2].....	4
Figure 1.9: Thesis outline	6
Figure 2.1: Axial, shear and principal stresses in a homogeneous elastic beam [11]	7
Figure 2.2: Principal compressive stress trajectories and inclined cracks [11]	8
Figure 2.3: Types of inclined cracks [12].....	9
Figure 2.4: Arch action in a very short shear span [11]	9
Figure 2.5: Failure modes of a very short shear span [11].....	9
Figure 2.6: Failure modes of a short shear span [11]	10
Figure 2.7: Internal forces in a cracked concrete beam without shear reinforcement [13]	10
Figure 2.8: Typical force-displacement curve of a reinforced concrete beam [15]	14
Figure 2.9: Distribution of shear resistance due to different mechanisms [11]	15
Figure 2.10: Strut-and-tie model of concrete beams with shear reinforcement [16].....	15
Figure 2.11: Cut section parallel to the struts	16
Figure 2.12: Cut section perpendicular to the struts	16
Figure 2.13: Relative bar displacement (slip) [17]	18
Figure 2.14: Local bond stress-slip law [17].....	18
Figure 2.15: Bar-concrete slip and wedging action [17]	19
Figure 2.16: Longitudinal splitting cracks [17]	19
Figure 2.17: Available effective length $l_{bd,aanw}$ in the compression zone for open straight-legged stirrups [10].....	23
Figure 2.18: Schematic overview of the shear load transfer mechanisms	24
Figure 3.1: Quadratic quadrilateral element [3].....	26
Figure 3.2: Quadratic hexahedron [3]	26
Figure 3.3: Integration points, 3x3-point Gauss [3]	26
Figure 3.4: Integration points, 3x3x3-point Gauss [3]	26
Figure 3.5: Discrete cracking vs. smeared cracking in an element [20]	28
Figure 3.6: Fixed crack model [20].....	29
Figure 3.7: Rotating crack model [20]	29
Figure 3.8: Hordijk softening [3].....	31
Figure 3.9: Parabolic compression diagram [3]	31
Figure 3.10: Examples of equivalent lengths [3].....	32
Figure 3.11: Stress-strain diagram for steel bars [3].....	32
Figure 3.12: Stress-strain diagram for prestressing steel [3]	32
Figure 3.13: Effect of tension-stiffening of a reinforced concrete member [29]	33
Figure 3.14: Fib bond-slip model [27].....	33
Figure 3.15: Comparison of bond-slip models.....	35
Figure 3.16: Shima bond-slip-strain model for different steel strains	35
Figure 3.17: Arc-length control.....	37
Figure 3.18: Regular Newton-Raphson method [1].....	39

Figure 3.19: Modified Newton-Raphson method [1].....	39
Figure 3.20: Secant (Quasi-Newton) method [1].....	39
Figure 3.21: Force displacement curve of a rotating crack model without shear reinforcement with 40, 100 and 2000 iterations per step [19]	39
Figure 3.22: Convergence norm parameters [1].....	40
Figure 4.1: Compared cross-sections.....	42
Figure 4.2: Stresses due to an axial force	42
Figure 4.3: Stresses due to a bending moment	43
Figure 4.4: Stresses due to a shear force.....	44
Figure 4.5: Internal vertical forces due to a shear force	44
Figure 4.6: St. Venant torsion and warping [33].....	45
Figure 4.7: Torsion with unrestrained and restrained warping [33]	45
Figure 4.8: Stresses due to a torsional moment	46
Figure 4.9: Internal shear forces due to a torsional moment	47
Figure 4.10: Test setup and acting forces and moments [2].....	49
Figure 4.11: Schematic view of the test setup [2]	49
Figure 4.12: No longer permitted stirrup types [2]	50
Figure 4.13: Section of the test beams [2].....	50
Figure 4.14: Cross-sections of relevant specimens [2]	51
Figure 4.15: Anchoring of the prestress tendons and longitudinal reinforcement on the active load introduction plate [2]	52
Figure 4.16: Shear force-displacement diagram of tests R2, R4 and R10	53
Figure 4.17: Shear force-deflection curves of test R11-gB and DLT1.1-RWTH [2]	54
Figure 4.18: Crack patterns at maximum shear load	55
Figure 4.19: Strain in stirrups at the ultimate shear load	56
Figure 4.20: Crack patterns and strains in the open straight-legged stirrups [2] (a) and (c) crack pattern and strains in stirrup 2 at a load level of 89% $V_{max} = 587$ kN (b) and (d) crack pattern and strains in stirrup 8 at a load level of 95% $V_{max} = 628$ kN	57
Figure 5.1: Layout of the 3D models.....	59
Figure 5.2: Reinforcement configuration of the concrete beams with closed stirrups.....	60
Figure 5.3: Reinforcement configuration for beams with open straight-legged stirrups	60
Figure 5.4: CHX60 [1].....	61
Figure 5.5: Finite element mesh for $h=50$ mm	61
Figure 5.6: Calculation spring stiffness for the first iteration	61
Figure 5.7: Boundary conditions at the passive side	62
Figure 5.8: Boundary conditions and point load at the active side.....	62
Figure 5.9: Hordijk tension for $h=50$ mm.....	63
Figure 5.10: Parabolic compression for $h=50$ mm	63
Figure 5.11: Stress-strain relationships for the reinforcements	65
Figure 5.12: Arc-length control nodes	65
Figure 5.13: Bond-slip models for the finite element model	71
Figure 6.1: Convergence behaviour solution strategy C1.2	76
Figure 6.2: Global behaviour of the experiment R2 and solution strategy C1.2	76
Figure 6.3: Crack development for Schramm R2 [2] and solution strategy C1.2	78
Figure 6.4: Stirrup strain development for experiment R2 (top) and solution strategy C1.2 (bottom)	79
Figure 6.5: Displacement Td_tZ after the peak load for solution strategy C1.2	79
Figure 6.6: Force-displacement curve for different iteration schemes	80
Figure 6.7: Force-displacement curves with compared load steps for C1.3 and C1.5	80

Figure 6.8: Crack strains Eknn of C1.3	81
Figure 6.9: Crack strains Eknn of C1.5	81
Figure 6.10: Strains EZZ in the stirrups for C1.3.....	82
Figure 6.11: Strains EZZ in the stirrups for C1.5.....	82
Figure 6.12: Crack width Ecw1 at $V_{ult} = 862$ kN for C1.3	82
Figure 6.13: Crack width Ecw1 at $V_{ult} = 1131$ kN for C1.5	82
Figure 6.14: Convergence behaviour solution strategy C1.3 (Full Newton-Raphson)	83
Figure 6.15: Convergence behaviour solution strategy C1.5 (Secant)	83
Figure 6.16: Force-displacement curve for different element sizes	84
Figure 6.17: Crack width Ecw1 at ultimate shear load for solution strategy C1.1	84
Figure 6.18: Crack width Ecw1 at ultimate shear load for solution strategy C1.3	84
Figure 6.19: Convergence behaviour solution strategy O2.9	87
Figure 6.20: Global behaviour of the experiment R4 and solution strategy O2.9	87
Figure 6.21: Crack development for Schramm R4 [2] and solution strategy O2.9.....	88
Figure 6.22: Displacement TDtZ after failure for O2.9.....	89
Figure 6.23: Stirrup strain development for experiment R4 (top) and solution strategy O2.9 (bottom)	89
Figure 6.24: Force-displacement curve for different reinforcement models	90
Figure 6.25: Crack width Ecw1 at ultimate loading for O2.1 (all reinforcements fully bonded)	90
Figure 6.26: Crack width Ecw1 at ultimate loading for O2.2 (LFB-SBS-PFB)	90
Figure 6.27: Crack width Ecw1 at ultimate loading for O2.2 (LBS-SBS-PFB)	91
Figure 6.28: Crack width Ecw1 at ultimate loading for O2.1 (all reinforcements bond-slip)	91
Figure 6.29: Convergence behaviour solution strategy O2.1 (all reinforcements modelled as fully bonded).....	91
Figure 6.30: Convergence behaviour solution strategy O2.4 (all reinforcement modelled with bond- slip).....	91
Figure 6.31: Force-displacement curve for different iteration schemes and crack orientations	92
Figure 6.32: Crack strain plot Eknn of O2.3 (Secant) at ultimate loading	93
Figure 6.33: Crack strain plot Eknn of O2.5 (Full Newton-Raphson) at ultimate loading.....	93
Figure 6.34: Crack strain plot Eknn of C1.5 (Secant) at ultimate loading.....	93
Figure 6.35: Crack strain plot Eknn of C1.3 (Full Newton-Raphson) at ultimate loading	93
Figure 6.36: Convergence behaviour solution strategy O2.3 (Secant).....	94
Figure 6.37: Convergence behaviour solution strategy O2.5 (Full Newton-Raphson)	94
Figure 6.38: Crack width Ecw1 at $70\%V_{ult} = 641$ kN for O2.3 (secant iteration scheme, rotating crack model)	94
Figure 6.39: Crack width Ecw1 at $70\%V_{ult} = 635$ kN for O2.8 (secant iteration scheme, fixed crack model)	95
Figure 6.40: Crack width Ecw1 at 550 kN for O2.5 (Newton-Raphson iteration scheme, rotating crack model)	95
Figure 6.41: Crack width Ecw1 at 550 kN for O2.9 (Newton-Raphson iteration scheme, fixed crack model)	95
Figure 6.42: Crack strain Eknn at 550 kN for O2.5 (Newton-Raphson iteration scheme, rotating crack model)	96
Figure 6.43: Crack strain Eknn at 550 kN for O2.9 (Newton-Raphson iteration scheme, fixed crack model)	96
Figure 6.44: Convergence behaviour solution strategy O2.5 (Rotating).....	96
Figure 6.45: Convergence behaviour solution strategy O2.9 (Fixed)	96
Figure 7.1: Critical crack Ecw1 at ultimate loading for C1.2	99

Figure 7.2: Critical crack E_{cw1} at ultimate loading for C1.3	99
Figure 7.3: Total strain EXX at ultimate loading for C1.2 (with a cut at the shear crack tip).....	100
Figure 7.4: Total strain EXX at ultimate loading for C1.3 (with a cut at the shear crack tip).....	100
Figure 7.5: Stress SZX at the cut (averaged over the width of the beam).....	100
Figure 7.6: Reinforcement stress SXX for the prestress tendons at ultimate loading for C1.2	101
Figure 7.7: Reinforcement stress SXX for the prestress tendons after prestressing and before loading for C1.2.....	101
Figure 7.8: Bond-slip evaluation for stirrup 11 at $V=646$ kN for solution strategy O2.5 (a) Concrete beam with stirrups (dashed rectangle is evaluated part of stirrup 11) (b) Stress SZZ in stirrups 1 (c) Bond-slip STSx along stirrup	104
Figure 7.9: Crack strains E_{knn} of O2.5	106
Figure 7.10: Crack strains E_{knn} of O2.1NR	106
Figure 7.11: Stirrup strains EZZ of O2.5	107
Figure 7.12: Stirrup strains EZZ of O2.1NR	107
Figure 7.13: Bond stress STSx of O2.5	107
Figure A.1: Force-displacement diagram of test beam R2 [2]	116
Figure A.2: Crack plots at different load levels of test beam R2 [2].....	117
Figure A.3: Strain in stirrups plots at different load levels of test beam R2 [2]	118
Figure A.4: Force-displacement diagram of test beam R4 [2]	119
Figure A.5: Crack plots at different load levels of test beam R4 [2].....	119
Figure A.6: Strain in stirrups plots at different load levels of test beam R4 [2]	120
Figure A.7: Force-displacement diagram of test beam R10 [2]	121
Figure A.8: Crack plots at different load levels of test beam R10 [2].....	121
Figure B.1: Force-displacement curve boundary springs vs. supports.....	122
Figure B.2: Principal strain E1 at 75% F_{ult} of solution strategy C1.1	123
Figure B.3: Principal strain E1 at 75% F_{ult} of solution strategy C1.1sup	123
Figure B.4: Displacement TDtX at F_{ult} of solution strategy C1.2.....	123
Figure B.5: Force-displacement curve stiffness of the steel plates.....	125
Figure B.6: Principal stresses S1 at the first load increment ($V=40$ kN) for solution strategy C1.1	125
Figure B.7: Principal stresses S1 at the first load increment ($V=40$ kN) for solution strategy C1.1Emod	125
Figure B.8: Crack width at ultimate loading for solution strategy C1.1Emod	125
Figure B.9: Force-displacement curve interface elements	127
Figure B.10: Principal strain E1 at 75% F_{ult} of solution strategy C1.1.....	127
Figure B.11: Principal strain E1 at 75% F_{ult} of solution strategy C1.1int1.....	127
Figure B.12: : Principal strain E1 at 75% F_{ult} of solution strategy C1.1int2.....	127
Figure C.1: Convergence behaviour solution strategy C1.1	128
Figure C.2: Convergence behaviour solution strategy C1.2	128
Figure C.3: Convergence behaviour solution strategy C1.3	129
Figure C.4: Convergence behaviour solution strategy C1.4	129
Figure C.5: Convergence behaviour solution strategy C1.5	130
Figure C.6: Convergence behaviour solution strategy O2.1	131
Figure C.7: Convergence behaviour solution strategy O2.2	131
Figure C.8: Convergence behaviour solution strategy O2.3	132
Figure C.9: Convergence behaviour solution strategy O2.4	132
Figure C.10: Convergence behaviour solution strategy O2.5	133
Figure C.11: Convergence behaviour solution strategy O2.6	133
Figure C.12: Convergence behaviour solution strategy O2.7	134

Figure C.13: Convergence behaviour solution strategy O2.8134
Figure C.14: Convergence behaviour solution strategy O2.9135
Figure C.15: Convergence behaviour solution strategy O2.10 (Divergence in final load step)135

List of tables

- Table 2.1: Influencing properties on the load transfer mechanisms13
- Table 5.1: Constant modelling assumptions.....66
- Table 5.2: Solution strategies for part 168
- Table 5.3: Bond-slip parameters longitudinal reinforcement and prestressing tendons71
- Table 5.4: Bond slip parameters stirrups.....71
- Table 5.5: Solution strategies for part 2.171
- Table 6.1: Overview of the results of part 175
- Table 6.2: Overview of the results of part 2.186
- Table 7.1: Summary of contribution to the shear resistance of the load-bearing mechanisms103
- Table 5.5: Solution strategies O2.1NR and O2.5.....105
- Table B.1: Geometrical properties of the concrete beam115
- Table B.2: Material properties of the test beams.....115
- Table C.1: Interface parameters of the two variants126

List of symbols

Greek

Symbol	Description	Unit
\emptyset	Bar diameter	[mm]
$\alpha_{c/3}$	Concrete compressive strain at 1/3 of the compressive strength	
α_1	Coefficient related to the form of the bars	
α_2	Coefficient related to the concrete cover	
α_3	Coefficient related to the effect of confinement by stirrups	
α_4	Coefficient related to the influence of welded transverse bars along the anchorage length	
α_5	Coefficient related to the pressure transverse to the plane of splitting	
α_c	Concrete compressive strain at the compressive strength	
α_{cw}	Factor that takes prestresses into account	
α_u	Ultimate concrete compressive strain	
γ_c	Partial factor for concrete	
$\varepsilon_1, \varepsilon_2, \varepsilon_3$	Principal strains	
ε_E	Energy convergence norm	
ε_F	Force convergence norm	
ε_n	Crack normal strain	
ε_s	Steel strain	
ε_u	Displacement convergence norm	
ε_{ult}	Ultimate concrete tensile strain	
η_1	Coefficient related to the quality of bond conditions	
η_2	Coefficient related to the bar diameter	
θ	Inclination of the shear crack	[Rad]
θ	Model uncertainty	
$\theta_{V,i}$	Model uncertainty for the ultimate shear strength for NLFEA solution strategy i	
ν	Poisson ratio	
ν^{cr}	Poisson ratio of cracked concrete	
ν_1	Reduction factor for cracked concrete due to shear	
ρ	Density	[kg/m ³]
ρ_l	Reinforcement ratio for longitudinal reinforcement	
$\sigma_1, \sigma_2, \sigma_3$	Principal stresses	[N/mm ²]
σ_{cp}	Axial prestress	[N/mm ²]
σ_M	Stress due to a bending moment	[N/mm ²]
σ_N	Stress due to an axial force	[N/mm ²]
σ_{sd}	Design stress of the bar	[N/mm ²]
σ_{swd}	Maximum design stress capacity of insufficiently anchored stirrups	[N/mm ²]
$\sigma_{xx}, \sigma_{yy}, \sigma_{zz}$	Normal stresses in x-, y and z-direction	[N/mm ²]
$\sigma_{xy}, \sigma_{yz}, \sigma_{zx}$	Shear stresses in xy-, yz- and zx-plane	[N/mm ²]
τ	Shear stress	[N/mm ²]
τ_1	Bond-stress at the onset of transverse cracking	[N/mm ²]
τ_2	Bond-stress at the onset of partial splitting	[N/mm ²]
τ_3	Bond-stress at the onset of through splitting	[N/mm ²]
τ_b	Bond-stress	[N/mm ²]
τ_{bf}	Bond stress after bond failure	[N/mm ²]
τ_{bmax}	Maximum bond stress	[N/mm ²]

Latin

Symbol	Description	Unit
A	Area of the cross-section	$[mm^2]$
A	Frictional resistance due to aggregate interlocking	$[kN]$
a	Shear span	$[mm]$
A_k	Area enclosed by the centrelines of the flanges and webs	$[mm^2]$
A_R	Area of the projection of a single rib	$[mm^2]$
A_{sw}	Cross-sectional area of a stirrup	$[mm^2]$
A_x	Frictional resistance due to aggregate interlocking in x-direction	$[kN]$
b	Width of the beam	$[mm]$
B_n	Dummy normal stiffness modulus	$[N/mm^3]$
B_t	Dummy shear stiffness modulus	$[N/mm^3]$
b_w	Effective width of the beam	$[mm]$
b_w	Width of the web	$[mm]$
c	Concrete cover	$[mm]$
D	Bar diameter	$[mm]$
d	Effective depth of a cross-section	$[mm]$
d_{agg}	Mean aggregate size	$[mm]$
d_b	Bar diameter	$[mm]$
E	Young's modulus	$[N/mm^2]$
E_c, E_{cm}	(Mean) Young's modulus of concrete	$[N/mm^2]$
E_s	Young's modulus of steel reinforcement	$[N/mm^2]$
$E1, E2, E3$	Principal strains in DIANA	
$Ecw1, Ecw2, Ecw3$	Crack width in principal directions in DIANA	$[mm]$
$Eknn$	Normal crack strain	
EXX, EYY, EZZ	Normal strains in x-, y- and z-direction in DIANA	
f_{bd}	Design ultimate bond stress for ribbed bars	$[N/mm^2]$
f_c, f_{cm}	(Mean) compressive strength	$[N/mm^2]$
f_{cd}	Concrete compressive design strength	$[N/mm^2]$
f_{ck}	Characteristic compressive cylinder strength of concrete	$[N/mm^2]$
f_{ct}	Concrete tensile strength	$[N/mm^2]$
f_{ctd}	Design concrete tensile strength	$[N/mm^2]$
$f_{p0.1k}$	Characteristic 0.1% proof stress for prestressing tendons	$[N/mm^2]$
$f_{p0.1k}$	Characteristic tensile strength for prestressing tendons	$[N/mm^2]$
f_R	Relative rib area	
f_{sy}, f_y	Steel yield strength	$[N/mm^2]$
f_t	Tensile strength	$[N/mm^2]$
f_{ywd}	Design yield strength of a stirrup	$[N/mm^2]$
G	Elastic shear modulus	$[N/mm^2]$
G^{cr}	Shear modulus of cracked concrete	$[N/mm^2]$
G_C	Compressive fracture energy	$[N/mm]$
G_F	Tensile fracture energy	$[N/mm]$
h	Height of the beam	$[mm]$
h_{eq}, h	Crack bandwidth	$[mm]$
I	Moment of inertia	$[mm^4]$
k	Size effect factor	
k_{spring}	Spring stiffness	$[N/mm]$
l	Length of the beam	$[mm]$
$l_{b,min}$	Minimum anchorage length	$[mm]$
$l_{bd,aanw}$	Existing effective/anchorage design length in the compression zone	$[mm]$

$l_{bd}, l_{b,rqd}$	Required effective/anchorage design length	[mm]
M	Bending moment	[kNm]
N	Axial force	[kN]
n	Number of ...	
p	Pressure	[N/mm ²]
Q	First moment of area	[mm ³]
R_{exp}	Result from experiment	
R_{NLFEA}	Result from nonlinear finite element analysis	
s	Shear flow	[N/mm]
s	Slip	[mm]
s	Spacing between stirrups	[mm]
s_R	Rib spacing	[mm]
$STsx$	Bond stress in DIANA	[N/mm ²]
$S1, S2, S3$	Principal stresses in DIANA	[N/mm ²]
T	Torsional moment	[kNm]
$t_{eff,i}$	Effective thickness of flange/web i	[mm]
t_i	Thickness of flange/web i	[mm]
$TDtx, TDty, TDtz$	Displacement in x-, y- and z-direction in DIANA	[mm]
u	Perimeter of the cross-section	[mm]
V	Shear force	[kN]
$V_{Rd,c}$	Design shear resistance	[kN]
$V_{Rd,max}$	Design maximum shear resistance of the concrete struts	[kN]
$V_{Rd,s}$	Design shear resistance of the stirrups in an inclined crack	[kN]
$V_{Rk,c}$	Characteristic shear resistance	[kN]
$V_{ult,exp}$	Ultimate experimental shear load	[kN]
$V_{ult,NLFEA,i}$	Ultimate shear load for NLFEA solution strategy i	[kN]
V_{ay}, V_{agg}, A_y	Frictional (shear) resistance due to aggregate interlocking in y-direction	[kN]
V_c	Shear resistance of the compression zone	[kN]
V_d	Shear resistance due to dowel action	[kN]
$V_{prestress}$	Shear resistance due to prestressing	[kN]
V_s	Shear resistance of the stirrups	[kN]
$V_{tendons}$	Vertical (shear resisting) component of prestressing tendons	[kN]
V_{ult}, V_{max}	Ultimate shear load	[kN]
V_{yield}	Shear load at the onset of stirrup yielding	[kN]
w_1, w_2, w_3	Crack width in the principal directions	[mm]
x_u, x	Height of the compression zone	[mm]
z	Distance in z-direction to the neutral line	[mm]
z	Lever arm between the compression and tension chord	[mm]

1 Introduction

1.1 Background and motivation

Rijkswaterstaat manages over 4000 bridges in the Netherlands, of which about 160 are concrete box-girder bridges. Most of them were built before 1990. Nowadays, the traffic load is much higher and the standards are much stricter. This means that most bridges require reassessment to guarantee structural safety. Many of the box-girder bridges are designed in the same way, so often the same problems occur. To clarify the problem this thesis focusses on, the Rooyensteijnse brug (bridge) in Tiel is used as an example (used case).

The Rooyensteijnse brug is a cantilever bridge consisting of box-girder beam elements varying in height, shown in Figure 1.1. Half of the cross-section at the third support from the left is shown in Figure 1.2. The open straight-legged stirrups in the web caused a problem with the reassessment of the bridge [4]. According to current engineering standards, the open ends at the top of the web are not allowed, as opposed to engineering standards of the past. Therefore, Eurocode 2 (EC2) does not take this type into account for the calculations of shear and torsion, resulting in lower shear and torsional resistance.

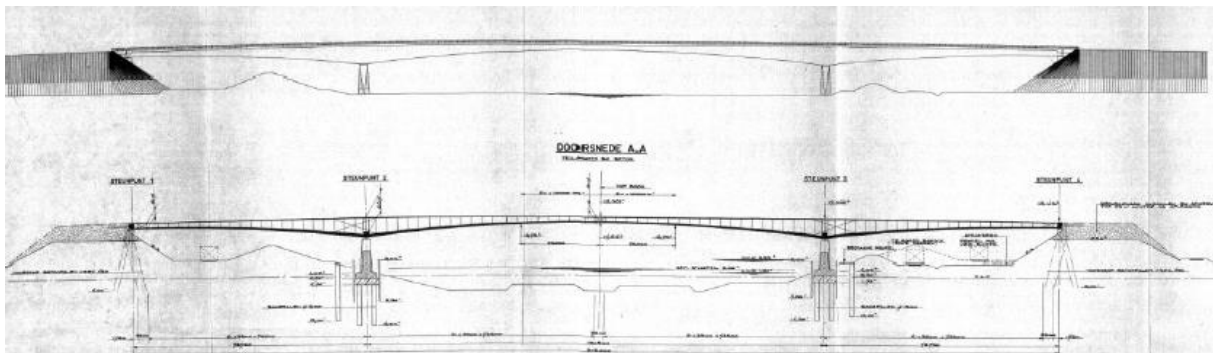


Figure 1.1: The Rooyensteijnse brug [5]

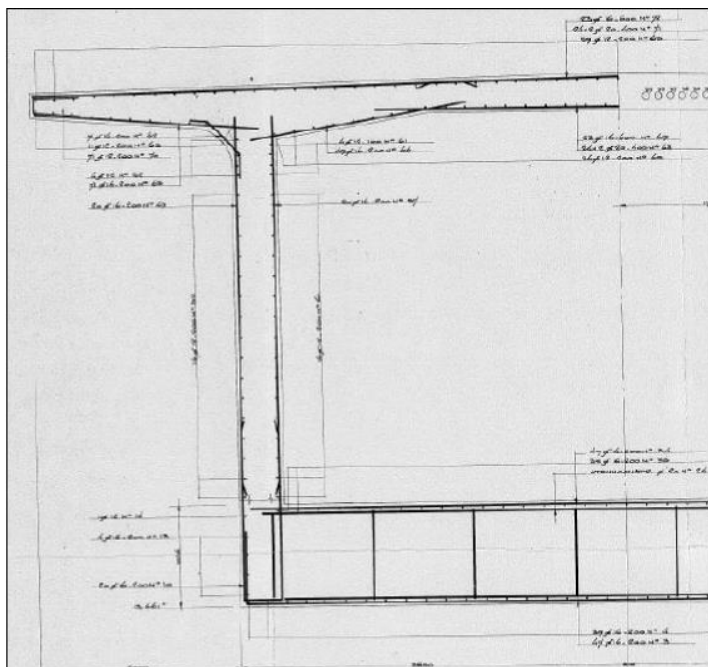


Figure 1.2: Half of the cross-section of the Rooyensteijnse brug at the third support from the left [6]

The shear resistance according to Eurocode 2 is based on the strut-and-tie model (Figure 1.3). This simplified approach idealizes stress patterns and is based on the lower bound theorem of plasticity [7]. It estimates the forces based on nodal equilibrium, with compression in the concrete diagonals (struts) and tension in the longitudinal and vertical shear reinforcement (ties). To satisfy nodal equilibrium, it must be possible to transfer forces in these nodes, so the struts and ties must be connected. In EC2, it is stated that stirrups should enclose the longitudinal tension reinforcement and the compression zone unless sufficient anchorage in the compression zone is possible. However, no requirements for the anchorage are described.

Figure 1.4 shows how longitudinal and shear reinforcement nowadays commonly are connected. The shear reinforcement encloses the top and bottom longitudinal reinforcement. Zooming in on the top part of the web of the Rooyensteijnse brug (see Figure 1.5), it can be seen that there is no closed connection between the top longitudinal reinforcement and the open stirrups. Following the approach of the strut-and-tie model, transfer of forces is not possible, so nodal equilibrium cannot be satisfied [8]. It is noted that torsional resistance is also based on a strut-and-tie model, but this is not discussed in detail within this thesis.

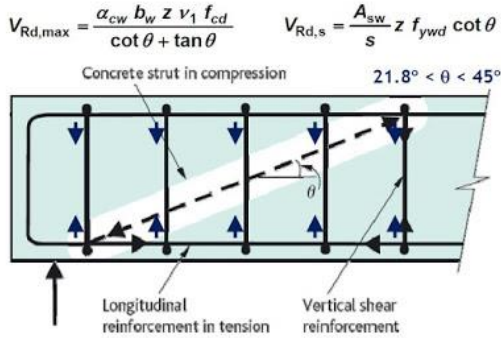


Figure 1.3: Strut-and-tie model for shear in concrete beams [9]

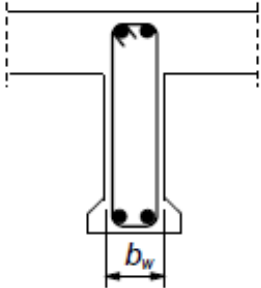


Figure 1.4: Correct detailing of stirrups [8]

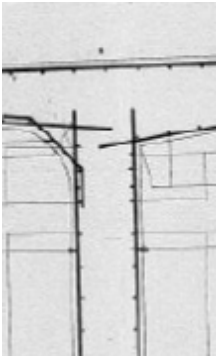


Figure 1.5: Incorrect detailing of stirrups [5]

Following the standards described in EC2, large cracks might be expected in the webs of the Rooyensteijnse brug. However, significant cracks are not yet observed, which indicates there are load-bearing reserves that are not taken into account.

To bridge the gap between current Eurocode standards, past practices as well as real-life observations, some extra requirements are proposed for insufficiently anchored stirrups in the Richtlijnen Bestaande Kunstwerken 1.2, or simply RBK1.2 [10]. For stirrups that do not enclose the compression zone, the existing and required effective design lengths $l_{bd,aanw}$ and l_{bd} in the compression zone (see Figure 1.6) are determined to judge if the stirrups are sufficiently anchored in the concrete, and therefore the possible amount of load transfer. This line of thought is adapted from the theory that is used to describe the anchorage of longitudinal reinforcement in EC2. This l_{bd} is the design length that is required to fully transfer the stresses from the concrete to the steel and vice versa. Then, the same equation as in EC2 for shear reinforcement is used, only the design yield strength in the stirrups f_{ywd} is replaced by the following equation [10]:

$$\sigma_{swd} = \frac{l_{bd,aanw}}{l_{bd}} f_{ywd} \leq f_{ywd} \tag{1.1}$$

In other words, it is assumed that the stirrups are anchored and part of the yield strength can be achieved. However, another requirement states that the stirrups should enclose the tension zone. This requirement is not met for some of the stirrups of the used case, because the tension zone close to the support is at the top side of the cross-section. So theoretically, for a part of the stirrups, it is still not possible to transfer loads according to the strut-and-tie model and no shear capacity can be derived for the open straight-legged stirrups.

Considering the approach of EC2 and the extra requirements described in the RBK 1.2, the following is concluded:

- The strut-and-tie model used in EC2 results in an underestimation of the actual shear resistance in concrete beams. Therefore it is always a safe approach for design, but it causes problems for the reassessment of existing structures with open straight-legged stirrups;
- According to EC2, it is possible to take insufficiently anchored stirrups into account for the determination of the shear capacity, but no requirements are given here;
- In RBK 1.2, requirements are given for insufficiently anchored stirrups to be able to take these into account for the determination of the shear capacity. According to TNO (TNO, personal communication, 21-04-2022), these requirements are based on the engineering judgement of the RBK committee and the assumption that open stirrups are anchored in the compression zone in terms of an anchorage length. If this anchorage length is sufficient, the same stress capacity as described in EC2 can be derived for the open stirrups. For shorter anchorage lengths, a reduced portion of the stress capacity may be taken into account. Also, stirrups must enclose the tension zone. These requirements are not validated based on shear tests, but the RBK committee assumes that it results in an underestimation of the actual shear capacity and therefore assumes that this is safe;
- Since EC2 and RBK1.2 state that the tension zone must be enclosed, it remains unknown what capacity can be assigned to stirrups where the open straight-legged ends are anchored in the tension zone.

Since both EC2 and RBK1.2 do not provide a complete solution to determine structural capacity, it is important to identify what the actual influence of the open straight-legged stirrups anchored in the tension zone is on the shear resistance and behaviour of the beam.

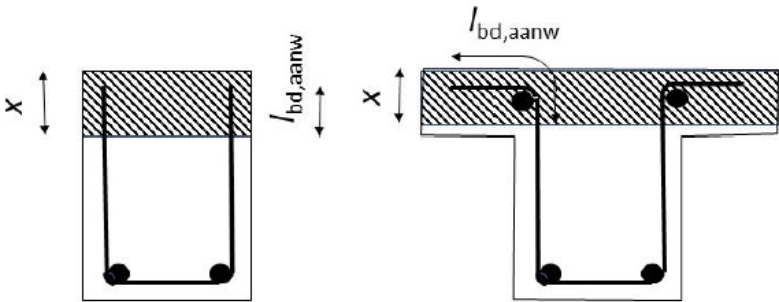


Figure 1.6: Existing effective length $l_{bd,aanw}$ in the compression zone for open stirrups [10]

Schramm [2] investigated the influence of multiple no longer permitted stirrup configurations (see Figure 1.7) for prestressed continuous beams with rectangular (and T-shaped) cross-sections (see Figure 1.8). This research is very useful and comparable to the problem due to three main reasons:

- The tested beams fail due to shear;
- Stirrup type (a) in Figure 1.7 has the same shape as used in the web of the used case;
- The test setup was based on a continuous beam, which leads to interaction between axial force, shear force and bending moment. This leads to failure in the middle support region, where the tension zone is not enclosed by the open straight-legged stirrups.

This research provides insight into the influence of open straight-legged stirrups in rectangular cross-sections with a relatively low shear reinforcement ratio. However, this knowledge is not directly applicable for general use (different load cases, cross-sections, reinforcement properties, etc.). To be able to provide a more accurate reassessment of existing bridges, a better understanding of the influence of open straight-legged stirrups under different circumstances is necessary.

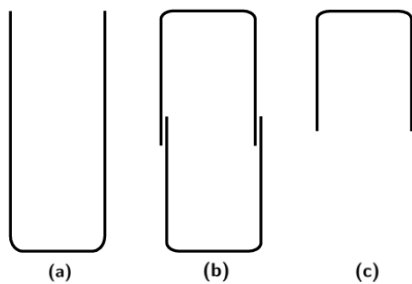


Figure 1.7: Incorrectly detailed stirrup types¹ [2]

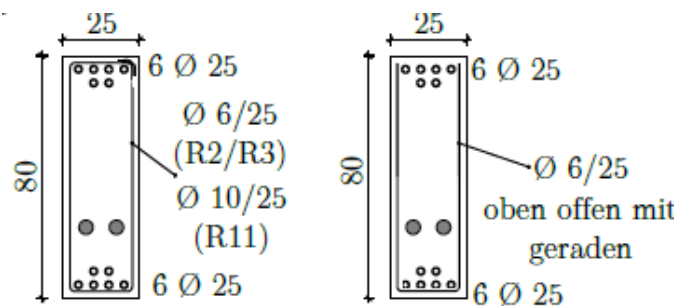


Figure 1.8: Relevant tested cross-sections [2]

It is important that a valid comparison between Schramm's research [2] and existing bridges with the same type of shear reinforcement can be made. Therefore, the behaviour of concrete structures with rectangular and box-girder cross-sections must be investigated to point out the assumptions that must be taken into account for comparison.

With the use of Finite Element Analyses (FEA), the behaviour of structures is evaluated and properties can be easily adjusted. This could be a useful tool to get a better understanding of the influence of open straight-legged stirrups under different circumstances. Usually, stirrups in Finite Element Models (FEM) are modelled with a perfect bond, assuming perfect anchorage. In general, such models show very good agreement with structures containing correctly detailed stirrups, like closed stirrups, since such stirrups are very well anchored by means of hooks, bends or welds. In reality, the bond between reinforcements and concrete is far from perfect and this bond is the only mechanism that provides the anchorage of the open straight-legged ends of an open straight-legged stirrup. Therefore, it is necessary to describe a more realistic anchorage behaviour for such stirrups. Finite Element Models using this stirrup configuration are not found in literature, so the possibilities within this field must be investigated as well.

¹ Stirrup type b is allowed in current engineering standards, provided that a sufficient overlap length is present. However, Schramm [2] investigated this type with a short overlap length.

1.2 Scope, research questions and methodology

This master thesis aims to provide a finite element modelling strategy that is able to accurately describe the behaviour of concrete beams with open straight-legged stirrups subjected to shear. This strategy contains a description of the constitutive and kinematic relations and the equilibrium conditions.

To achieve this, the focus is on describing the behaviour of rectangular concrete beams with open and closed straight-legged stirrups with finite element models in DIANA 10.5 [1]. These models are based on and validated with the experimental results from Schramm [2]. The following main question is defined:

*How can the **behaviour of open straight-legged stirrups** in concrete beams subjected to **shear** be explained with a **finite element model**?*

To answer this main question, the following sub-questions are defined:

1. How do different mechanisms of a concrete beam contribute to the shear resistance?
2. How are these different mechanisms taken into account in a finite element model?
3. How do concrete beams with open straight-legged stirrups sustain shear forces?

The first sub-question focusses on which mechanisms contribute to the shear resistance, how these mechanisms resist shear and which properties influence the capacity of these mechanisms. The answer to this follows from literature. The second sub-question connects the theory and FEM. Common modelling methods are described for the shear load-bearing mechanisms, as well as other important aspects of finite element modelling. The final sub-question focusses on the evaluation of different FE solution strategies for beams with closed and open straight-legged stirrups, including kinematic, constitutive and equilibrium relations, and compares these with Schramm's experimental results [2].

1.3 Thesis outline

The thesis outline is visually presented in Figure 1.9. Chapters 2 and 3 contain the literature study. In chapter 2, the theory of shear in concrete beams is described. After this chapter, it is clear which and how different mechanisms contribute to the shear resistance of a concrete beam. This is followed by explanations and recommendations from literature for the modelling of prestressed reinforced concrete beams in Chapter 3. After this chapter, it is clear how the relevant mechanisms are taken into account in a finite element model.

Chapter 4 contains the experimental benchmark of Schramm [2]. This chapter comprises two parts. In the first part, a comparison between the cross-sections of a box-girder and rectangular beam are compared, focussing on stress flows due to axial forces, bending, shear and torsion. Here, it is validated if Schramm's experiments are relevant to compare with box-girder bridges. The second part describes relevant aspects of Schramm's research, including the experimental setup and results.

Chapters 5, 6 and 7 describe the numerical study, where a distinction is made between FE models with closed and open straight-legged stirrups. In Chapter 5, the FEM approach is described, including the modelling choices for the investigated solution strategies and the judgement of the results. In Chapter 6, the FE results for the multiple solution strategies are presented and compared with the experimental results. Notable results are discussed in Chapter 7. Lastly, the research questions are answered and recommendations for further research are given in Chapter 8.

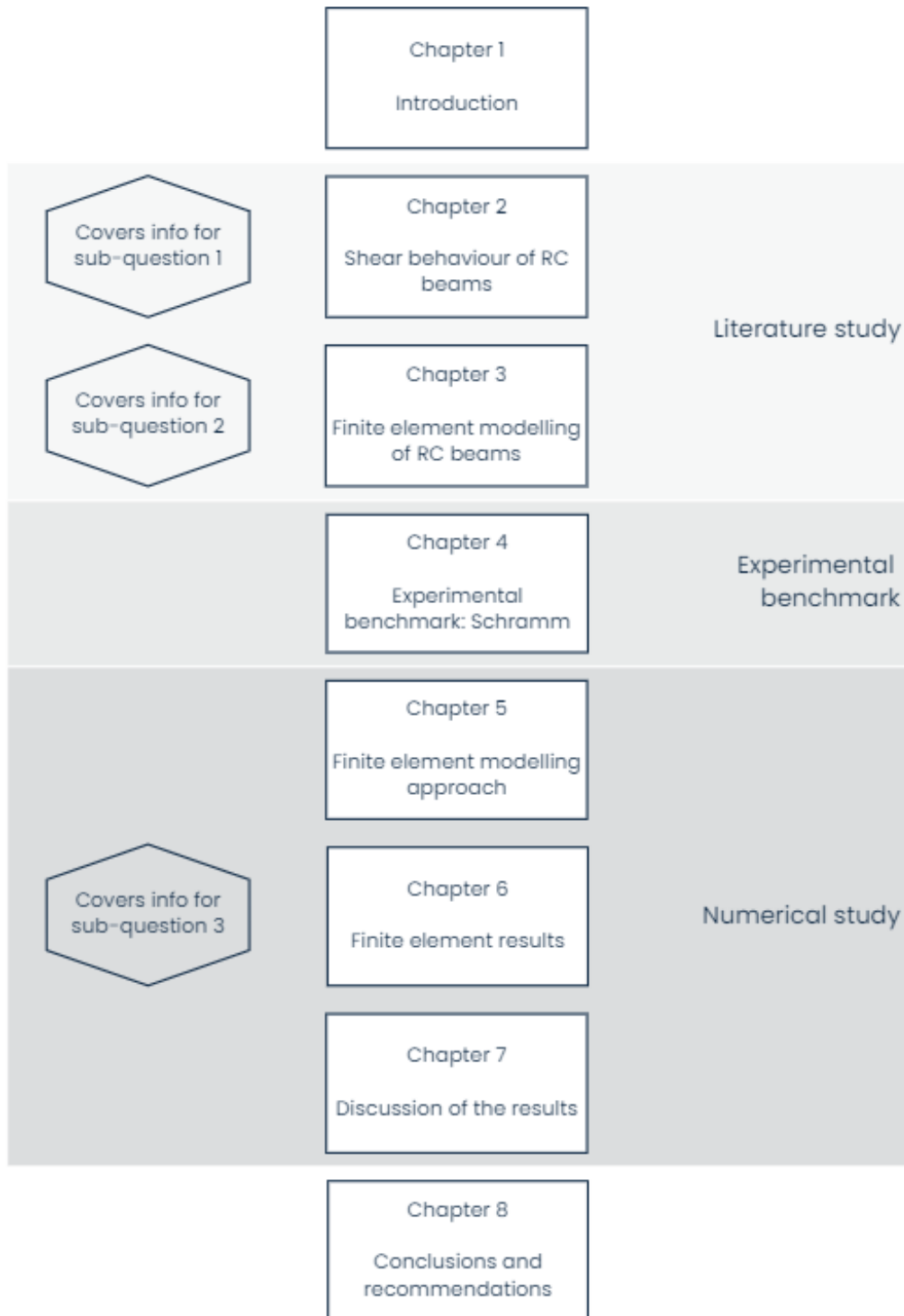


Figure 1.9: Thesis outline

2 Shear behaviour of RC beams

This chapter focusses on the theoretical background of the shear resistance of Reinforced Concrete (RC) beams. Multiple mechanisms and many different properties influence the shear behaviour of concrete beams and are covered in this chapter.

2.1 Shear in an uncracked concrete beam

Uncracked concrete beams subjected to shear and bending behave like homogeneous elastic beams. In Subsection 4.1.4, the acting shear stresses due to a shear force on an elastic beam are discussed in more detail. The resulting shear stress is:

$$|\tau| = \frac{VQ}{bI} \quad (2.1)$$

Where:

- τ Shear stress
- V Shear force
- Q First moment of area
- b Width of the beam
- I Moment of inertia

This results in maximum shear stress in the middle of a rectangular cross-section. Since a vertical force acting on a beam also causes a bending moment, shear stresses occur in combination with tensile or compressive stresses shown in Figure 2.1a. The bending causes a linear distribution of axial (or flexural) stresses, with maximum compression at the top and maximum tension at the bottom. Taking the axial and shear stresses into consideration, the principal stresses can be found by rotating the elements in the beam, which is shown in Figure 2.1c [11].

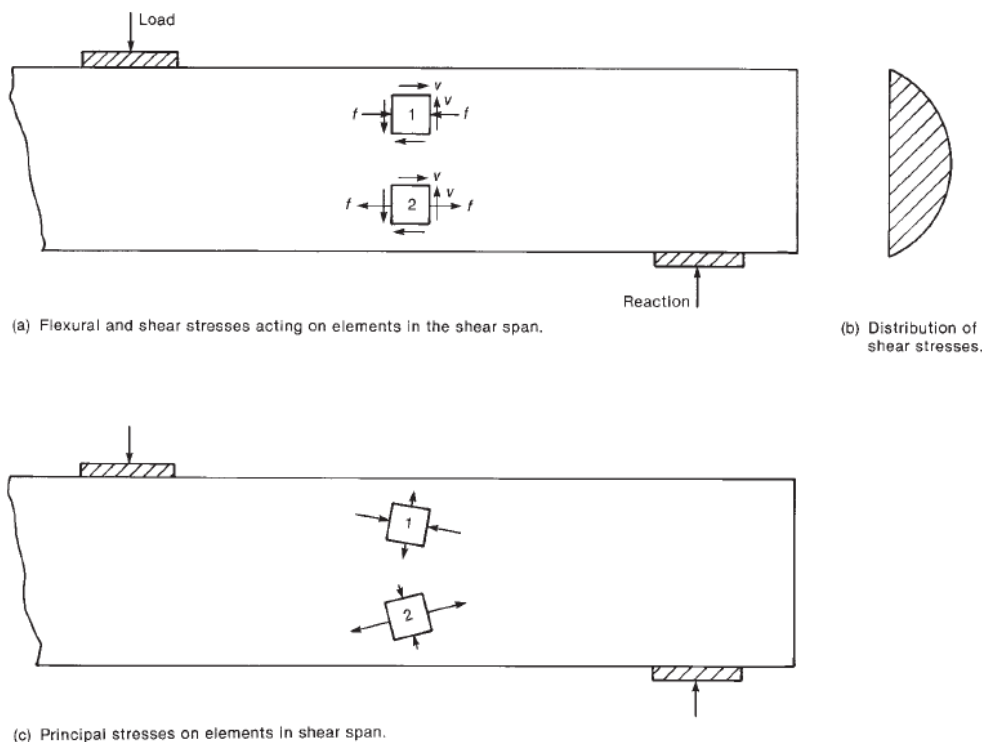


Figure 2.1: Axial, shear and principal stresses in a homogeneous elastic beam [11]

The principal stress directions can be evaluated for the whole beam. Doing this for the part between the acting load and support results in the compressive stress trajectories shown in Figure 2.2a. The trajectories at the bottom of the beam are vertical because the shear stresses are zero at the bottom and tensile stresses occur due to bending. At the top, the shear stresses are also zero, but compressive stresses occur due to bending, resulting in horizontal trajectories. Perpendicular to these compressive trajectories act the principal tensile stresses. Since concrete has a very small tensile strength, cracks are expected along these compressive trajectories [11].

When a crack develops, redistribution of stresses is necessary to maintain equilibrium. When there is no longitudinal reinforcement, tensile stresses occur above the crack, leading to the further development of this crack. Again, this leads to redistribution of stresses, causing further development of the crack and so on until the beam fails. This process occurs fast, so when a crack occurs, the beam almost immediately fails. Therefore, some minimum longitudinal reinforcement is required.

In Figure 2.2b, a cracked concrete beam with longitudinal reinforcement at the bottom is shown. Below the acting load, vertical flexural cracks occur due to large flexural tensile stresses. The diagonal cracks occur between the load and support, where there is an interaction between flexure and shear. These cracks are commonly referred to as inclined cracks, shear cracks or diagonal tension cracks [11].

The flexural and inclined cracks somehow show some correspondence with the expected direction following from the principal compressive stress trajectories. However, this relationship is far from tight. In general, flexural cracks occur before shear stresses at midheight become critical. The tensile strength perpendicular to these cracks becomes zero. To maintain equilibrium, a major redistribution of stresses is necessary and is therefore extremely difficult to predict [11].

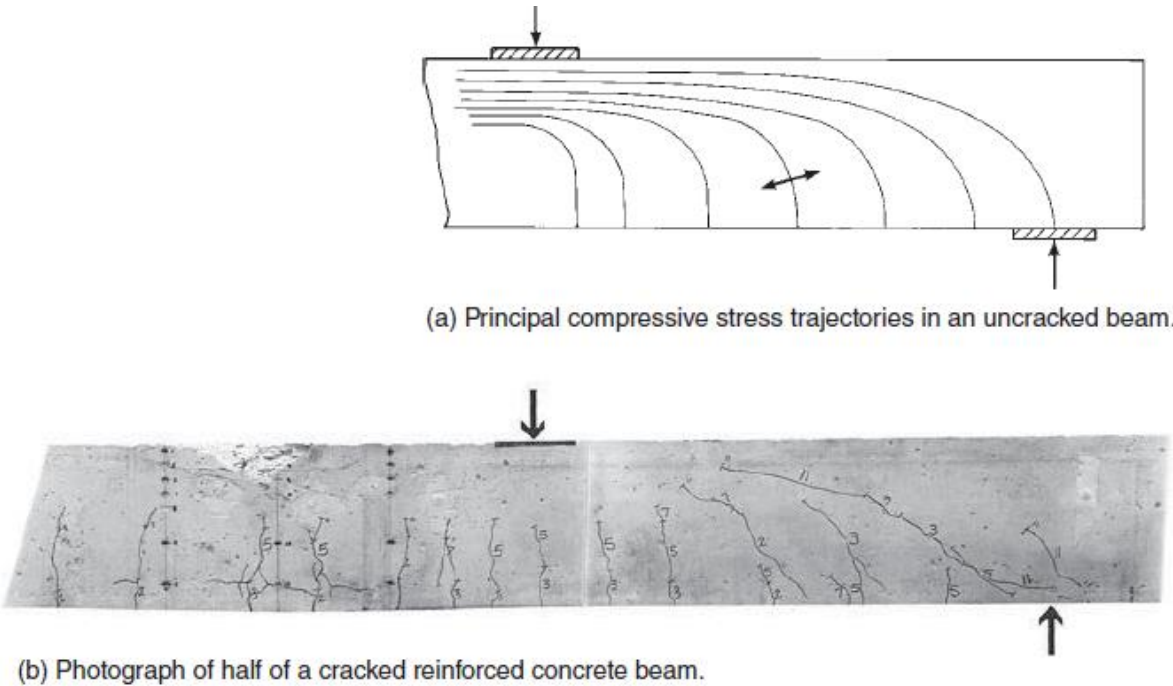


Figure 2.2: Principal compressive stress trajectories and inclined cracks [11]

2.2 Shear resistance of a cracked concrete beam without stirrups

The behaviour of a cracked concrete beam without transverse reinforcement failing in shear is dependent on many factors and load transfer mechanisms. The possible failure mechanisms, the load transfer (or load-bearing) mechanisms and their influencing properties are investigated.

2.2.1 Failure mechanisms

A concrete beam can fail in shear in different ways, but before it can fail in shear, inclined cracks have to develop. Two types of inclined cracks are possible: web-shear cracks (or diagonal tension cracks) and flexure-shear cracks. The types are shown in Figure 2.3. Web-shear cracks occur where flexural stresses are small and only shear stresses occur. These cracks are likely to occur around midheight because the shear stresses are largest there. Flexure-shear cracks occur where flexural and shear stresses are present. First flexural cracks develop. Some of these flexural cracks could further develop diagonally, which are the flexure-shear cracks. This type of cracking cannot be predicted by calculating the principal stresses, which makes it difficult to estimate the shear strength of reinforced concrete beams. Therefore, empirical equations based on experiments are used in current standards.

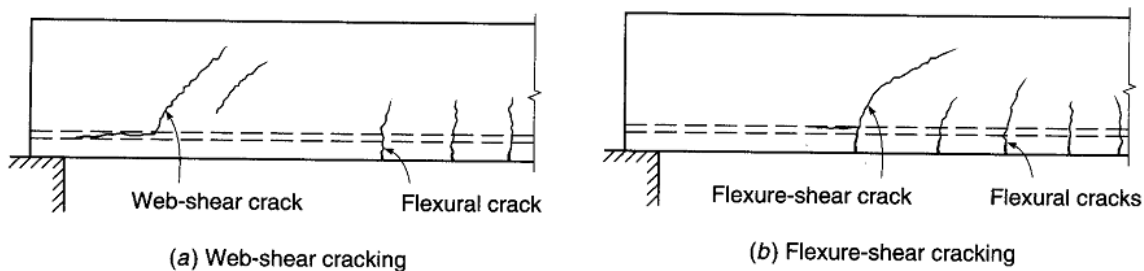


Figure 2.3: Types of inclined cracks [12]

Two important parameters for the possible failure mode are the shear span a and effective depth d , often used as the shear span to depth ratio a/d . These parameters determine the possible stress flows and therefore the possible failure mechanisms. Four types of shear spans are defined: very short, short, slender and very slender shear spans.

Very short shear spans ($0 \leq a/d \leq 1$) develop shear cracks from the support to the load. Since this crack cuts to almost the whole shear span, horizontal shear flow is not possible. The load is transferred to the support using arch action (see Figure 2.4) instead of beam action (see Figure 2.10). The longitudinal reinforcement acts as a tension tie with uniform tensile stresses from support to support. The most common failure mode is anchorage failure, but also bearing failure, flexural failure and failure of the compression strut can occur. The failure modes are shown in Figure 2.5.

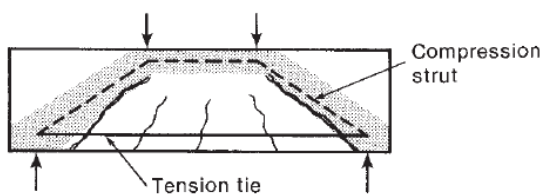


Figure 2.4: Arch action in a very short shear span [11]

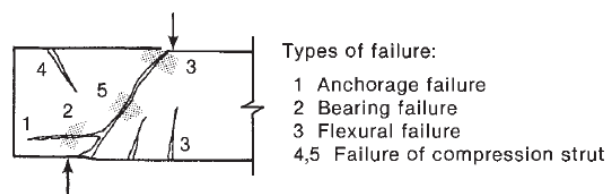


Figure 2.5: Failure modes of a very short shear span [11]

Short shear spans ($1 \leq a/d \leq 2.5$) also develop shear cracks and can carry additional load partly due to arch action. Multiple flexural and inclined cracks could develop. Eventually, failure occurs caused by bond or dowel failure along the longitudinal reinforcement (shear-tension failure) or by crushing of the compression zone on top of the crack (shear-compression failure). These failure modes are shown in Figure 2.6. The inclined cracks generally extend higher than flexural cracks, causing failure at less than the flexural moment capacity.

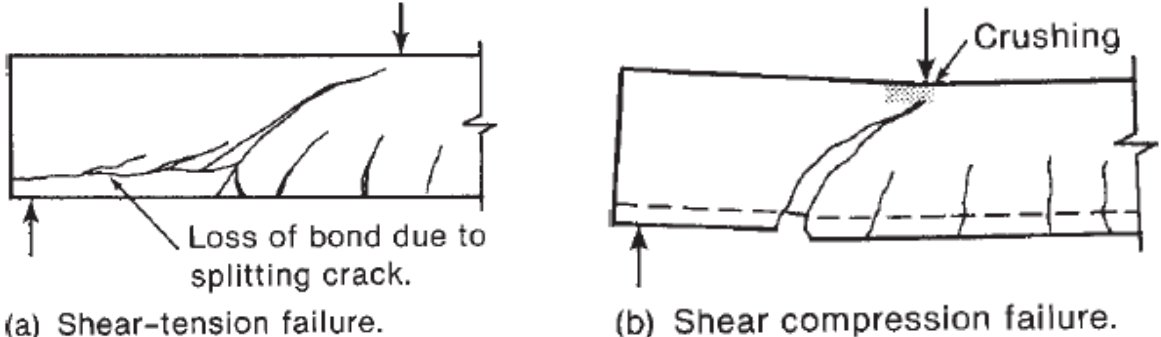


Figure 2.6: Failure modes of a short shear span [11]

Slender shear spans ($2.5 \leq a/d \leq 6$) immediately fail after inclined cracks occur. This is because the load must be completely transferred by beam action, which can be explained with a strut-and-tie model shown in Figure 2.10. The shear force is transferred downwards with a compressive diagonal strut but has not reached the support. Therefore this force must be brought back to the top with a tensile tie, where it can be transferred downwards again until it reaches the support. When an inclined crack occurs, it is nearly not possible to transfer the load back to the top, because the residual tensile strength perpendicular to the inclined crack quickly drops to zero. Therefore it is not possible to satisfy equilibrium, causing failure directly after inclined cracking. This brittle failure is unwanted, so shear reinforcement is almost always required for this type of beam.

Very slender beams ($a/d > 6$) tend to fail in flexure, because the flexural capacity is reached before inclined cracking occurs.

2.2.2 Load transfer mechanisms

In a beam without stirrups, shear is resisted by shear in the compression zone V_c , aggregate interlocking along the crack A_y and dowel action of the longitudinal reinforcement V_d . This is graphically presented in Figure 2.7.

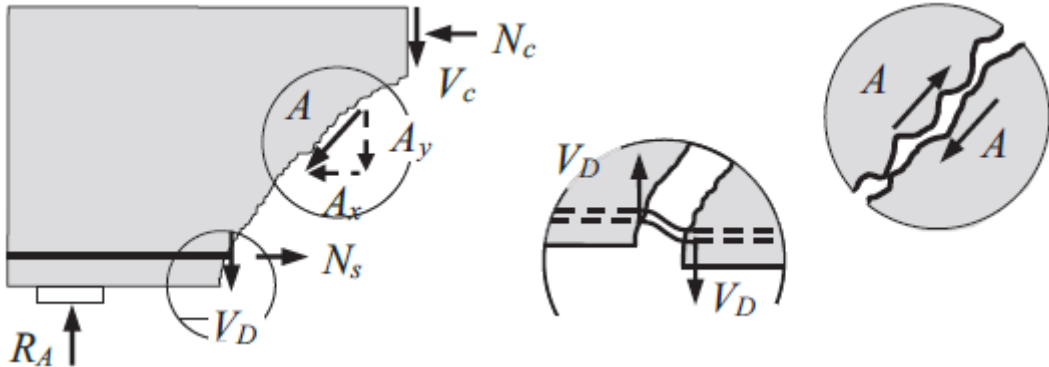


Figure 2.7: Internal forces in a cracked concrete beam without shear reinforcement [13]

The shear resistance of the compression zone is described with cracked-elastic behaviour, which means that shear is resisted in the same way as uncracked concrete described in the previous section.

Aggregate interlocking is the phenomenon where shear stresses can be transferred due to the roughness of the surface of the crack. The two surfaces of the crack need to slide over each other, which causes friction, so shear resistance. The rougher the surfaces, the harder it is to slide over each other, so the larger the shear resistance.

Shear stresses resisted by the longitudinal reinforcement is done by dowel action. When a crack forms, the crack surfaces tend to slip, causing a deflection in the reinforcement. This deflection is resisted by the bar, resulting in a vertical shear force and a bending moment. Thicker reinforcement bars result in a larger shear resistance.

Bogdány [13] investigated the shear resistance of a concrete member without shear reinforcement according to Eurocode 2. The characteristic shear resistance without prestressing, assuming sufficient longitudinal reinforcement, is [8]:

$$V_{Rk,c} = \gamma_c V_{Rd,c} = 0.18k(100\rho_l f_{ck})^{\frac{1}{3}} b_w d \quad (2.2)$$

$$k = 1 + \sqrt{\frac{200}{d}} \leq 2.0 \quad (2.3)$$

Where:

$V_{Rk,c}$	Characteristic shear resistance
$V_{Rd,c}$	Design shear resistance
γ_c	Partial factor for concrete
k	Size effect factor
ρ_l	Reinforcement ratio for longitudinal reinforcement
f_{ck}	Characteristic compressive cylinder strength of concrete
b_w	Width of the web
d	Effective depth of the cross-section

This equation assumes that shear is completely resisted by the compression zone, so aggregate interlocking and dowel forces are neglected. This seems arbitrary, but it is valid when the ultimate shear load is approached. This can be explained as followed:

- With an increasing shear force, the shear cracks widen, causing a decrease in aggregate interlocking;
- Splitting cracks in the concrete along the longitudinal reinforcement form with increasing shear force, causing a decrease in bond strength between the concrete and reinforcement. This means that it becomes harder to transfer shear stresses between the concrete and reinforcement, reducing the dowel forces.

Bogdány [13] compared experimental results with the shear resistance according to Eurocode 2 [8] and showed good correspondence. It was therefore concluded that the assumptions above are correct and that the shear resistance of a concrete beam without shear reinforcement is well described by the shear resistance of the compression zone. Still, it could be valuable to investigate the influencing properties of aggregate interlocking and dowel action, because it might be of larger influence for beams with open stirrups.

Also, prestressing of a concrete beam significantly contributes to the shear behaviour. Assuming a garland-shaped prestressed tendon, the shear resistance is improved in terms of the following [14]:

1. The axial prestress σ_{cp} on the beam causes the beam to be in compression. Therefore, the tensile stresses compared to a non-prestressed beam are reduced. This means that a larger force is required to reach the tensile strength of the concrete and initiate the cracking of the beam. This contributing part is also taken into account in Eurocode 2 [8], where it is added to the contribution of the concrete:

$$V_{prestress} = 0.15\sigma_{cp}b_wd \quad (2.4)$$

2. The vertical component of the prestressing tendon directly contributes to the shear resistance in the same way stirrups do.
3. The prestress tendon reduces the propagation and widening of diagonal shear cracks in the same way stirrups do.

2.2.3 Properties that influence the shear capacity

It is not possible to describe the shear behaviour of a reinforced concrete beam with the theory of principal stresses, which makes it difficult to determine the shear capacity. For this reason, shear capacity equations are derived empirically from many tests varying in dimensions, concrete strength, reinforcement ratio etc. Below, the most important properties that determine the shear strength and how these properties influence the shear strength are described [11]. These properties and some other factors are summarized in Table 2.1.

Tensile and compressive strength of concrete

Both the tensile and compressive strength of concrete influence the shear capacity of uncracked concrete, so the shear resistance of the compression zone. The failure criterion used in Eurocode 2 is based on compressive strength (or tensile strength, since these strengths are also related) and has therefore a large impact on the ultimate shear resistance of concrete beams without shear reinforcement. It also influences the aggregate interlocking, since the onset of cracking is also dependent on the strength of the concrete.

Longitudinal reinforcement ratio

The longitudinal reinforcement ratio contributes to all three load-bearing mechanisms. First, from moment equilibrium, it follows that the horizontal forces caused by the compression zone and longitudinal reinforcement should be equal (neglecting the horizontal force caused by aggregate interlocking). Therefore, the height of the compression zone is a function of the longitudinal reinforcement ratio [13]. Second, longitudinal reinforcement causes a decrease in the length and width of flexural cracks, resulting in a larger shear resistance due to aggregate interlocking. Third, a larger cross-sectional area of the longitudinal reinforcement results in a larger dowel force [11]. It can be concluded that a larger longitudinal reinforcement ratio results in an increase in shear resistance for all three mechanisms.

Type and size of aggregate

The type and size of aggregates influence the shear resistance due to aggregate interlocking. In theory, an increase in aggregate size causes a rougher crack surface, so an increase in shear resistance. However, sometimes the cracks cut right through the aggregate, causing a smoother surface. For instance, this is the case in high-strength concrete beams [13]. Therefore the type of aggregate is also important.

Shear span to depth ratio (a/d)

The shear span to depth ratio determines if additional shear capacity is possible due to arch action. This is the case for short shear spans and changes the behaviour of the beam. For larger values for a/d , this factor has very little influence.

Effective depth

From tests, it followed that an increasing depth has a negative influence on the shear resistance. This size effect is a remarkable phenomenon which is not entirely clear. It is therefore investigated a lot. Recent literature tends to reason it has to do with aggregate interlocking. An increase in size means that wider cracks are possible, so a decrease in aggregate interlocking. However, a size effect factor is applied in design formulas based on the shear resistance of the compression zone.

Axial forces

Axial forces have a direct influence on the shear strength. Tension increases strain in the longitudinal reinforcement, causing wider cracks, so lower shear resistance due to aggregate interlocking. Compression does the opposite, so reducing strain in longitudinal reinforcement leads to increasing shear resistance. This means that prestressing has a positive influence on the shear resistance.

Table 2.1: Influencing properties on the load transfer mechanisms

Load transfer mechanisms	Influencing properties
Shear resistance of the compression zone	Compressive and tensile strength of concrete Longitudinal reinforcement ratio Effective depth (in design formulas) Axial forces (due to prestress)
Aggregate interlocking	Compressive and tensile strength of concrete Longitudinal reinforcement ratio Type and size of aggregate Effective depth (presumed in recent literature) Axial forces (due to prestress)
Dowel action	Longitudinal reinforcement ratio Concrete cover Bond strength of concrete and reinforcement Anchorage of longitudinal reinforcement

2.3 Shear resistance of a cracked concrete beam with closed stirrups

In the previous section, it is shown that failure due to shear is very brittle, which is unwanted in design. Due to this reason, stirrups are commonly used to increase the shear resistance of concrete beams. If sufficient shear reinforcement is used, the concrete beam can sustain shear forces until the flexural capacity is reached, resulting in flexural failure. Thus, this ductile failure is safer since the structure 'warns' before it ultimately fails.

2.3.1 Typical behaviour of a reinforced concrete beam with stirrups

A typical force-displacement curve of a reinforced concrete beam is shown in Figure 2.8. The contribution to the shear resistance for different mechanisms is shown in Figure 2.9 (V_{cy} = shear in compression zone, V_d = dowel action, V_{ay} = aggregate interlocking, V_s = stirrups).

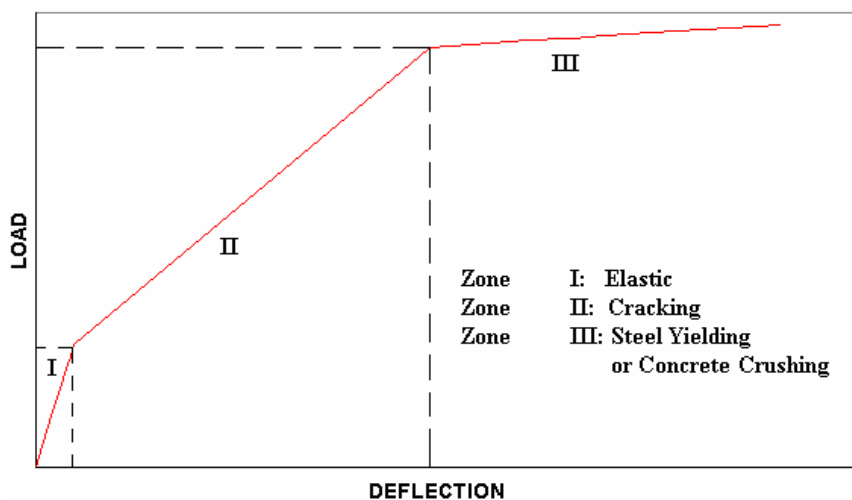


Figure 2.8: Typical force-displacement curve of a reinforced concrete beam [15]

In the uncracked elastic stage, the strain in stirrups is the same as the concrete around it. Since the concrete cracks at a very low strain, the stresses remain small in the steel in the uncracked stage. This means that stirrups do not prevent inclined cracking, but start to contribute to the shear resistance when cracks have formed. In the elastic stage, shear is completely resisted by the compression zone until the first flexural cracks.

At the onset of flexural cracking, dowel action and aggregate interlocking also start to contribute to the shear resistance. In the cracking stage, stirrups restrict the growth of diagonal cracks. When inclined cracks start to develop, strains in the crossing stirrups develop, resulting in axial resistance in these stirrups. The strut-and-tie model is commonly used to describe the behaviour of beams with stirrups. This approach is also used in Eurocode 2 [8], which is described in Subsection 2.3.2.

In Figure 2.9, it can be seen that the relative shear resistance due to dowel action remains small. The shear resistance due to aggregate interlock increases until inclined cracking, but after this decreases due to widening and rotation of the cracks. However, stirrups significantly increase the effect of aggregate interlocking, since it restrains the propagation and widening of cracks. When the stirrups start yielding, the crack width rapidly increases, causing a rapid decrease in the aggregate interlocking capacity. Eventually, the shear is completely resisted by the compression zone and stirrups.

In the plastic stage, the steel yields or the concrete crushes (or both). Usually, steel has some hardening capacity after yielding, so still a small increase in the load capacity of the RC beam is possible before it fails. When the concrete crushes, a softening behaviour is observed, which means that the load capacity decreases for larger deflections. Eventually, no load-bearing capacity is left, leading to failure.

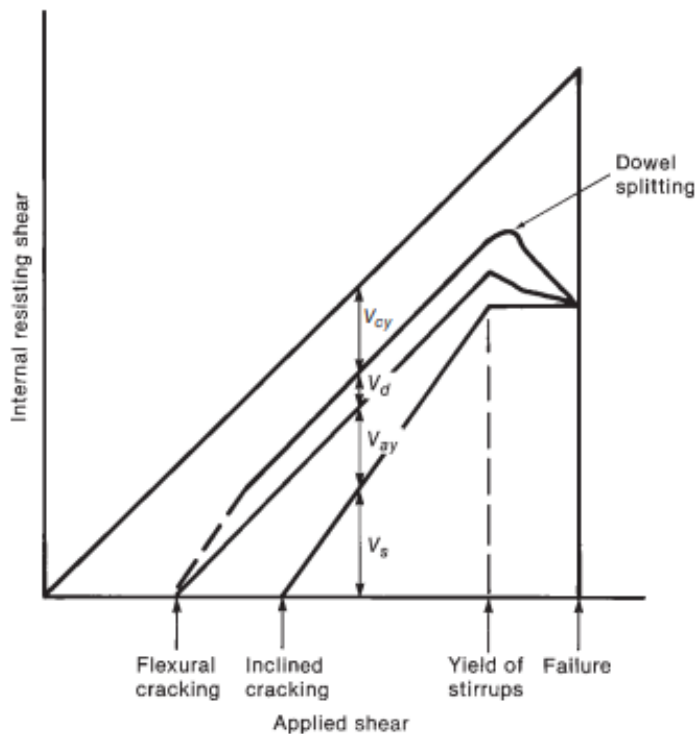


Figure 2.9: Distribution of shear resistance due to different mechanisms [11]

2.3.2 Shear resistance according to Eurocode 2 [8]

As was stated in the introduction of this thesis, the shear resistance of reinforced concrete beams with shear reinforcement is based on the lower bound theorem, in the form of a strut-and-tie model. For simplicity, vertical stirrups are assumed. The stirrups form the tensional ties, concrete between the inclined cracks forms the compressive struts, the compression zone forms the compression chord and the longitudinal reinforcement forms the tension chord (see Figure 2.10). Based on this model and neglecting other bearing mechanisms, only two failure mechanisms limit the ultimate shear resistance: the yielding of the stirrups and the crushing of the concrete struts. Below, the derivation of the ultimate shear resistance is described. In these derivations, the design values are used.

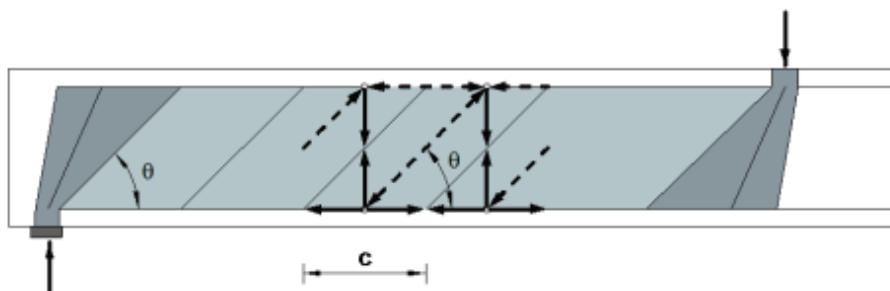


Figure 2.10: Strut-and-tie model of concrete beams with shear reinforcement [16]

Yielding of stirrups

To derive the shear resistance of the stirrups, a cut section parallel to the struts is shown in Figure 2.11. The internal forces are also presented here. From vertical equilibrium follows the shear resistance of the stirrups [8]:

$$V_{Rd,s} = \frac{A_{sw}}{s} z f_{ywd} \cot \theta \quad (2.5)$$

Where:

- $V_{Rd,s}$ Design shear resistance of the stirrups in an inclined crack
- A_{sw} Cross-sectional area of a stirrup
- s Spacing between stirrups
- z Lever arm between the compression and tension chord
- f_{ywd} Design yield strength of the stirrups
- θ Inclination of the shear crack

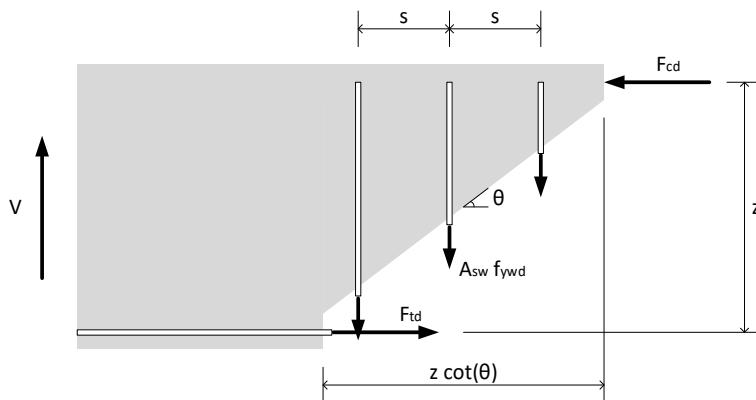


Figure 2.11: Cut section parallel to the struts

Crushing of the concrete struts

For the derivation of the shear resistance of the concrete struts, a cut section perpendicular to the struts is shown in Figure 2.12.

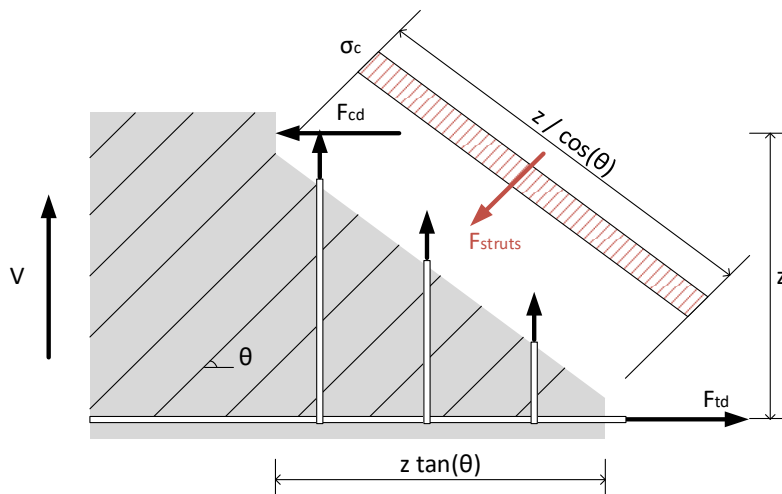


Figure 2.12: Cut section perpendicular to the struts

First, the force due to the compressive struts F_{struts} can be calculated:

$$F_{struts} = \sigma_c b_w \frac{z}{\cos \theta} \quad (2.6)$$

The total vertical force due to the stirrups in this cut section is:

$$F_s = \frac{z \tan \theta}{s} A_{sw} f_{ywd} \quad (2.7)$$

Rewriting Equation 2.5 (assuming yielding of the stirrups) and substituting it in Equation 2.7 results in:

$$V \tan \theta = \frac{A_{sw}}{s} z f_{ywd} \quad (2.8)$$

$$F_s = V \tan^2 \theta \quad (2.9)$$

Now, from horizontal equilibrium it follows:

$$V + V \tan^2 \theta = \sigma_c b_w \frac{z \sin \theta}{\cos \theta} \quad (2.10)$$

$$V = \sigma_c b_w z \frac{\tan \theta}{1 + \tan^2 \theta} = \sigma_c b_w z \frac{1}{\cot \theta + \tan \theta} \quad (2.11)$$

Finally, the maximum stress in the concrete struts according to Eurocode 2 can be substituted, resulting in the maximum shear resistance of the struts [8]:

$$\sigma_c = \alpha_{cw} v_1 f_{cd} \quad (2.12)$$

$$V_{Rd,max} = \alpha_{cw} b_w z v_1 f_{cd} \frac{1}{\cot \theta + \tan \theta} \quad (2.13)$$

Where:

$V_{Rd,max}$ Design maximum shear resistance of the concrete struts

α_{cw} Factor that takes prestresses into account (see EC2 [8])

b_w Effective width of the beam

v_1 Reduction factor for cracked concrete due to shear (see EC2 [8])

f_{cd} Concrete compressive design strength

Inclination angle

In both Equations 2.5 and 2.13, the inclination angle θ is an unknown variable. In Eurocode 2, this angle is limited between 21.8° and 45° . The lower limit is set due to the limited plastic deformation of concrete. With a small angle, the stirrups should elongate a lot, widening the crack. This reduces the shear resistance of the compressive struts. The upper limit is derived from the minimum strain energy principle, assuming that the longitudinal reinforcement is much stiffer than the shear reinforcement [16]. A commonly used approach to determine the inclination angle is assuming both yielding of the stirrups and crushing of the struts at the same time ($V_{Rd,s} = V_{Rd,max}$).

Anchorage of the shear reinforcement

A very relevant aspect of this strut-and-tie model is the anchorage of the shear reinforcement. A connection between the stirrups and the compression and tension chord is necessary to be able to transfer forces and achieve force equilibrium. According to Eurocode 2 [8], anchorage of shear reinforcement can be achieved by bends, hooks or welds. No distinction is made between anchorage in the tension or compression zone of the concrete.

2.4 Bond behaviour between concrete and reinforcement

The bond between concrete and reinforcement is an important mechanism for the transfer of internal forces. The behaviour depends on many factors and plays a major part in the anchorage of the open ends of the straight-legged stirrups investigated in this thesis.

2.4.1 Bond-slip relation

Since tensile stresses in the rebar are transferred to the surrounding concrete, the tensile force in the rebar changes along its length, as well as the force in the surrounding concrete. This allows a difference in strain between the concrete and rebar, causing a relative displacement between the steel and concrete, also known as 'slip' (see Figure 2.13). The behaviour of this interface is described with a local bond stress-slip law shown in Figure 2.14. This is characterized by four different stages in FIB bulletin 10 [17]:

Stage I (uncracked concrete)

For low bond-stress values ($\tau_b \leq \tau_1 = (0.2 - 0.8)f_{ct}$), the bond is mostly assured by chemical adhesion. A secondary occurring mechanism is the micromechanical interaction between the rough steel surface and concrete at the interface. However, these mechanisms play a minor role in the complete bond behaviour, which is also confirmed by relatively small peak stresses for the pull-out failure of plain bars (stage IVa).

In the first stage, no relative slip at the interface occurs, but still, a nonzero slip value is shown in Figure 2.14. This is because the slip is measured relative to a reference point in the undisturbed concrete region (see Figure 2.13). Due to this, the measured slip consists of two parts: the relative bar slip at the interface and the shear deformation of the concrete in the disturbed region. Thus, the slip in the first stage is caused by shear deformations close to the interface.

Stage II (first cracking)

For higher bond-stress values ($\tau_1 \leq \tau_b \leq \tau_2$), the chemical adhesion decreases. For ribbed bars, the transversal ribs (or "lugs") cause large bearing stresses in the concrete (p^* in Figure 2.15) and transverse microcracks at the tips of the ribs allow the rebar to slip. However, the concrete is still able to resist the bearing stresses, limiting the wedging action of the ribs and still preventing splitting cracks.

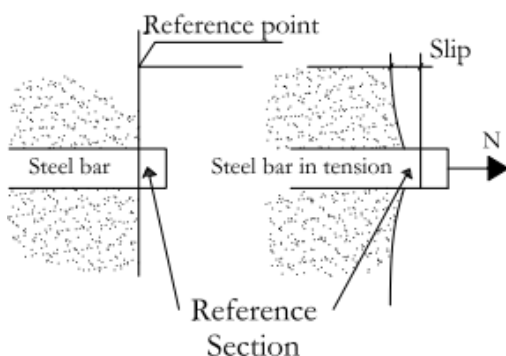


Figure 2.13: Relative bar displacement (slip) [17]

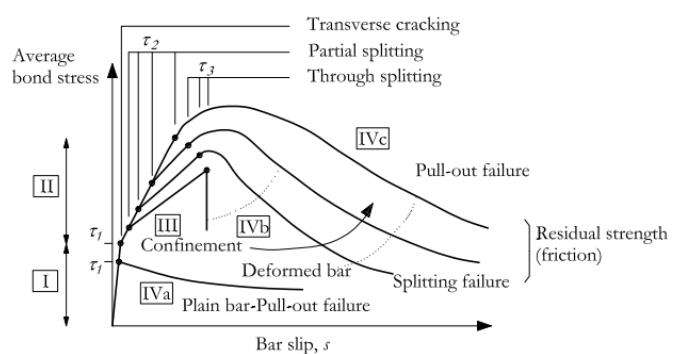


Figure 2.14: Local bond stress-slip law [17]

Stage III (splitting cracks)

For still higher bond-stress values ($\tau_2 \leq \tau_b \leq \tau_3$), longitudinal splitting cracks form radially (see Figure 2.16) due to concrete crushing caused by the wedging action. The outward component of the pressure (p^{**} in Figure 2.15) is resisted by hoop stresses in the surrounding concrete. This causes a confinement effect on the rebar, where the bond strength and stiffness are mostly assured by interlocking around the rebar, concrete struts radiating from the bar and the undamaged outer ring.

Stage IV (failure)

This stage describes the bond failure. However, three different types of failure could be defined:

Stage IVa (pull-out failure of a plain bar)

Since plain bars do not have ribs, pull-out failure occurs directly after the loss of the chemical adhesion (stage I). From this point, the bond is provided by friction.

Stage IVb (splitting failure)

Longitudinal splitting cracks keep developing until these cracks reach the outer surface of the concrete member and/or bar spacing (τ_3 , through splitting). The bond tends to fail abruptly, where the concrete cover is spalled-off from the rest of the member. However, if sufficient stirrups are provided, a bond can still be provided due to the confinement effect of stirrups. Splitting failure usually happens when no confinement and/or a limited concrete cover is present.

Stage IVc (pull-out failure of a ribbed bar)

When splitting failure does not happen due to sufficient concrete cover or sufficient confinement, a pull-out failure will lead to a decrease in bond. As the name of the failure mode supposes, the rebar is 'pulled out' of the concrete. The force transfer mechanism is changed from rib bearing to friction. The further degradation of the bond is caused by smoothing of the interface.

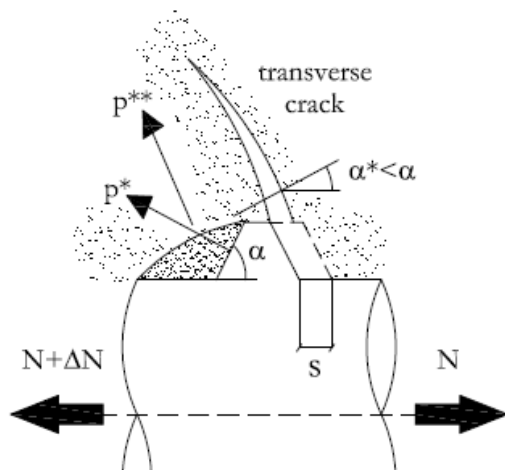


Figure 2.15: Bar-concrete slip and wedging action [17]

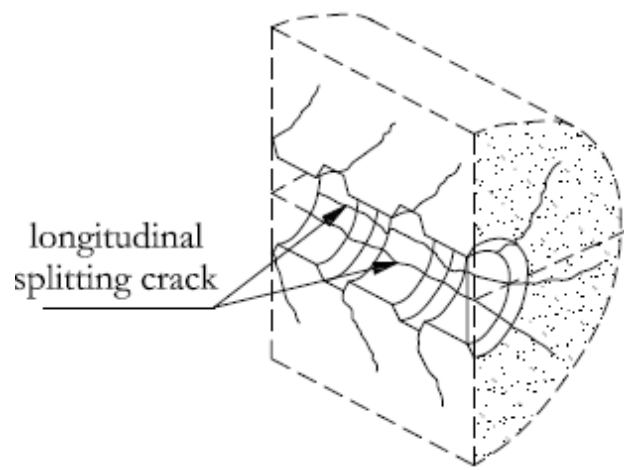


Figure 2.16: Longitudinal splitting cracks [17]

2.4.2 Influencing factors on bond behaviour

The bond behaviour depends on many different factors and parameters, which are basically the properties of the concrete and the rebar and stress states in these two materials. Some properties are already mentioned above, like the concrete cover and confinement. Below, the most important factors for non-prestressed reinforcements are summed up and explained in how they influence the bond behaviour. Also, some less important factors are mentioned to provide a larger understanding of the mechanical behaviour under different circumstances.

Concrete

Concrete strength

This parameter is straightforward since concrete crushing and splitting are governing parts of the bond behaviour described above. Therefore, both the tensile and compressive strength highly affect the overall bond behaviour [17].

Position of the bar

The position of the bar is even more important than the concrete strength. The bond performance is best when horizontal bars are placed close to the bottom of the formwork or vertical bars loaded against the casting direction. This is because the ribs are pushed against the less porous mortar. Also, the opposite is true, where water microbubbles get stuck under horizontal bars close to the top of the formwork and vertical bars loaded in the casting direction, so ribs are pushed against more porous mortar [17].

Concrete cover and bar spacing

As was stated earlier, the concrete cover and bar spacing highly influence the bond failure mechanism (splitting or pull-out failure). If sufficient concrete cover and/or bar spacing is present, where splitting cracks do not reach the outer surface of the member, higher bond strengths can be achieved and a pull-out failure occurs.

Confinement

Confinement has a positive effect on the bond. Active confinement delays the onset of splitting but is almost irrelevant to frictional resistance. Passive confinement (stirrups) is only activated after certain slipping and crack opening, so is helpful after splitting. It can therefore be concluded that active confinement is helpful pre-peak and passive confinement is helpful post-peak [17].

Concrete stress state

The concrete stress state around the bar has a significant effect on the bond. Transverse compression confines the rebar, increasing the bond strength. Transverse tension decreases the bond strength since it stimulates splitting along the bar. If the transverse tension is large enough, it could even change a pull-out failure into a splitting failure [17]. Desnerk, Lees and Morley [18] found that a single transverse crack reduces the bond strength by 44% on average.

Reinforcement

Bar geometry

The bar geometry, and especially the rib geometry, is an important factor in the bond behaviour. As was stated earlier, the ribs govern the resistance due to rib bearing. An often-used coefficient to classify the bar geometry is the relative rib area:

$$f_r = \frac{A_R}{\pi d_b s_R} \quad (2.14)$$

Where:

f_R	Relative rib area
A_R	Area of the projection of a single rib
d_b	Bar diameter
s_R	Rib spacing

It was found that the ultimate bond strength linearly increases with the relative rib area. In general, values between 0.05 and 0.10 for the relative rib area are presumed to represent good bond conditions [17].

Reinforcement stress state

When considering the stress state in a rebar, a distinction must be made between different governing force transfer mechanisms. If rib bearing governs the bond strength, which is usually the case for ribbed bars, the change of stress over the length of the rebar is not significant and can be neglected. This is because concrete crushing in front of the ribs and concrete cover splitting are hardly affected by the stress state in the steel and the transverse deformation of the rebar due to the Poisson effect is also negligibly small with respect to the change in the relative rib area.

However, the stress state in the rebar is relevant if friction governs the force transfer. Especially the transverse contraction due to the tension in the bar is relevant since it significantly influences the surface roughness and reduces the radial compressive stress, as also the frictional bond stress.

In the elastic range, the influence of the stress state in ribbed bars is small, but yielding has a huge negative impact on the bond behaviour. However, this phenomenon is not yet well understood. It is expected that the transverse deformation due to contraction of the bar at and after yielding significantly reduces the frictional resistance and relative rib area, as also rib bearing [17].

Environmental effects and load time-history

Also, other factors play a part in the bond behaviour, like environmental effects and load time history. However, these are not as significant as the factors described above, especially for this thesis. However, for informative reasons, a short description of some effects is provided below.

Steel corrosion

Steel corrosion has a positive influence on lower corrosion rates due to the expansion of iron oxides. However, for larger corrosion rates, a decrease in bond is observed due to the build-up of a soft layer of loose corrosion products on the top layer of the bar [17].

Bar rusting

Bar rusting seems to have a positive influence on the bond behaviour, as well as an inhibited function for corrosion [17].

High and low temperatures

High and low temperatures both mainly influence the structural behaviour of concrete. A high temperature decreases both the concrete and bond strength and a low temperature increases both the concrete and bond strength [17].

Load time-history

As expected, the number of load cycles negatively affects the bond strength. This has mainly to do with the degradation of the concrete strength, which could also affect the failure mode. This effect increases for reverse cycling. Also, for higher loading rates, the bond strength is larger [17].

2.4.3 Anchorage of reinforcements according to Eurocode 2 [8] and RBK1.2 [10]

In chapter 8.4 of Eurocode 2 [8], the detailing rules for the anchorage of longitudinal reinforcement are discussed. It also uses certain assumptions concerning bond behaviour. It is based on the assumption that a constant maximum bond stress is achieved over a certain length of a bar, the anchorage length. If the existing anchorage length is larger than the required anchorage length, then it is assumed that anchorage failure (splitting or pull-out) is prevented.

The design ultimate bond stress for ribbed bars is:

$$f_{bd} = 2.25 \eta_1 \eta_2 f_{ctd} \quad (2.15)$$

Where:

- f_{bd} Design ultimate bond stress for ribbed bars
- η_1 Coefficient related to the quality of bond conditions,
 $\eta_1 = 1.0$ for 'good' bond conditions and $\eta_1 = 0.7$ for other bond conditions
- η_2 Coefficient related to the bar diameter
 $\eta_2 = 1.0$ for $\emptyset \leq 32 \text{ mm}$ and $\eta_2 = (132 - \emptyset)/100$ for $\emptyset > 32 \text{ mm}$
- f_{ctd} Design concrete tensile strength

It can be seen that the calculation for the ultimate bond strength only considers the bond conditions and bar diameter as relevant factors. Other factors are taken into account in the calculation of the design anchorage length, but first, the required anchorage length is calculated. For this, force equilibrium between the bond stress at the area around the bar and the axial force in the bar must be reached. From this, the required anchorage length can be calculated, resulting in:

$$l_{b,rqd} = \frac{\emptyset \sigma_{sd}}{4 f_{bd}} \quad (2.16)$$

Where:

- $l_{b,rqd}$ Required anchorage length
- σ_{sd} Design stress of the bar

This required anchorage length is the maximum anchorage length that is required, so it is an upper limit in this case. However, many factors are not taken into account yet. For the design anchorage length, other favourable factors are considered, where the actual required anchorage length possibly reduces. The equation for this is:

$$l_{bd} = \alpha_1 \alpha_2 \alpha_3 \alpha_4 \alpha_5 l_{b,rqd} \geq l_{b,min} \quad (2.17)$$

$$l_{b,min} = \max(0.3l_{b,rqd}; 10\phi; 100 \text{ mm}) \quad (2.18)$$

Where:

- l_{bd} Design anchorage length
- α_1 Coefficient related to the form of the bars
- α_2 Coefficient related to the concrete cover
- α_3 Coefficient related to the effect of confinement by stirrups
- α_4 Coefficient related to the influence of welded transverse bars along the anchorage length
- α_5 Coefficient related to the pressure transverse to the plane of splitting
- $l_{b,min}$ Minimum anchorage length

So in the end, nearly all the important influencing factors are taken into account. A detailed description of these coefficients is not discussed here and can be found in Section 8.4 of EC2 [8].

This approach is also used for the principle described in RBK1.2 [10]. For this, the design anchorage length for open straight-legged stirrups is calculated according to Eurocode 2. However, when evaluating the total shear capacity of the stirrups, a reduction of the maximum possible stress is accounted for stirrups where less than the design anchorage length is available. The available anchorage length is the open end of the stirrups that is situated in the compression zone x (see Figure 2.17). The maximum stress in these stirrups is then:

$$\sigma_{swd} = \frac{l_{bd,aanw}}{l_{bd}} f_{ywd} \leq f_{ywd} \quad (2.19)$$

Where:

- σ_{swd} Design stress of the stirrup
- $l_{bd,aanw}$ Available anchorage length in the compression zone
- f_{ywd} Yield strength of the stirrup

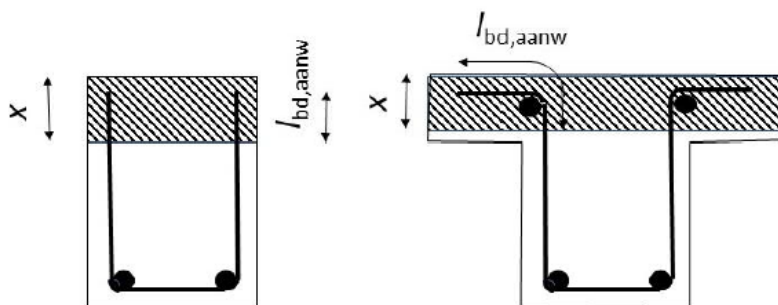


Figure 2.17: Available effective length $l_{bd,aanw}$ in the compression zone for open straight-legged stirrups [10]

2.5 Summary of shear load transfer mechanisms

Based on the literature study described in this chapter, the governing load-bearing mechanisms in a concrete beam are shear resistance in the compression zone, aggregate interlocking, dowel action, axial stress resistance in stirrups and prestressing tendon. Also, the shear contribution of the compression zone and aggregate interlocking increases due to axial compression of the prestressing, which is separately expressed as the contribution due to prestress. In common engineering models, the contribution of aggregate interlocking and dowel action is neglected due to its decreasing contribution for an increasing crack width. Also, the contribution of the stirrups can only be accounted for if the stirrups are sufficiently anchored using bends, hooks, welds or sufficient bond with the surrounding concrete.

Assuming that the yielding of stirrups is decisive over the crushing of the compression struts and that the stirrups are sufficiently anchored, the mechanisms as shown in Figure 2.18 describe the shear resistance of a concrete beam. An important additional factor that is not shown in the figure is the contribution of prestressing ($V_{prestress}$) in the concrete, because it has no physical meaning.

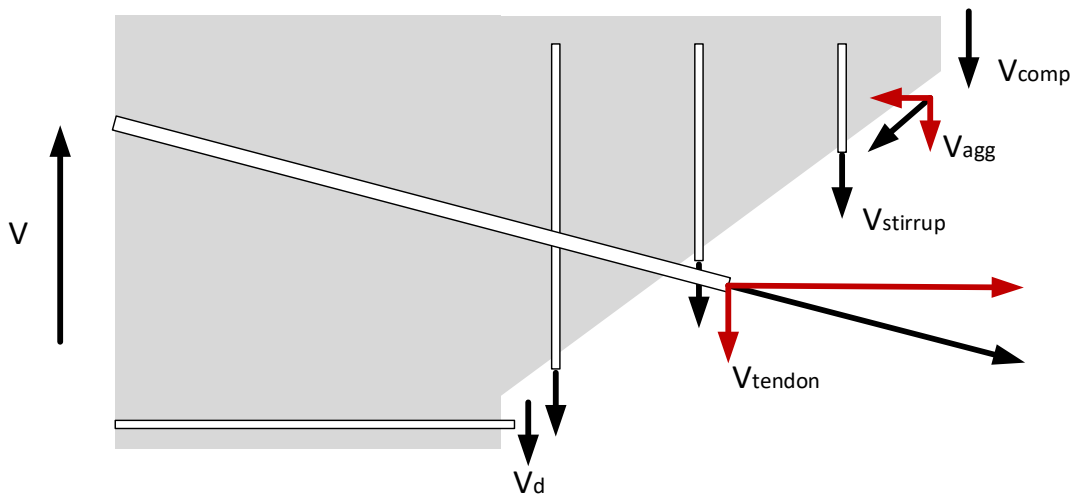


Figure 2.18: Schematic overview of the shear load transfer mechanisms

3 Finite element modelling of RC beams

In this chapter, common modelling considerations for the kinematic relations, constitutive relations and equilibrium conditions are described. The choices made within these aspects translate the behaviour of concrete beams to a finite element model. Therefore it is significant to understand the possible options to be able to define a suitable nonlinear finite element modelling strategy. In this chapter, all relevant options and recommendations are discussed. In Chapter 5, these options are considered and choices for the approach of finding suitable solution strategies are made.

Many definitions are used to describe various aspects of finite element modelling, which are not always explained in detail. For a complete understanding of this chapter, certain prior knowledge of finite element modelling is expected.

3.1 Kinematic relations

The kinematic modelling considerations describe the relationship between strains and displacements. Next to boundary conditions, kinematic compatibility in a finite element analysis also concerns finite element discretization and element types. The following aspects are discussed:

1. Element type for concrete and reinforcements
2. Element size
3. Boundary conditions
4. Interfaces

3.1.1 Element type for concrete and reinforcements

An important choice for finite element discretization is the element types for concrete and reinforcements. The element type is defined by shape, interpolation and numerical integration. For the whole finite element mesh, it applies that a regular mesh with less than 5% distorted elements must be generated.

Element type for concrete

Linear elements are not advised, because they tend to show locking behaviour. Quadratic elements are better suited to describe deformations and shear failure. For concrete beams, 8-node quadrilateral elements (see Figure 3.1) for 2D simulations and 20-node hexahedral elements (see Figure 3.2) for 3D simulations are preferred.

Full numerical Gauss integration should be used because reduced-order integration for quadratic elements could lead to spurious modes due to a small element stiffness due to cracking [3]. The sampling points for the quadratic elements are shown in Figure 3.3 and Figure 3.4.

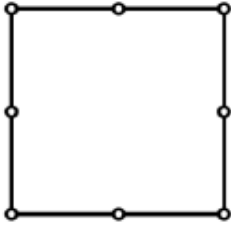


Figure 3.1: Quadratic quadrilateral element [3]

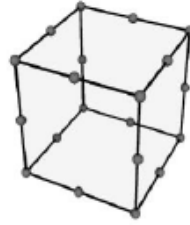


Figure 3.2: Quadratic hexahedron [3]

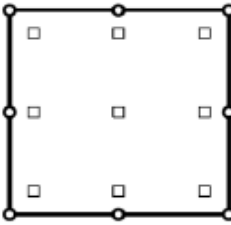


Figure 3.3: Integration points, 3x3-point Gauss [3]

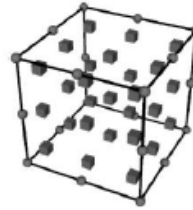


Figure 3.4: Integration points, 3x3x3-point Gauss [3]

Element type for reinforcements

For reinforcements, multiple different element types could be used, dependent on the application of the model. First of all, embedded reinforcements are preferred instead of overlay elements. Overlay elements also have a shear stiffness defined, which is usually ignored because the shear stiffness of reinforcement bars is usually very small.

There are also multiple embedded reinforcement types. The first option is to completely ignore the slip between concrete and reinforcement. This means that the concrete and reinforcement are fully bonded and the strains in the reinforcement are the same as in the concrete. The second option is to use an embedded bond-slip model, where embedded reinforcement and interface models are combined. This interface model describes the constitutive slip behaviour. See Subsection 3.2.2 for different constitutive bond-slip models.

For bond-slip elements, a distinction is made between truss and beam bond-slip bars. Trusses only deform in the longitudinal direction, while beams may also show shear deformation, curvature and torsion.

The shape of the embedded reinforcement is a line and the order of interpolation should be the same as the concrete elements, otherwise, the elements are incompatible.

The numerical integration scheme could be both full or reduced, since the reinforcement is inhibited by the embedding concrete elements, so spurious displacement modes are prevented [3].

3.1.2 Element size

The element size is usually determined based on the computational time and the required accuracy of the results. However, minimum and maximum element size is given by the RTD1016-1 [3] to ensure both a reasonable computational time and a sufficiently accurate model.

For concrete, the minimum element size is 1.5 times the maximum aggregate size.

The maximum element size is limited due to two reasons. Concrete is a softening material and if the equivalent length is too large, the post-peak response can show snap-back behaviour. The initial slope of the post-peak stress-strain diagram must be larger than the Young's modulus of concrete to prevent snap-back. Therefore the equivalent length must be smaller than:

$$h_{eq} < \frac{EG_F}{f_t^2} \quad (3.1)$$

Where:

h_{eq}	Crack bandwidth
E	Young's modulus
G_F	Tensile fracture energy
f_t	Tensile strength

To ensure that this is satisfied, the maximum element size should be approximately half of the maximum equivalent length.

The second upper limit for the element size is to guarantee relatively smooth stress fields. This is based on the beam dimensions. For a 3D beam, the maximum element size is [3]:

$$\min\left(\frac{l}{50}, \frac{h}{6}, \frac{b}{6}\right) \quad (3.2)$$

De Putter [19] received the best results with 20 elements over the height for multiple models with various properties. It must be noted that his selection of experiments did not contain many deep beams so it is not guaranteed that this recommendation results in the best results. It is always wise to perform multiple analyses with several different element sizes.

3.1.3 Boundary conditions

The boundary conditions in the model should represent the supports of the structure. However, to reduce local stress concentrations (singularities), it is advised to use support and loading plates. A possible material choice is steel with linear elastic properties, with an interface between the support/loading plate and the concrete beam. The details of this interface are discussed in the following subsection.

3.1.4 Interfaces

As is stated in subsection 3.1.1, the constitutive properties of the interfaces of bond-slip reinforcement are defined with a bond-slip model and its compatibility is automatically generated by DIANA.

If other interfaces are used, for instance between a support/loading plate and the concrete beam, the stiffnesses in multiple directions must be defined manually. If the interface does not represent a physical meaning, like a support/loading plate, so-called dummy stiffnesses are defined. The interface of a support/loading plate should be a no-tension/no-friction interface, with relatively high compressive stiffness ($1000E_c/h_{eq}$) and relatively low tension and shear stiffness.

3.2 Constitutive relations

The constitutive modelling aspects describe the stress-strain relations for different materials. The following aspects are relevant and discussed:

1. Concrete: Elastic and nonlinear (cracking and crushing) behaviour
2. Steel reinforcement: Elastic and yielding behaviour

3.2.1 Concrete

From the previous chapter, it is known that cracking and crushing of concrete play a crucial part in the behaviour of concrete beams. It is therefore necessary to accurately predict these phenomena. The two most used approaches in finite element models are discrete crack models and smeared crack models. The difference between a discrete and a smeared crack model is shown in Figure 3.5.

For discrete cracking, the location of the crack must be known in advance. At this location, a geometrical discontinuity is modelled and the surrounding elements can be kept elastically. It is difficult to predict the crack locations for the beams that are investigated in this thesis, which makes the discrete crack approach unsuitable and pointless to investigate the options of this approach in this case.

A smeared crack model (or total strain-based crack model) describes cracks as a stiffness reduction in the continuum. A crack is 'smeared' over an element causing a strain. Because it is not possible to accurately determine the location of the cracks, the smeared crack approach is used. This is also recommended by RTD1016-1 [3]. Different smeared crack models (fixed and rotating) are described below.

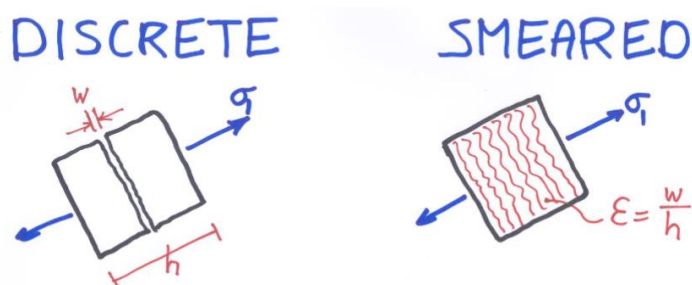


Figure 3.5: Discrete cracking vs. smeared cracking in an element [20]

Fixed and rotating crack models

For smeared crack models, a distinction is made between fixed and rotating crack models. In a fixed model, the direction of a crack is fixed when the principal stress rotates (see Figure 3.6). It requires a shear retention model to describe the shear stiffness along the crack (aggregate interlocking), which must be chosen adequately to avoid spurious shear locking. In a rotating model, the cracks rotate along with the principal stress direction (see Figure 3.7). Therefore, the shear stresses along the crack remain zero, so a shear retention model is not required here.

Shear locking is a phenomenon where an element is not able to accurately describe the kinematics of deformation. For instance, the curvature of a beam cannot be described with linear elements, causing additional shear stresses to reach equilibrium. The element behaves much stiffer than it actually should be [21].

In smeared crack models, no actual geometrical discontinuity is described, but with a reduction of the stress (and an increase of strain). Therefore it does not lead to a relaxation of their neighbouring elements, causing stiffer neighbouring elements than they should be (locking). Shear locking is possible in both rotating and fixed crack models, but fixed crack models tend to suffer more from stress locking [19].

The RTD1016-1 [3] and De Putter [19] recommend rotating crack models for beams with shear reinforcement since these models predict the failure load and mechanism quite well.

However, De Putter concluded that rotating crack models often overpredict the failure load of beams without shear reinforcement due to overrotation of the critical inclined crack. The failure mechanism can still be found based on engineering judgement, where a small drop in the force-displacement curve can be seen and a drastic change in the crack pattern should be observed. Fixed models with a damage-based shear retention model showed better results in predicting the flexural shear failure mode [19].

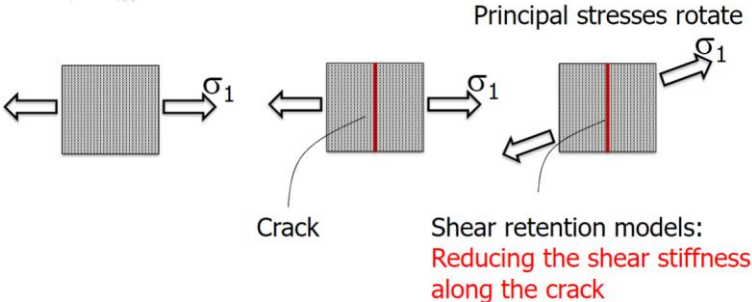


Figure 3.6: Fixed crack model [20]

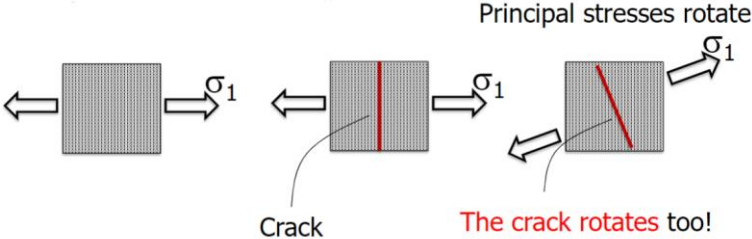


Figure 3.7: Rotating crack model [20]

Tensile behaviour

The tensile behaviour is described with a quasi-brittle stress-strain relation. The behaviour is linear until the ultimate tensile strength is reached. After this peak, a softening behaviour is described until the stress reduces to zero at the ultimate strain ϵ_{ult} . Multiple softening branches are possible. The RTD1016-1 [3] advises an exponential-type softening diagram because these diagrams will result in more localized cracks and avoids large areas of diffuse cracking. Hordijk [22] investigated the tensile behaviour of concrete and described a constitutive model based on experimental results with an exponential-type softening branch. This model is shown in Figure 3.8. As can be seen, the area below the stress-strain diagram is equal to G_F/h_{eq} .

The ultimate strain ε_{ult} according to Hordijk [22] is:

$$\varepsilon_{ult} = 5.136 \frac{G_F}{h_{eq} f_t} \quad (3.3)$$

The tensile fracture energy according to the RTD1016-1 [3] is:

$$G_F = 0.7 \times 0.073 f_{cm}^{0.18} \quad (3.4)$$

Where:

f_{cm} Mean compressive strength

The Poisson effect ceases to exist for concrete in a cracked state. To model this phenomenon, a damage-based formulation of the Poisson's ratio is implemented in DIANA, where the Poisson's ratio reduces after crack initiation [1]. It is highly recommended by the RTD1016-1 [3] to use this reduction model.

Compressive behaviour

The compressive behaviour of concrete is described with a parabolic softening curve (see Figure 3.9). This behaviour is dependent on the compressive strength f_c , the compressive fracture energy G_C and the equivalent length h_{eq} .

The compressive fracture energy according to the RTD1016-1 [3] is:

$$G_C = 250 \times \frac{f_{ck}}{f_{cm}} \times 0.073 f_{cm}^{0.18} \quad (3.5)$$

$$f_{ck} = f_{cm} - 8 \quad (3.6)$$

Where:

f_{ck} Characteristic cylinder compressive strength

The tension-compression interaction is an important but complicated aspect of the behaviour of concrete beams. It is thought that compression softening is influenced by lateral cracking. Vecchio and Collins [23] investigated this phenomenon and proposed a compression reduction model due to lateral cracking, which is implemented in DIANA. According to the RTD1016-1 [3], compression-tension interaction must be taken into account when the model is subjected to a multi-axial stress state. Vecchio and Collin's reduction model is mentioned as an acceptable option, with a limited reduction factor of 0.4 to avoid an unrealistic response of the structure.

Due to the Poisson effect, lateral displacements due to an axial load occur. If these displacements are constrained, a confinement effect occurs, causing an increase in compression strength. Selby and Vecchio [24] modelled this effect, which is implemented in DIANA. Since confinement increases the compressive strength, it is conservative to ignore it. If a confinement model is used, the relevance should be motivated.

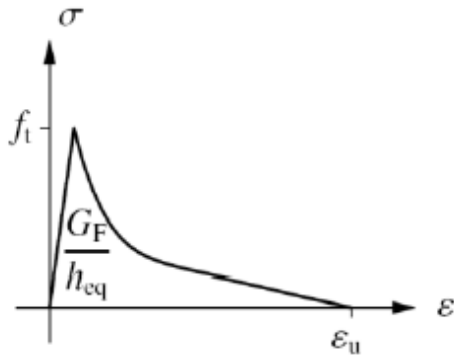


Figure 3.8: Hordijk softening [3]

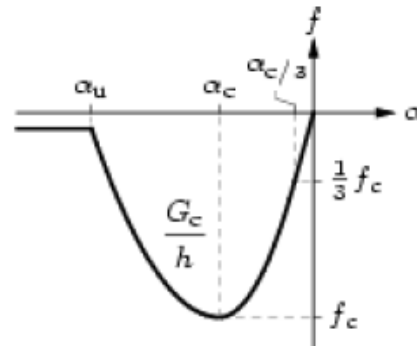


Figure 3.9: Parabolic compression diagram [3]

Shear retention model for fixed crack models

The modelling of shear behaviour is only necessary for fixed crack models, where the shear stiffness should reduce after cracking. In DIANA, many different shear models exist. The RTD1016-1 [3] recommends two models:

- A damage-based retention model, where the secant shear stiffness degrades at the same rate as the tensile stiffness due to cracking. It is known that the elastic modulus and the Poisson effect degrade in a cracked state. The shear modulus is then calculated as followed [1]:

$$G^{cr} = \frac{E^{cr}}{2(1 + \nu^{cr})} \quad (3.7)$$

- An aggregate size-based model, where the shear stiffness gradually degrades to zero for a crack width of half the average aggregate size. The shear modulus is then calculated as followed [1]:

$$G^{cr} = \beta G \quad (3.8)$$

$$\beta = 1 - \frac{2}{d_{agg}} \varepsilon_n h_{eq} \quad (0 \leq \beta \leq 1) \quad (3.9)$$

Where:

- G Elastic shear modulus
- d_{agg} Mean aggregate size
- ε_n Crack normal strain

Crack bandwidth

The equivalent length (or crack bandwidth) is the length over which a crack (and also the fracture energy) is smeared out. It is possible to define user-assigned values, but these are usually inaccurate. It is therefore recommended to use an automatic procedure to determine the equivalent length [3]. In DIANA, two automatic procedures are available: Rots' Element Based Method and Govindjee's Projection Method. In the first method, the equivalent length depends on the size, shape and interpolation function of the finite element [25]. This method is useful and accurate for regular meshes but is less applicable for irregular meshes and arbitrary crack directions. In the second method, which is an improvement of the first method, the crack bandwidth is based on the element size, element aspect ratio and crack orientation [26]. Since this is also applicable to beams with arbitrary cracks, it is recommended to use Govindjee's Projection Method. In Figure 3.10, equivalent lengths are given for some quadratic quadrilateral elements.

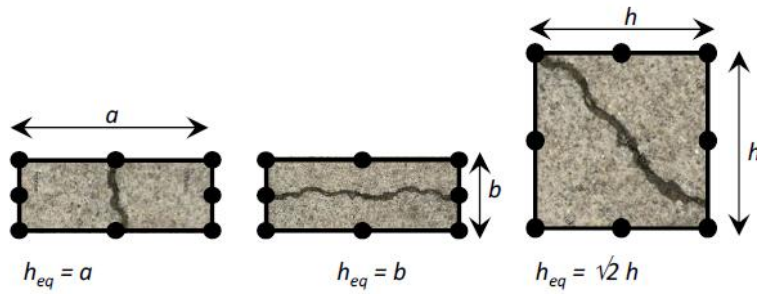


Figure 3.10: Examples of equivalent lengths [3]

3.2.2 Steel reinforcement

The RTD1016-1 [3] advises using an elasto-plastic material model with hardening for both steel bars and prestressing steel (see Figure 3.11 and Figure 3.12). If rupture is modelled, it should be done by defining steep softening branches after reaching the ultimate strength.

In reality, the interaction between concrete and (bonded) reinforcement is the main mechanism for stress redistribution after cracking. However, this is based on details on micro- and meso-scale with complex influencing factors, which can only be modelled if very small elements are used. It is therefore common to simplify this behaviour on macro-scale, distinguishing this behaviour in tension-stiffening, bond slip and dowel action. These three aspects are tightly connected to the finite element discretization of the reinforcements, which are discussed in Subsection 3.1.1.

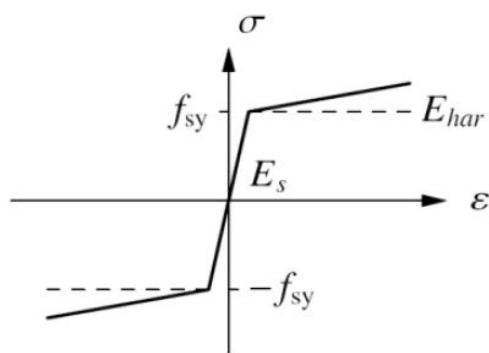


Figure 3.11: Stress-strain diagram for steel bars [3]

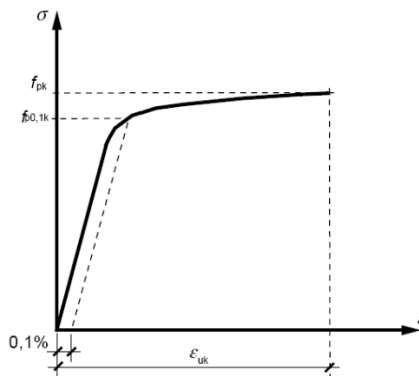


Figure 3.12: Stress-strain diagram for prestressing steel [3]

Tension-stiffening

The most important aspect of the concrete-reinforcement interaction is the tension-stiffening of the reinforcement. The tension behaviour of a reinforced bar is tightly connected to the number of cracks that can form and the crack width since a crack induces a local strain in a crossing reinforced bar and the reinforced bar counteracts the widening of the crack. This causes a redistribution of stresses and is an essential load-carrying mechanism. After the development of a stabilized crack pattern, the stiffness of a reinforced tensile member is still higher than the stiffness of the reinforcement bar alone, which is referred to as tension-stiffening [3]. This effect is shown in Figure 3.13.

Bond-slip

For the bond-slip behaviour, multiple interface models are implemented in DIANA. Independent of the chosen bond-slip model, a dummy normal (B_n) and shear (B_t) stiffness modulus must be defined. These are only relevant for the first step in the bond-slip relation when a bond-slip model is defined but has little influence on the overall behaviour. The dummy stiffnesses can be calculated with:

$$B_n = \frac{100E_{cm}}{h_{eq}} \quad (3.13)$$

$$B_t = 0.1B_n \quad (3.14)$$

Below, relevant bond-slip models that are implemented in DIANA are described.

Fib bond-slip model

The fib Model Code for Concrete Structures 2010 [27] describes a local bond-slip model, where a distinction is made for different failure mechanisms (see Figure 3.14). It is the only model that also describes post-peak behaviour. The total behaviour is split up into four stages, which are described by the following relation:

$$\tau_b = \begin{cases} \tau_{bmax}(s/s_1)^\alpha & \text{for } 0 \leq s \leq s_1 \\ \tau_{bmax} & \text{for } s_1 \leq s \leq s_2 \\ \tau_{bmax} - (\tau_{bmax} - \tau_{bf})(s - s_2)/(s_3 - s_2) & \text{for } s_2 \leq s \leq s_3 \\ \tau_{bf} & \text{for } s > s_3 \end{cases} \quad (3.15)$$

The parameters in the equation above are given in the fib Model Code for Concrete Structures 2010 [27]. The power function in the first stage with $\alpha < 1$ causes an undefined stiffness in the origin. To overcome this issue, a linear development in the first stage until s_0 is defined, where $s_0 < s_1$.

Shima bond-slip relation

The Shima bond-slip relation is based on the concrete strength and diameter of the bar. This relation is valid for bars under the boundary condition that the slip and steel strain are zero. This is usually valid when a relatively long embedment length is present [28]. The relation is based on a pull-out failure and is given as:

$$\tau_b = f_c^{\frac{2}{3}} \left(1 - e^{-40 \left(\frac{s}{D} \right)^{0.6}} \right) \quad (3.16)$$

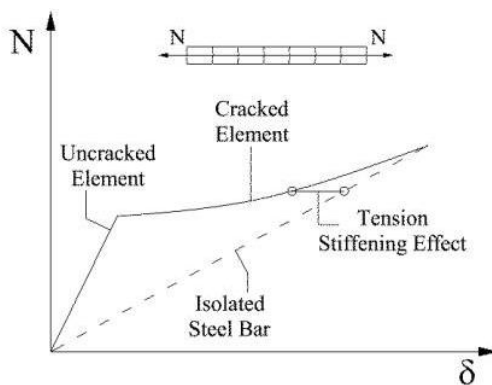


Figure 3.13: Effect of tension-stiffening of a reinforced concrete member [29]

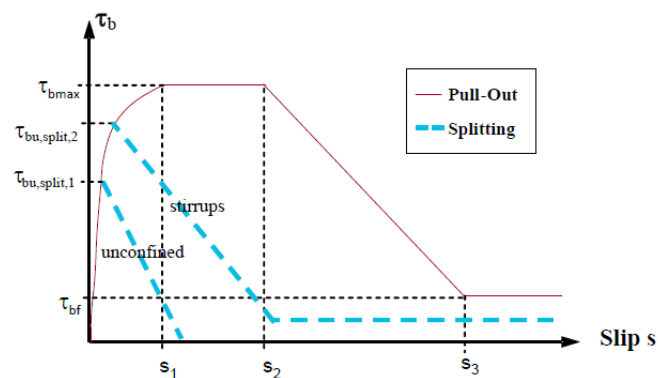


Figure 3.14: Fib bond-slip model [27]

Shima bond-slip-strain relation

In the research of Shima, Chou and Okamura [28], it was found that the bond-slip relationship is dependent on the location along the bar under the boundary condition that the slip is zero and the steel strain is nonzero, or the slip nonzero and the steel strain zero. This is usually the case when relatively short embedment lengths are present. As a result, a bond-slip-strain model based on a pull-out failure was proposed, where the steel strain is also implemented in the relation:

$$\tau_b = f_c \frac{0.73 \left(\ln \left(1 + 5000 \frac{s}{D} \right) \right)^3}{1 + \varepsilon_s \times 10^5} \quad (3.17)$$

Dörr bond-slip relation:

The difference between the Dörr bond-slip relation and the relations described above is the stress state of the concrete around the bar. In the previous relations, concrete was assumed to be in compression. Dörr [30] investigated the local bond behaviour for concrete loaded in tension and pull-out failure, resulting in the following relation:

$$\tau_b = \begin{cases} f_{ct} \left(5 \left(\frac{s}{s_0} \right) - 4.5 \left(\frac{s}{s_0} \right)^2 + 1.4 \left(\frac{s}{s_0} \right)^3 \right) & \text{for } 0 \leq s < s_0 \\ 1.9 f_{ct} & \text{for } s \geq s_0 \end{cases} \quad (3.18)$$

Comparison of bond-slip models

In Figure 3.15, a comparison between the bond-slip models is shown ($D = 6 \text{ mm}$, $f_c = 37.6 \text{ MPa}$, $f_{ct} = 3.3 \text{ MPa}$). It can be seen that the models differ a lot, especially concerning the ultimate bond strength. The Dörr model ($s_0 = 0.1 \text{ mm}$) results in the lowest ultimate bond strength, since it is based on a lower bond strength due to concrete in tension.

The ultimate bond strength of the fib splitting model is slightly higher, with a rapid decrease in bond strength after the peak. This model is based on a different failure mechanism, so could be useful if a splitting failure is expected.

The Shima bond-slip relation increases rapidly for small slip values (until $s = 0.2 \text{ mm}$), but becomes approximately constant for larger slip values. Since this model is valid for long embedment lengths, this model is especially relevant for longitudinal reinforcement.

The fib pull-out model describes the largest bond strength, which is still changing for large slip values. In the fib Model Code for Concrete Structures 2010 [27], reductions of the bond stress are described due to the influence of transverse cracking, yielding, transverse stress, longitudinal cracking and cyclic loading. However, these reductions are not implemented in DIANA and are also difficult to determine, since these parameters are usually dependent on many factors.

Dowel action

Dowel action is optional to model, but easy-to-use and robust models are commonly not available in finite element codes. However, dowel action can be taken into account when beam elements for reinforcements are used. This is because beam elements also resist shear deformation and curvature (next to axial deformation), hence dowel action is modelled.

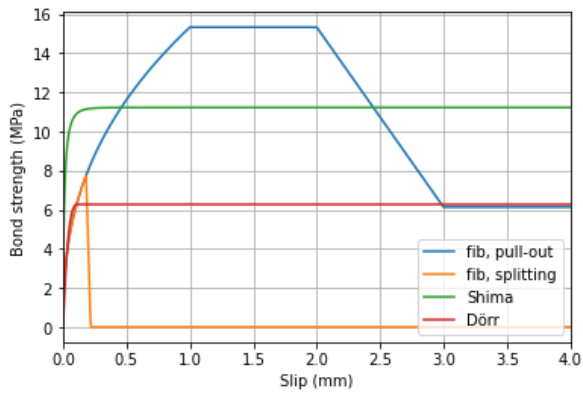


Figure 3.15: Comparison of bond-slip models

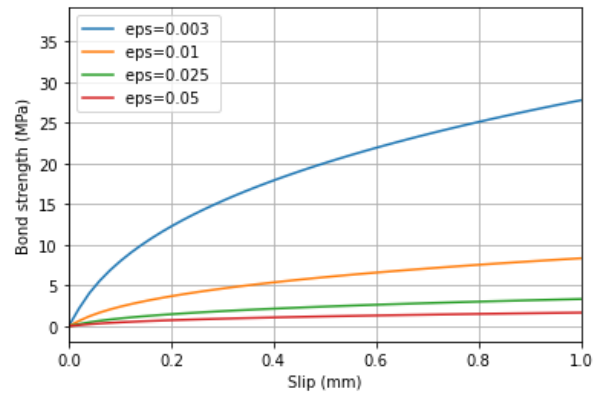


Figure 3.16: Shima bond-slip-strain model for different steel strains

3.3 Equilibrium conditions

The equilibrium conditions describe the relation between forces and stresses. This has a huge influence on the solving procedure in a finite element analysis, which makes it important to consider the different options of the following aspects:

1. Type of loading
2. Prestress (post-tensioning)
3. Load incrementation
4. Analysis control
5. Equilibrium iteration scheme and maximum number of iterations
6. Convergence criteria

3.3.1 Type of loading

For the investigated experiments, three different loads act on the beam: dead weight, prestressing and the acting force caused by the test frame [2]. The prestressing is discussed in the next subsection.

The dead weight should be modelled as an initial load. In general, this dead weight causes a non-uniform stress field, which is beneficial in nonlinear analysis, because it avoids spurious localizations.

For the acting force caused by the stress frame, two options are available. The first option is force control, where the load is applied as a concentrated load. This method alone is not able to capture the post-peak and snap-back behaviour since it incrementally increases the load and calculates the fitting displacement. To be able to find the post-peak and snap-back behaviour, it must be combined with an arc-length control method, which is explained in Subsection 3.3.4.

The second option is displacement control, where an equivalent displacement is applied. This method is often more stable than force control and is able to capture the post-peak behaviour. If it is required to investigate snap-back behaviour, the arc-length control method is also necessary. A disadvantage is that a certain point in the structure is restricted to a certain prescribed displacement, which is often not suitable for structures with multiple different loads [3].

3.3.2 Prestress (post-tension)

Assuming that embedded fully bonded reinforcement elements are chosen for the prestressing tendons, the post-tensioning load should be applied as followed:

1. In the material property panel for the prestressing tendon, the option 'not bonded to mother element' should be chosen. This represents the tendon before grouting, which contains the following properties [1]:
 - The stiffness of the tendon does not contribute to the stiffness of the reinforced beam.
 - The deformation of the concrete beam does not cause stresses and strains in the tendon.
 - If a prestress is applied to the tendon then the equivalent element forces are applied as external forces to the element.

2. A post-tensioning load is applied to the prestressing tendons. This is defined as nodal anchor forces, which can be applied on one side or both sides. The anchor retention length, coulomb friction coefficient and wobble factor can be defined as well. According to the RTD1016-1 [3], short-term prestress losses due to wobble, friction and anchor retention should be taken into account.
3. After the application of the post-tension load, the tendon should be grouted. In DIANA, this is done by bonding the tendon to the mother element. This can be done by defining multiple phases, where, in the first phase, the unbonded material properties and the application of the post-tension load are selected. In the next phase, the bonded material properties are selected. After this bonding, the tendon contributes to the stiffness of the reinforced beam and strains and stresses are transferred.

Other options are also possible for post-tensioned reinforcements. For instance, the same modelling approach as described above could be used with weak/strong bond-slip reinforcements instead of unbonded/bonded reinforcements.

3.3.3 Load incrementation

The load incrementation describes how the loads are applied in the nonlinear analysis. The dead weight and the prestressing should be applied in the initial load step. After the initial load step, the concentrated load can be incrementally applied manually or with an automatic procedure. This automatic procedure tries to take as few load steps as possible and at the same time tries to limit the number of iterations. It recovers from non-convergence.

3.3.4 Analysis control

A commonly used analysis control method is the arc-control method. This method could be combined with force-control or displacement-control but adds an extra constraint to the incremental displacement to a prescribed value. This means that the 'distance' along the force-displacement curve between to load steps is prescribed (see Figure 3.17). In DIANA, this is done by adapting the increment size, so changing the increment size as the path becomes non-linear. Due to this extra constraint, it is also possible to capture snap-back behaviour [1].

Arc-length control needs control nodes. All nodes in the structure could be selected, but nodes in the cracking area behave very differently with respect to other nodes. This could lead to divergence in an early stage. It is therefore recommended to select the nodes where the load-displacement curve remains relatively the same and nonzero.

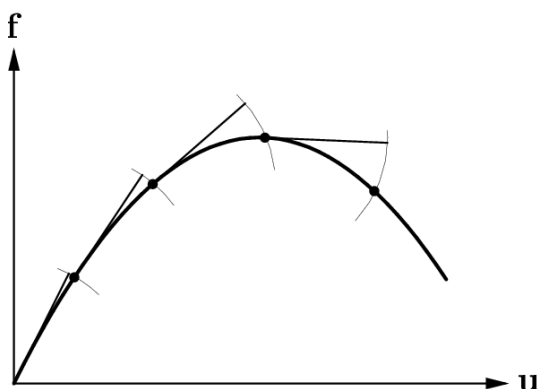


Figure 3.17: Arc-length control

3.3.5 Equilibrium iteration scheme and maximum number of iterations

In a nonlinear analysis, an unbalance in internal and external forces for every load step occurs. With the use of convergence criteria, a limit of this unbalance is defined, resulting in equilibrium between internal and external forces. Multiple methods for this equilibrium calculation exist, but the most commonly used method is the Newton-Raphson method because it is sufficiently accurate and efficient. It is possible to apply an updated stiffness matrix in every iteration (regular or full), where usually fewer iterations are necessary, or only use an update of the stiffness matrix in the first iteration, where more iterations are usually necessary, but only one stiffness matrix is calculated (modified). Graphical representations of the regular and modified Newton-Raphson methods are shown in Figure 3.18 and Figure 3.19.

A third option is the secant (Quasi-Newton) method, where the stiffness matrix is not updated for every iteration. The stiffness matrix is only computed for the first iteration. After this, the stiffness matrix is modified based on the out-of-balance force vector from the previous iteration and the current displacement vector. This means that the stiffness for the next iteration is the same as the slope between the point on the load path from the previous and current iteration (see Figure 3.20) [1].

Evangelidou [31] found that the secant method is more robust than the regular Newton-Raphson method in the case of shear failure in RC beams without shear reinforcement. The Newton-Raphson method has difficulties assessing the stiffness due to extensive cracking, which already occurs in an early stage. The stiffness assessment is more robust when using the secant method [31].

It is also necessary to use arc-length control to adjust the load increments. Otherwise, a local or global maximum could cause instability in the calculation, leading to spurious results [3].

Since cracking results in very nonlinear behaviour of concrete, it is helpful to add a line search algorithm. This algorithm uses the incremental displacement to minimize the energy potential. This can increase the convergence rate, especially at very nonlinear behaviour [1].

If a sufficient maximum number of iterations is chosen, where enough load steps reach convergence, then allowing more iterations is usually unnecessary.

De Putter [19] investigated the difference between a maximum of 40 and 100 iterations for both rotating and fixed crack models. For both crack models, 100 iterations per step showed the best results for beams with shear reinforcement. For rotating crack models without shear reinforcement, it is a bit more complex due to overrotation of the rotating cracks. It was found that the model can find a new equilibrium after the failure load by overrotating cracks, causing additional bearing capacity. However, this transition can be better observed when more iterations are used, since this causes a steeper drop in the load-displacement curve. This is shown in Figure 3.21. It is therefore advised to use at least 100 iterations per step for both crack models.

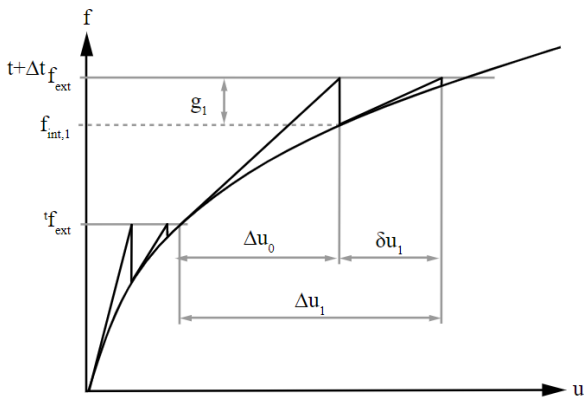


Figure 3.18: Regular Newton-Raphson method [1]

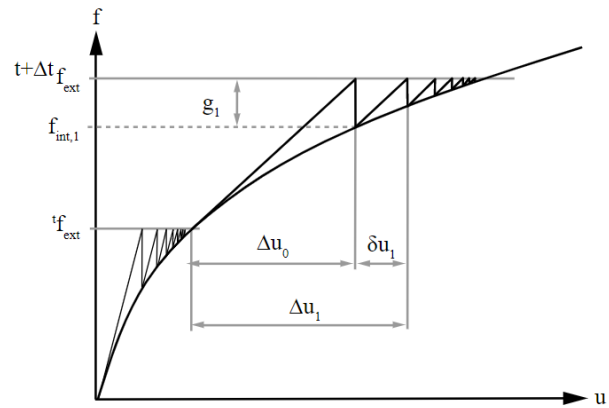


Figure 3.19: Modified Newton-Raphson method [1]

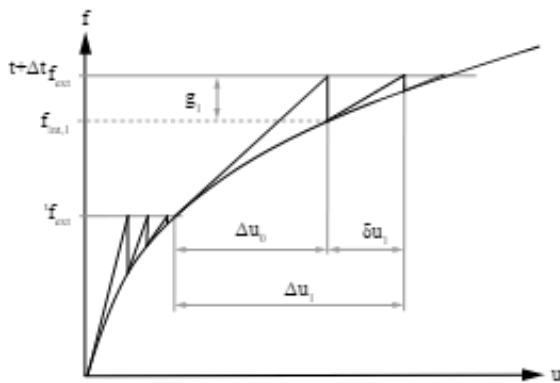


Figure 3.20: Secant (Quasi-Newton) method [1]

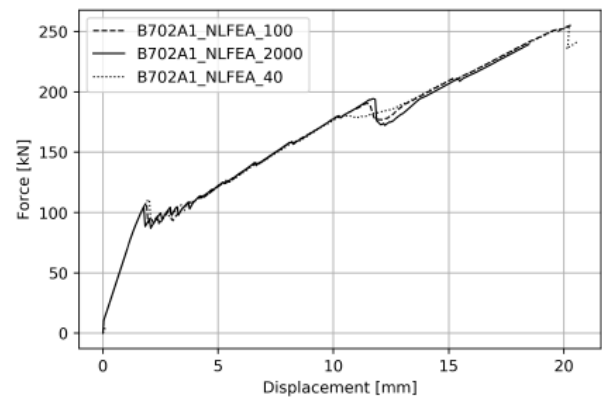


Figure 3.21: Force displacement curve of a rotating crack model without shear reinforcement with 40, 100 and 2000 iterations per step [19]

3.3.6 Convergence criteria

The convergence criteria define when the results of an iteration are sufficient and the iteration process can be stopped. In this case, a load step is converged. If the iteration process is stopped after several iterations and the convergence criteria are not met, the load step is non-converged. If the results from the iterations drift away from the solution, i.e. the convergence norms become larger with every iteration, the iteration process is also stopped and the load step has diverged.

Multiple criteria are possible, but the most used norms are the force, displacement and energy norms. For all norms, the norm is calculated as the ratio between the current and the first iteration of the load step. The exact equations for the force, displacement and energy norm are shown in the equations below, respectively. The parameters used in these equations are graphically declared in Figure 3.22.

$$\varepsilon_F = \frac{\sqrt{\mathbf{g}_i^T \mathbf{g}_i}}{\sqrt{\mathbf{g}_0^T \mathbf{g}_0}} \quad (3.19)$$

$$\varepsilon_u = \frac{\sqrt{\delta \mathbf{u}_i^T \delta \mathbf{u}_i}}{\sqrt{\Delta \mathbf{u}_0^T \Delta \mathbf{u}_0}} \quad (3.20)$$

$$\varepsilon_E = \frac{\delta E_1}{\Delta E_0} = \left| \frac{\delta \mathbf{u}_i^T (\mathbf{f}_{int,i+1} + \mathbf{f}_{int,i})}{\Delta \mathbf{u}_0^T (\mathbf{f}_{int,1} + \mathbf{f}_{int,0})} \right| \quad (3.21)$$

RTD1016-1 [3] describes that convergence criteria based on an energy and a force norm are preferable. Based on the guidelines, a force norm tolerance of 0.01 and an energy norm tolerance of 0.001 are suggested. If one of the two norms is satisfied, the load increment can be considered as converged. Non-converged load increments can still be admissible, but they must be followed by converged steps and an explanation for the temporary non-convergence. In concrete beams, non-convergence often indicates a change in behaviour due to cracking.

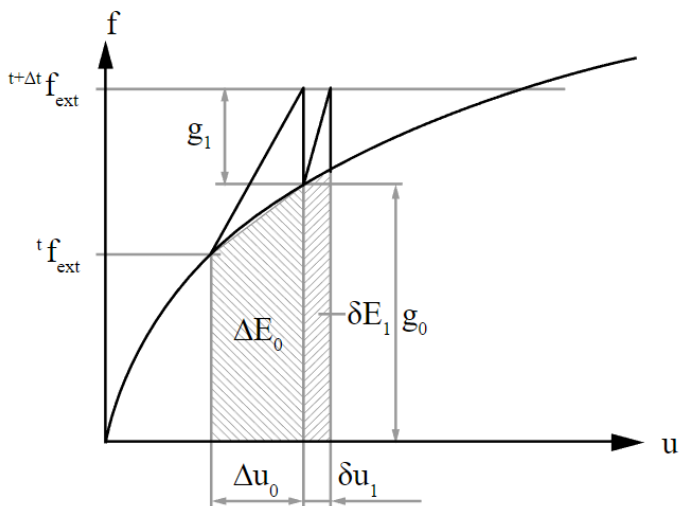


Figure 3.22: Convergence norm parameters [1]

4 Experimental benchmark: Schramm [2]

The problem that this thesis focusses on came to light during the reassessment of some box-girder bridges. The calculated deficits in the shear resistance of existing concrete bridges are not only a problem in the Netherlands but occur on a global scale. This means that there is a large demand for insights into this problem, but so far very few relevant shear tests for these stirrup types and cross-sectional dimensions are documented in literature.

Schramm [2] developed shear models for prestressed concrete beams with three different incorrectly detailed stirrup types, which should provide a better estimate of the shear resistance. For the development of these shear models, multiple shear tests for relatively large cross-sectional dimensions were performed. The results of these tests are used as the experimental benchmark for this thesis.

His research focussed on rectangular and T-shaped cross-sections. It is important to understand the similarities and differences of the behaviour and load transfer of different types of cross-sections to be able to make valid assumptions and simplifications for comparison and modelling. In the first part, the stress distributions for rectangular and box-girder beams are described. This is done per stress type for both the rectangular and box-girder beams.

In the second part, the experimental benchmark of Schramm [2] is discussed. Here, the relevant aspects of his research are elaborated, containing his test setup, material properties and experimental results. In Appendix A, a detailed overview of the geometrical and material properties and relevant results are given.

4.1 Comparison between rectangular and box-girder cross-sections

4.1.1 Cross-sections and assumptions

In this part, two simplified rectangular and box-shaped cross-sections are compared, which are shown in Figure 4.1. The comparison is qualitative and focuses on the stress flows and distribution based on linear elastic behaviour, so obeying Hooke's Law [32]. This provides a simplified insight into the behaviour of such cross-sections, where assumptions follow from.

Especially the stresses in the web of the box-girder are important to compare with a rectangular section because the open straight-legged stirrups are also situated in the webs of box-girder bridges. This simple comparison gives an insight into the similarities and differences between a rectangle and a web of a box-girder. From this, simple assumptions can be made to compare the results from Schramm [2] with the web of a box-girder bridge. The web of the box-girder has the same dimensions as the rectangle. Cantilevers of a box-girder are not considered, since these do not contribute much to the resistance of the cross-section.

In reality, the concrete and steel do not behave linear-elastically and interaction between the webs and flanges of the concrete box is also dependent on multiple factors. So, the focus is purely on the distribution of loads and not on the resistance of these loads. Therefore, it is valuable to investigate the nonlinear behaviour to be able to compare concrete rectangular cross-sections and concrete box-girder beams. From this, accurate assumptions and adjustments could be derived to describe the behaviour of concrete box-girder beams with open straight-legged stirrups. However, this is not covered in the scope of this thesis.

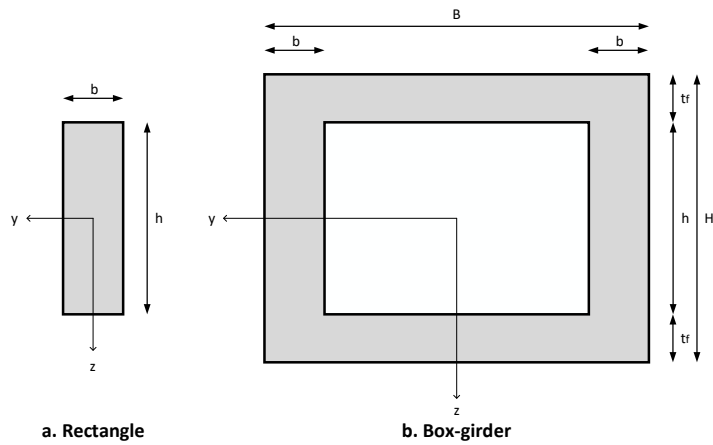


Figure 4.1: Compared cross-sections

4.1.2 Axial forces

The stress due to an axial force is:

$$\sigma_N = \frac{N}{A} \quad (4.1)$$

Where:

- σ_N Stress due to an axial force
- N Axial force
- A Area of the cross-section

This means that the stress is constant over the whole cross-section. The rectangle and the web of the box-girder behave in the same way. The area of the rectangle and the web of the box-girder are the same. This means that no additional assumptions or adjustments must be made to compare these cross-sections regarding axial forces.

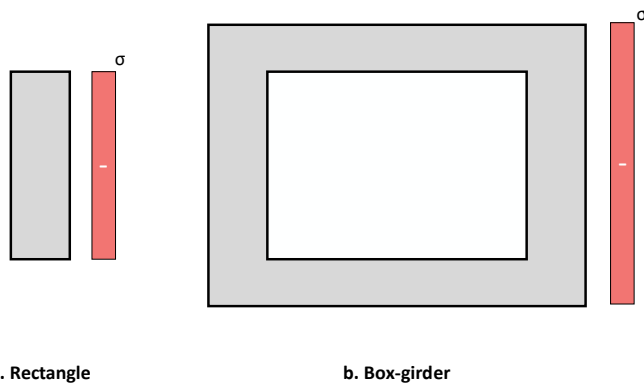


Figure 4.2: Stresses due to an axial force

4.1.3 Bending moment

The stress due to a bending moment is:

$$\sigma_M = \frac{Mz}{I} \quad (4.2)$$

Where:

- σ_M Stress due to a bending moment
- M Bending moment
- z Distance in z-direction to the neutral line
- I Moment of inertia

This means that the stress varies linearly over the height of the cross-section (see Figure 4.3). Therefore the largest stresses occur at the top and bottom. For a box-girder beam, the most resistance is generated by the flanges. However, when a web is 'cut out' of a box-girder, it results in the same stress distribution as for the rectangular cross-section. From this, it can be assumed that an acting bending moment is dealt with in the same way for a rectangular cross-section and a web of a box-girder beam. This means that no additional assumptions or adjustments must be made to compare these cross-sections regarding bending moments.

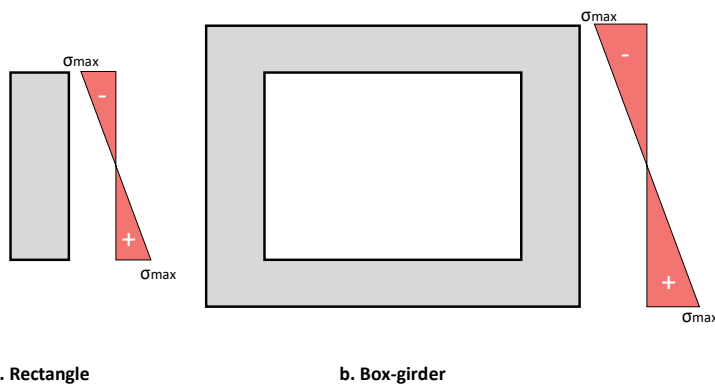


Figure 4.3: Stresses due to a bending moment

4.1.4 Shear forces

To understand the resistance to shear forces, the analogy of a shear flow is used. A downward-acting shear force is assumed. This force 'flows' from top to bottom. For a rectangular cross-section, it is assumed that the shear flow and stress over the width of the cross-section are the same. This is valid for thin beams. For the box-beam, assuming thin webs and flanges, this means that the shear flow in the flanges is vertical and constant over the width and in the webs horizontal and constant over its height. This is shown in Figure 4.4. The shear flow and shear stress are formulated as:

$$|s| = \frac{VQ}{I} \quad (4.3)$$

$$|\tau| = \frac{VQ}{bI} \quad (4.4)$$

Where:

- s Shear flow
- τ Shear stress
- V Shear force
- Q First moment of area
- b Width of the beam

Assuming a vertical shear flow, this is defined as the area above the axis of interest (for the area above the neutral axis) times the distance from the neutral axis to the centroid of the area. This results in maximum shear stresses at the neutral axis for both cross-sections. The stress distributions are shown in Figure 4.4.

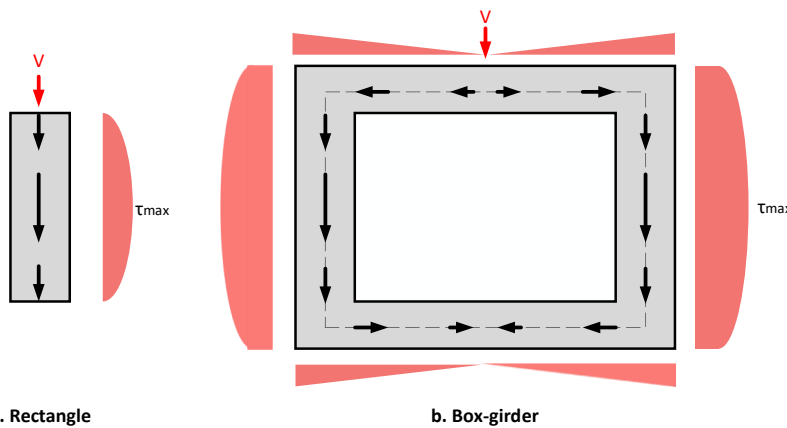


Figure 4.4: Stresses due to a shear force

The shear force acting on the rectangle is resisted equally over the width, so one resulting force can be generated. For the box-girder, this is slightly different. The horizontal shear flow in the top and bottom cancel each other out, resulting in a total horizontal force of $\sum H = 0$. The vertical shear flow in the webs of the box-girder generates the resistance to the shear force, resulting in half of the shear force in both webs. This is shown in Figure 4.5.

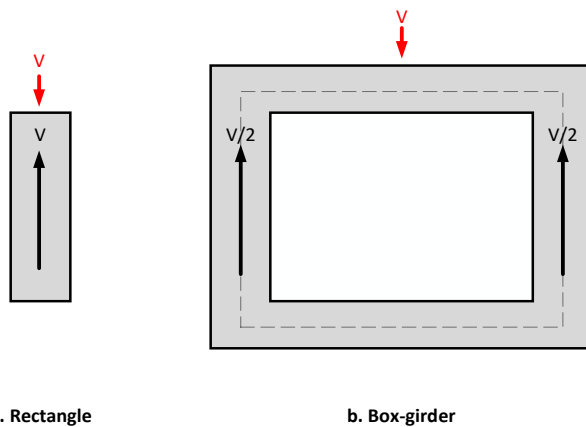


Figure 4.5: Internal vertical forces due to a shear force

4.1.5 Torsion

Torsion is a phenomenon that occurs when a shear force acts eccentrically from the shear centre. This causes a torsional moment in the cross-section. Two types of torsion can occur: St. Venant torsion (or pure or uniform torsion) and warping (see Figure 4.6). For St. Venant torsion, it is assumed that “plain sections remain plain”. Therefore, there are no stresses perpendicular to the surface of the cross-section and the torsional moment is resisted purely by shear stresses. Warping is a type of torsion where plain cross-sections deform as well, possibly causing additional axial stresses. For unrestrained warping, no additional stresses occur since the cross-section is free to warp. When a cross-section is restrained, additional bending stresses occur, so the torsional moment is also resisted by axial stresses. Figure 4.7 shows examples of unrestrained and restrained warping.

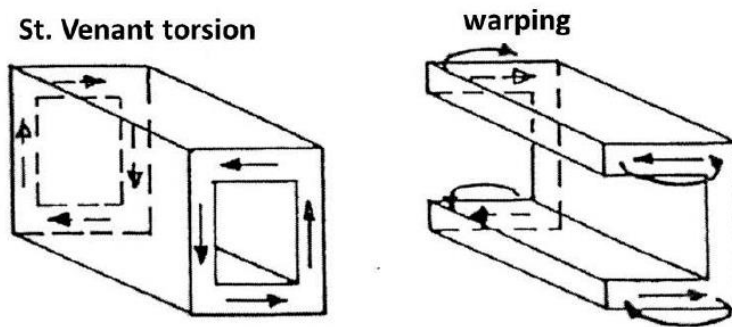


Figure 4.6: St. Venant torsion and warping [33]

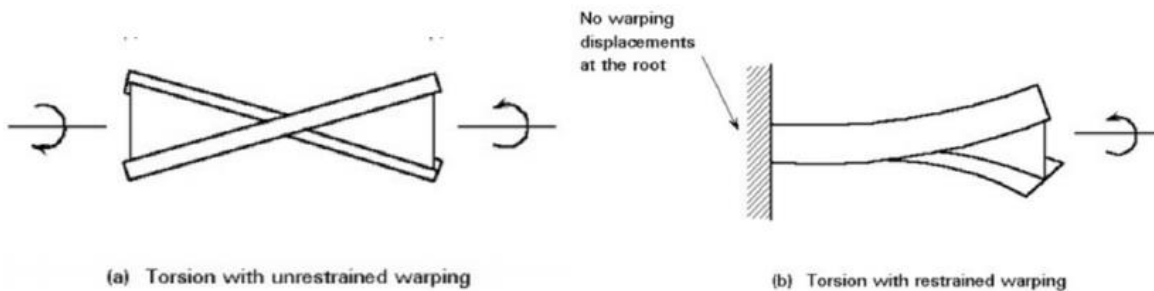


Figure 4.7: Torsion with unrestrained and restrained warping [33]

In Eurocode 2 [8], warping is neglected in closed and solid cross-sections, because it has a small contribution to the total torsional resistance. There are some cases where significant restrained torsional warping of box-girder bridges could occur. This effect is not significant in very thin-walled box-girders but can cause problems for thicker walls [34]. For simplicity, very thin-walled box-girders are assumed, so warping is negligible².

Therefore only uniform warping for both cross-sections is described. Again, the analogy of a shear flow can be used to describe pure torsion. For a solid cross-section, this means that the shear stress is zero in the shear centre and largest along the edges (see Figure 4.8). This linear gradient is the same for box-girders, but since there is no core, only stresses in the outer shell develop.

² This assumption is made for simply supported girders with a straight span (the supports are placed perpendicular to the span of the girder). When there is a significant skew angle, torsional moments in the box-girder can also result in forces in longitudinal direction.

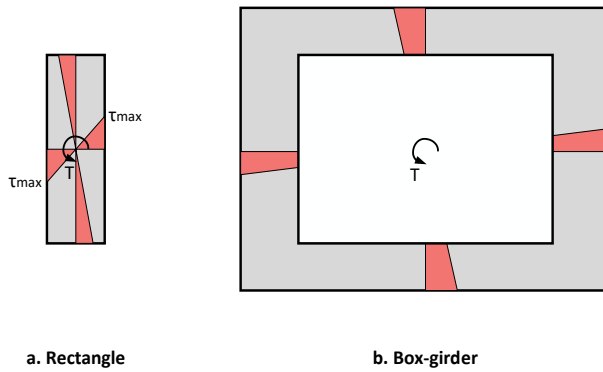


Figure 4.8: Stresses due to a torsional moment

The core in a solid cross-section has a relatively small contribution to the total torsional stiffness and is therefore neglected in many design approaches. In Eurocode 2 [8], a constant shear flow is assumed, which leads to the following equation:

$$\tau_i t_i = \frac{T}{2A_k} \quad (4.5)$$

Where:

- τ_i Shear stress in flange/web i
- t_i Thickness of flange/web i
- T Torsional moment
- A_k Area enclosed by the centrelines of the flanges and webs

This means that the largest shear stress occurs at the flange or web with the smallest thickness. For solid cross-sections, this approach is also used, where the effective thickness of the outer part is determined and the resistance of the core is neglected. The effective thickness (for both solid and box-girder cross-sections) is defined as:

$$t_{eff,i} = \min\left(\frac{A}{u}, t_i, 2c\right) \quad (4.6)$$

Where:

- $t_{eff,i}$ Effective thickness of flange/web i
- u Perimeter of the cross-section
- c Concrete cover for the longitudinal reinforcement

the acting shear force in a flange or web can be determined with:

$$V_i = \tau_i t_i z_i \quad (4.7)$$

Where:

- V_i Acting shear force in flange/web i
- z_i Length of flange/web i

The resulting shear forces are shown in Figure 4.9.

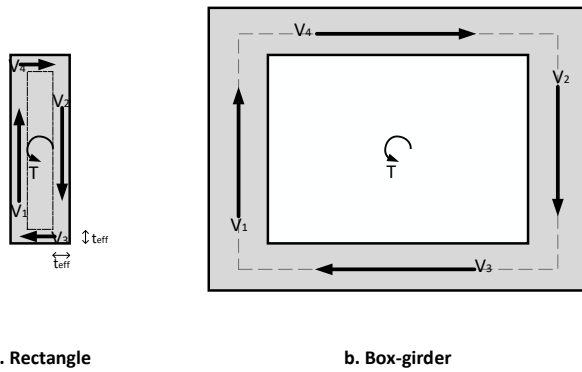


Figure 4.9: Internal shear forces due to a torsional moment

Here it can be seen that the shear forces in the rectangle and the web of the box-girder are different. In the box-girder, the shear force acts in one direction per web or flange. In the rectangle, the torsional moment generates shear forces at the outer part of the cross-section. Therefore, it is not valid to directly compare these cross-sections concerning torsion. For a valid comparison between rectangular cross-sections and the web of a box-girder, it is important to prevent shear stresses due to torsion.

4.1.6 Conclusion

Concluding this first part, it can be stated that both cross-sections handle axial stresses, caused by axial forces or bending moments, the same.

In a box-girder, the acting shear force is distributed equally over both webs, which means that half of the acting shear force is distributed over one web. Based on this assumption, the box-girder should be able to resist twice as much as a rectangular-shaped beam with the same dimensions as the webs. However, this does not change the behaviour of an individual web, which concludes that shear stresses are handled the same for a web of a box-shaped and a rectangular cross-section.

In the case of torsion, a distinction was made between St. Venant torsion and warping. Since the influence of warping is small for both cross-sections (assuming thin-walled box-girders), this type of torsion is neglected. St. Venant torsion causes shear stresses. When shear and torsion both act on a box-girder (which is almost always the case), torsion causes an additional shear force in both webs, but in the opposite direction. This means that the shear forces due to the shear load and torsion add up in one web and subtract in the other. In a rectangular cross-section, the shear flow due to torsion also 'flows around', but in the cross-section itself. This results in a varying stress distribution over the cross-section, which is unwanted for a straightforward comparison. As long as significant shear stresses due to torsion in a rectangular beam are prevented, it can be concluded that it is not necessary to devote extra attention to torsion and a direct comparison is possible.

It is important to realize that these conclusions are based on the assumption of linear elastic behaviour. In reality, many aspects (reinforcement, cracking, loading history etc.) determine the actual behaviour of a concrete beam. To be able to accurately compare the behaviour of rectangular and box-girder beams under different loading conditions, further research into their nonlinear behaviour is necessary. Especially, the behaviour of box-girders under restrained warping requires more research.

4.2 Schramm's research [2]

4.2.1 Relevant aspects for this thesis

Schramm's dissertation [2] includes more than only tests for no longer permitted stirrups. The aim was to develop more accurate shear models for prestressed concrete beams with these stirrup types. Schramm started his investigation with literature research, where the current knowledge and design basics for shear resistance of reinforced and prestressed concrete are described. Then, the test setup, the test specimens and the experimental results are described. Especially this part of the dissertation is used for this thesis. After this, different shear models for different cross-sections and stirrups are proposed and compared to the experiments. These shear models showed good correspondence with the experiments.

In short, his dissertation provides insight into the behaviour of prestressed concrete beams with no longer permitted stirrups and proposes an engineering method to assess such beams. This is exactly the information Rijkswaterstaat desires, but the experiments and shear models only describe beams with rectangular and T-shaped cross-sections. In other cross-sections, like box-girders, other factors could play a part in the shear resistance, for instance, the cooperation between the webs and flanges of a box-girder. It is therefore necessary to perform further investigations.

This thesis focuses on the results of the rectangular beams with closed and open straight-legged stirrups. In Schramm's dissertation [2], these tests are referred to as tests R2, R3 and R4, R5 respectively. Also, for basic understanding and to describe a lower bound of the shear resistance, the experimental results for the concrete beam without stirrups (test R1 and R10) are used. Since the failure mechanism for concrete beams without stirrups is completely different than for concrete beams with stirrups, this experimental result is not further investigated and modelled with a finite element analysis. The T-shaped beams are also not considered due to limited time but are interesting to evaluate for further research. Finally, his conclusions are considered, which can be used and compared to the conclusions of this thesis.

4.2.2 Test setup and material properties

This research was focused on continuous prestressed concrete beams. To test this, an innovative and efficient testing procedure was used, which can be seen in Figure 4.10. A beam on three supports with two external forces at the midspans was evaluated, but for the test, only the decisive beam part was considered, which is part of the beam where the largest shear forces and bending moments occur. The boundary conditions of this part were taken into account, which can be seen at the bottom of Figure 4.10.

A schematic view of the test rig, the so-called 'substructure technique', is shown in Figure 4.11. The test beams were clamped jointed to two solid steel plates, where trapezoidal shear cams were milled in to ensure shear force transfer between the beam and plates. These plates had removable fitting parts with holes and special anchoring devices.

On the active loading plate, four horizontal hydraulic cylinders were placed, which were used to transfer a bending moment. Two vertical hydraulic cylinders on top of the loading plate were used to apply a shear force. The hydraulic cylinders had some axial displacement capacity and could rotate to a maximum of 7° , which allowed the test rig to compensate for initial imperfections in the transverse and axial direction of the test beams. This half part of the beam is identified as the active side, field area or area with a positive bending moment.

On the passive loading plate, four horizontal rigid reaction rods were placed to ensure the balance of moments and two roller supports under the plate ensured the balance of vertical forces and prevent transverse displacements. This half part of the beam is identified as the passive side, support area or area with a negative bending moment.

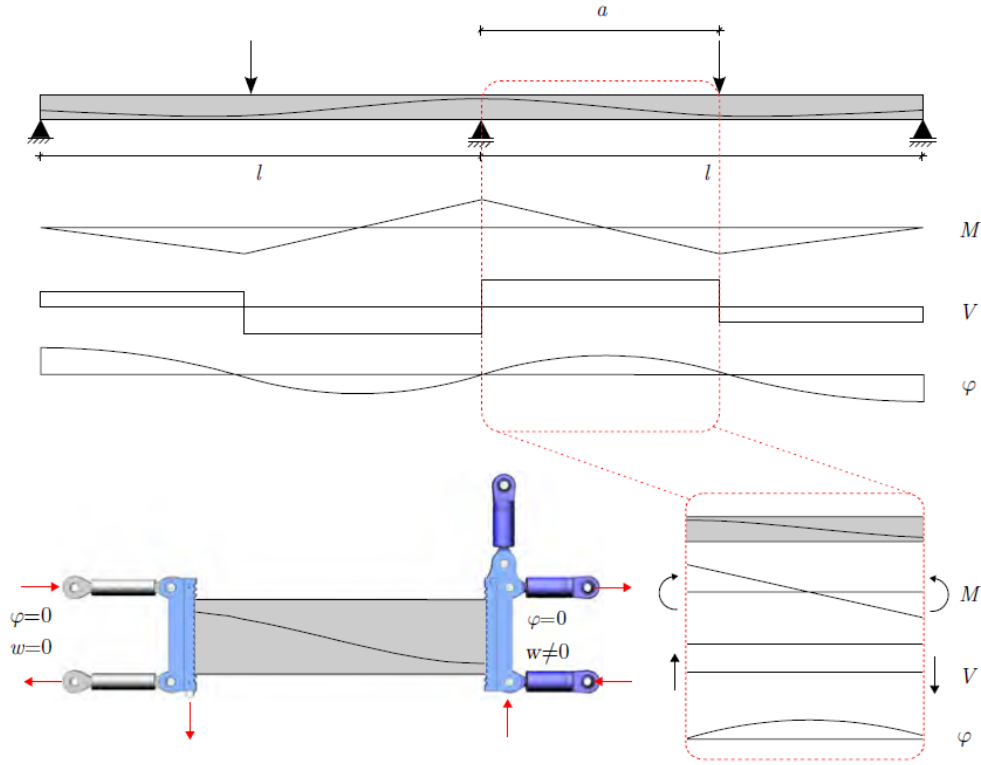


Figure 4.10: Test setup and acting forces and moments [2]

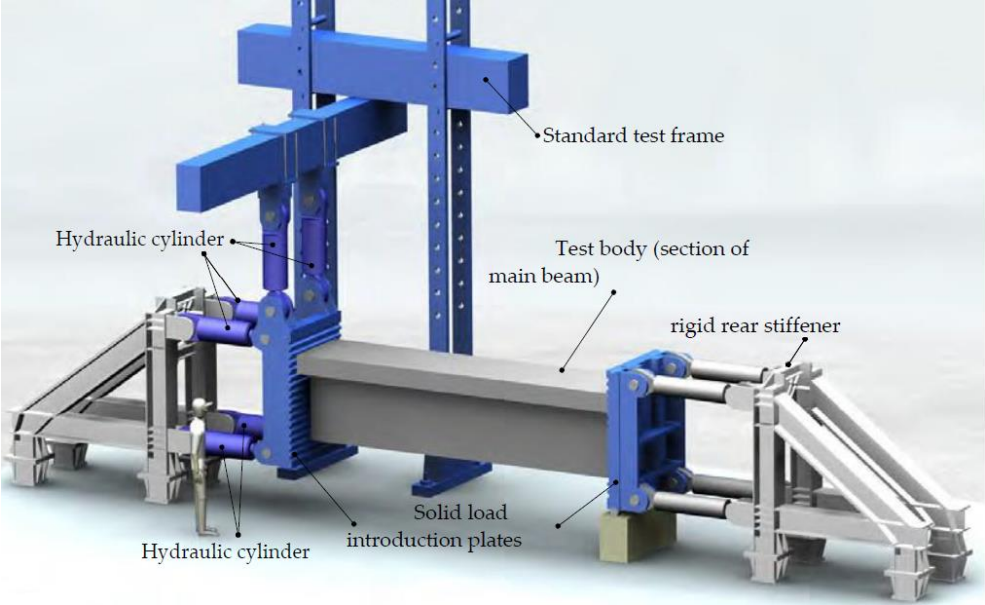


Figure 4.11: Schematic view of the test setup [2]

The tests of the rectangular beams varied in shear reinforcement ratio and stirrup type. Figure 4.12 shows which stirrup types were investigated. For this thesis, only the results for the open straight-legged stirrups (Figure 4.12a) are relevant. To estimate the influence of these stirrup types also beams without stirrups and closed stirrups were tested. With fibre-optical measurements, the strains along the stirrups were measured, which gives an insight into the shear behaviour of the stirrups. With this test setup, 14 tests in total were performed.

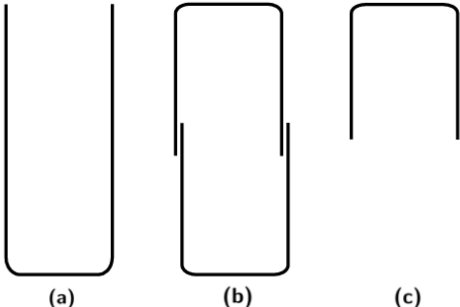


Figure 4.12: No longer permitted stirrup types [2]

The tested beams were 3.5 m long, 0.8 m high and 0.25 m wide in the test area. The ends of the beams (load application areas) were linearly widened with a maximum width of 0.5 m at the ends (see Figure 4.13). The concrete target strength was C30/37, but the measured compressive cylinder strength varied between 37.6 and 48.1 MPa. The maximum grain diameter is 8 mm. The beams contained prestressing steel, longitudinal reinforcement and shear reinforcement, which can be seen in the cross-sections shown in Figure 4.14. For a detailed description of the test beams is referred to the original dissertation. In Appendix A.1, a detailed overview of the geometrical and material properties is given. However, extra attention is paid to the reinforcement configuration, the ends of the beams and the load application. See Appendix A.16 of Schramm’s original dissertation for the detailed reinforcement configuration [2].

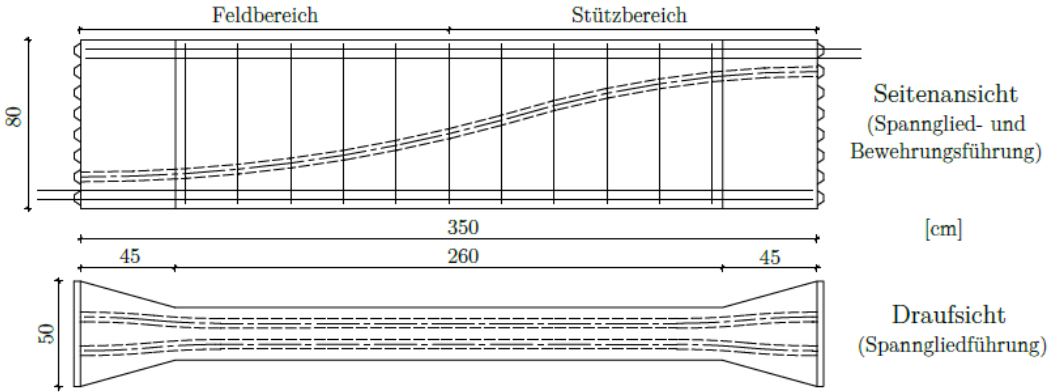


Figure 4.13: Section of the test beams [2]

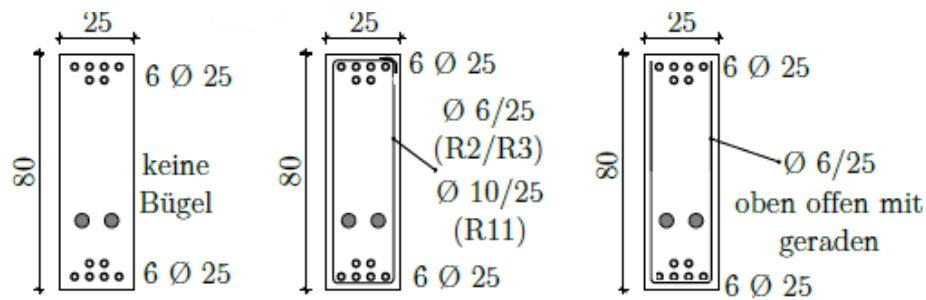


Figure 4.14: Cross-sections of relevant specimens [2]

Reinforcement configuration

Longitudinal reinforcement

At both the top and bottom sides of the beams, 6 steel bars (B500B) with a diameter of 25 mm were placed in the longitudinal direction. To reduce any slipping or friction losses close to the support, the longitudinal reinforcement was connected to the loading plate with extension nuts and hand-tight pre-tensioned. This connection is shown in Figure 4.15. Please note, Figure 4.15 shows a connection for a T-beam, where the reinforcement configuration is different (10 bars instead of 6). The top bars were connected with the passive loading plate and the bottom bars with the active load introduction plate.

Shear reinforcement

For the beams with closed and open straight-legged stirrups (B500B), the stirrups were ribbed, had a diameter of 6 mm and were placed every 250 mm in the longitudinal direction in the test area of the beam ($\rho_w=0.905\%$). For the beams with open straight-legged stirrups, the open ends point upwards. This way, the behaviour of the straight bar ends can be investigated in both the bending tension zone and the bending compression zone.

Post-tensioned tendons

All the test specimens with a rectangular cross-section contained two post-tensioned garland-shaped tendons (QP190) with an area of $3 \times 140 \text{ mm}^2$, generating a prestress of $\sigma_{cp} = 2.5 \text{ MPa}$. This means that about 250 kN per tendon was preloaded. The shape is chosen such that there is no internal force resulting from the statically indeterminate effect of the prestress. The tendons were inserted in the installed test setup and wedged into the anchor sleeves after approval, with multi-part spacer washers provided on both sides between the loading plates and anchor sleeves. This made it possible to release the prestress between the loading plates and the anchor sleeves when the test was finished and the beam was removed. The tendons were loaded on the passive loading side, so on the high point end of the tendons. After tensioning, the formwork was grouted. The compaction of the grout was ensured with a special sealing compound and siliconization. A special anchoring design was used for the strands, which caused almost no wedge slip losses. This anchoring is shown in Figure 4.15.

Ends of the test beams

The load application areas were widened linearly and were provided with a significantly higher shear reinforcement ratio to avoid failure close to the supports. The most important content of this shear reinforcement was the closed stirrups (B500B) with a diameter of 12 mm and a spacing of 80 mm. the width of these stirrups also varies linearly, like the width of the beam, providing a constant concrete cover for all stirrups.

Load application

To be able to control the test in lower shear force ranges, an initial shear force of 30 to 60 kN was applied at the beginning of the tests. The torsional moments and normal forces were controlled. So if a vertical displacement of a loading plate happened, the corresponding bending moment was set accordingly. Therefore, a constant shear force and linearly varying bending moment are guaranteed.

The control method is a combination of load and displacement control, with the shear force calculated from the pressure sensors and the inclination of the hydraulic cylinders as the main control variables. The shear force over time was defined. When the actual and target value of the shear force deviated, which indicates a fracture, an immediate switch to displacement control was made. This is a robust control method which is also capable to investigate post-fracture behaviour.

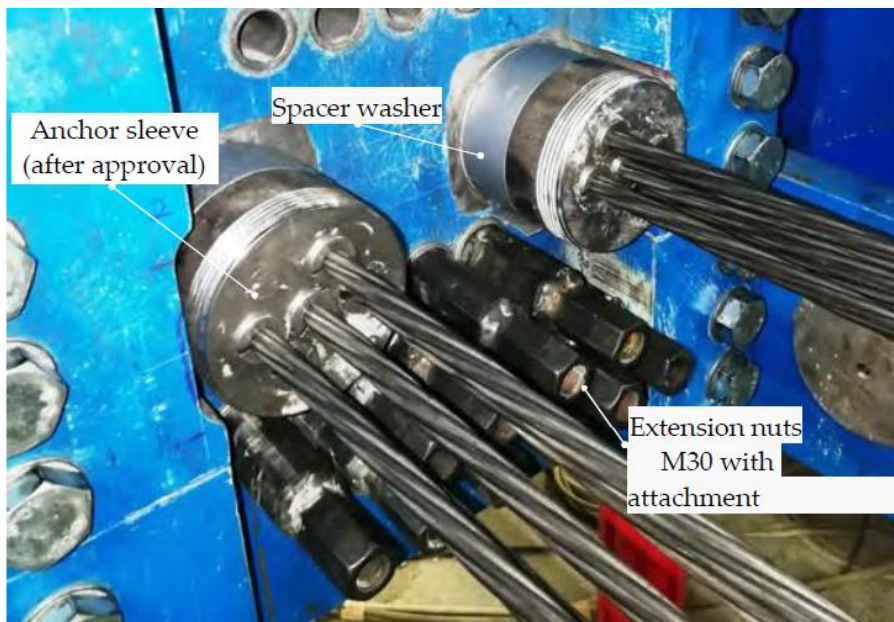


Figure 4.15: Anchoring of the prestress tendons and longitudinal reinforcement on the active load introduction plate [2]

4.2.3 Experimental results

The experimental results of the prestressed concrete beams are discussed below. The results concerning the ultimate shear strength, crack development and strain development in the stirrups are used to examine the behaviour of the different beams.

Test beams R1 and R10 are concrete beams without stirrups and show more or less the same results, so it is redundant to analyse both cases. For test beam R10, the crack patterns of the concrete are also available (this is not the case for R1) and therefore only this beam is considered. This also applies to the beams with closed stirrups R2 and R3, where R2 is considered. For the beams with open straight-legged stirrups R4 and R5, beam R4 is considered, because the results of beam R5 were an outlier, showing clear bending cracks, failure at a low maximum load and very flat shear cracks early in the test.

Ultimate shear strength

The ultimate shear strengths of the beams without stirrups (R10), with closed stirrups (R2) and with open straight-legged stirrups (R4) were 596 kN, 711 kN and 659 kN respectively. From this, it can be stated that the open straight-legged stirrups do contribute significantly to the total shear resistance. Comparing the contribution of closed and open straight-legged stirrups, it follows that the contribution of the open straight-legged stirrups to the total shear resistance is approximately 55% of the closed stirrups.

The figure below shows the shear force-displacement diagram. The lower values in the graph describe the shear crack loads. This is the load at which a shear crack penetrates to half of the beam height. The difference in shear crack load between the beam with the closed and open stirrups is small (345 kN vs. 365 kN). All tests show about the same development, but the largest differences are in the region before failing. The beam without stirrups suddenly collapses after the ultimate shear force and has no resistance left after this. The beams with stirrups do not immediately collapse after the ultimate load but seem to have some resistance left. Especially the beam with open straight-legged stirrups is interesting since the ultimate resistance is reached after one decrease in strength but still has some capacity after this. This indicates a drastic redistribution of stresses.

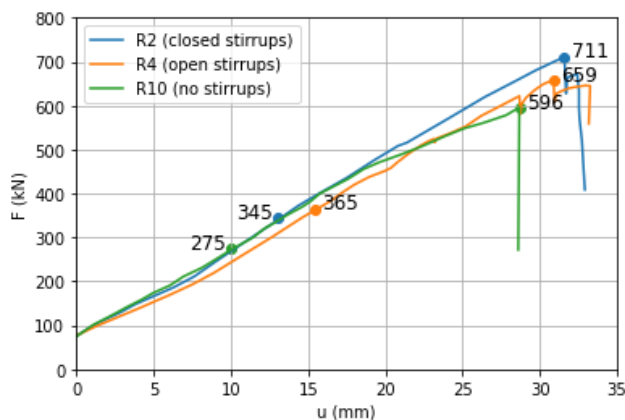


Figure 4.16: Shear force-displacement diagram of tests R2, R4 and R10

It is important to mention that the stiffness of the tests with this substructure technique was considerably lower than the stiffness of reference tests, where continuous beams were used. This difference is especially large in the linear elastic range. One particular comparison with reference test DLT1.1-RWTH Aachen is shown in Figure 4.17. According to Schramm [2], This lower stiffness of the substructure is caused by imperfections in the fitting accuracy of the shear beams between the steel loading plates and the clamping restraints are less effective due to the lack of participation of the concrete in the tension zone. The difference in ultimate strength is due to a difference in concrete compressive strength and load introduction.

Another comparison of a 60 cm high I-beam with 3-point bending tests was made, where corresponding tests on which only half of the beam were designed to use for the substructure technique. This comparison also showed good agreement between the failure mode, ultimate load and crack pattern, except for the deformations of the beams.

In short, Schramm [2] concluded that tests performed with the substructure technique are able to accurately predict the failure modes, ultimate loads and crack patterns of continuous concrete beams. On the other hand, beams behave less stiff than expected, resulting in larger deformations. It was also stated that further validation of this substructure technique should be carried out within the framework of future investigations.

Due to the shortage of research including RC beams with open straight-legged stirrups, the conclusions stated in the paragraph above are considered and accepted. This means that the deviations in the results from his tests compared to reference tests are accepted and not further investigated in this thesis.

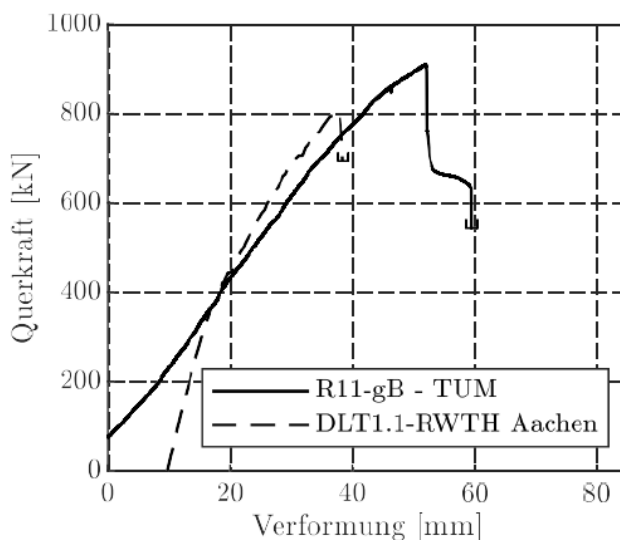


Figure 4.17: Shear force-deflection curves of test R11-gB and DLT1.1-RWTH [2]

Crack development

In Figure 4.18, the crack patterns at the maximum shear load of the test beams are shown. In Appendix A.2, the full crack development of the tests is presented, where the crack patterns are shown at a load of 50%, 75% and around 94% of the ultimate load and after failure. In these figures, it can be seen that the shear cracks are a result of propagating bending cracks. These bending cracks develop first in all tests. It is remarkable that these bending cracks only develop on the passive loading side since the acting bending moment and resistance should be approximately the same on both sides. A possible explanation found by Schramm [2] is that the tension resistance on the passive side is a bit smaller due to a small prestressing loss due to wedge slip.

With increasing load, these cracks develop diagonally, which implies flexural shear cracks. When looking at the crack patterns in Figure 4.18, it can be seen that all beams fail due to transverse shear in the area with a negative bending moment. In the beam with open straight-legged stirrups (R4), a stronger crack formation in this region is observed.

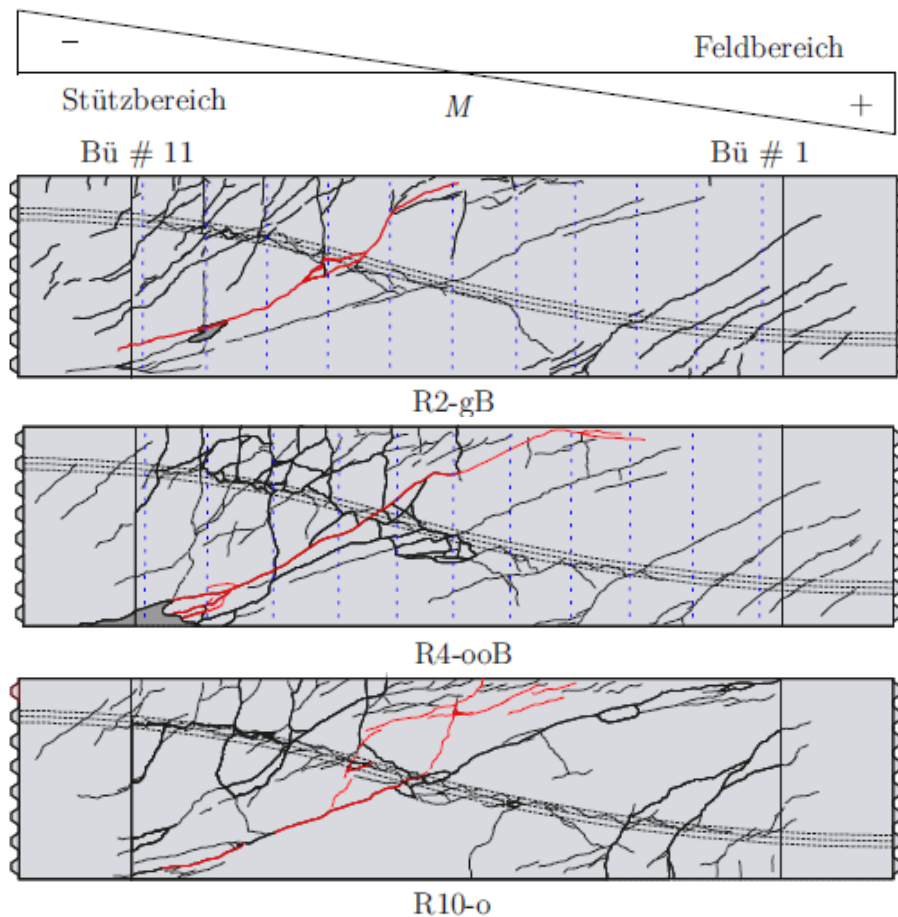


Figure 4.18: Crack patterns at maximum shear load

Strain development in stirrups

The full strain development of beams R2 and R4 are shown in Appendix A.2, where the strains in the stirrups are shown at a load of 50%, 75% and 100% of the ultimate load and after failure. Figure 4.19 shows the strain in the stirrups at the ultimate shear load. On average, yielding of the stirrups occurs at a strain of 2970 $\mu\text{m}/\text{m}$ and therefore a legend range of up to 3000 $\mu\text{m}/\text{m}$ is mapped.

The strain distribution is uneven over the height of the stirrups. This is because the local strain is highly dependent on the crack formation. When comparing the crack patterns from Figure 4.18 and the strains in the stirrups from Figure 4.19, it can be seen that the strain peaks occur at the locations where inclined cracks cross the stirrup.

Schramm [2] measured the contribution of the stirrups by subtracting the total shear resistance of the beam without stirrups (R10) from the beam with stirrups. For instance, the contribution of the stirrups for beam R2 is 711-596 = 115 kN. However, the axial resistance of the stirrups could also be measured by summing up the contributions of the stirrups in the critical crack. For example, for beam R2, six stirrups are yielding due to the critical crack. The contribution is then:

$$V_s = n \times A \times f_y = 6 \times \left(2 \times \frac{1}{4} \times \pi \times 6^2 \right) \times 588.2 = 200 \text{ kN}$$

This difference is probably due to the relatively low shear reinforcement ratio, where the shear reinforcement becomes less effective due to less cooperation between the stirrups.

At the ultimate load, many inclined cracks are formed. However, a difference in behaviour is observed between the closed stirrups and open straight-legged stirrups. The closed stirrups achieve strain peaks over the whole height, while the open straight-legged stirrups cannot achieve strain peaks at the straight bar ends, regardless of the stresses due to the bending moment. The open ends require an anchorage area to be able to transfer stresses to the concrete, resulting in a reduced shear resistance compared to beams with closed stirrups. Except for this, the same load-bearing behaviour as for closed stirrups is observed.

In addition to the investigation of the behaviour of open straight-legged stirrups, Figure 4.20 shows the crack patterns and strains of two stirrups at different load levels. Stirrup 2 is situated in the field area, where the open ends are located in the compression zone. In Figure 4.20c, it can be seen that the 'closed' bottom side of the stirrup develops a similar strain progression as closed stirrups. This is very different for stirrup 8, where the open ends are located in the cracked tension zone. In Figure 4.20d, strains close to the yield strain are developed within the anchorage length at a load close to the ultimate load. Shortly after this load, the straight ends were pulled out, decreasing the load capacity of this stirrup to zero in this area. The existing anchorage length above the crack was insufficient to allow full anchorage up to the yield strength.

This explains the lower shear resistance of the beams with open straight-legged stirrups, where stirrups that are crossed by an inclined crack within the anchorage length do not (fully) contribute to the shear resistance. These stirrups fail due to pull-out before the yield strain can be reached.

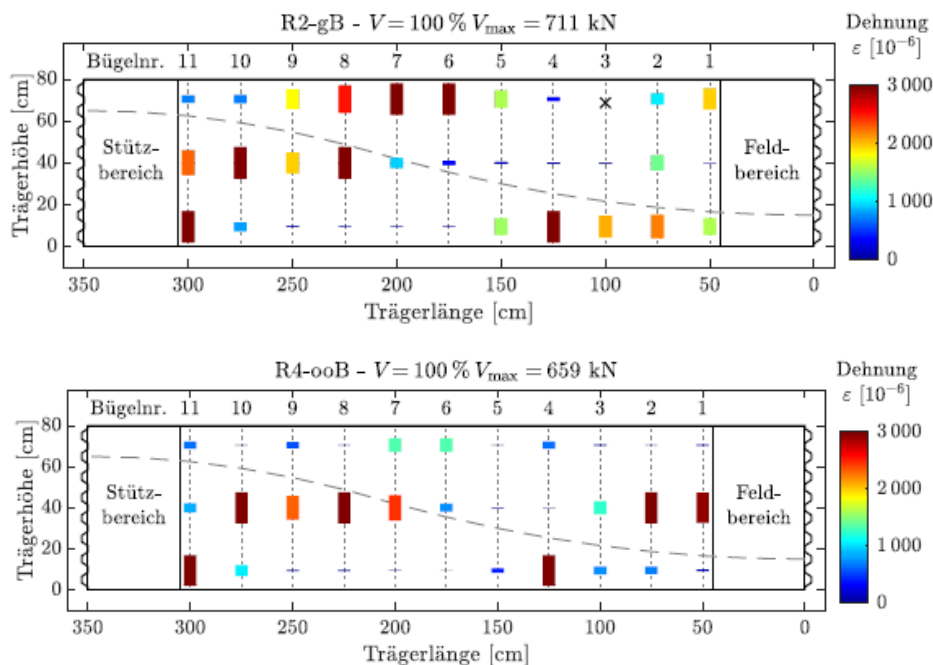


Figure 4.19: Strain in stirrups at the ultimate shear load

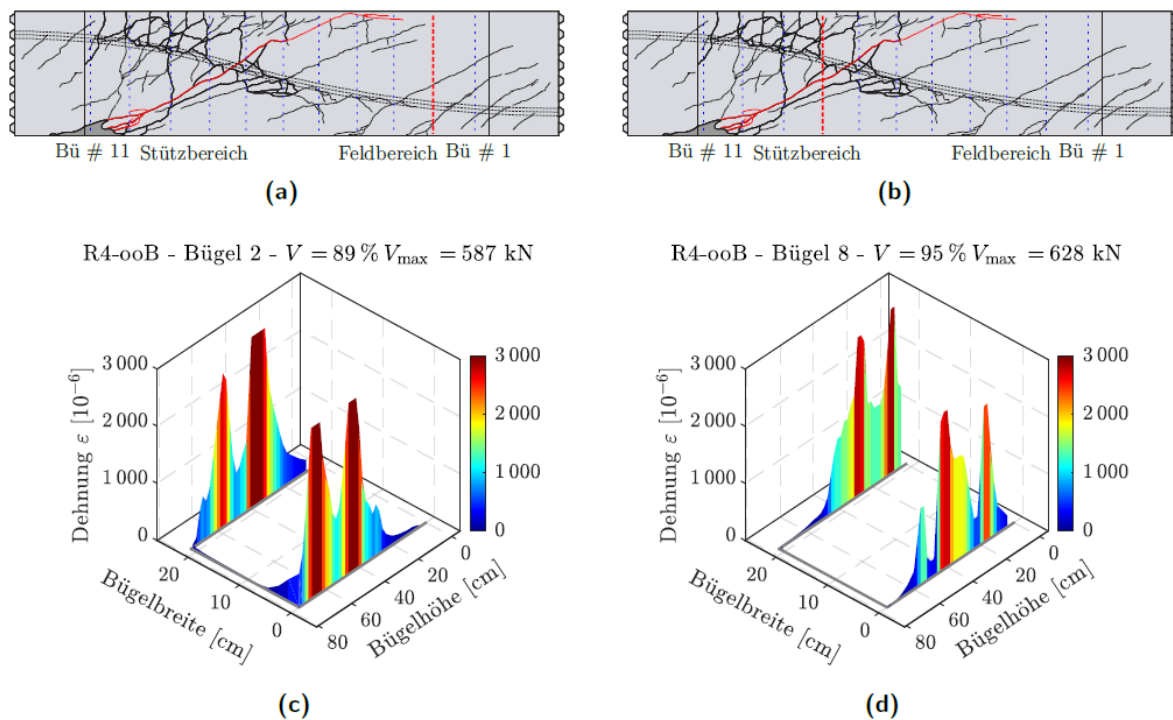


Figure 4.20: Crack patterns and strains in the open straight-legged stirrups [2]
 (a) and (c) crack pattern and strains in stirrup 2 at a load level of $89\% V_{max} = 587 \text{ kN}$
 (b) and (d) crack pattern and strains in stirrup 8 at a load level of $95\% V_{max} = 628 \text{ kN}$

4.2.4 Conclusions

Below, the most important conclusions are summed up:

- The substructure technique can predict the failure mode, ultimate load and crack pattern with sufficient accuracy, but shows a lower stiffness than the stiffness in reference tests. This is due to deviations in the fitting accuracy and less effective clamping restraints due to the lack of participation of concrete in tension. However, these deviations are accepted and the results are assumed to be valid.
- All beams fail due to a combination of crushing of concrete and yielding of stirrups (if stirrups are present). Those beams all fail in the area with a negative bending moment, but also show serious inclined cracking in the area with a positive bending moment. It is therefore also possible that critical shear failure occurs in the area with positive bending moments.
- Beams with open straight-legged stirrups do contribute to the shear resistance. According to Schramm's tests [2], this contribution is approximately 55% compared to closed stirrups, which is significantly less. It is highly dependent on the anchorage length of the open ends. This anchorage length determines the degree of anchorage, which again influences the possibility of strain development in the stirrups. If sufficient anchorage is reached, strain development in the stirrups up to the yield strength is possible and the same behaviour as closed stirrups is observed. If not, the open end is pulled out at a certain stress level before yielding, which means that no shear resistance can be accounted for in this individual stirrup.
- More cracks develop in the tension zone, which decreases the bond, and occur close to the open end of the stirrups, which makes it more likely that a pull-out failure occurs here.

5 Finite element modelling approach

In this chapter, the approach for finding a suitable solution strategy for beams with closed stirrups and open straight-legged stirrups is described. Most assumptions are based on the recommendations of the RTD1016-1 [3], but some different choices are mentioned and motivated in this chapter. To quantify and understand the effect of the modelling choices on the results of the finite element analyses, this research is split up into two parts. Part 1 focusses on the closed stirrups and part 2 on the open straight-legged stirrups. First, the finite element model is described which contains the constant modelling choices for (almost) all investigated solution strategies in both parts. Then, the details of the two parts are described and the choices are motivated. Finally, the judgement of the results is specified.

5.1 Finite element model

For the investigation of the numerical models, DIANA 10.5 [1] was used. At the start of the modelling, a 2D model based on recommendations of the RTD1016-1 [3] was used to investigate the contribution of the different aspects of the model, like the influence of longitudinal reinforcement, post-tensioned tendons and boundary conditions. Since a 2D model requires fewer elements with fewer integration points than a 3D model, the computational time is much shorter than for 3D models. When these models worked properly, a shift to 3D models was made. In this thesis, only the modelling considerations and results for 3D models are described.

Also, it should be noted that large differences in stiffness between the preliminary models and Schramm's tests [2] were observed. In Schramm's tests, the stiffness is dependent on the behaviour of the reinforced concrete beam, but also the behaviour of the connection between the concrete beam and plates, the plates itself, the rigid stiffeners, the hydraulic cylinders and geometrical and material imperfections are of influence. Also, it was stated in Chapter 4 that the substructure technique used by Schramm resulted in a less stiff behaviour than expected due to fitting imperfections.

This causes struggles with the judgement and necessity of modelling the stiffness according to Schramm's results. On the one hand, modelling the beams as similar to the experiments as possible could provide a more detailed and accurate comparison. On the other hand, it is known that the stiffness in the experiment is also not quite accurate, which makes it seem redundant to spend a lot of time accurately modelling similar limitations and imperfections.

The fundamental idea that is pursued in this thesis is to model the concrete beams as close to the theoretical situation, maintaining the boundary conditions on both sides clamped. However, the difference in stiffness with Schramm's experiments [2] is too large to ignore for a qualitative and quantitative comparison with the models. Therefore, short research is covered in Appendix B, where the influences of the boundary conditions, stiffness of the support plates and the interface between plate and concrete on the behaviour of the concrete beam are investigated. The considerations and conclusions are also mentioned in this chapter.

5.1.1 Geometry of the models

De Putter [19] found that 2D models are perfectly capable of accurately describing the behaviour of concrete beams with closed stirrups, as long as a suitable solution strategy is used. Nevertheless, it is necessary to investigate the behaviour of 3D models, because the goal of this thesis is to describe the behaviour of beams with open straight-legged stirrups. For this, a detailed comparison between these beams is valuable, especially concerning the anchorage of both types of stirrups. This is best described with a 3D model, where a more detailed trajectory of the stirrups can be described.

Also, the widened ends of the beams are better described with a 3D model. The transition between the test and load application areas was modelled with fillets, which are rounded corners. This rounding helped the analysis to calculate continuous stresses and strains around these corners without extreme singularities due to a sudden angle change. In Figure 5.1, the layout of the 3D models is shown, where the x, y and z-axis are in the longitudinal, lateral and vertical direction.

The steel plates had the same width and height as the end of the concrete beams and is 100 mm thick. These dimensions are different from the plates in Schramm's experiments [2]. Since the only function of the plates is to transfer the forces caused by external loads and boundary conditions to the concrete, it is unnecessary to model longer, thicker and wider plates.

The reinforcement configurations of the concrete beam with closed and open straight-legged stirrups are shown in Figure 5.2 and Figure 5.3. the only difference was the modelling of the stirrups in the test area. The dimensions were the same as used in Schramm's experiments [2], which are summed up in Appendix A.1. In the widened ends of the beams, more and thicker stirrups were used, which, in combination with the widening, ensured failure in the middle area (test area). It widens linearly with the width of the beam, ensuring the same concrete cover for every stirrup.

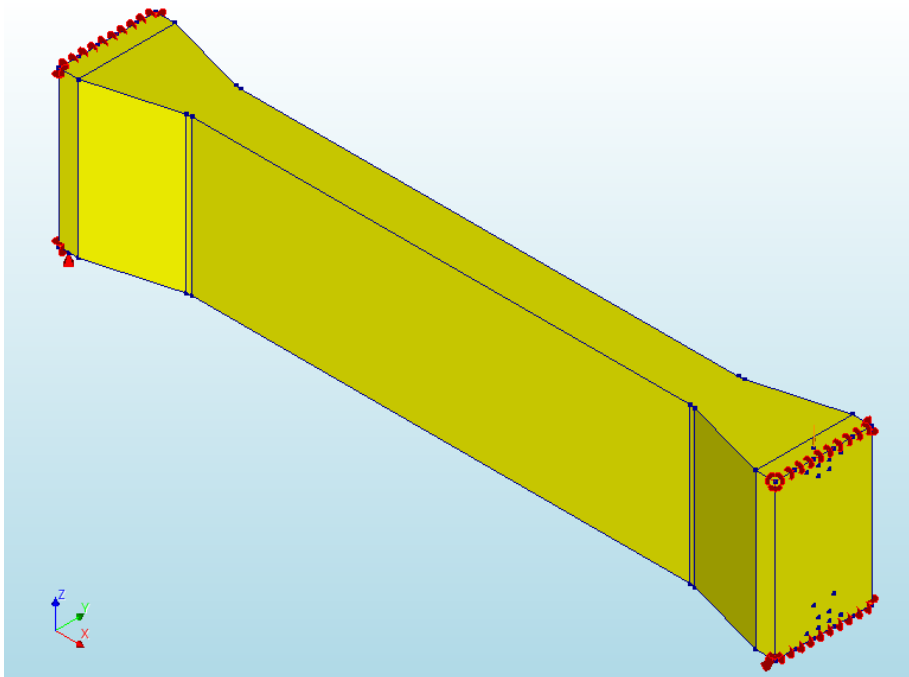


Figure 5.1: Layout of the 3D models

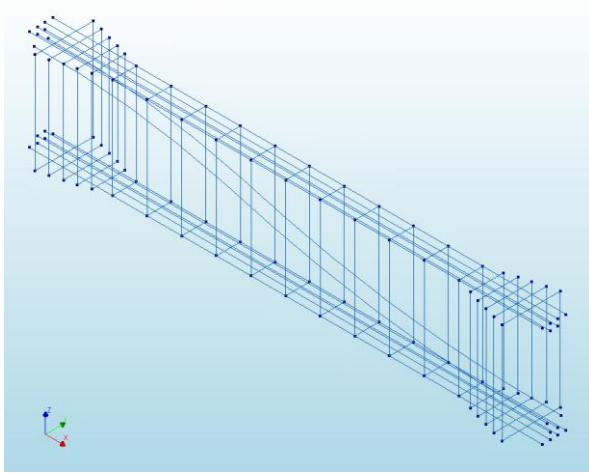


Figure 5.2: Reinforcement configuration of the concrete beams with closed stirrups

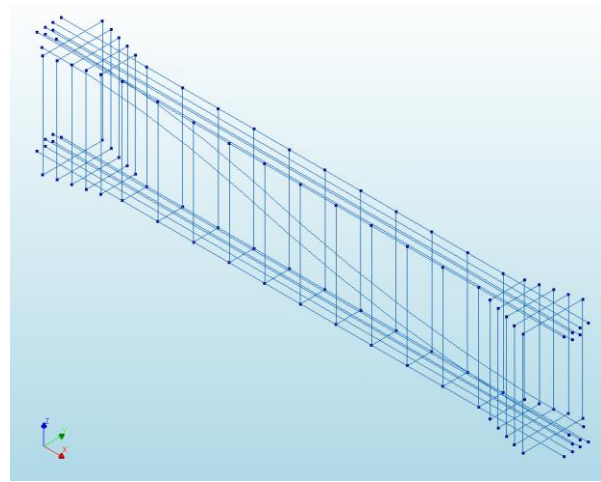


Figure 5.3: Reinforcement configuration for beams with open straight-legged stirrups

5.1.2 Constant kinematic relations

Element type and size

As was advised by the RTD1016-1 [3], hexahedral elements with quadratic interpolation and 3x3x3 Gauss integration were used for the concrete and the loading plates. In DIANA, this implies the twenty-noded isoparametric solid brick element CHX60 (see Figure 5.4). For the complete mesh, an aspect ratio of 1:1:1 was applied where possible. This means that the lengths, widths and heights are equal. However, the element width might be smaller due to the widening of the support areas, especially in the test area. Since the aspect ratio remained small, the effect on the accuracy should be negligible [35].

Finite element models tend to be mesh dependent. To investigate this behaviour, multiple element sizes were used throughout all the modelling strategies. To investigate the mesh dependency of the models, but also remain a reasonable computational time and effort, the following element sizes were chosen: 100 mm, 75 and 50 mm.

The boundary springs were modelled as one-noded translational spring/dashpot elements (SP1TR), with translation, elongation and axial force in 1 direction as variables. Reinforcements were described as embedded in its 'mother elements', which were the CHX60 elements. The finite element mesh for an element size of 50 mm is shown in Figure 5.5, where the yellow dots at the ends of the support plates represent the spring elements.

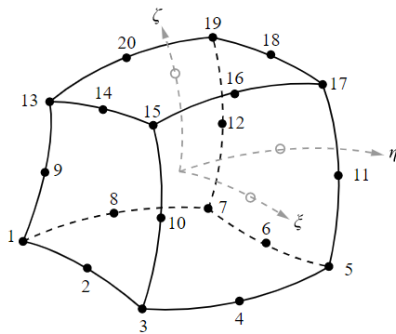


Figure 5.4: CHX60 [1]

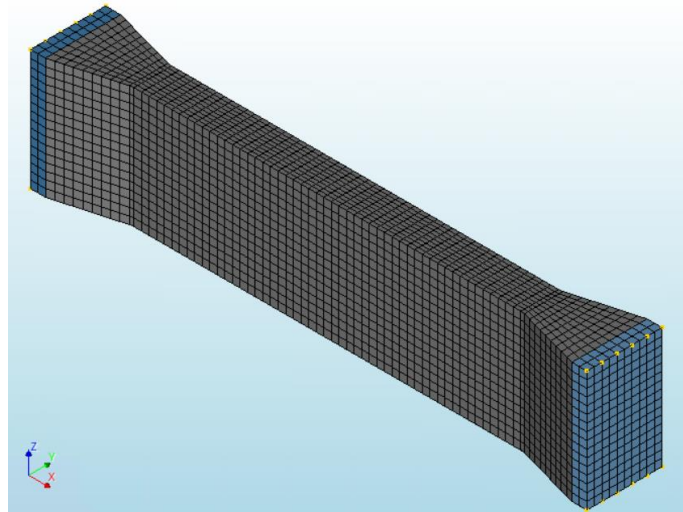


Figure 5.5: Finite element mesh for $h=50$ mm

Boundary conditions and interfaces

On the passive loading plate (left side of the model), the roller supports were modelled as a line support in the middle of the plate with translation in the z -direction restrained. On the active side, one vertex at the bottom of the loading plate was restrained in the y -direction to prevent lateral displacements.

A restraining in the x -direction at the top and bottom edge on both plates, effectively clamping the sides, resulted in a much too stiff response of the model. Finite element models containing RC beams that were clamped on both sides were not found in literature, so a modelling strategy for such boundary conditions is proposed.

In theory, no rotation is possible. However, in practice, there is always a small rotation. Rotational springs are not suitable for brick elements, since no rotational degrees of freedom are defined. To allow small rotations in the models, very stiff boundary springs were used at the top and bottom edges. To prevent large stresses in corners (singularities), line supports are better suitable than point supports. However, in DIANA it is not possible to select boundary springs distributed over an edge. Therefore, 6 boundary springs (spacing = 100 mm) at the top and bottom edges of both loading plates were introduced.

The spring stiffnesses were iteratively determined, where the stiffness in the z -direction sufficiently approached the expected stiffness and the maximum absolute displacement in the x -direction at the boundary springs is approximately 2 mm. For the first iteration, the spring stiffness is approximated based on moment equilibrium for a linear elastic situation with a shear force equal to the ultimate shear force for test R2 ($V_{ult} = 711$ kN). The calculation is shown in Figure 5.6.

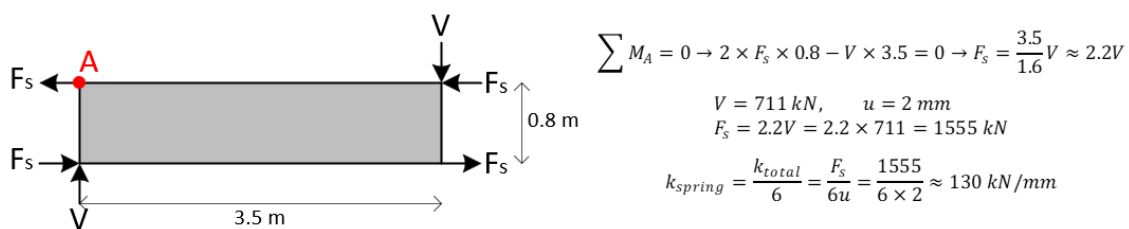


Figure 5.6: Calculation spring stiffness for the first iteration

This resulted in an initial spring stiffness of 130 kN/mm. Since the stiffness of concrete reduces after cracking, this resulted in a lower global stiffness than the experiments. Therefore, a higher spring stiffness is used for the next iteration. Eventually, a spring stiffness of 200 kN/mm for all boundary springs on both sides sufficed for the tested beam, because the rotations remained small, the expected stiffness is approached and the correct failure mechanism was modelled.

In Appendix B.1, the comparison between boundary springs and supports is made and the application of boundary springs was validated. Based on this comparison, it can be stated that, in the case of an RC beam clamped on both sides, complete restraining in longitudinal direction results in a too-stiff response. By allowing a little rotational freedom in the form of boundary springs, the stiffness of the beam can be manipulated without changing the overall load-bearing behaviour. As a basic principle, a maximum longitudinal displacement of approximately 1-2 mm at the top and bottom springs can be assumed. Based on this, the required spring stiffnesses of the boundary springs can be iteratively determined.

The boundary conditions of the passive and active sides are shown in Figure 5.7 and Figure 5.8. The point load is also shown at the top of the plate on the active side.

The connections between the steel loading plates and the concrete beams were assumed to be rigid, so no interface elements are used. Since the concrete has a very small tensile strength, it was expected that the concrete splits along steel plates in the tension zone at an early loading stage. From this point, only compression (and shear in fixed crack models) could be transferred between the plates and the concrete. The longitudinal reinforcement and prestress tendons took care of force transfer to the plates in the tension zone. This assumption is validated in Appendix B.3.

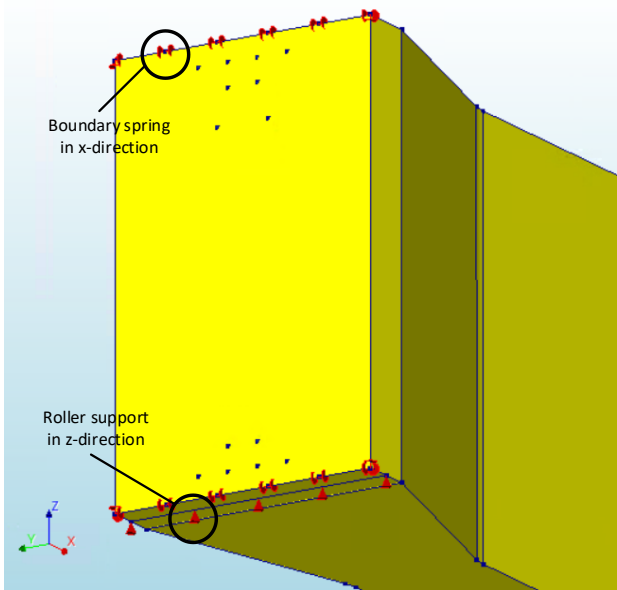


Figure 5.7: Boundary conditions at the passive side

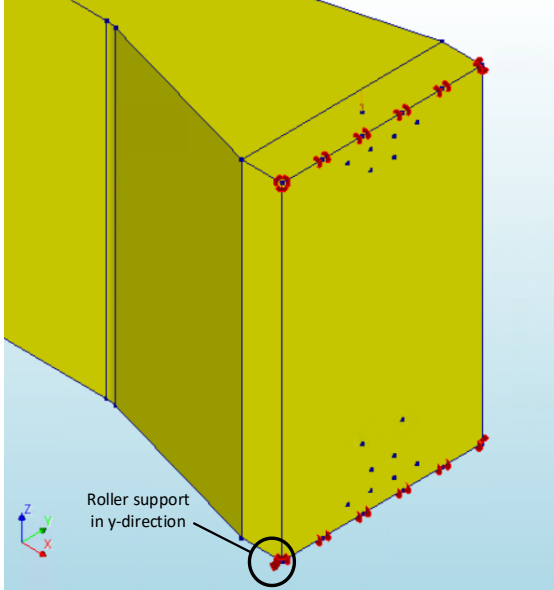


Figure 5.8: Boundary conditions and point load at the active side

5.1.3 Constant constitutive relations

In this subsection, the material models for the concrete, steel plates and reinforcements are described, which are based on the recommendations of the RTD1016-1 [3]. The material properties are based on the properties of test beams R2 and R4 in Schramm's research [2] and are given in Appendix A.1.

Concrete and support plates

The Young's modulus, tensile and compressive strength for the concrete followed directly from Schramm's tests [2]. The mass density was based on reinforced concrete, where there is no mass density defined for the individual reinforcements. The mass of the beam does have some influence on the stresses and strains and is easy to implement in the models, so was taken into account.

A smeared total strain-based crack model was applied. Both a fixed and rotating crack orientation were investigated (see the following subsection). The recommended tensile and compressive curves (Hordijk and parabolic) were used to model the nonlinear behaviour of the concrete. The Hordijk tension relation and parabolic compression relation are shown in Figure 5.9 and Figure 5.10, assuming a crack bandwidth of 50 mm. The tensile and compressive fracture energies are calculated with Equations 3.4 and 3.5. These values differ for the models with closed and open straight-legged stirrups since the material properties obtained from cylindrical compression tests slightly varied for Schramm's test specimens [2]. To model the behaviour as accurate as possible, the damage-based Poisson's ratio reduction, compressive softening due to lateral cracking and stress confinement were implemented. Stress confinement is optional according to the RTD1016-1 [3], but since this factor should contribute to the accuracy to describe the realistic behaviour of concrete beams and is easy to implement in DIANA, it was taken into account.

In Appendix B.2, it was found that a realistic Young's modulus for the steel plates influenced the global stiffness significantly at lower load levels due to significant deformations of these plates. Therefore, the support plates were modelled as a linear elastic material with a high Young's modulus to keep the strains in the plates and interface between the plate and concrete beam small. This way, the local deformations at the individual nodes connected to a boundary spring were adapted by the 'rigid' plate, so the side of the beam remained straight. The weight of these plates was ignored.

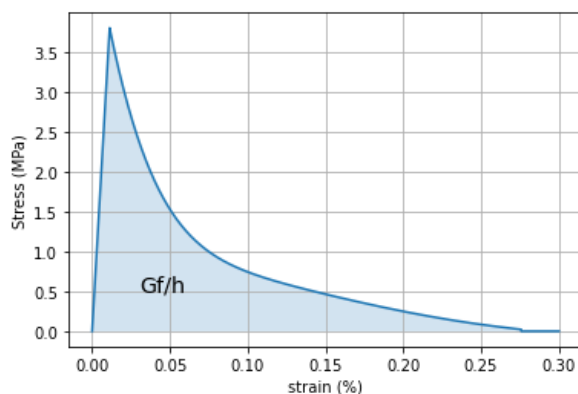


Figure 5.9: Hordijk tension for $h=50$ mm

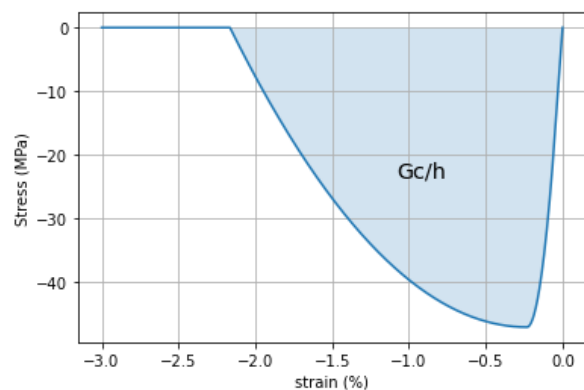


Figure 5.10: Parabolic compression for $h=50$ mm

Steel reinforcement

The steel reinforcements were modelled as discrete bars with Von Mises plasticity models and linear hardening functions. It was chosen to ignore possible rupture of reinforcements, because Schramm [2] does not describe any occurrence of steel rupture, implying this did not happen in these tests. The Young's moduli, yield strengths and ultimate strengths for the reinforcements were directly taken from Schramm's test beams. The ultimate strains were not given, so an ultimate plastic strain of 5% is used. According to RTD1016-1 [3], the ultimate strain must be larger than 5%, which was therefore satisfied. The reinforcement material models are shown in Figure 5.11.

The stress-strain relationship for the prestress tendons was also modelled with linear hardening, using the 0.1% proof stress and ultimate stress as yield strength and ultimate strength. Two different material models were defined, where the only difference was the bonding to the mother element of the tendons (unbonded or fully bonded).

5.1.4 Constant equilibrium conditions

Load application

The acting forces on the concrete beam were separated into two phases. In the first phase, the self-weight of the beam was applied and the tendons were tensioned, where these tendons are unbonded to the mother element. The tendons were tensioned with a post-tensioning load acting on both sides. The anchor force on both ends of the tendons was 250 kN, which resulted in the desired prestress of 2.5 MPa in the cross-section. To maintain this prestress level in the test area, prestress losses due to wobble, friction and anchor retention were neglected. Also, less information about the prestress losses in these tests was available, which made it difficult to model this accurately.

In the second phase, the tendons were bonded to the mother element. A start step was introduced to maintain the self-weight. Notice that there should not be any difference in results between this step and the previous step. Then, the point load at the top of the right support was incrementally applied with an initial load step of 20 kN. Due to the reduction of step sizes caused by the arc-length control method (see next paragraph), a maximum number of 125 load steps was chosen. This is sufficient to capture the behaviour until and after the peak load.

Analysis control

The analysis was controlled with arc-length control. This control method reduced the step sizes when the model showed nonlinear behaviour, which allows the analysis to capture nonlinear stages and post-peak behaviour more accurately. By default, the displacements of all nodes are used in the arc-length control method, which is suitable for global failure. However, concrete structures usually fail locally and then it is better to use a selection of nodes. In this case, the nodes with the largest displacements were used, which were the nodes at the edge of the right support (see purple nodes in Figure 5.12).

Iteration scheme and convergence criteria

The regular Newton-Raphson iteration scheme with tangential initial stiffness or the secant (Quasi-Newton) iteration scheme with the stiffness from the previous iteration was used. This is further discussed in the following subsection. A maximum of 100 iterations per load step was allowed. A line search algorithm was also applied to help reach convergence.

The convergence norms and tolerances were based on the recommendations of the RTD1016-1 [3], namely energy ($\epsilon = 0.001$) and force ($\epsilon = 0.01$). If one of the two norms were satisfied, the load step was considered as converged. Finally, the analysis was stopped when divergence occurred or the 125 load steps were finished.

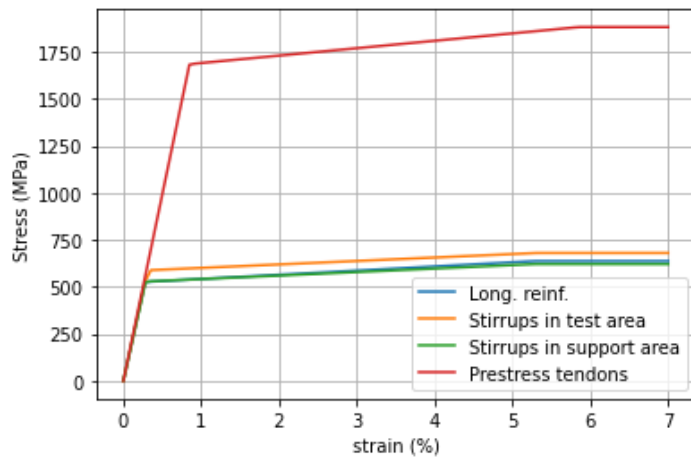


Figure 5.11: Stress-strain relationships for the reinforcements

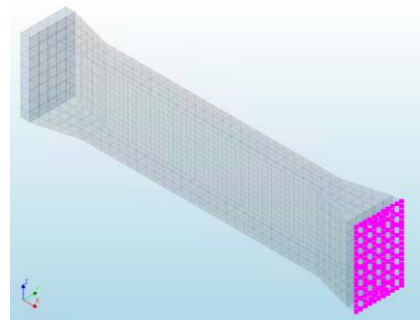


Figure 5.12: Arc-length control nodes

5.1.5 Summary of the finite element model

Table 5.1: Constant modelling assumptions

Geometry of the model	
Geometry	3D
Kinematic assumptions	
<u>Mesh</u>	
Element type	20-noded hexahedral
Element name	CHX60
Degrees of freedom	60
Interpolation scheme	Quadratic
Integration scheme	3x3x3 Gauss
Shape dimension	3D
Topological dimension	3D
Aspect ratio	1:1:1 (where possible)
Stress components	$\sigma_{xx}, \sigma_{yy}, \sigma_{zz}, \sigma_{xy}=\sigma_{yx}, \sigma_{yz}=\sigma_{zy}, \sigma_{zx}=\sigma_{xz}$
Inclusion of shear deformations	Yes
Element size	100 mm, 75 mm or 50 mm
<u>Boundary spring elements</u>	
Element type	One-node translation spring
Element name	SP1TR
Spring stiffness	200 kN/mm
<u>Boundary conditions and interface</u>	
Left end	Top and bottom edge: 6 boundary springs in the x-direction Bottom: line restraint in the z-direction
Right end	Top and bottom edge: 6 boundary springs in the x-direction 1 node: restrained in the y-direction
Constitutive relations	
<u>Concrete material model</u>	
Density	2500 kg/m ³
Poisson ratio	0.2
Crack model	Smearred total strain-based (rotating or fixed)
Tensile behaviour	Hordijk
Tensile fracture energy	G_F (according to Eq. 3.4) 0.102 N/mm (closed stirrups) 0.098 N/mm (open straight-legged stirrups)
Crack bandwidth	Govindjee
Compressive behaviour	Parabolic
Residual compressive strength	0 N/mm ²
Compressive fracture energy	G_C (according to Eq. 3.5) 30.284 N/mm (closed stirrups) 27.599 N/mm (open straight-legged stirrups)
Lateral cracking reduction model	Vecchio & Collins 1993
Lower bound reduction factor	0.4

Confinement model	Selby & Vecchio
<i>Steel plates</i>	
Density	0 kg/m ³
Poisson ratio	0.3
Young's modulus	1 x 10 ⁸ N/mm ²
<i>Reinforcements</i>	
Density	0 kg/m ³
Plasticity model	Von Mises
Hardening curve	Linear
Hardening type	Isotropic strain hardening
Ultimate plastic strain	5%
Prestress tendon bonding	Unbonded during tensioning Bonded during loading
Equilibrium conditions	
Type of loading	Force control
Initial load step	20 kN
Maximum number of load steps	125
Iteration scheme	Regular Newton-Raphson with tangential stiffness and a line search algorithm OR Secant (Quasi-Newton) with stiffness from the previous iteration and a line search algorithm
Maximum number of iterations per load step	100
Convergence norms (convergence tolerance)	Energy (0.001) OR Force (0.01)
Analysis control	Arc-length control method
Arc-length control nodes	Nodes with the largest displacement

5.2 Description of part 1: RC beams with closed stirrups

Part 1 focused on the modelling of RC beams with closed stirrups. For standard RC concrete beams with closed stirrups, as good as all recommendations are described in RTD1016-1 [3]. Therefore, a rotating crack orientation and embedded reinforcements were used.

According to Evangeliou [31], the secant method is more robust than the full Newton-Raphson method for beams without shear reinforcement. This is also investigated for beams with open straight-legged stirrups. For comparison with the open straight-legged stirrups, the secant iteration scheme is also used for beams with closed stirrups.

Also, the mesh dependency was studied by varying the element size. This led to the solution strategies described in Table 5.2. The names for the solution strategies were based on the stirrup type, part and solution strategy in that part. So:

- C1.1 = Closed stirrups, part 1, solution strategy 1 in part 1
- O2.4 = Open stirrups, part 2, solution strategy 4 in part 2

Table 5.2: Solution strategies for part 1

	Iteration scheme	Element size (mm)
C1.1	Full Newton-Raphson	100
C1.2	Full Newton-Raphson	75
C1.3	Full Newton-Raphson	50
C1.4	Secant	100
C1.5	Secant	50

5.3 Description of part 2: RC beams with open straight-legged stirrups

Recommendations for the modelling of RC beams with open straight-legged stirrups were not found in literature. In the preliminary models with open straight-legged stirrups, it became clear that the behaviour of these models were very susceptible to the modelling choices that were made. Due to this reason, the investigation of RC beams with open straight-legged stirrups was split into two sections, where different aspects of the finite element modelling were investigated.

Part 2.1 contains the calibration of the model, where different factors were investigated to find a suitable model to describe shear behaviour in beams with open straight-legged stirrups. Subsequently, the conclusions drawn from this study were used for part 2.2, where the constitutive and kinematic modelling of the open straight-legged stirrups were supposed to be investigated focussing on the shear capacity of the stirrups and the anchorage behaviour of the open ends. However, this study was not carried out due to difficulties in the calibration of the finite element model (part 2.1), where these results are described in Section 6.2. Still, some recommendations for a further finite element study of beams with open straight-legged stirrups are described in Subsection 5.3.2.

5.3.1 Part 2.1: Calibration

Part 2.1 focused on the modelling of the concrete, longitudinal reinforcement, prestressing tendons and the equilibrium iteration scheme. This calibration provides recommendations for the modelling of RC beams with open straight-legged stirrups except for the modelling of the open straight-legged stirrups itself. In this study, it is important that the correct failure mode is generated, where the detailed anchorage behaviour of the stirrups is of smaller importance. This is the focus of part 2.2, where the anchorage modelling of the open straight-legged stirrups is discussed.

In preliminary studies, it was found that beams with open stirrups modelled as bond-slip reinforcement tend to behave completely differently than previous models with closed stirrups, independent of the chosen bond-slip model. This indicates that a different solution strategy than for beams with closed stirrups is required and that many different parameters could influence the outcome of the analyses.

A possible explanation for the different behaviour is the following: When looking at a beam with open straight-legged stirrups, a different situation can be described for the tension zone at the top or bottom due to a different stirrup configuration. The situation for the bottom longitudinal reinforcement concerning the interaction with stirrups is the same as for beams with closed stirrups because the longitudinal reinforcement in the tension zone is enclosed by the stirrups. Therefore, forces can be transferred according to the strut-and-tie model. However, the top longitudinal reinforcement has no clear and straight-forward interaction with the open ends of the stirrups, which means that it is expected that the beam at the top side transfer stresses in a different, unknown and less effective way.

The above explanation is an oversimplified situation, which might not accurately describe the realistic situation. However, the top part of the beams in the finite element models showed similar problems as for beams without shear reinforcement described in literature. Below, multiple parameters that were investigated in this section are described. The solution strategies are summarized in Table 5.5. The chosen element size is 50 mm to provide detailed crack patterns.

Concrete constitutive model: rotating vs fixed crack model

The constitutive modelling of concrete plays a major part in the behaviour of the beam. For RC beams with stirrups, a rotating crack model is advised [3]. Beams without shear reinforcement modelled with rotating crack models often show difficulties describing shear failure. Then, a fixed crack model with a damage-based shear retention model is a better alternative [19] [36]. Both the rotating and the fixed (with damage-based shear retention) crack models were investigated here. The aggregate size-based shear retention model is not evaluated since the exact mean aggregate size is not known and preliminary models showed that the results were very dependent on the chosen aggregate size.

Reinforcement bond models: fully bonded vs bond-slip

For RC beams without shear reinforcement and modelled with a rotating crack model, it is not advised to use embedded reinforcement due to an inaccurate failure mode where it cracks along the longitudinal reinforcement [19]. Therefore, a bond-slip model (described in section 3.2.2) should be used, which requires truss or beam elements. The difference in results between truss and beam elements should be negligible [19]. Therefore, the influence of beam elements was not taken into account in this study. Also, for the stirrups modelled with a bond-slip relation, truss elements were used. For the longitudinal reinforcement, stirrups and prestress tendons, the influence of the kinematic modelling (embedded fully bonded truss or bond-slip truss) was investigated.

For the longitudinal reinforcement and prestressing tendons, the Shima bond-slip model was used. In the preliminary study, it was concluded that the influence of the chosen bond-slip model for the longitudinal reinforcement is small, with exception of the fib splitting model. Here, a bond-slip failure of the longitudinal reinforcement occurred, causing divergence at a much lower load level than expected. Considering these outcomes, the influence of the bond-slip model for the longitudinal reinforcement is not further investigated and discussed in this thesis.

For the prestress tendons modelled with bond-slip, a weak bond was used during the tensioning. In the next phase, a strong bond was defined (the same bond as for the longitudinal reinforcement). The tendons were also attached (anchored) to the loading plates.

For the stirrups, the fib pull-out model was used. Here, it was only used to investigate the influence of a bond-slip truss instead of an embedded fully bonded truss. The bond-slip model was also applied to the end stirrups.

The bond-slip parameters were calculated following the equations in section 3.2.2 and are described in Table 5.3 and Table 5.4. The bond-slip models are also presented in Figure 5.13.

Iteration scheme: full Newton-Raphson vs secant method

The influence of the iteration scheme was investigated, where the full Newton-Raphson scheme and the secant iteration scheme were used. Even though the RTD1016-1 describes that the Newton-Raphson method is sufficiently accurate and efficient, Evangelidou [31] found that the secant method is more robust than the full Newton-Raphson method in the case of shear failure in RC beams without shear reinforcement. Since it is not exactly known how beams with open straight-legged stirrups behave, this secant method might also positively influence these finite element results.

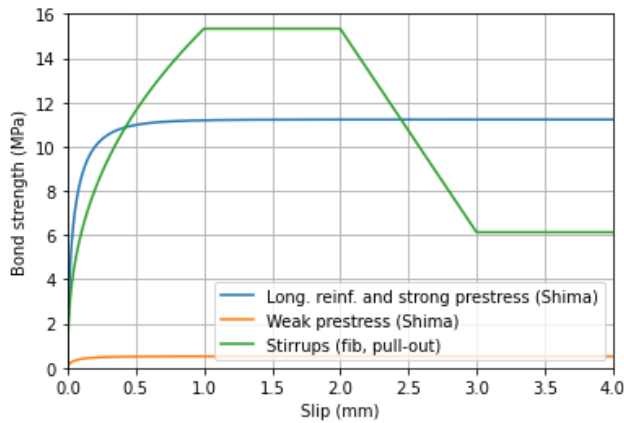


Figure 5.13: Bond-slip models for the finite element model

Table 5.3: Bond-slip parameters longitudinal reinforcement and prestressing tendons

Reinforcement type	Bond-slip model	f_c (N/mm ²)	D (mm)	B_n (N/mm ³)	B_t (N/mm ³)
Longitudinal reinforcement	Shima	37.6	25	33130	3313
Prestress tendons	Shima, weak	37.6*0.01	25	1000	0.002
	Shima, strong	37.6	25	1000	20

Table 5.4: Bond slip parameters stirrups

Reinforcement type	Bond-slip model	τ_{bmax} (N/mm ²)	τ_{bf} (N/mm ²)	s_0 (mm)	s_1 (mm)	
Stirrups	Fib pull-out	15.33	6.13	0.1	1.0	
		s_2 (mm)	s_3 (mm)	α	B_n (N/mm ³)	B_t (N/mm ³)
		2.0	3.0	0.4	33130	3313

Table 5.5: Solution strategies for part 2.1

	Crack orientation	Longitudinal reinforcement modelling	Stirrups modelling	Prestress tendons modelling	Iteration scheme
O2.1	Rotating	Fully bonded	Fully bonded	Unbonded, fully bonded	Secant
O2.2	Rotating	Fully bonded	Bond-slip	Unbonded, fully bonded	Secant
O2.3	Rotating	Bond-slip	Bond-slip	Unbonded, fully bonded	Secant
O2.4	Rotating	Bond-slip	Bond-slip	Weak bond, strong bond	Secant
O2.5	Rotating	Bond-slip	Bond-slip	Weak bond, strong bond	Newton-Raphson
O2.6	Fixed	Fully bonded	Fully bonded	Unbonded, fully bonded	Secant
O2.7	Fixed	Fully bonded	Bond-slip	Unbonded, fully bonded	Secant
O2.8	Fixed	Bond-slip	Bond-slip	Unbonded, fully bonded	Secant
O2.9	Fixed	Bond-slip	Bond-slip	Unbonded, fully bonded	Newton-Raphson
O2.10	Fixed	Fully bonded	Bond-slip	Unbonded, fully bonded	Newton-Raphson

5.3.2 Part 2.2: Constitutive and kinematic modelling of open straight-legged stirrups

For the development of the models in part 2.2, the conclusions from part 2.1 were used. Due to the unexpected and inaccurate results for the calibration of the models with open straight-legged stirrups with a bond-slip model, it was not very promising, or even useless, to investigate which bond-slip model fits the best for these stirrups.

Within the calibration of the finite element model (see Section 6.2), no solution strategy was found that is sufficiently able to describe the load-bearing behaviour of open straight-legged stirrups, where the bond-slip model should describe the anchorage of the open ends in the finite element model. Some stirrups should locally fail due to a pull-out failure, causing a drastic decrease in shear resistance.

Even though it is not possible to describe the local anchorage of the open ends, this does not mean that it is impossible to describe the global behaviour of RC beams with open straight-legged stirrups. In finite element models, the open straight-legged stirrups can be modelled as embedded, fully bonded reinforcements with a reduced length at the open ends. Based on the results in this thesis, this modelling choice has the most potential to accurately describe the global behaviour of such beams. From an engineering point of view, it is also much easier to implement in finite element models than complicated assumptions on the bond-slip behaviour. It is also very suitable for 2D models, which is also preferable due to computational time.

However, the effect of the reduced length at the open ends should be investigated. This reduced length could be chosen randomly, based on required anchorage lengths calculated in common engineering models or derived from bond-slip models. Also, it should be investigated if all stirrups should be reduced in length or only some of them. The cracking behaviour of a model could change if all stirrups are shortened. For instance, instead of a diagonal crack crossing the stirrups a crack above open ends could develop. Overall, this comprises a large investigation that is not performed in this thesis due to limited time.

5.4 Judgement of the results

For the investigation of the results, it is useful to define a consistent framework for the judgement of the different aspects. This way, it is possible to compare results objectively and judge the quality and accuracy of the models. The most relevant aspects of the results are the ultimate shear force, crack development, strain development in the stirrups and convergence behaviour.

5.4.1 Ultimate shear force and force-displacement curve

For the judgement of the ultimate shear force, the definition of the model uncertainty was used [37]:

$$\theta = \frac{R_{exp}}{R_{NLFEA}} \quad (5.1)$$

This definition can be used in three situations:

1. One experiment is predicted with multiple NLFEA solution strategies.
2. Multiple nominally equal experiments are predicted with one NLFEA solution strategy.
3. Multiple experiments are predicted with their corresponding NLFEA solution strategies.

In this case, the first situation was used for the estimation of the model uncertainty for the ultimate shear strength. This results in the following equation:

$$\theta_{V,i} = \frac{V_{ult,exp}}{V_{ult,NLFEA,i}} \quad (5.2)$$

The closer to 1 this result is, the better the estimation of the ultimate shear force.

In Section 4.2, it was discussed that Schramm's experiments [2] were not able to describe the initial elastic stage of the concrete beams due to imperfections in the fitting accuracy. In the finite element analyses, these imperfections are not modelled. Therefore, the difference between the elastic and cracking stage was better observable in the force-displacement diagrams for the finite element analyses. The displacements for the finite element analyses are adjusted to the displacements in the experiments. This is fitted on the onset of cracking in the test area for both the analyses and experiments, which is around 250 kN for the experiment. For the analyses, this was observed as a 'kink' in the force-displacement curve.

5.4.2 Crack development and strain development in the stirrups

The load-bearing behaviour, failure mode and significant events can all be found in the crack development of the concrete and strain development in the stirrups. For comparison between models or experiments, plots at approximately the same load levels were compared. The representative load levels were based on the experiments, where approximately the same load level of the finite element analysis was fitted to. This was graphically shown in a force-displacement diagram with the representative load levels included.

The yield strain for the stirrups is:

$$\varepsilon_{strain} = \sigma_{yield}/E = 588.2/187900 = 3.13e - 3$$

Due to this reason, the legend range for stirrup strains is from 0 to 3 mm/m for both the experimental and finite element results.

The crack and stirrup strain plots are also useful to check if stirrups yield, which was used for the estimation of stirrup contribution to the shear resistance. The contribution of the stirrups at the ultimate shear force was measured as followed: the crack plot and stirrup strains were observed at the ultimate shear load. The load step after the ultimate load usually shows where the beam failed, which means that the critical shear crack could be identified. Therefore, it was also possible to indicate which stirrups and the location where these were crossed by the critical shear crack. Then, the crack plot and stirrups strain plot were compared and the yielding stirrups that were crossed by the critical shear crack were identified. Since the stresses in the stirrups do not increase much after yielding, it was assumed that the stress in the yielding stirrups is equal to the yield stress. Then, the stirrup contribution was calculated as followed:

$$V_s = n \times f_{y,stirrup} \times (2 \times \frac{1}{4} \pi \phi_{stirrup}^2) \quad (5.3)$$

Caution is necessary when comparing this with Schramm's experiments since the difference in ultimate load is calculated between a beam without stirrups and with stirrups here. This resulted in a lower contribution than when all yielding stirrups are summed up.

The contribution of the concrete beam was then:

$$V_{concrete} = V_{ult} - V_s \quad (5.4)$$

The contribution of the concrete could also be separated into the contribution of the compression zone, aggregate interlock, dowel action and prestress tendon. This was only evaluated for solution strategies which contribute to the understanding of the models. These calculations and comparisons with Eurocode 2 can be found in Chapter 7. Also, the shear load at the onset of stirrup yielding V_{yield} was measured.

5.4.3 Convergence behaviour

A solution strategy should contain mostly converged steps since the analysis continues after a non-converged step. In this check, a justification for the number of iterations, the reached convergence norms and an explanation for non-converged steps were given to describe the convergence behaviour.

6 Finite element results

In this chapter, the numerical results are shown and the effect of multiple modelling choices is discussed.

6.1 Part 1: RC beams with closed stirrups

In Table 6.1, an overview of the results for part 1 is shown. The table also shows the shear force at the onset of stirrup yielding (V_{yield}) and raw predictions of the shear resistance of the stirrups (V_s) and the rest of the beam ($V_{concrete}$). First, the model (C1.2) that shows the most agreement with Schramm's test R2 is described below as a reference case.

Table 6.1: Overview of the results of part 1

	Changing parameters	V_{yield} (kN)	$V_{concrete}$ (kN)	V_s (kN)	V_{ult} (kN)	$\theta_{V,i}$	Failure mode
R2 (Schramm)	-	533	596	115	711	-	Yielding and crushing in the support area
C1.1	FNR-100	507	523	332	690	1.03	Yielding and crushing in the field area
C1.2	FNR-75	537	570	300	720	0.99	Yielding and crushing in the field area
C1.3	FNR-50	540	729	300	862	0.82	Yielding and crushing in the field area
C1.4	S-100	679	788	266	922	0.77	Horizontal cracks between crack regions
C1.5	S-50	716	1003	232	1131	0.63	Horizontal cracks between crack regions
V_{yield}	= Shear force at the onset of yielding						
$V_{concrete}$	= Contribution of the concrete beam (except for the stirrups)						
$V_{stirrups}$	= Contribution of the stirrups at ultimate shear force						
V_{ult}	= Ultimate shear force						
$\theta_{V,i}$	= Model uncertainty of the ultimate shear force						
FNR/S	= Full Newton-Raphson/Secant iteration scheme						
100/75/50	= Element size of 100/75/50 mm						

6.1.1 Comparison between finite element results (C1.2) and experimental benchmark (R2)

The results of solution strategy C1.2 show the most agreement with Schramm's test beam R2 [2]. From Table 6.1, it follows that the model uncertainty is 0.99, meaning that the predicted ultimate shear load is very comparable. Also, the onset of stirrup yielding is predicted quite closely. The contribution of the stirrups is estimated a lot higher in the model since the location and orientation at which the beam fails are different. Therefore, more stirrups are activated by the crack. Also, the stirrup contribution is estimated differently by Schramm [2], where the difference in ultimate load is calculated between a beam without stirrups and with stirrups. This results in a lower contribution than when all yielding stirrups are summed up.

The convergence behaviour is very similar for all solution strategies. The convergence behaviour for C1.2 is shown in Figure 6.1. In the first few load steps, very few iterations are needed to reach convergence, where both the force and energy norm converge due to the elastic behaviour of the beam. After this, steps with a large and small number of iterations alternate each other, where only the energy norm converges. The non-converged force norm remains in the order of magnitude of 10^{-1} , which is, in combination with the converged energy norm, sufficient to trust the analyses. A large number of iterations in the cracking stage implies extensive cracking, so many new elements crack. All steps before the ultimate load are converged. After the ultimate shear load is reached, no convergence is reached anymore, where both the energy and force norm significantly increase.

The global behaviour is shown in Figure 6.2. The crack development is shown in Figure 6.3, with the crack patterns from experiment R2 in the background. The stirrup strain development for the experiment R2 and solution strategy C1.2 is shown in Figure 6.4. For every load level, the top figure represents the experimental strains and the bottom figure the finite element results. The stirrups are numbered in the same way as was done in Schramm's experiment [2].

Since rupture was not modelled, it is necessary to check if the strains do not exceed the ultimate strain of 5%. For all solution strategies, including C1.2, the largest strain did not exceed 2.5%, so this is sufficient.

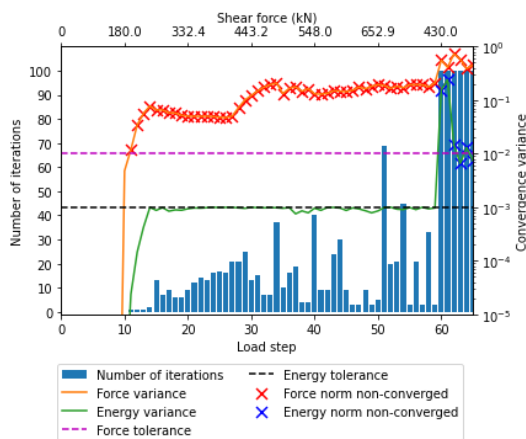


Figure 6.1: Convergence behaviour solution strategy C1.2

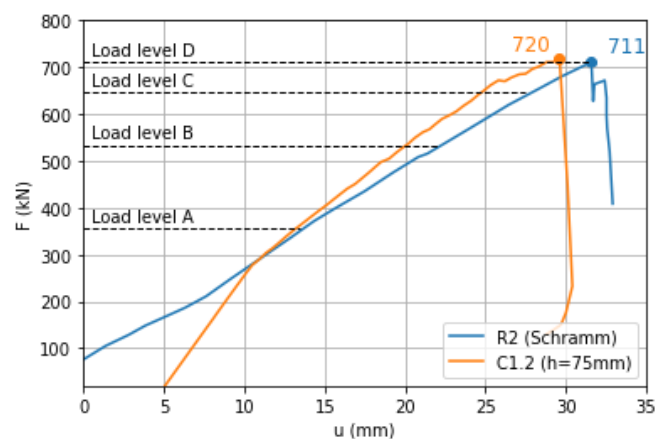


Figure 6.2: Global behaviour of the experiment R2 and solution strategy C1.2

Below, a detailed description of the crack and stirrup strain development per load level is described, where a distinction is made between the crack development of solution strategy C1.2 and experiment R2.

Load level a:

C1.2 show some first bending cracks at the top left side and bottom right side. Looking at Figure 6.3a, a starting flexure-shear crack can be seen. Also, a crack along the left and right edges of the concrete develop. The location and orientation of this crack remain the same for all load steps, but the crack width increases. In Figure 6.4a, it can be seen that almost no strains in the stirrups are building up. Stirrup 1 elongates a bit at the bottom and stirrup 11 at the top. This is at the same location where cracks are initiated. Also, the stirrups within the ends of the beam elongate a bit. This elongation, however, will remain small in future loading steps.

In the experiment, a stronger bending crack pattern at the top in the support area is observed, where the tips already twist diagonally. At the bottom of the field area, no bending cracks are observed. Almost no strain build-up in the stirrups is achieved in the experiment.

Load level b:

In the model, the bending cracks further develop under an angle. This cracking is smeared over a respectively large area in this region, which makes it somewhat difficult to spot individual cracks. A larger and stronger stirrup strain development in the same area where the cracks form is observed. At some locations in some stirrups, the yield strain is already achieved, which means that hardening occurs. At this point, the stirrups are very active and significantly contribute to the shear resistance of the concrete beam.

In the experiment, multiple flexure-shear cracks developed at the top left side. At the bottom right side, multiple web-shear cracks developed. As well as observed in the models, a stronger strain development in the stirrups is observed in the experiment. The location of this local strain build-up is slightly different than in the models due to small deviations in the locations of the cracks. However, the regions where this happens are the same.

Load level c:

In the model, the concrete strain increases and little new cracks form, especially shear cracks form here. A small increase of the smeared cracking area occurs.

In the experiment, some new cracks are formed and the crack width of the existing cracks is increased.

Load level d:

In the model, two smeared cracks become very large in a diagonal direction. Also, many stirrups are yielding over a larger length. This is at the location of the larger cracks. All stirrups in the crossing crack are almost used to their full potential, which means that the ultimate shear capacity of the stirrups is reached. In the next load step, the beam fails in the compression zone in the field area. The deformation after failing is shown in Figure 6.5.

In the experiment, two long cracks developed: one at the midspan and one slightly to the left of the midspan. The stirrup strain build-up of the previous load step is continued, increasing the strains in these regions, causing more stirrups to yield. Eventually, crushing occurs in the compression zone in the support area.

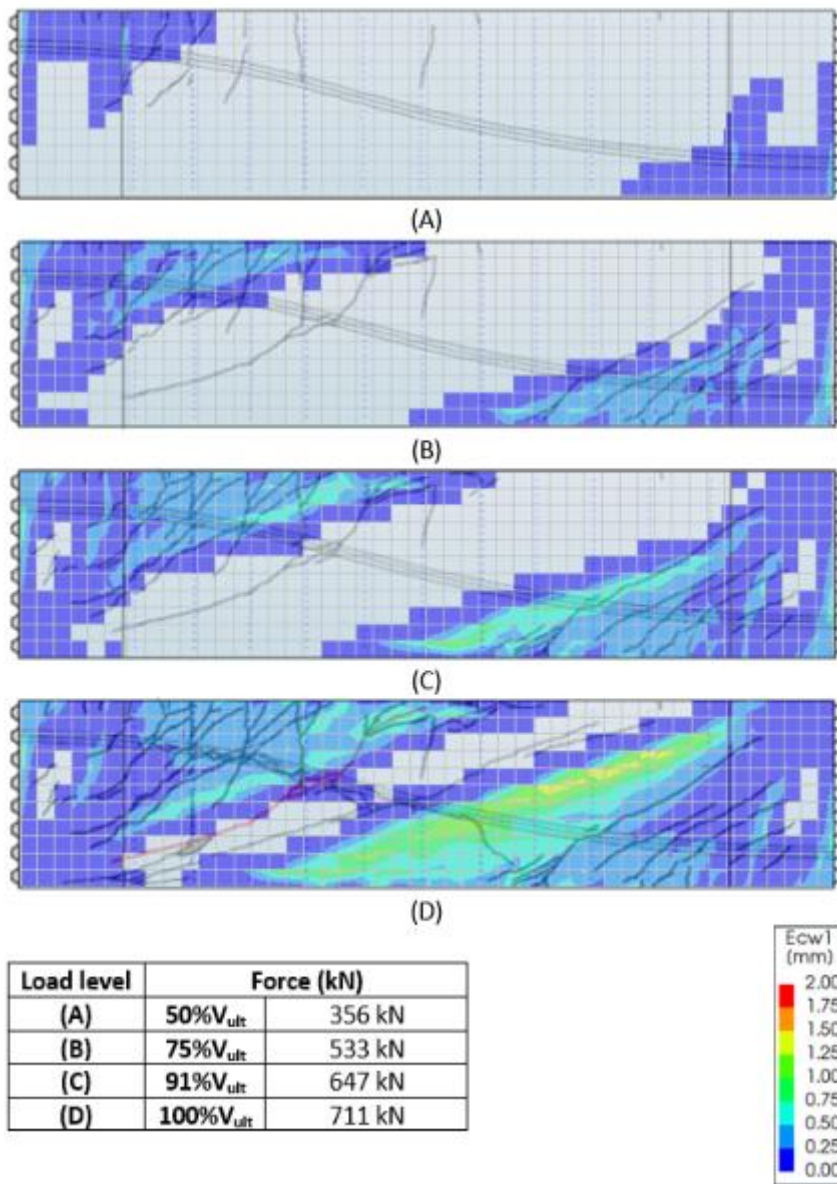


Figure 6.3: Crack development for Schramm R2 [2] and solution strategy C1.2

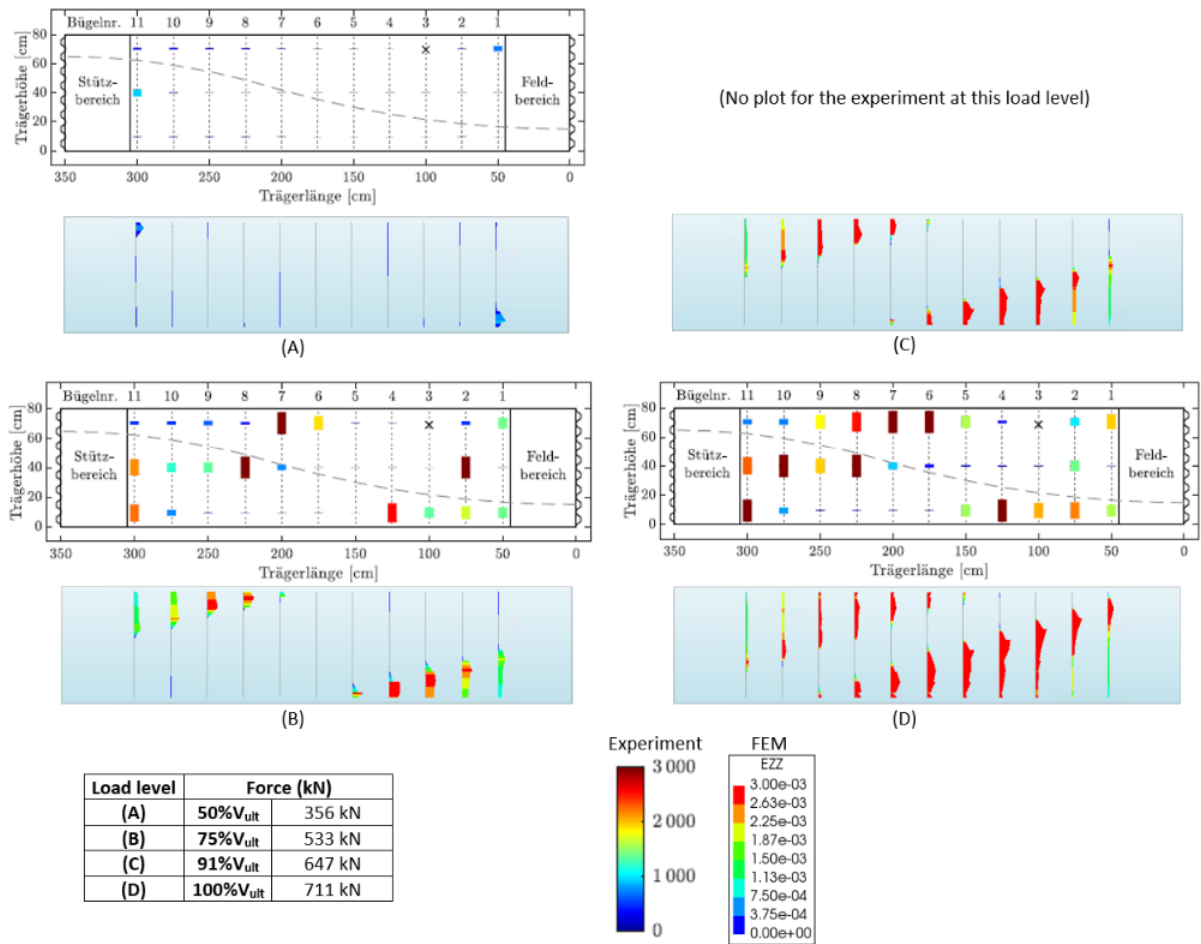


Figure 6.4: Stirrup strain development for experiment R2 (top) and solution strategy C1.2 (bottom)

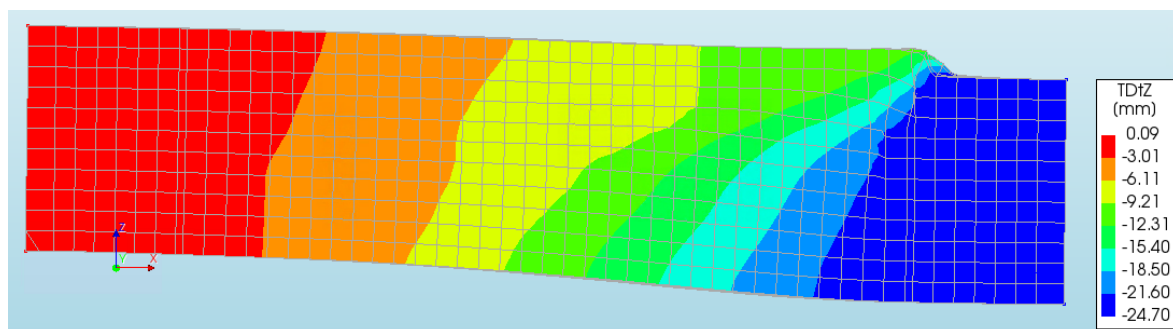


Figure 6.5: Displacement TDtZ after the peak load for solution strategy C1.2

6.1.2 Effect of the iteration scheme: Full Newton-Raphson vs. secant

Figure 6.6 show the force-displacement curves for multiple solution strategies with full Newton-Raphson and secant iteration schemes. Both schemes are used in combination with an element size of 100 mm and 50 mm. The first thing to notice is that the secant iteration scheme (C1.4 and C1.5) results in much larger failure loads than with the full Newton-Raphson iteration scheme (C1.1 and C1.3). Also, the stiffness after cracking of these solution strategies is slightly higher. There are also some differences between the failure modes of strategies C1.4 and C1.5, which indicates the mesh dependency here. This is further discussed in the next subsection, where the effect of the element size is discussed.

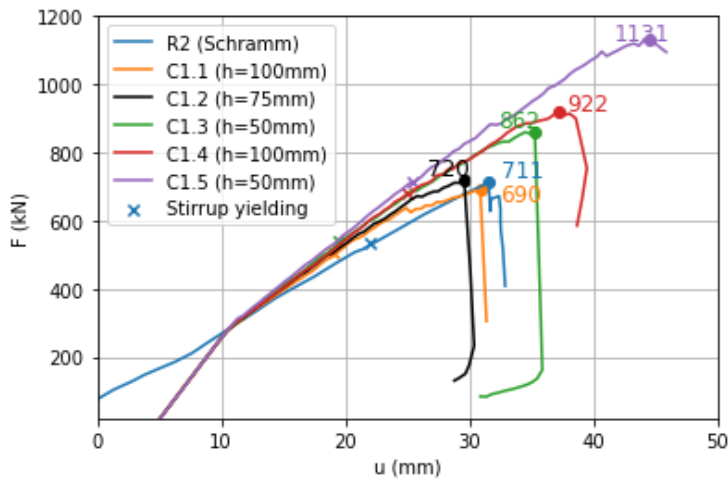


Figure 6.6: Force-displacement curve for different iteration schemes

A detailed comparison is described below, where solution strategies C1.3 and C1.5 are compared. In Figure 6.7, different load steps are pointed out that are used for the comparison. The following load steps are shown: A = onset of cracking for both solution strategies, B = Onset of stirrup yielding in C1.3, C = onset of stirrup yielding in C1.5, D = ultimate load in C1.3 and E = ultimate load in C1.5. A noticeable observation is a decrease in the stiffness of the Newton-Raphson model after initial stirrup yielding, whereas the stiffness of the secant model barely changes after initial yielding. For comparison, the results for both solution strategies are shown at the same deflection of the load steps.

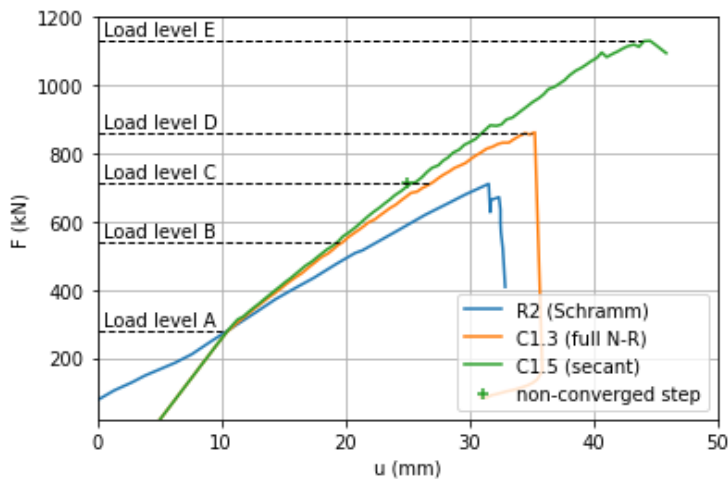


Figure 6.7: Force-displacement curves with compared load steps for C1.3 and C1.5

Figure 6.8 and Figure 6.9 show the crack development for both solution strategies. Concerning the crack patterns, the solution strategies show very similar results. The most significant difference is the values of the crack strains, especially at larger load steps. C1.3 develops much larger crack strains than C1.5. This is also confirmed by the stirrup strains shown in Figure 6.10 and Figure 6.11.

The strains for C1.3 develop at a much lower load level than is the case for C1.5. However, both strategies result in stirrup yielding, but this is at a higher load level for solution strategy C1.5. It is also noticeable that the secant iteration method shows non-convergence in the first steps after stirrup yielding.

Figure 6.12 and Figure 6.13 show the crack width at the ultimate loads. It can be seen that the crack widths are smaller for solution strategy C1.5. However, the area where significant crack widths develop is larger than for C1.3. These figures also show the difference in behaviour. C1.3 eventually fails due to crushing at the top of the field area resulting in a drastic drop in capacity, which is similar to the reference case (see Figure 6.5). C1.5 develops two horizontal cracks that eventually connect two cracked areas. When these areas are connected, the ultimate load is reached, but there is no drastic drop in the force-displacement curve. Instead, the capacity slowly decreases and the formed cracks widen.

Based on these results, it can be stated that the full Newton-Raphson is better suitable to describe the behaviour of RC beams with closed stirrups. The secant iteration method overpredicts the failure load, has difficulties developing the formed cracks resulting in smaller stirrup strains than expected and eventually leads to a false failure mechanism.

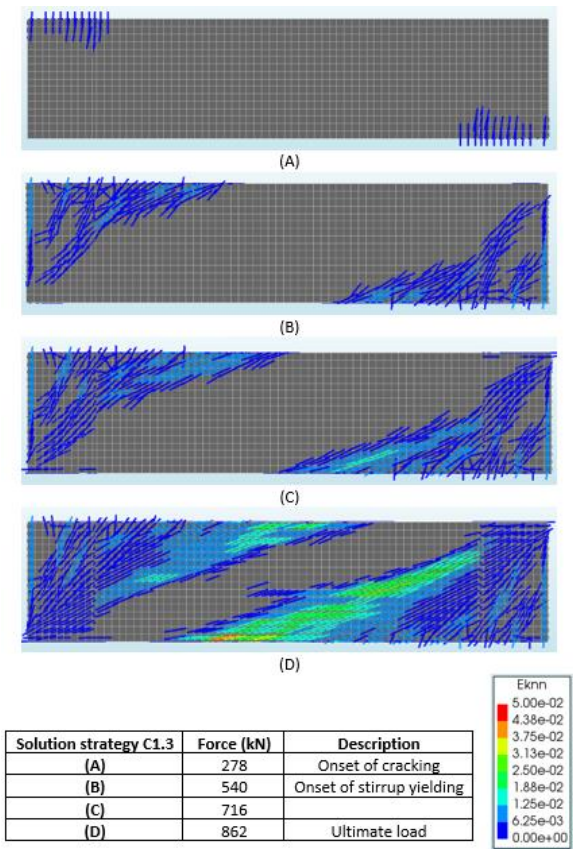


Figure 6.8: Crack strains Eknn of C1.3

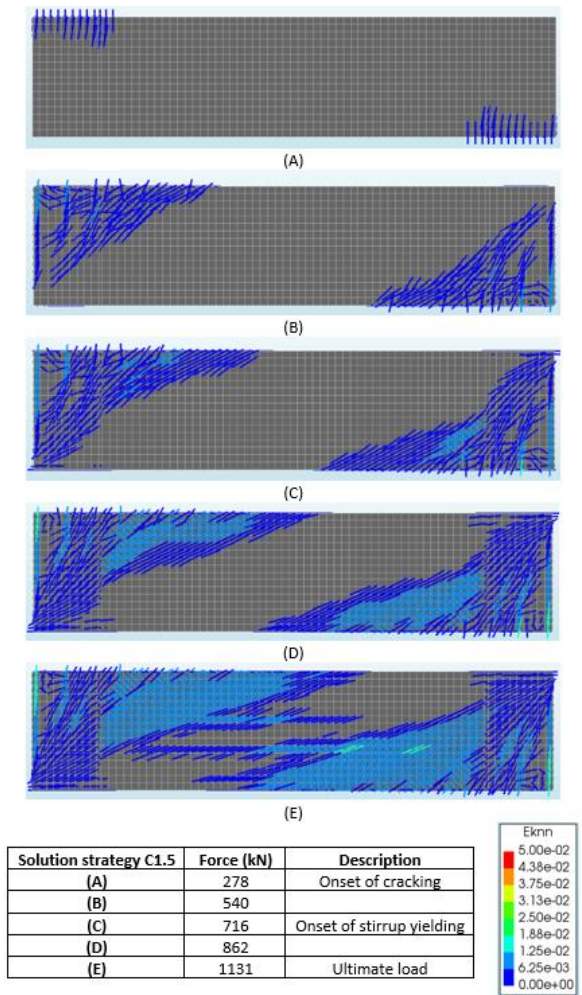
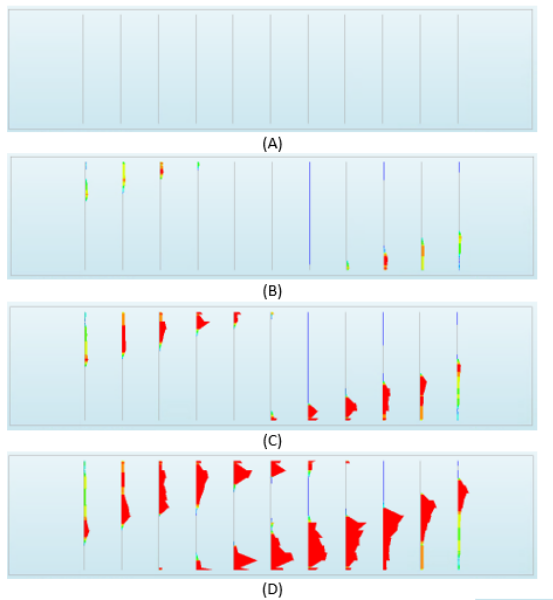
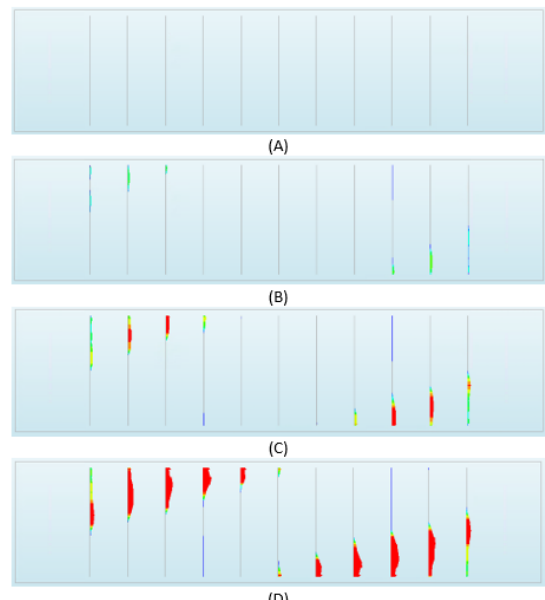
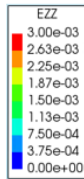


Figure 6.9: Crack strains Eknn of C1.5



Solution strategy C1.3	Force (kN)	Description
(A)	278	Onset of cracking
(B)	540	Onset of stirrup yielding
(C)	680	-
(D)	862	Ultimate load



Solution strategy C1.5	Force (kN)	Description
(A)	278	Onset of cracking
(B)	540	Onset of stirrup yielding
(C)	680	Onset of stirrup yielding
(D)	862	Onset of stirrup yielding
(E)	1131	Ultimate load

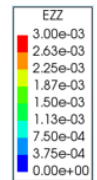


Figure 6.10: Strains EZZ in the stirrups for C1.3

Figure 6.11: Strains EZZ in the stirrups for C1.5

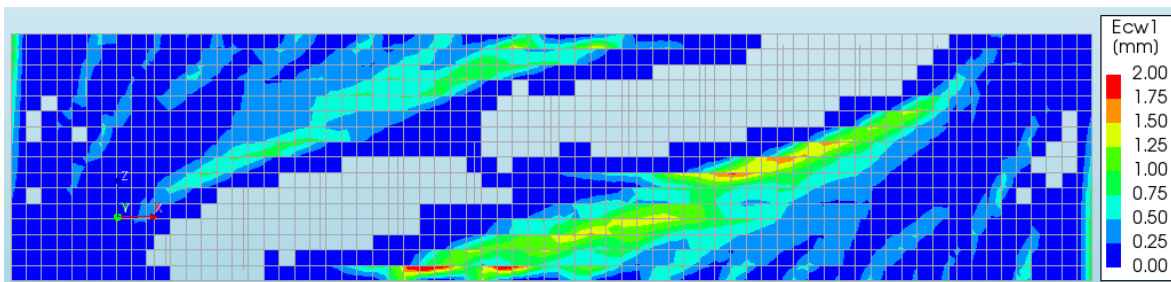


Figure 6.12: Crack width Ecw1 at $V_{ult} = 862$ kN for C1.3

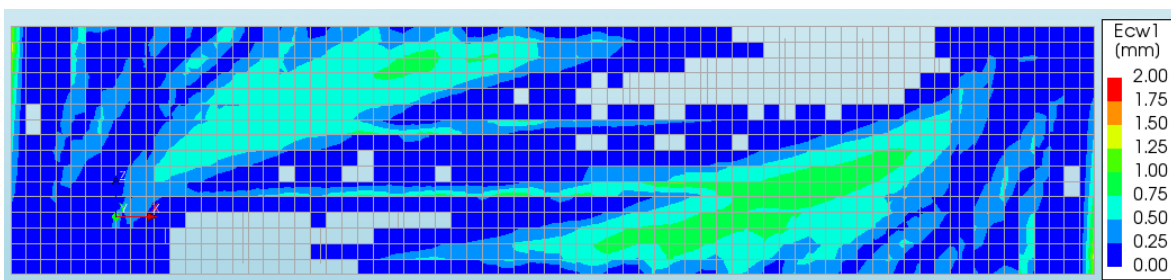


Figure 6.13: Crack width Ecw1 at $V_{ult} = 1131$ kN for C1.5

Concerning the convergence behaviour, some differences between the full Newton-Raphson and secant iteration schemes were observed. The convergence behaviour for C1.3 and C1.5 are shown in the figures below. Overall, the secant iteration scheme requires more iterations to reach convergence. For the solution strategies, most steps before the ultimate load are converged, except for some iterations around 80% of the ultimate load for the solution strategies with the secant iteration scheme. This is when the first stirrups start to yield, but after a few load steps, convergence is reached again. However, the non-converged energy norm is still very close to the energy tolerance. Therefore, these non-converged steps are still admissible. As for the reference case, for both the Newton-Raphson and secant iteration scheme only the energy norm converges after cracking and no convergence is found anymore after the peak load is reached.

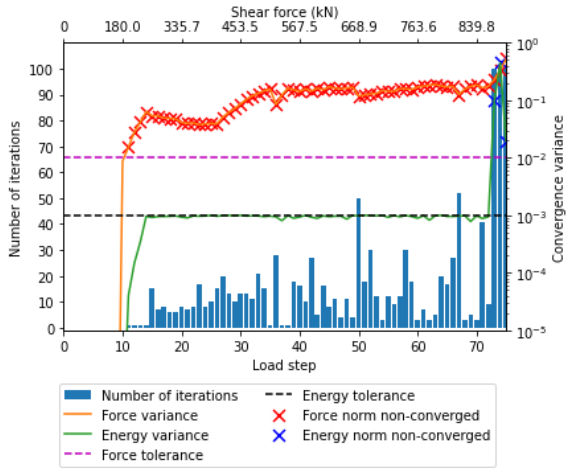


Figure 6.14: Convergence behaviour solution strategy C1.3 (Full Newton-Raphson)

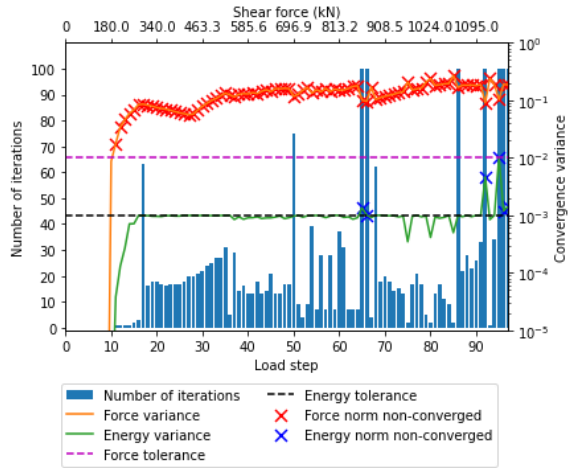


Figure 6.15: Convergence behaviour solution strategy C1.5 (Secant)

6.1.3 Effect of the element size

Figure 6.16 shows the force-displacement curve for solution strategies C1.1, C1.2 and C1.3. These strategies vary in element size. It can be seen that all solution strategies behave the same in the elastic region. After crack initiation, all models behave slightly stiffer than experiment R2. Also, small differences in stiffness are observed between the models, where a smaller element size results in a stiffer response of the model. The most important result is that the ultimate load increase when the element size decreases.

When comparing the results from the solution strategies, some differences can be seen in the crack plots. For example, the crack widths at the ultimate load for C1.1 and C1.3 are shown in Figure 6.17 and Figure 6.18. A significant difference is that larger crack widths are achieved when the element size is larger, especially at higher load levels. Also, the crack pattern for C1.1 is much coarser due to the larger elements. It is difficult to find individual cracks, which complicates the judgement on the accuracy of the behaviour. A sign of inaccuracy is that there is almost no difference in cracking zones since the whole beam seems to be cracked. For C1.3, two cracking zones in the field and support area can be distinguished, as well as some individually formed (bending) cracks.

As expected, the stirrup strain development is in line with the above-mentioned observations. For all solution strategies, the strains in the stirrups increase where cracks form and widen. The stirrup strains for solution strategy C1.1 show a slightly different strain distribution at the ultimate load due to the different locations of the largest crack.

When comparing C1.4 and C1.5, a different failure mode is found. This indicates that the mesh size could also change the structural behaviour of the model. However, no significant differences in convergence behaviour are observed. In this case, an element size of 100 mm results in a more accurate estimation of the failure mode.

Convergence plots in Appendix C show that a decreasing element size does not affect the convergence behaviour, only the number of load steps due to the larger failure load.

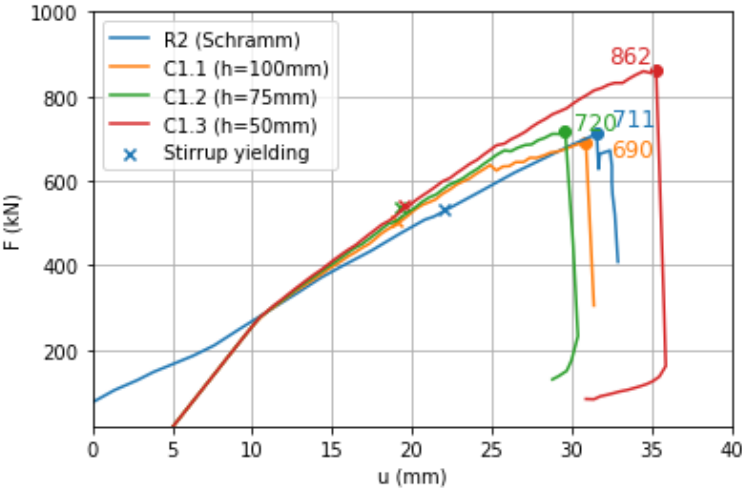


Figure 6.16: Force-displacement curve for different element sizes

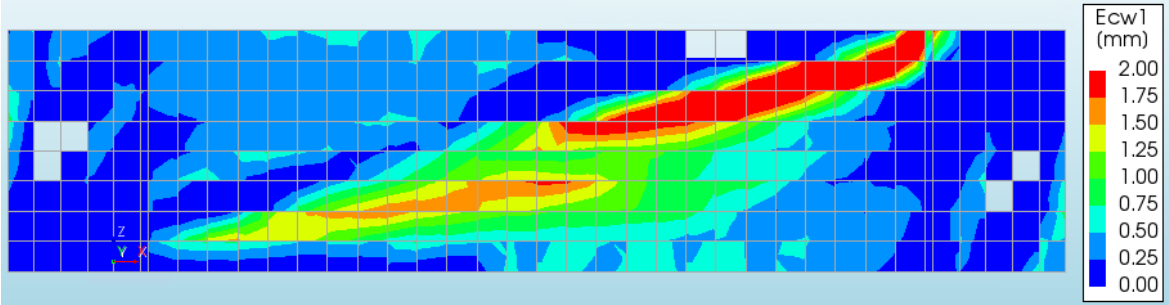


Figure 6.17: Crack width Ecw1 at ultimate shear load for solution strategy C1.1

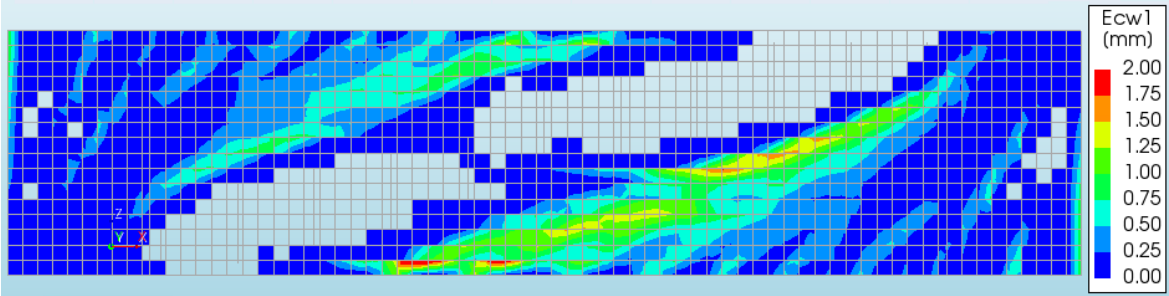


Figure 6.18: Crack width Ecw1 at ultimate shear load for solution strategy C1.3

6.1.4 Conclusions

The conclusions based on the finite element results are summed up below.

- It was found that solution C1.2, a rotating crack model with a mesh size of 75 mm and the full Newton-Raphson iteration scheme, predicts the behaviour of the RC beam with closed stirrups the best. The ultimate load is accurately predicted and the crack development is sufficiently detailed and accurate to predict a realistic pattern and contribution of the stirrups.
- The models with the full Newton Raphson method show the same cracking behaviour as was observed in Schramm's experiment R2 [2], except for the location of failure. In his test, the critical shear crack and crushing of the compression zone occur in the support area, while the models predict this behaviour in the field area. In theory, the loading and capacity conditions on the active and passive sides should be the same and therefore failure on both sides is possible.
- The modelling assumptions for the solution strategies with the full Newton-Raphson scheme were generally based on the recommendations of De Putter [19], where he stated that the failure mode is almost always predicted correctly. It appears that these recommendations indeed resulted in a correct prediction of the failure mode.
- The models with the secant iteration scheme are incapable of describing the behaviour of RC beams with closed stirrups. Significantly higher failure loads than expected are predicted and a faulty failure mode is calculated where crack widths remain small, reducing the influence of stirrups.
- All solution strategies seem to overestimate the contribution of the stirrups due to a different location and angle of the critical crack in the models. Also, the contributions of the stirrups in the models are estimated differently than in Schramm's experiments. It is therefore more reliable to compare the strains in the stirrups than the resistance of the stirrups.
- The finite element results are highly mesh dependent. The smaller the mesh size, the higher the predicted failure mechanism, but also the more detailed individual cracks are detected. An element size of 100 mm or larger is insufficient since crack plots are very rough and it is difficult to identify individual cracks. In this case, an element size of 75 mm resulted in the best prediction, but further investigations are required to provide a full understanding of this mesh dependency. De Putter [19] also found severe mesh dependency for beams with a height larger than 600 mm.

6.2 Part 2.1: RC beams with open straight-legged stirrups, Calibration

The evaluation of the results in this part is slightly different from the previous part. The purpose of this investigation is to find out which modelling assumptions are best to use to predict the behaviour of RC beams with open straight-legged stirrups. Here, it is most important to predict the expected failure mode, where the crack and stirrup strain development are used for the judgement. This is a calibration of the finite element model. The results are given in Table 6.2.

Table 6.2: Overview of the results of part 2.1

	Changing parameters	V_{yield} (kN)	V_{concrete} (kN)	V_s (kN)	V_{ult} (kN)	$\theta_{V,i}$	Failure mode
R4 (Schramm)		530	596	63	659	-	Yielding and crushing in the support area
O2.1	R-LFB-SFB-PFB-S	705	910	230	1025	0.64	Horizontal cracks between crack regions
O2.2	R-LFB-SBS-PFB-S	753	877	230	992	0.66	Horizontal cracks between crack regions
O2.3	R-LBS-SBS-PFB-S	785	861	166	943	0.70	Horizontal cracks between crack regions
O2.4	R-LBS-SBS-PBS-S	742	849	100	899	0.73	Large crack along the plates due to bond loss of the longitudinal reinforcement
O2.5	R-LBS-SBS-PBS-FNR	671	740	100	790	0.83	Delamination of concrete cover at the top
O2.6	F-LFB-SFB-PFB-S	705	784	230	899	0.73	Horizontal cracks between crack regions
O2.7	F-LFB-SBS-PFB-S	739	806	166	889	0.74	Horizontal cracks between crack regions
O2.8	F-LBS-SBS-PFB-S	770	808	198	907	0.73	Horizontal cracks between crack regions
O2.9	F-LBS-SBS-PFB-FNR	604	624	34	641	1.03	Delamination of concrete cover at the top
O2.10	F-LFB-SBS-PFB-FNR	590	587	66	620	1.06	Delamination of concrete cover at the top
V_{yield}	= Shear force at the onset of yielding						
V_{concrete}	= Contribution of the concrete beam (except for the stirrups)						
V_{stirrups}	= Contribution of the stirrups at ultimate shear force						
V_{ult}	= Ultimate shear force						
$\theta_{V,i}$	= Model uncertainty of the ultimate shear force						
R/F	= Rotating/Fixed crack orientation						
LFB/LBS	= Fully bonded/Bond-slip (longitudinal reinforcement)						
SFB/SBS	= Fully bonded/Bond-slip (stirrups)						
PFB/PBS	= Unbonded+Fully bonded/Weak+strong Bond (Prestress tendon)						
FNR/S	= Full Newton-Raphson/Secant iteration scheme						

6.2.1 Comparison between finite element results (O2.9) and experimental benchmark (R4)

Schramm's beam R4 [2] failed due to stirrup yielding and crushing of the compression zone in the support area. Comparing this with the results of the models, it can be stated that none of the solution strategies can accurately reproduce the expected failure mechanism. However, solution strategies O2.9 and O2.10 do predict the ultimate failure load quite closely to the experimental failure load. Therefore, O2.9 is used as a reference case for comparison with experiment R4 here.

The convergence behaviour is shown in Figure 6.19. In the second load step, the force norm is already non-converged. This is the first load step where the vertical point load acts and the displacement in z-direction changes direction, also significantly changing the stress distribution in the beam. Apparently, the analysis has difficulties reaching force convergence here, possibly due to difficulties with the longitudinal bond-slip reinforcement. However, the force norm immediately converges after this step. From this point, similar behaviour as for the analyses in part 1 is observed. After initial cracking, the force norm does not converge anymore and remains in the order of magnitude of 10^{-1} . Convergence is completely dependent on the energy norm, but this always converges until the peak load is reached. Here, only one non-converged step is observed with a relatively high energy norm. After this, the analysis converges again, which differs from the observations in part 1. However, unrealistic crack widths larger than 40 mm was predicted here, which makes these load steps not admissible and the analysis was stopped here.

The global behaviour is shown in Figure 6.20. In this figure, it can be seen that the stiffness after cracking for solution strategy O2.9 is slightly larger than for experiment R4, but no remarkable differences in behaviour can be seen here. However, the crack development shown in Figure 6.21 shows something completely different. In the first two load levels, more bending cracks develop in the experiment than in the model, but the initiation of inclined cracks in load level B does show some agreement, especially at the loading side (right side in the figure). The differences become more significant for larger load levels.

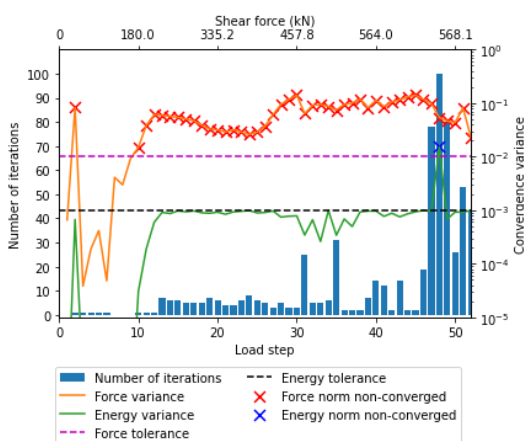


Figure 6.19: Convergence behaviour solution strategy O2.9

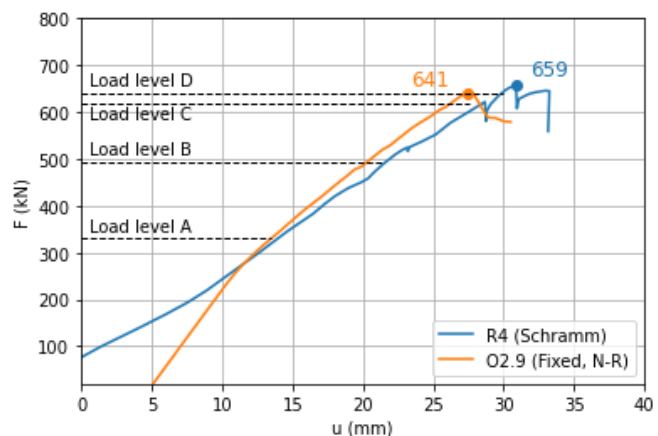


Figure 6.20: Global behaviour of the experiment R4 and solution strategy O2.9

At load level C, it can be seen that the solution strategy O2.9 do not develop new shear cracks which occur in the experiment, but the existing shear cracks further develop along the longitudinal reinforcement, implying significant bond loss between the reinforcement and concrete cover. In load step D, these crack is further developed, leading to the delamination of the concrete cover as shown in Figure 6.22. This results in a completely different failure mode as found in the experiment. Due to this crack pattern, very few stirrups are activated, underestimating the contribution of the stirrups as well as an imprecise prediction of the location of stirrup yielding (see Figure 6.23).

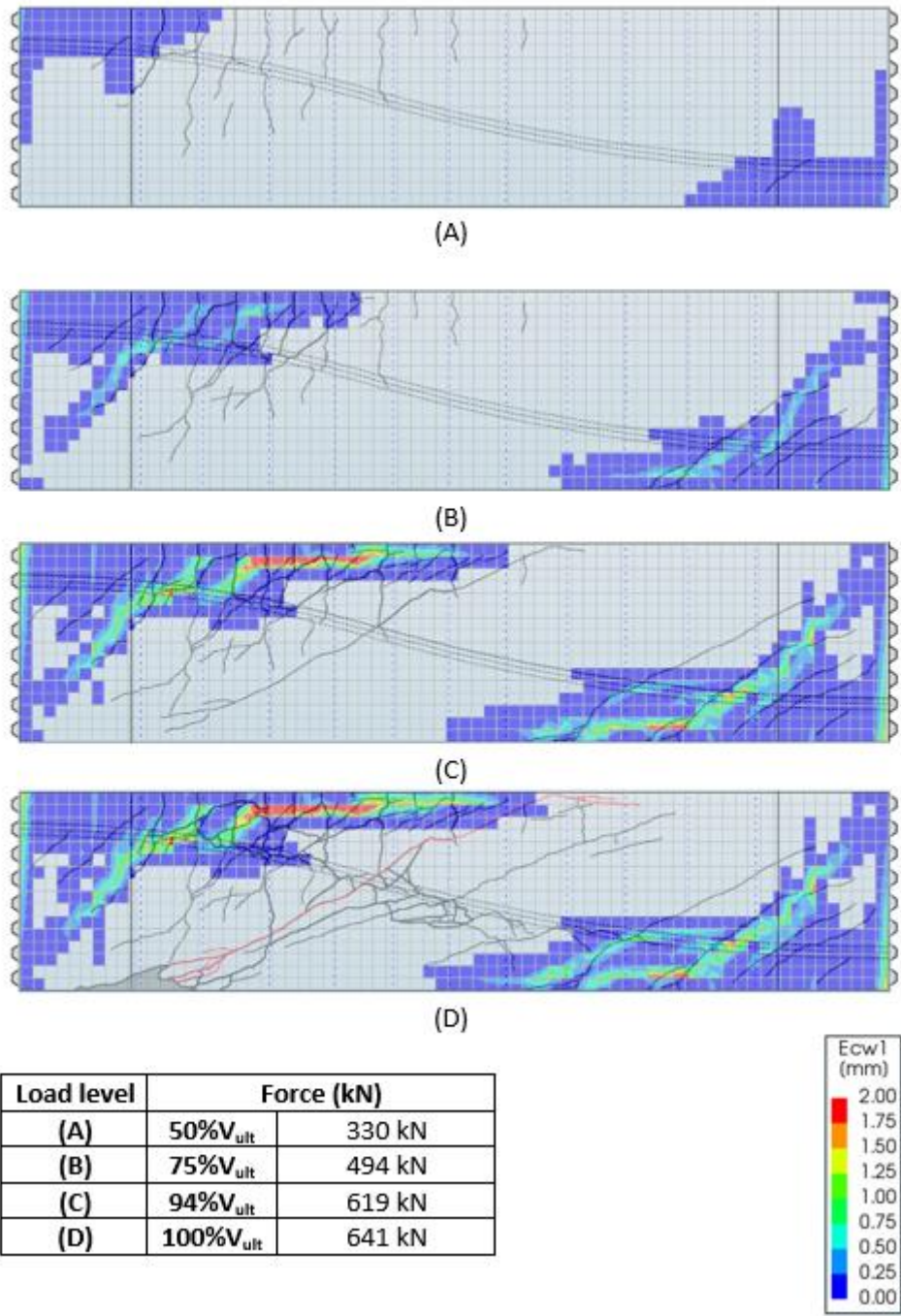


Figure 6.21: Crack development for Schramm R4 [2] and solution strategy O2.9

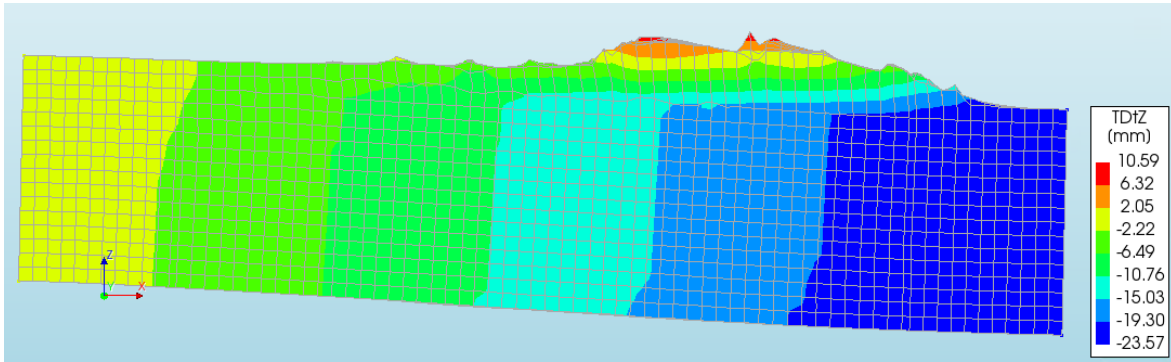


Figure 6.22: Displacement TDtZ after failure for O2.9

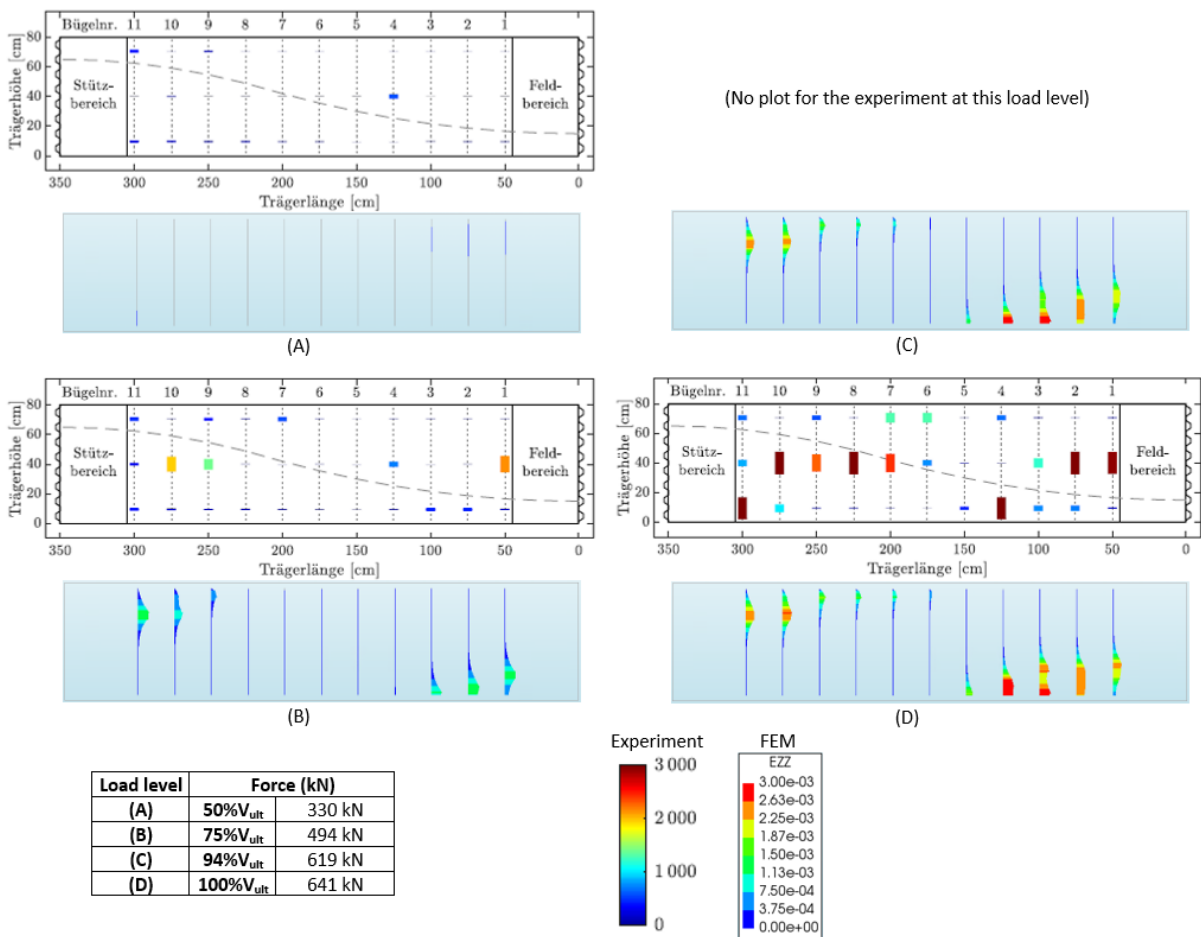


Figure 6.23: Stirrup strain development for experiment R4 (top) and solution strategy O2.9 (bottom)

The type of failure is highly dependent on the modelling choices that are made and are not always similar to this reference case. In the subsections below, the effects of those choices are discussed.

6.2.2 Effect of the reinforcement modelling: Fully bonded vs. bond-slip

Figure 6.24 shows the force-displacement curves for solution strategies varying in reinforcement modelling. Here, the longitudinal reinforcement, stirrup and prestress modelling seem to have little influence on the structural behaviour of the beams. The shear capacity is slightly smaller when the reinforcements are modelled with a bond-slip model. This is caused by the allowance of larger crack widths due to a necessary slip before the local stresses in the reinforcements can be resisted.

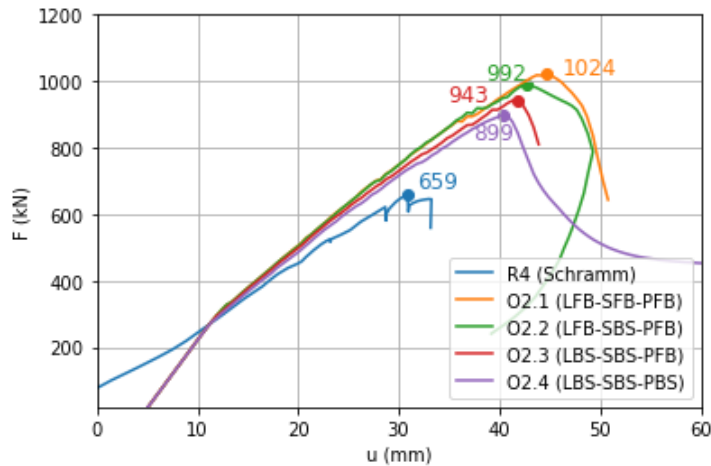


Figure 6.24: Force-displacement curve for different reinforcement models

The crack widths at ultimate loading of the four solution strategies are shown in the figures below. It can be seen that the failure mode does not significantly due to the reinforcement modelling, but the crack area becomes slightly smaller when more bond-slip reinforcements are used. Eventually, the beams fail due to horizontal cracks between the crack areas. An exception to this is O2.4, where the prestressing tendons are modelled with a bond-slip relation. Here, the slip of the longitudinal reinforcements becomes significantly large, that the cracks between the plates and concrete are not effectively resisted anymore by the reinforcement. Therefore, the crack width becomes rapidly larger, resulting in a drop in the shear resistance (and non-convergence).

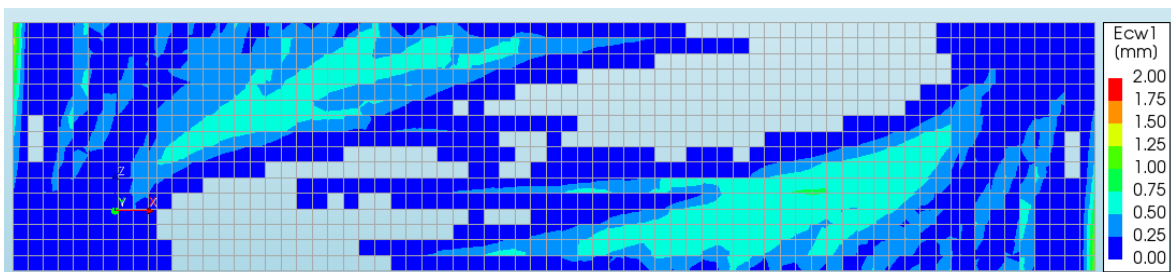


Figure 6.25: Crack width E_{cw1} at ultimate loading for O2.1 (all reinforcements fully bonded)

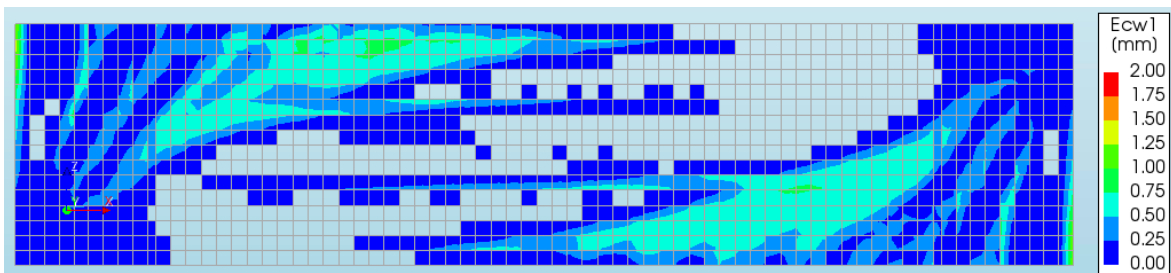


Figure 6.26: Crack width E_{cw1} at ultimate loading for O2.2 (LFB-SBS-PFB)

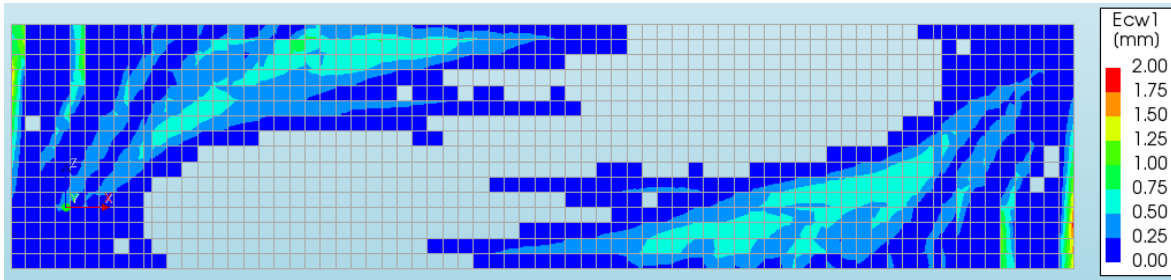


Figure 6.27: Crack width E_{cw1} at ultimate loading for O2.2 (LBS-SBS-PFB)

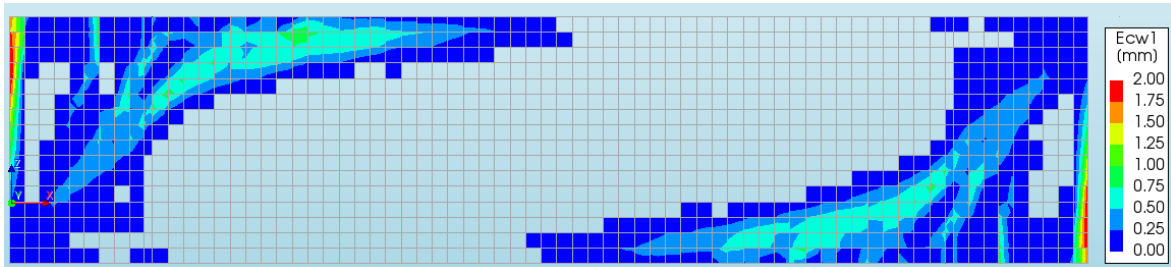


Figure 6.28: Crack width E_{cw1} at ultimate loading for O2.1 (all reinforcements bond-slip)

The convergence behaviour of a model with only fully bonded reinforcements and only bond-slip reinforcements is shown in Figure 6.29 and Figure 6.30. Due to the initial slip of the bond-slip reinforcements, more iterations are required in the first iteration and both the energy and force norms are larger. For O2.4, the bond-slip prestress tendons are less effective before loading, which results in some first cracks along the plates. Therefore, the force norm shows non-converged steps from the beginning of the analysis. For some solution strategies (see Appendix C), one of the two norms might not converge in the first few load steps, especially when bond-slip reinforcements are combined with the full Newton-Raphson iteration scheme.

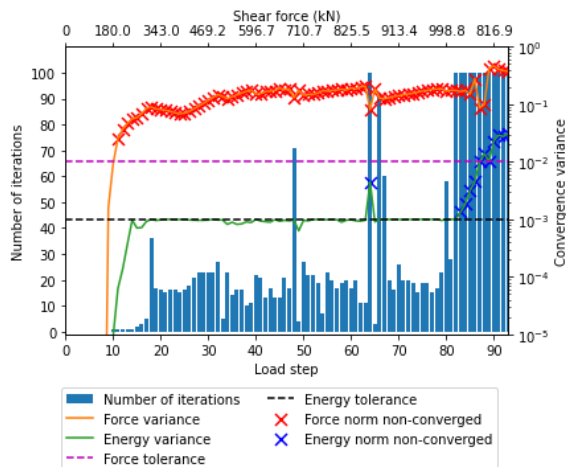


Figure 6.29: Convergence behaviour solution strategy O2.1 (all reinforcements modelled as fully bonded)

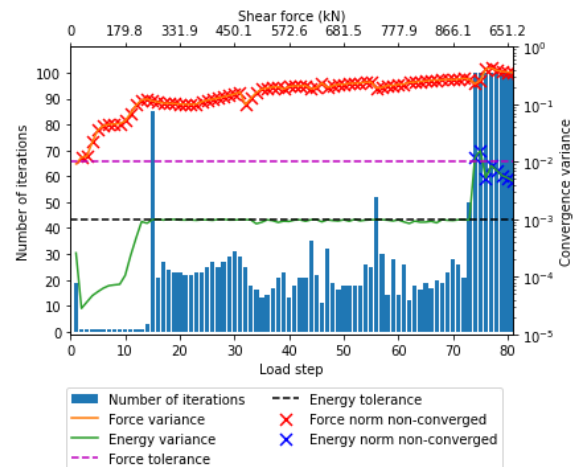


Figure 6.30: Convergence behaviour solution strategy O2.4 (all reinforcement modelled with bond-slip)

The solution strategies included in the figures in this subsection are all modelled with the secant iteration scheme. For models with the full Newton-Raphson scheme, the influence of the longitudinal reinforcement modelling is also very small. However, a comparison between fully bonded and bond-slip stirrups is not possible with this set of solution strategies due to the lack of a solution strategy with fully bonded stirrups and the full Newton-Raphson scheme. Therefore, an additional study is performed in Section 7.3, where the bond behaviour of the stirrups is investigated combined with the full Newton-Raphson scheme.

6.2.3 Effect of the iteration scheme: Full Newton-Raphson vs. secant

As well as in the previous part, large differences are observed between the different iteration schemes. shows the force-displacement curves for multiple solution strategies varying in iteration scheme and crack orientation. Just like what was observed in part 1, it can be seen that the models with the secant iteration scheme approximately contain the same stiffness after the elastic stage until failure, whereas the models with Newton-Raphson become less stiff when the load increases. Also, the ultimate load is much higher than in the models with the Newton-Raphson iteration scheme.

The differences between fixed and rotating crack models are much smaller for the secant iteration scheme. This indicates that the secant iteration method is more robust and the results are less influenced by other modelling choices. Solution strategy O2.5 (rotating, N-R) and O2.9 (fixed, N-R), on the other hand, differ much more in ultimate load. The fixed crack model fails at a much lower load. This is further discussed in the next subsection.

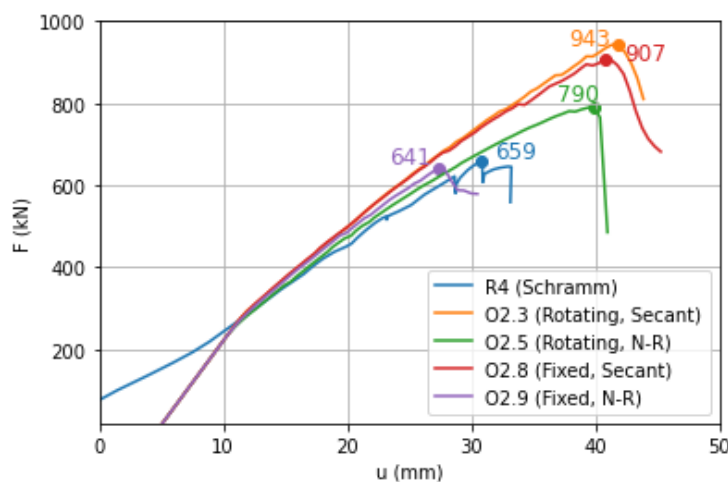


Figure 6.31: Force-displacement curve for different iteration schemes and crack orientations

It is noticed that the effect of the iteration scheme highly influences the load-bearing behaviour and failure mode. The main difference in the results is the behaviour after the initial shear crack. The models with the secant iteration scheme keep increasing the crack area resulting in the crack pattern shown in Figure 6.32, where multiple horizontal cracks between the crack areas develop, which is very similar to the closed stirrup model C1.5 (see Figure 6.34). This is the case for all models with the secant iteration method.

On the other hand, the models with the full Newton-Raphson scheme further develop the initial shear cracks along the longitudinal reinforcement (see Figure 6.21 of the reference case). The crack strains at ultimate loading for model O2.5 is shown in Figure 6.33. Here, a horizontal crack close to the top propagates, This indicates the delamination of the concrete cover along the top reinforcement. Due to this crack development, almost no stirrups are activated, which makes it impossible to analyse the anchorage behaviour of the stirrups. This failure mode is not observed in the models with closed stirrups, like C1.3 (see Figure 6.35), and Schramm’s experiments [2].

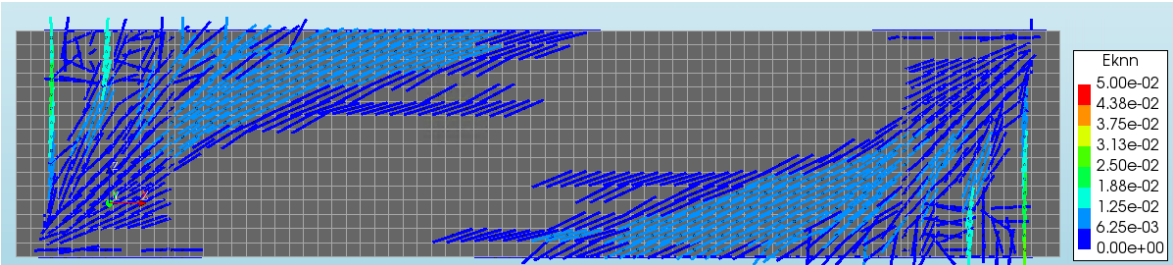


Figure 6.32: Crack strain plot Eknn of O2.3 (Secant) at ultimate loading

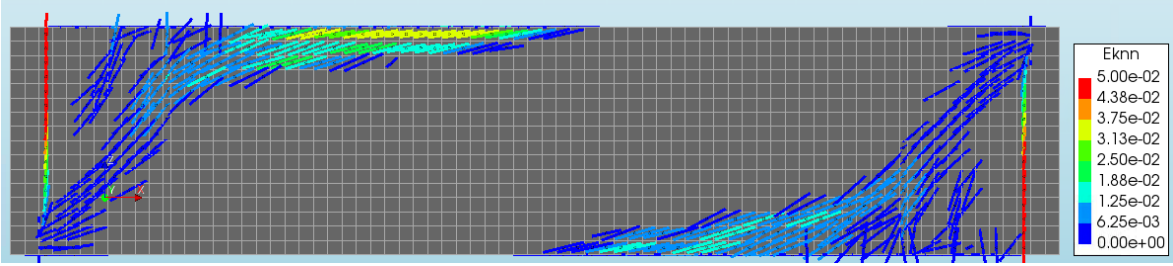


Figure 6.33: Crack strain plot Eknn of O2.5 (Full Newton-Raphson) at ultimate loading

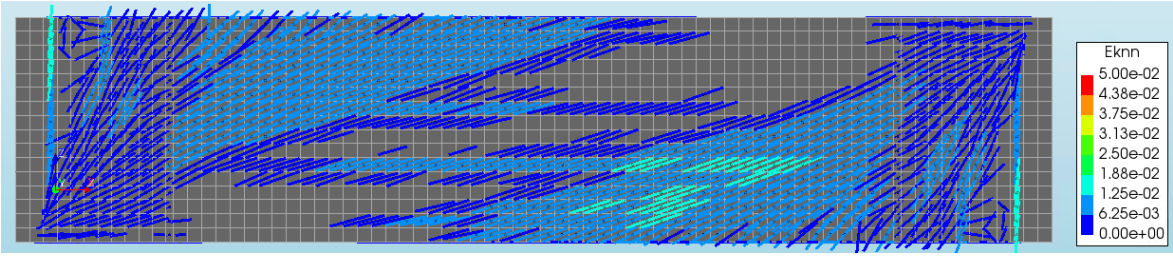


Figure 6.34: Crack strain plot Eknn of C1.5 (Secant) at ultimate loading

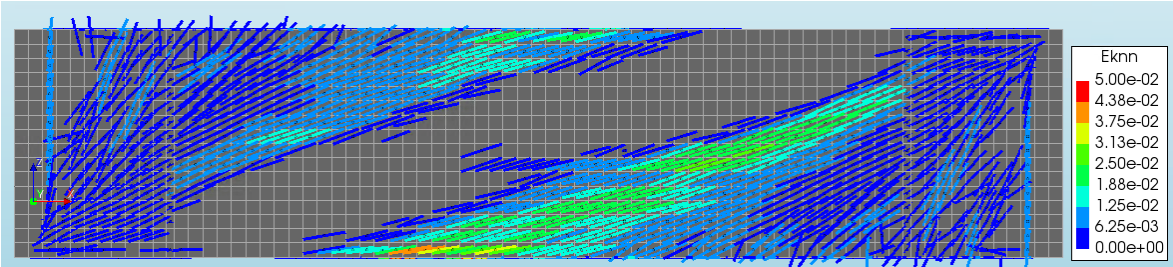


Figure 6.35: Crack strain plot Eknn of C1.3 (Full Newton-Raphson) at ultimate loading

The convergence plots are shown in Figure 6.36 and Figure 6.37. Very similar results for the iteration scheme as for part 1 concerning the convergence behaviour are observed. The secant iteration method requires more iterations per load step to reach convergence and almost all steps converge only on the energy norm before failure.

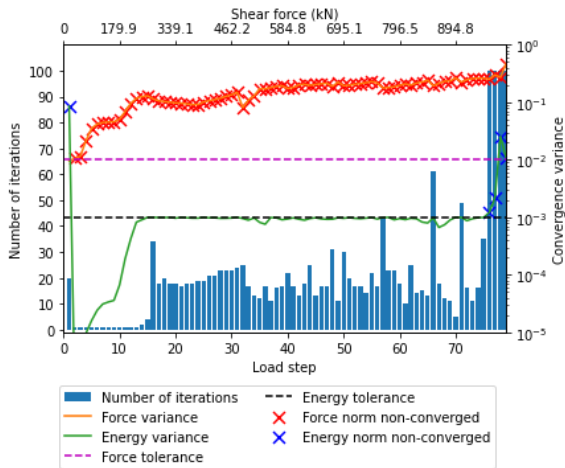


Figure 6.36: Convergence behaviour solution strategy O2.3 (Secant)

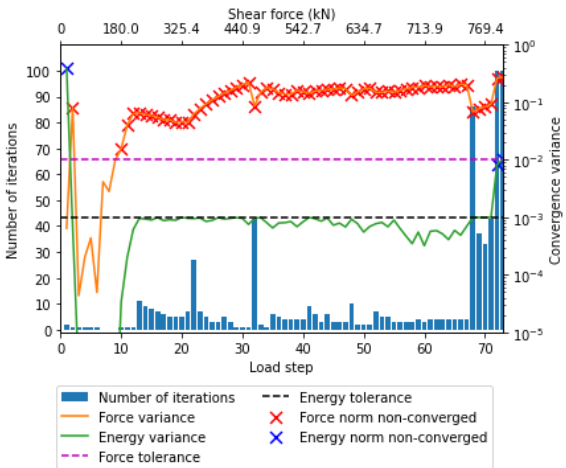


Figure 6.37: Convergence behaviour solution strategy O2.5 (Full Newton-Raphson)

6.2.4 Effect of the crack orientation: Rotating vs. fixed

As was stated in the previous subsection, the failure mode is mostly dependent on the chosen iteration scheme. However, some differences between rotating and fixed (with damage-based shear retention) crack models can be observed. A comparison between ultimate shear forces presented in Table 6.2 indicates that the fixed crack models result in more conservative results than the rotating crack models. The ultimate shear force is smaller for all fixed crack models when comparing the individual models with the same assumptions except the crack orientation, i.e. O2.1 vs. O2.6, O2.2 vs. O2.7, O2.3 vs. O2.8 and O2.5 vs. O2.9 or O2.10. For the secant iteration scheme, the differences are smaller than for the Newton-Raphson iteration scheme.

First, a comparison is made for the secant iteration scheme. The load-bearing behaviour of the models is not very different. For example, the crack widths at 70% of the ultimate shear force for solution strategies O2.3 and O2.8 are shown in Figure 6.38 and Figure 6.39. The crack pattern itself is very similar, but the crack widths are slightly larger for the fixed crack model. The similarity in behaviour is confirmed by the force-displacement curves shown in .

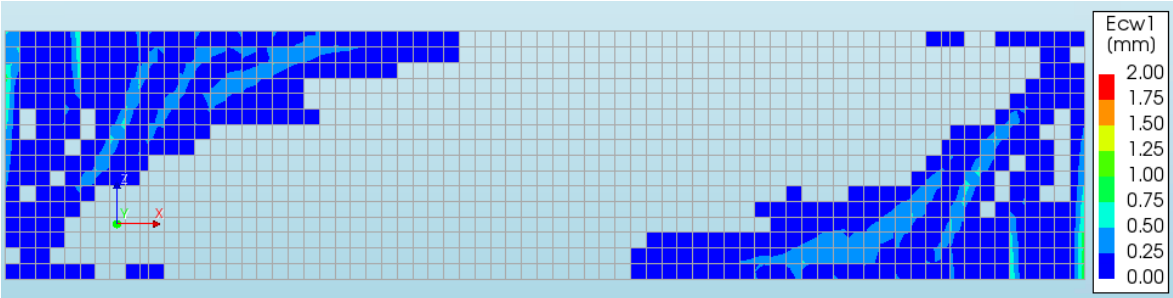


Figure 6.38: Crack width E_{cw1} at 70%V_{ult} = 641 kN for O2.3 (secant iteration scheme, rotating crack model)

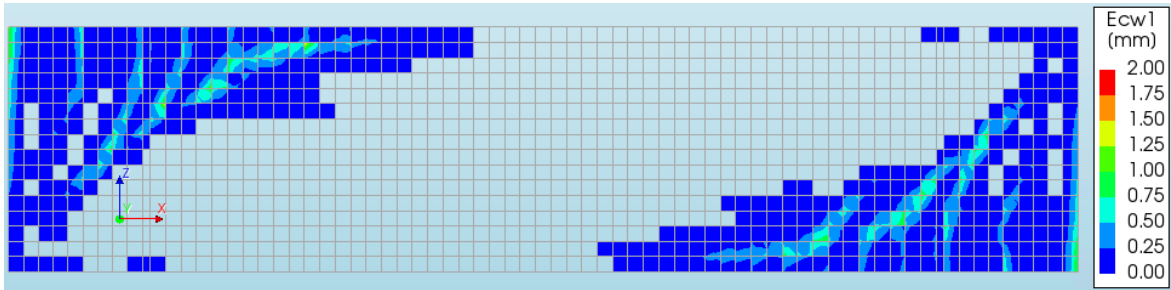


Figure 6.39: Crack width E_{cw1} at $70\%V_{ult} = 635 \text{ kN}$ for O2.8 (secant iteration scheme, fixed crack model)

For the Newton-Raphson iteration scheme, the differences are larger between the rotating and fixed crack models. The crack widths in the fixed model are again larger than for the rotating crack model (see Figure 6.40 and Figure 6.41). The crack propagation is not entirely the same as well, which results from the difference in shear retention behaviour. This can also be observed in the crack strain plots in Figure 6.42 and Figure 6.43. Especially the orientation at the top of the beam shows a different crack propagation. The rotating crack model O2.5 has overrotated the bending cracks and is almost horizontal. This is not possible in the fixed crack model, where the bending cracks remain vertical. These vertical bending cracks keep developing to approximately $1/3$ of the length of the beam, where these cracks eventually also develop under an angle due to the small bending moment in the middle part of the beam.

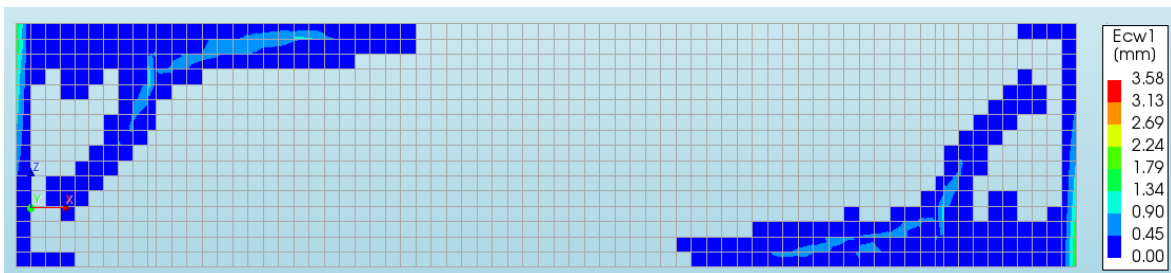


Figure 6.40: Crack width E_{cw1} at 550 kN for O2.5 (Newton-Raphson iteration scheme, rotating crack model)

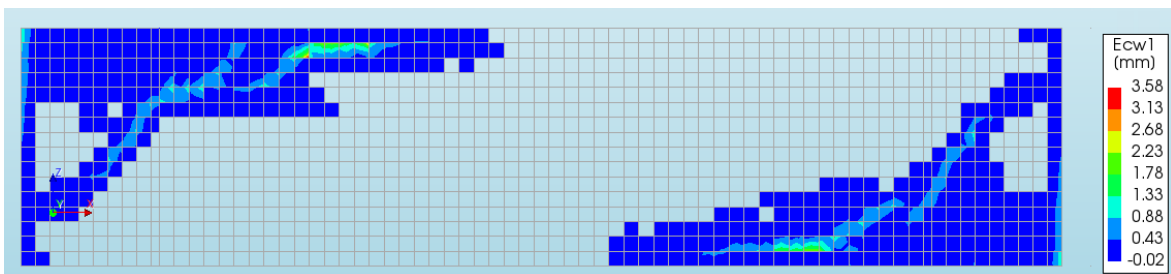


Figure 6.41: Crack width E_{cw1} at 550 kN for O2.9 (Newton-Raphson iteration scheme, fixed crack model)

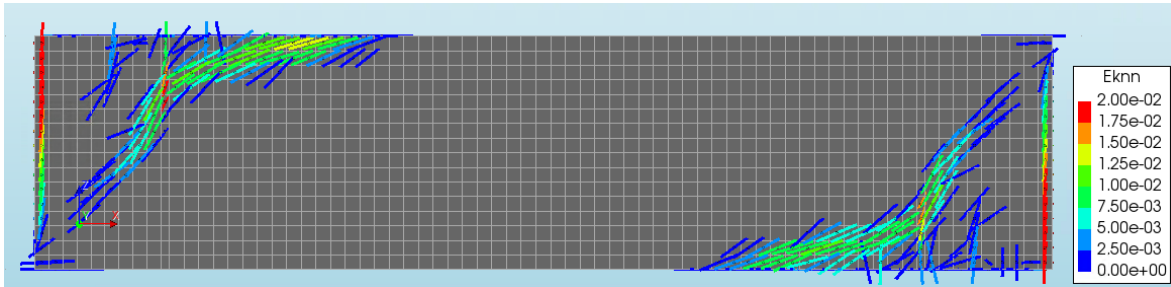


Figure 6.42: Crack strain E_{knn} at 550 kN for O2.5 (Newton-Raphson iteration scheme, rotating crack model)

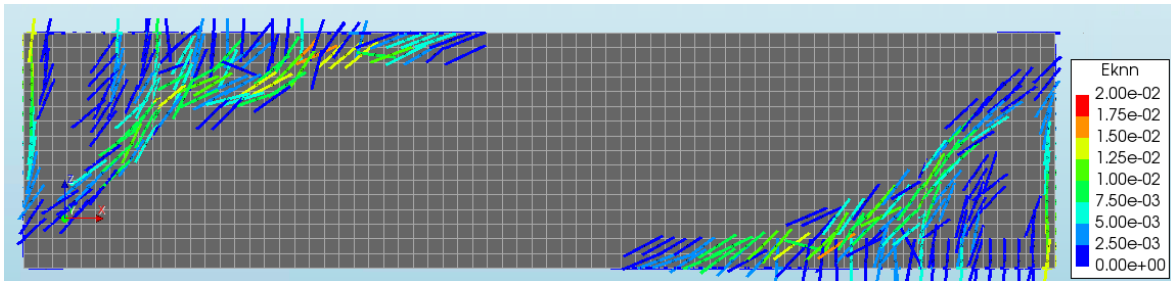


Figure 6.43: Crack strain E_{knn} at 550 kN for O2.9 (Newton-Raphson iteration scheme, fixed crack model)

The convergence behaviour of a rotating and fixed crack model is shown in Figure 6.44 and Figure 6.45. Here, it is shown that there are no noticeable differences in convergence behaviour due to the rotating or fixed crack orientation.

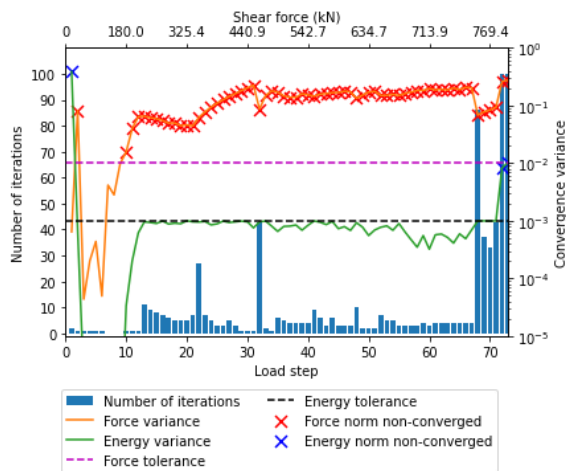


Figure 6.44: Convergence behaviour solution strategy O2.5 (Rotating)

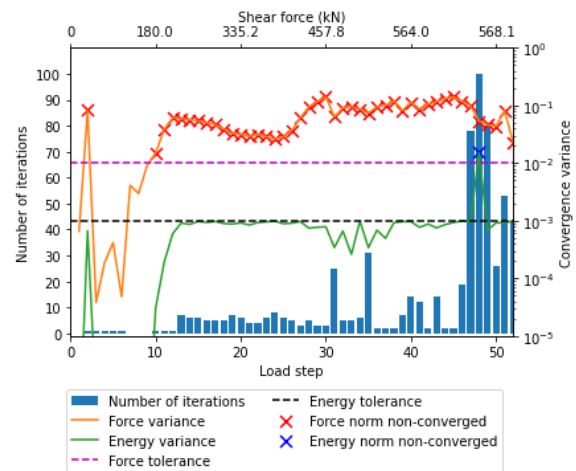


Figure 6.45: Convergence behaviour solution strategy O2.9 (Fixed)

6.2.5 Conclusions

The conclusions based on the finite element results are summed up below.

- All solution strategies are unable to predict the correct failure mode when the open straight-legged stirrups are modelled with a bond-slip relation. Therefore, it can be stated that it is not possible to describe the anchorage behaviour of the open ends of the stirrups with a finite element analysis.
- The modelling of the bond between the longitudinal and prestress reinforcements and the concrete, i.e. fully bonded or with a bond-slip relation, has little influence on the load-bearing behaviour. This opposes the findings of De Putter [19], since he found that the overrotation of cracks in beams without shear reinforcement was solved by applying a bond-slip relation for the longitudinal reinforcement. Unfortunately, the overrotation of cracks is not solved for these models with the full Newton-Raphson scheme.
- The choice of the iteration scheme has a huge impact on the load-bearing behaviour. Completely different failure modes were observed for models with the secant iteration scheme and the Newton-Raphson iteration scheme. However, both schemes were unable to accurately predict the correct failure mode.
- The secant iteration scheme is very consistent in the prediction of the crack development, where the variation of other parameters did not significantly change the finite element results. The shear cracks develop where expected, but at a larger load level than expected and also do not lead to the expected failure mode. The cracking patterns were very similar to the beams with closed stirrups. It is not entirely clear why the models with the secant iteration scheme are much less affected by the reinforcement modelling than the models with the full Newton-Raphson scheme.
- Differences in the failure mode between the rotating and fixed (with damage-based shear retention) crack models were only significant for models with the Newton-Raphson scheme. Here, larger crack widths for the fixed crack model and slightly different crack propagations were observed. De Putter [19] stated that beams with shear reinforcement modelled with a fixed crack model usually result in more conservative predictions than rotating crack models, which agrees with the results in this study.

7 Discussion of the results

The results in the previous chapter did not always match the expectations and results of the experiment. In this chapter, unexpected outcomes are further investigated and the reasons for this behaviour are searched for. First, the contributions of all load-bearing mechanisms in a finite element model are estimated and compared to calculations formulated in Eurocode 2 [8] and RBK1.1 [38], to provide a better understanding of the behaviour of the model. Then, multiple modelling choices are validated or analysed to come to conclusions about the inaccurate behaviour of the models.

7.1 Contribution per load-bearing mechanism

Next to the contribution of the stirrups, it is useful to understand and quantify the contribution of the other load-bearing mechanisms. This is evaluated at ultimate loading, so the final load step before failure. Below, the calculations are elaborated for solution strategy C1.2 ($h=75$ mm) and C1.3 ($h=50$ mm). These strategies predict the behaviour of an RC beam with closed stirrups quite accurately and are therefore valid to check the contributions of the load-bearing mechanisms.

First, the critical crack is identified for the estimation of the load-bearing mechanisms. This is shown in Figure 7.1 and Figure 7.2, where the red line represents the cut section that is used. Aggregate interlock and dowel action are both not modelled, so these contributions are zero. The contribution of the stirrups was already estimated, where 9 yielding stirrups contribute for both solution strategies resulting in a total contribution of $V_s = 300$ kN.

The beam should always be in equilibrium, so the sum of the load-bearing mechanisms should be equal to the acting shear force, so $V_{R,total} = V_{E,total}$. Some small deviations are possible, since the numerical results are always an approximation of a real situation, where the convergence criteria define the accepted error. This should be taken into consideration, especially since the force norm does not converge after cracking.

In the finite element models, the total acting shear force was estimated based on the vertical reaction forces at the supports ($F_{reaction} = V_{ult}$), including the self weight of the beam. The part of the self-weight that is accounted for in the cut section here is (first part consists of the self-weight up to the crack ($x=0$ m to $x=2.2$ m) and the second part is the extra widening at the end of the beam):

$$F_{selfweight} = 2500 \times 9.81 \times (0.25 \times 0.8 \times 2.2 + 0.25 \times 0.8 \times 0.45) \times 10^{-3} = 13 \text{ kN}$$

This results in the following acting shear forces:

$$V_{E,total,C1.2} = F_{reaction,C1.2} - F_{selfweight} = 720 - 13 = 707 \text{ kN}$$

$$V_{E,total,C1.3} = F_{reaction,C1.3} - F_{selfweight} = 862.0 - 13.0 = 849 \text{ kN}$$

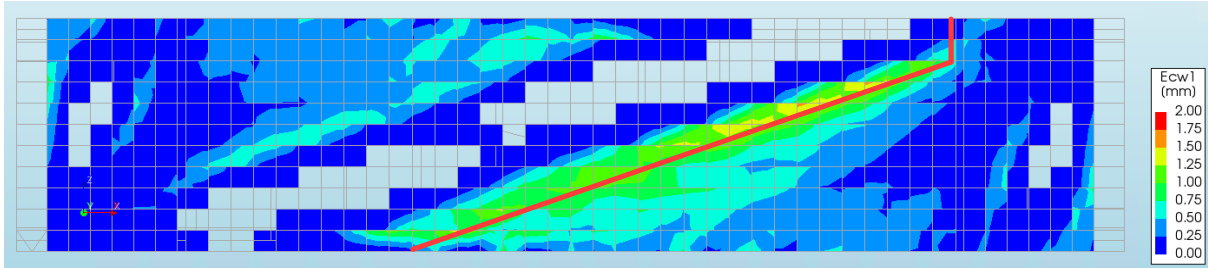


Figure 7.1: Critical crack E_{cw1} at ultimate loading for C1.2

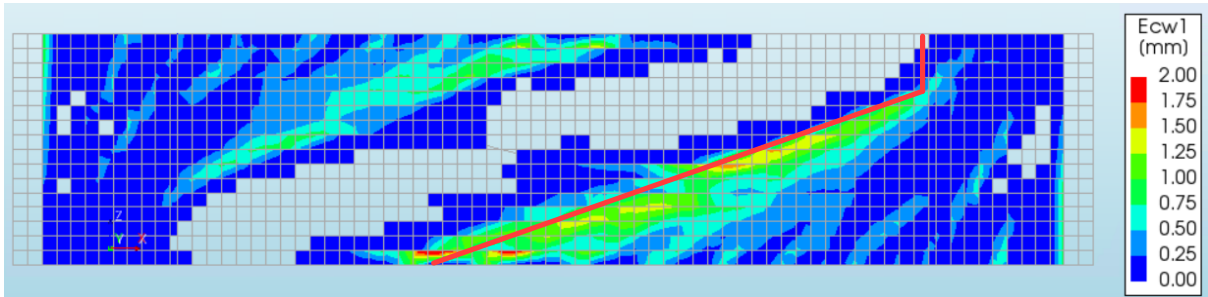


Figure 7.2: Critical crack E_{cw1} at ultimate loading for C1.3

7.1.1 Contribution of the compression zone

For the estimation of the contribution of the compression zone, it is first necessary to identify the height of the compression zone above the shear crack tip. In Figure 7.2, it appears to be approximately 2 elements high for C1.2 and 4 elements for C1.3. As a check, the strains E_{XX} at ultimate loading are shown in Figure 7.3 and Figure 7.4. Here, a cut is shown at the tip of the shear crack with only two contour levels to show the distinction between tension and compression. For C1.2, it can be seen that the top two rows of elements in the cross-section are in compression, which confirms that the compression zone height is $x_{u,c1.2} = 150 \text{ mm}$. For C1.3, approximately 4.25 elements are in compression, resulting in $x_{u,c1.3} = 225 \text{ mm}$.

The figure below shows the evaluated absolute shear stress S_{ZX} averaged over the width of the beam at the cut section as shown in the figures above. Since the width of the beam is constant, the stresses are averaged over the whole compression zone, resulting in:

- C1.2: $z = 650 \text{ mm to } z = 800 \text{ mm} \rightarrow S_{ZX} = -5.55 \text{ N/mm}^2$
- $V_{comp,C1.2} = |S_{ZX}|x_u b = 5.55 \times 150 \times 250 \times 10^{-3} = 208 \text{ kN}$
- C1.3: $z = 575 \text{ mm to } z = 800 \text{ mm} \rightarrow S_{ZX} = -7.54 \text{ N/mm}^2$
- $V_{comp,C1.3} = |S_{ZX}|x_u b = 7.54 \times 225 \times 250 \times 10^{-3} = 424 \text{ kN}$

Note that the influence of the horizontal prestresses is already included in the compression zone.

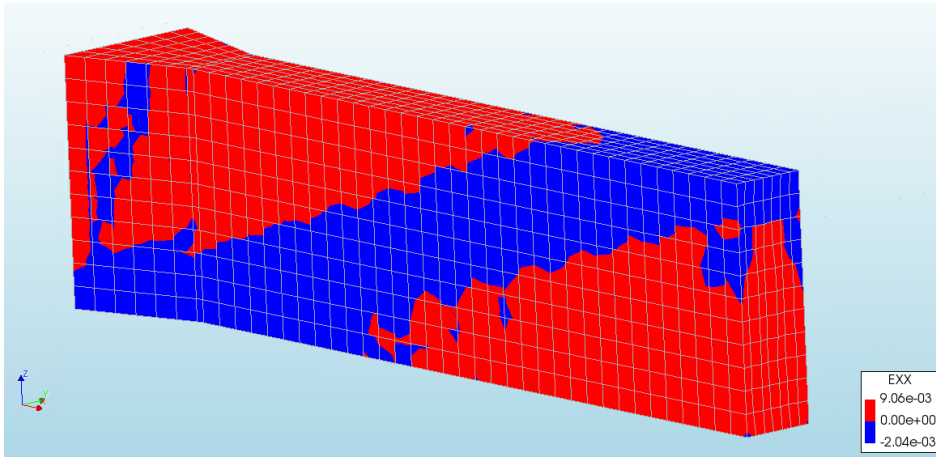


Figure 7.3: Total strain EXX at ultimate loading for C1.2 (with a cut at the shear crack tip)

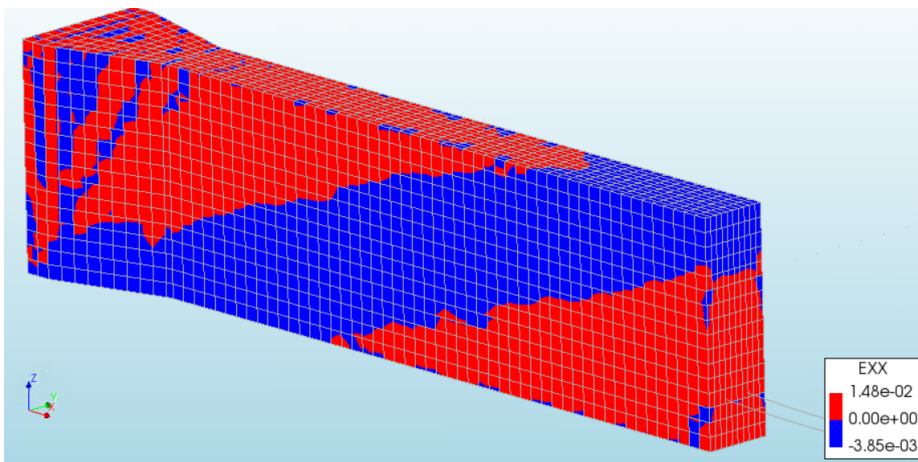


Figure 7.4: Total strain EXX at ultimate loading for C1.3 (with a cut at the shear crack tip)

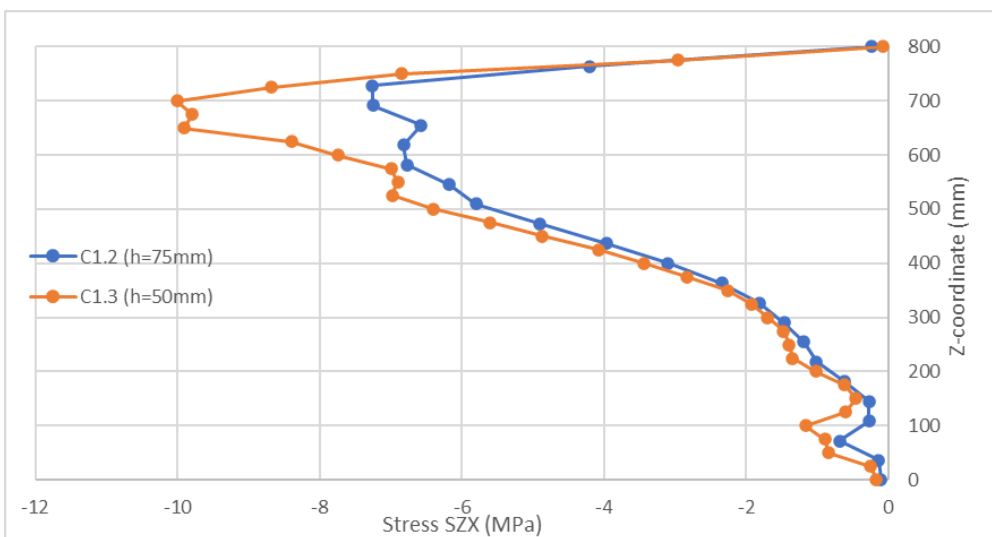


Figure 7.5: Stress SZX at the cut (averaged over the width of the beam)

7.1.2 Contribution of vertical component in tendons

The vertical stress component is evaluated at the location where the tendons cross the critical crack, which is represented by the red line in Figure 7.6 and Figure 7.7. To estimate the increase in stress in the tendons due to cracking at the critical crack, The stress SXX , which is approximately equal to the stress parallel to the reinforcement, is approximated at ultimate loading ($SXX_{ult,C1.2} = 790 \text{ N/mm}^2$ and $SXX_{ult,C1.3} = 850 \text{ N/mm}^2$) and right after prestressing ($SXX_{ini} = 571 \text{ N/mm}^2$). The tendon is inclined at approximately 11° where it crosses the critical crack for both solution strategies. This results in a total shear contribution of the two tendons:

$$V_{t,C1.2} = n \times (SXX_{ult,C1.2} - SXX_{ini})A_p \sin(\alpha) = 2 \times (790 - 571) \times 420 \times \sin(11^\circ) \times 10^{-3} = 35 \text{ kN}$$

$$V_{t,C1.3} = n \times (SXX_{ult,C1.3} - SXX_{ini})A_p \sin(\alpha) = 2 \times (850 - 571) \times 420 \times \sin(11^\circ) \times 10^{-3} = 45 \text{ kN}$$

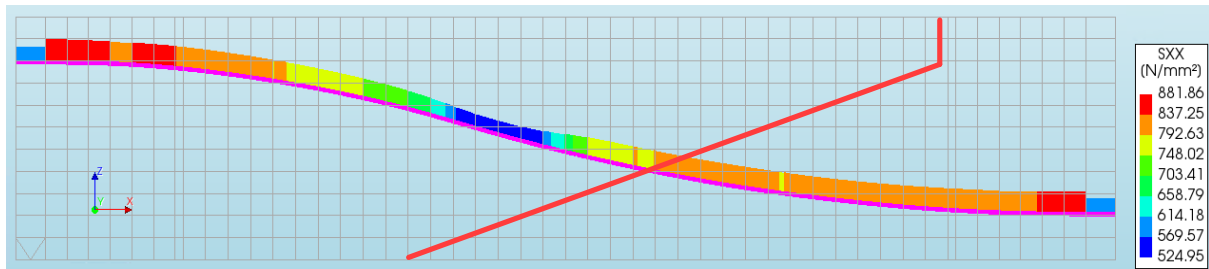


Figure 7.6: Reinforcement stress SXX for the prestress tendons at ultimate loading for C1.2

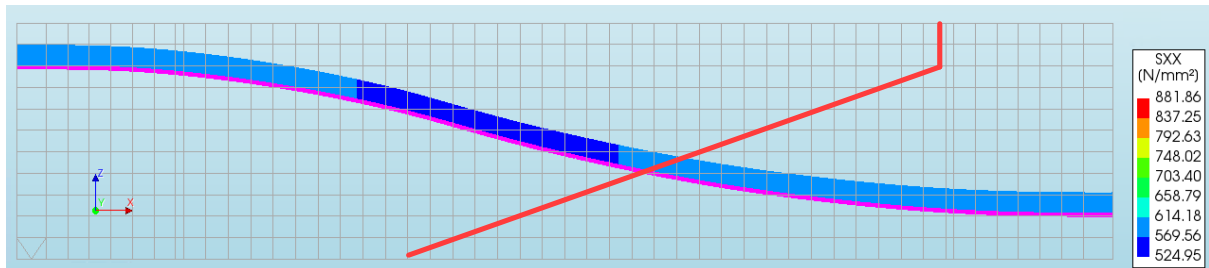


Figure 7.7: Reinforcement stress SXX for the prestress tendons after prestressing and before loading for C1.2

7.1.3 Contributions according to Eurocode 2 [8]

As a comparison, the maximum capacity for multiple mechanisms according to Eurocode 2 [8] is also calculated. Here, the material safety factors are neglected, since the mean values are used for comparison. These calculations are shortly illustrated below and explanations are given where necessary. The mean material properties measured by Schramm [2] are used.

First, the contribution of the compression zone, where x_{2b-4b} is the distance between the bottom 4 bars and the bottom 2 bars (resulting normal force is at $\frac{1}{3}x_{2b-4b}$ above the bottom 4 bars):

$$d = h - \left(c + \varnothing_s + \frac{1}{2}\varnothing_{long} + \frac{1}{3}x_{2b-4b} \right) = 800 - \left(20 + 6 + \frac{1}{2} \times 25 + \frac{1}{3} \times (83.5 - 38.5) \right) = 747 \text{ mm}$$

$$k = 1 + \sqrt{\frac{200}{d}} = 1 + \sqrt{\frac{200}{747}} = 1.52$$

$$\rho_l = \frac{A_l}{bd} = \frac{6 \times 0.25\pi \times 25^2}{250 \times 747} = 0.0158$$

(Use only bottom reinforcement)

$$V_{Rm,c} = 0.163k(100\rho_l f_{cm})^{\frac{1}{3}} b_w d = 0.163 \times 1.52 \times (100 \times 0.0158 \times 47)^{\frac{1}{3}} \times 250 \times 747 \times 10^{-3} = 194 \text{ kN}$$

Also, the contribution of the prestress is estimated:

$$V_{prestress} = 0.225\sigma_{cp} b_w d = 0.225 \times 2.5 \times 250 \times 747 \times 10^{-3} = 105 \text{ kN}$$

The total contribution of the concrete is then:

$$V_c = V_{Rm,c} + V_{prestress} = 194 + 105 = 299 \text{ kN}$$

Now, the contribution of the stirrups. According to EC2 [8], the contribution of the stirrups is only accountable if $\rho_w \geq \rho_{w,min}$. This is checked below for concrete C30/37 and reinforcement B500:

$$\rho_w = \frac{A_{sw}}{s \times b_w \times \sin(\alpha)} = \frac{2 \times 0.25\pi \times 6^2}{250 \times 250 \times \sin(90^\circ)} \times 10^2 = 0.091\% \quad \rightarrow \rho_w > \rho_{w,min} \rightarrow \text{sufficient}$$

$$\rho_{w,min} = 0.08 \frac{\sqrt{f_{ck}}}{f_{yk}} = 0.08 \frac{\sqrt{30}}{500} = 0.088\%$$

So the contribution of the stirrups is accountable. According to EC2, the minimum angle is limited to $\theta = 21.8^\circ$. Therefore, the maximum contribution of the stirrups is:

$$z \approx 0.9d = 0.9 \times 747 = 672 \text{ mm}$$

$$V_{Rm,s} = \frac{A_{sw}}{s} z f_{yw} \cot \theta = \frac{2 \times 0.25\pi \times 6^2}{250} \times 672 \times 588.2 \times \cot(21.8^\circ) \times 10^{-3} = 224 \text{ kN}$$

RBK1.1 [38] describes that the contributions of compression zone AND stirrups for existing structures are only allowed to take into account under the condition that the crack angle is 30° for prestressed concrete. In this case, the stirrup contribution is:

$$V_{Rm,s} = \frac{A_{sw}}{s} z f_{yw} \cot \theta = \frac{2 \times 0.25\pi \times 6^2}{250} \times 672 \times 588.2 \times \cot(30^\circ) \times 10^{-3} = 155 \text{ kN}$$

As a check, the shear resistance of the compression struts $V_{Rm,max}$ must be larger than the resistance of the stirrups. The smaller the angle, the smaller $V_{Rm,max}$, so the minimum angle of 21.8° is checked:

$$\alpha_{cw} = 1 + \frac{\sigma_{cp}}{f_{cm}} = 1 + \frac{2.5}{47} = 1.05 \text{ for } 0 < \sigma_{cp} < 0.25f_{cm}$$

$$v_1 = v = 0.6 \left(1 - \frac{f_{cm}}{250}\right) = 0.6 \left(1 - \frac{47}{250}\right) = 0.49$$

$$V_{Rm,max} = \frac{\alpha_{cw} b_w z v_1 f_{cm}}{\cot(\theta) + \tan(\theta)} = \frac{1.05 \times 250 \times 672 \times 0.49 \times 47}{\cot(21.8^\circ) + \tan(21.8^\circ)} \times 10^{-3} = 1401 \text{ kN}$$

This resistance of the compression struts is much larger, so the resistance of the stirrups is decisive.

7.1.4 Comparisons and conclusions

The measured values for the contributions are summarized in Table 7.1. The sum of the mechanisms is also evaluated.

Table 7.1: Summary of contribution to the shear resistance of the load-bearing mechanisms

Shear load-bearing mechanism	FEM C1.2 (kN)	FEM C1.3 (kN)	EC2 (kN)	RBK1.1 (kN)	$V_{FEM,C1.2}/V_{EC2}$	$V_{FEM,C1.3}/V_{EC2}$	$V_{FEM,C1.2}/V_{RBK1.1}$	$V_{FEM,C1.3}/V_{RBK1.1}$
Concrete, V_c	208	424	299	299	0.70	1.42	0.70	1.42
Stirrups, V_s	300	300	224	155	1.34	1.34	1.94	1.94
Tendons, V_t	35	45	-	-	-	-	-	-
$V_c + V_s$	508	724	-	454	-	-	1.12	1.59
Total capacity, $V_{R,total} = V_c + V_s + V_t$	543	769	299 ³	454	1.82	2.57	1.20	1.69

First, the equilibrium between the acting shear forces and resistances is checked:

- C1.2: $V_{E,total,C1.2} = 707 \text{ kN}$, $V_{R,total,C1.2} = 543 \text{ kN} \rightarrow \Delta = 707 - 543 = 164 \text{ kN}$
- C1.3: $V_{E,total,C1.3} = 849 \text{ kN}$, $V_{R,total,C1.3} = 769 \text{ kN} \rightarrow \Delta = 849 - 769 = 80 \text{ kN}$

It can be seen that the difference between the acting shear forces and resistance is quite small for C1.3, but this difference is much larger for C1.2. This relatively large variance is mostly caused by the rough estimation of the location of the shear crack tip at section A-A. Especially for solution strategy C1.2, where the element size is larger, a rougher crack pattern is predicted. For instance, if the crack tip was estimated at $z = 612.5 \text{ mm}$ (increase x_u of 37.5 mm), the contribution of the compression zone above the crack tip is 271 kN , which is an increase of 63 kN . The contribution of the stirrups barely changes, since all stirrups are still crossed by the critical crack where yielding occurs. The contribution of the vertical component of the tendons also barely changes, since the location where these tendons are crossed by the crack barely changes. Considering the relatively large variance in the contribution of the compression zone, the estimations are found to be sufficient for comparison but are interpreted with caution. The estimation of the correct location of the crack tip is therefore a starting point for further research into the shear contribution of the compression zone in finite element models, as well as possible extra capacity due to load-bearing reserves of tension softening in the crack tip.

For both solution strategies, the results concerning the contribution of concrete compared to EC2 and RBK1.1 are very different, but remarkably on the other side of the spectrum. C1.2 results in a smaller contribution and C1.3 in a larger contribution than calculated with EC2. As stated above, the estimation of the contribution of the compression zone in the finite element models is a very rough prediction with a relatively large variance. Therefore, it is possible that calculation deficiencies result in an imprecise comparison. However, the large difference in contribution tends to presume a significant mesh dependency of the shear contribution of the compression zone, where significant differences occur in the shear stress SZX and the height of the compression zone.

³ According to Eurocode 2 [8], the total shear capacity of the a concrete beam is the largest value of V_c and V_s .

The stirrup contributions estimated by EC2 and RBK1.1 are both significantly smaller than estimated in the finite element models. This is caused by the limited crack angle which was used in the calculations by EC2 ($\theta=21.8^\circ$) and RBK1.1 ($\theta=30^\circ$), where the crack angle in the finite element models is approximately 19° . Therefore, fewer stirrups are activated, resulting in a lower stirrup contribution.

Finally, the total contributions are compared. From this, it can be concluded that the shear resistance calculated with EC2 and RBK1.1 result in a safe estimation. However, the estimation based on EC2 is over-conservative and the RBK1.1 results in much better approximations due to the allowance of the summation of the concrete and stirrup contributions. Also, both methods should be less conservative if the crack angle was not limited, where the use of the actual crack angle or a closer approximation could lead to even better approximations of the shear resistance.

7.2 Validation of the bond-slip relation

To check if the bond-slip acts according to the expectations, a hand calculation is done, where the equilibrium between the bond and axial force in a stirrup is checked. In Figure 7.8, the bond axial stress of a stirrup at a load of 646 kN for solution strategy O2.5 is shown. In Figure 7.8b, the maximum axial stress is approximately 360 N/mm^2 . At this location, the bond stress is equal to zero. The maximum bond stress at the top of the stirrup is 11.64 N/mm^2 . Between these points, the average bond stress is estimated, resulting in an average bond stress of 6.9 N/mm^2 .

The length between these points, which is approximately 73.5 mm, should be equal to the anchorage length. For equilibrium, this length should be:

$$l_b = \frac{\sigma_s}{4 \tau_{b,ave}} = \frac{6 \times 360}{4 \times 6.9} = 78.3 \text{ mm}$$

Since these lengths are roughly equal, where the deviation is caused by rough estimations of the stresses and length, it can be stated that the bond-slip reinforcement works properly.

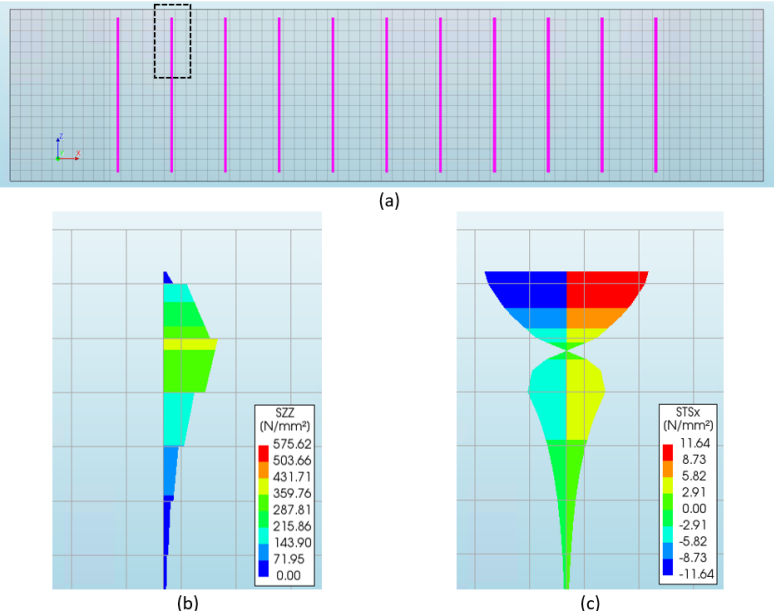


Figure 7.8: Bond-slip evaluation for stirrup 11 at $V=646 \text{ kN}$ for solution strategy O2.5
 (a) Concrete beam with stirrups (dashed rectangle is evaluated part of stirrup 11)
 (b) Stress SZZ in stirrups 1 (c) Bond-slip STSx along stirrup

7.3 The consistent failure mode and overprediction of the secant iteration scheme

The solution strategies based on the secant iteration scheme resulted in very consistent crack patterns. Here, independent of other kinematic assumptions, the same crack propagation was modelled. The region of crack propagation was quite accurate, but the crack widths remained very limited, causing a limited contribution of the stirrups. Eventually, stirrup yielding occurs, but at a too-large shear load. Eventually, failure occurs due to developed horizontal cracks between the crack areas, hindering the arch action between the compression zones.

Another noticeable aspect is that all solution strategies modelled with the secant iteration scheme result in significant overpredictions of the failure load. The reason for this is not entirely clear. Based on these observations, a possible explanation could be the inaccurate and unreliable prediction of the resistance of the compression zone. However, this should be further investigated.

7.4 Investigation of the bond behaviour of open straight-legged stirrups

An explanation is searched for the incorrect development of the failure mechanism in beams with open straight-legged stirrups modelled with a bond-slip relation. For this investigation, an additional solution strategy is performed, called O2.1NR. This strategy is the same as O2.1, except for the full Newton-Raphson scheme instead of the secant iteration scheme. The variations are shown in Table 7.2.

Table 7.2: Solution strategies O2.1NR and O2.5

	Crack orientation	Longitudinal reinforcement modelling	Stirrups modelling	Prestress tendons modelling	Iteration scheme
O2.1 NR	Rotating	Fully bonded	Fully bonded	Unbonded, fully bonded	Newton-Raphson
O2.5	Rotating	Bond-slip	Bond-slip	Weak bond, strong bond	Newton-Raphson

In the figures below, the crack development for solution strategies O2.5 and O2.1NR are shown. It can be seen that crack development for both strategies is quite similar until load level C, which is approximately 550 kN. From this point, solution strategy O2.1NR keeps increasing the crack area. Here, approximately the same crack development is observed as in C1.3. On the other hand, a longitudinal crack along the longitudinal reinforcements develops and widens for O2.5 and the crack orientation becomes almost horizontal. Due to this crack pattern, almost no stirrups are activated. Remarkably, this also occurs on the active side, where the tension zone is enclosed with the closed side of the stirrups. The bond-slip model of the open straight-legged stirrups changes the load-bearing behaviour drastically, causing a completely different crack path.

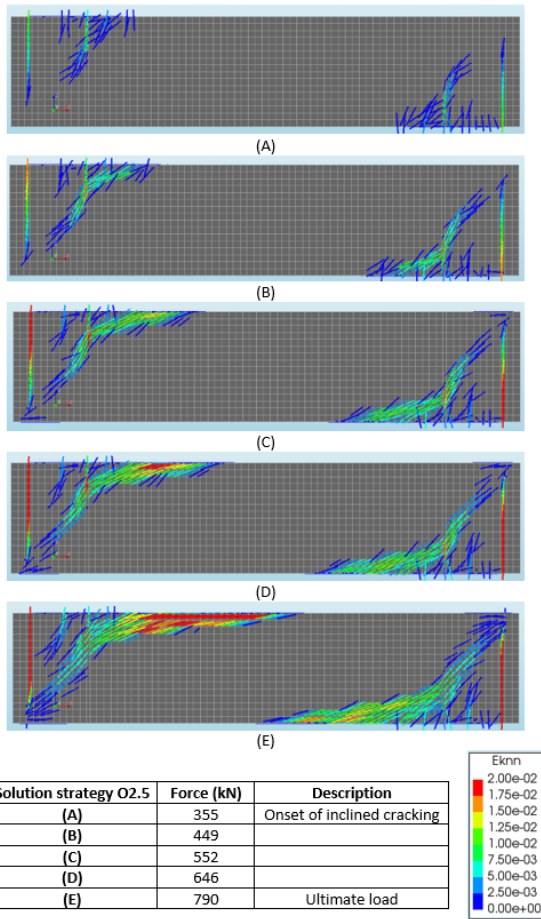


Figure 7.9: Crack strains E_{knn} of O2.5

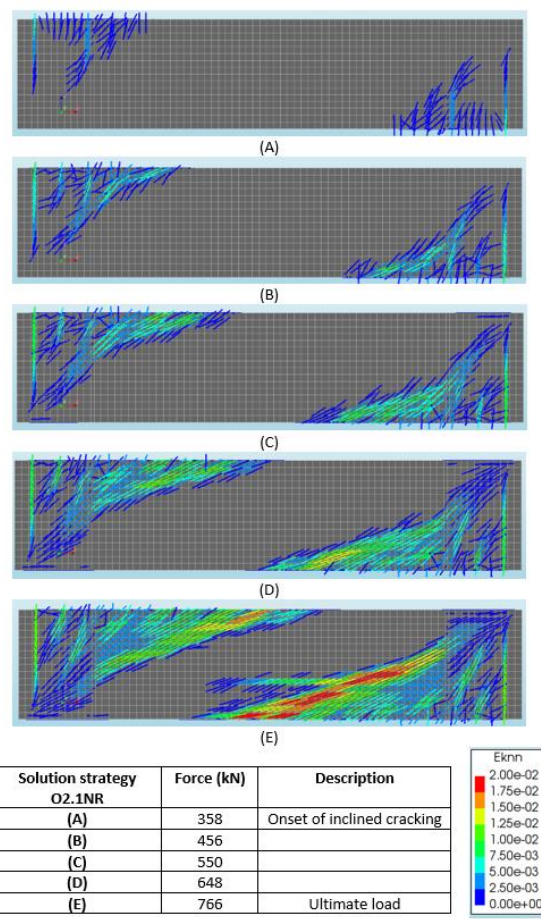
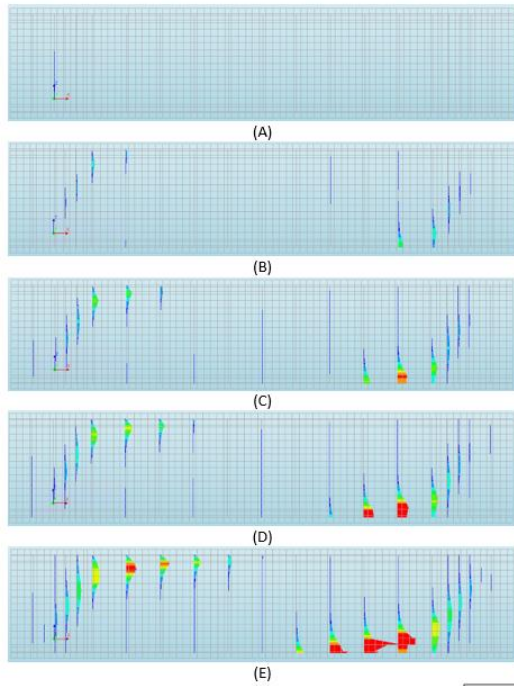


Figure 7.10: Crack strains E_{knn} of O2.1NR

Similar behaviour is observed when comparing the stirrup strains shown in Figure 7.11 and Figure 7.12. As expected, the strains develop where cracks are formed. However, the stirrup strains are already significantly smaller for the slipping bond-slip reinforcements used in solution strategy O2.5 at load level B. This is the consequence of the bond-slip relation, where a certain slip over a certain length is required before the axial force in the stirrup is resisted. The bond stresses are shown in .

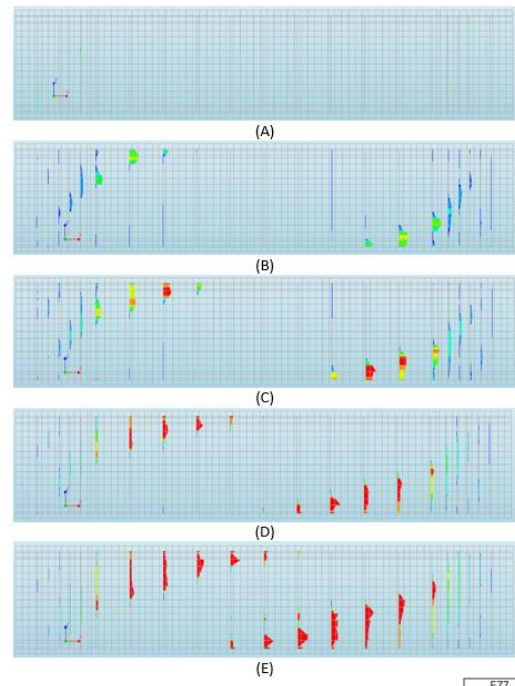
A possible explanation for the incorrect crack development is that due to this slip, larger crack widths can develop. As a consequence, further progression of this inclined crack is possible, where it reaches close to the longitudinal reinforcement. At the top of the beam, the longitudinal reinforcement provides resistance in the x-direction. However, at the top, almost no resistance is provided by the stirrups due to the very short anchorage length. Therefore, the principal stresses can rotate until they are almost horizontal. This causes the cracking along this reinforcement, eventually causing delamination of the concrete cover. This is also happening for fixed crack models, where the uncracked elements close to the longitudinal reinforcement crack horizontally for increasing shear loads. A different bond-slip law would also not help, since all laws require an initial slip for significant traction.

Based on these results, it is concluded beams with bond-slip stirrups are not able to predict the correct failure mode and that fully bonded stirrups are the only solution here to approach a realistic global behaviour of the beam.



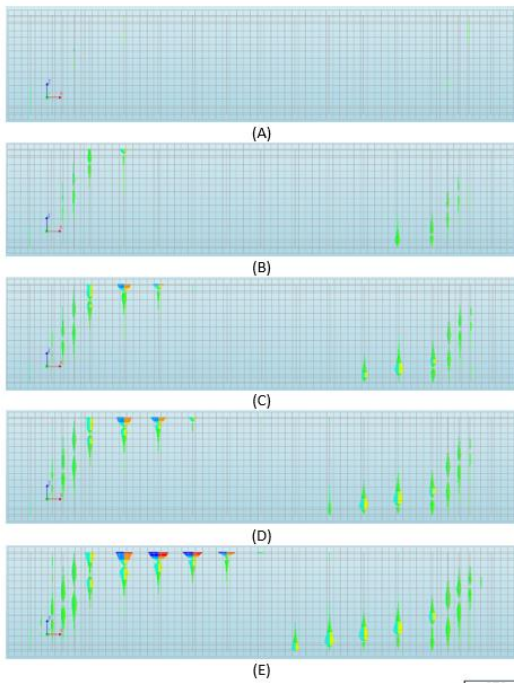
Solution strategy O2.5	Force (kN)	Description
(A)	355	Onset of inclined cracking
(B)	449	
(C)	552	
(D)	646	
(E)	790	Ultimate load

Figure 7.11: Stirrup strains EZZ of O2.5



Solution strategy O2.1NR	Force (kN)	Description
(A)	358	Onset of inclined cracking
(B)	456	
(C)	550	
(D)	648	
(E)	766	Ultimate load

Figure 7.12: Stirrup strains EZZ of O2.1NR



Solution strategy O2.5	Force (kN)	Description
(A)	355	Onset of inclined cracking
(B)	449	
(C)	552	
(D)	646	
(E)	790	Ultimate load

Figure 7.13: Bond stress STSx of O2.5

Rotating-to-fixed crack model

A rotating-to-fixed crack model could solve the problem of overrotation. This option was already considered beforehand but is not used for any models. The reason for this is the complexity of using this crack orientation for practical use. A threshold crack strain must be defined at which a crack is fixed. This is different for every situation and needs to be thoroughly investigated, which is not part of the scope of this thesis.

7.5 Influence of element size

In part 1, the solution strategies varied in element size, which resulted in a significant difference in ultimate shear load for decreasing element sizes. However, the failure modes remain very similar. This problem has a large impact on the reliability of the finite element analysis, so further research is required to find a clear explanation for the mesh dependency. De Putter [19] stated that this influence is especially large for deep beams. Considering this, a possible explanation for the mesh dependency in part 1 could be that the finite element model is not able to accurately describe the capacity of the compression zone. This is also concluded in Section 7.1.

8 Conclusions and recommendations

In this chapter, the conclusions of this thesis are given, where the main question is repeated and answered. Also, recommendations are given for further research.

8.1 Conclusions

In this thesis, a suitable finite element solution strategy is searched that is able to accurately describe the behaviour of open straight-legged stirrups in concrete beams subjected to shear. This has resulted in the following main question: *'How can the **behaviour of open straight-legged stirrups in concrete beams subjected to shear** be explained with a **finite element model**?' To find such a solution strategy, the behaviour of reinforced concrete beams subjected to shear and how this is implemented in finite element models is investigated.*

From the literature study, it is found that the shear load-bearing behaviour in reinforced concrete beams consists of various complex mechanisms dependent on many properties and the load transfer of the other mechanisms. This complex behaviour complicates the assessment of the shear-resisting contributions of the individual mechanisms. However, current engineering standards quantify the shear resistance based on lower bound theorems, where the governing load-bearing mechanisms are the shear resistance of the concrete, including the effects of prestressing, and the axial resistance of the stirrups due to a crossed inclined crack. This shear resistance of the concrete is governed by the resistance of the compression zone since the contributions of aggregate interlocking and dowel action significantly decrease for increasing loads. The contribution of the stirrups can only be accounted for if the stirrups are sufficiently anchored using bends, hooks, welds or sufficient bond with the surrounding concrete. It is found that this bond behaviour is described with a bond-slip relation, which is also possible to model in a nonlinear finite element analysis. Also, stirrups control the crack width, increasing aggregate interlocking.

From the experimental benchmark, it turns out that open straight-legged stirrups can significantly contribute to the shear resistance of a reinforced concrete beam. However, the contribution compared to closed stirrups is significantly smaller due to the worse anchorage of the open ends. Closed stirrups are anchored using bends and are therefore sufficiently anchored over the whole length of the stirrup. The anchorage of the open ends of open straight-legged stirrups is entirely dependent on the bond between the steel and the concrete and therefore requires a sufficient bond strength and anchorage length to resist axial stresses in the stirrup. Otherwise, a local pull-out failure occurs, which reduces the shear resistance of that individual stirrup. The bond strength in the tension zone is smaller due to cracking and inclined cracks occur closer to the open ends of the stirrups, which makes it more likely that a pull-out failure occurs in the cracked tension zone.

For the finite element models, many constitutive, kinematic and equilibrium modelling aspects are based on the recommendations from the RTD1016-1 [3], except for the boundary conditions. Modelling clamped restraints with supports on both sides of the beam result in a too-stiff response. By allowing a little rotational freedom in the form of boundary springs, the stiffness of the beam can be manipulated without changing the overall load-bearing behaviour.

From the finite element results with closed stirrups, it follows that the recommendations from the RTD1016-1 [3] in combination with the boundary springs are able to predict the shear behaviour of beams with closed stirrups. The best results are obtained with a rotating crack model and a full-Newton Raphson iteration scheme, where a realistic crack and stirrup strain development is predicted. However, the ultimate shear load is very mesh dependent, where a larger shear resistance is found for smaller element sizes. It follows that especially the contribution of the compression zone is very susceptible to the mesh size.

From the finite element results with open straight-legged stirrups, it follows that the bond-slip relation between the concrete and the open straight-legged stirrups results in incorrect cracking behaviour, independent of other modelling choices. It is found that the chosen iteration scheme in combination with this kinematic reinforcement modelling determines the failure mode. Models with the full Newton-Raphson iteration scheme can predict the ultimate shear load within a 20% margin, but delamination of the concrete cover is modelled instead of a shear failure, activating very few stirrups. A direct cause for this behaviour is not found, but it is presumed that larger crack widths due to the initial slip of reinforcements cause further development of inclined cracks leading up to the longitudinal reinforcement, where the direction of the crack twists due to almost no resistance of the stirrups. Models with the secant iteration scheme consistently overpredict the ultimate shear load for both beams with closed and open straight-legged stirrups and are consistent in the prediction of the crack propagation, but the crack width development and therefore the stirrup contributions are consistently underestimated.

Within this study, no suitable solution strategy is found that is able to explain the behaviour of open straight-legged stirrups in concrete beams subjected to shear. The anchorage of the open ends is defined with a bond-slip relation, but the inclusion of such relation for open straight-legged stirrups results in incorrect failure modes.

8.2 Recommendations

It was identified that numerical modelling of the anchorage of the open straight-legged stirrup cannot be described with a bond-slip relation. From an engineering point of view, only the ultimate load and the damage evolution are relevant in an ultimate limit state analysis. It is not required to find the local anchorage behaviour of an open end of a stirrup, only if and how much this stirrup contributes to the shear resistance. Therefore, it is recommended to investigate the behaviour of concrete beams modelled with fully bonded open straight-legged stirrups with a reduced length at the open ends. Recommended parts for this investigation are:

- The effect of the reduced length, where this reduced length could be chosen randomly, based on required anchorage lengths calculated in common engineering models or derived from bond-slip models.
- The effect of reducing the open ends of all stirrups or only some of these. The cracking behaviour of a model could change if all stirrups are shortened. For instance, instead of a diagonal crack crossing the stirrups a crack above the open ends could develop where it is not expected.

The stiffness of Schramm's experiments, especially in the linear elastic range, was considerably lower than was found in reference tests due to imperfections in the fitting accuracy and less effective clamping restraints of the substructure technique. Due to limited available research on beams with open straight-legged stirrups, these results were accepted, but further validation of this test setup is recommended. Another alternative is to perform an experimental study on these open straight-legged stirrups with a different test setup.

A possible solution for the overrotation of cracks is a rotating-to-fixed crack model. However, due to the complexity for practical use, this option was not investigated. A better understanding or guidelines for the use of this crack model are required, both for beams with and without shear reinforcement.

The comparison between a rectangular and box-girder beam was based on linear elastic behaviour and only focussed on the stress distribution in the cross-section. To be able to accurately compare the behaviour of rectangular and box-girder beams under different loading conditions, further research into their nonlinear behaviour based on both load distribution and resistance is necessary. Especially, the behaviour of box-girders under restrained warping requires more research.

Also, since the results for the secant iteration scheme were very consistent and the crack development at lower load levels was predicted quite accurately, it can be stated that this iteration scheme could lead to very promising estimations. However, the overpredictions due to this should be investigated and resolved first.

Finally, the mesh dependency, especially for deep beams, provides problems for the reliability of finite element analyses. The reason for this is not entirely clear and further research is required. An investigation into the individual contributions of multiple shear load-bearing mechanisms showed that the contribution of the compression zone is most susceptible to a change in element size. Therefore, it is recommended to focus on this aspect in a mesh dependency study.

9 References

- [1] "DIANA Manuals," 2021. [Online]. Available: <https://manuals.dianafea.com/d105/Diana.html>.
- [2] N. O. Schramm, "Zur Querkrafttragfähigkeit von Spannbeton-balkenelementen unter besonderer Berücksichtigung der Bügelform," München, 2021.
- [3] Max A.N. Hendriks, Marco A. Roosen, "Guidelines for Nonlinear Finite Element Analysis of Concrete Structures," 2019.
- [4] Wagemaker, "Rooyensteinse brug herberekening," Wagemaker, 2020.
- [5] *Bestektekening Rooyensteinse brug B.27254*, Rijkswaterstaat Archive, 1975.
- [6] *Bestektekening Rooyensteinse brug B.28083*, Rijkswaterstaat Archive, 1975.
- [7] M. Nielsen and L. Hoang, *Limit Analysis and concrete Plasticity*, Taylor and Francis Group, 2011.
- [8] NEN, "NEN-EN 1992-1-1+C2 Eurocode 2: Ontwerp en berekening van betonconstructies - Deel 1-1: Algemene regels en regels voor gebouwen," Nederlands Normalisatie Instituut, 2011.
- [9] U. O. Uzodimma, "Comparison of Shear Design Procedures According to EC2 and BS8110-1:1997," 11 July 2017. [Online]. Available: <https://structville.com/2017/07/comparison-of-shear-design-procedures-according-to-ec2-and-bs-8110-11997.html>.
- [10] Rijkswaterstaat, "Richtlijnen Beoordeling Kunstwerken 1.2," 2022.
- [11] J. K. Wight, *Reinforced Concrete: Mechanics and Design*, 7 ed., Pearson, 2016.
- [12] "Quora," 2019. [Online]. Available: <https://www.quora.com/How-does-the-presence-of-a-crack-affect-the-strength-of-a-simply-supported-beam>.
- [13] B. Bogdándy, "The shear resistance of a member without shear reinforcement according to Eurocode 2; the error of the calculated value and the mechanical explanation of the problem," Debrecen, 2021.
- [14] J.-Q. W. Z. J. M. a. T. T. Jia-Nan Qi, "Shear Behavior of Externally Prestressed Concrete Beams with Draped Tendons," *ACI structural journal*, 2020.
- [15] Z. N. Tagieddin, "Elasto-plastic and damage modeling of reinforced concrete," Louisiana, 2008.
- [16] Davor Grandic, Paula Sculac, Ivana Stimac Grandic, "Shear resistance of reinforced concrete beams in dependence on concrete strength in compressive struts," 2015.
- [17] "FIB Bulletin 10. Bond of Reinforcement in Concrete, State-of-art report," International Federation for Structural Concrete, Lausanne, Switzerland, 2000.

- [18] P. Desnerk, J. M. Lees and C. T. Morley, "Bond behaviour of reinforcing bars in cracked concrete," Cambridge, 2015.
- [19] A. D. Putter, "Towards a uniform and optimal approach for safe NLFEA of reinforced concrete beams, Quantification of the accuracy of multiple solution strategies using a large number of samples," Delft, 2020.
- [20] "CIE5148 Lecture 7 - Smearred Cracking," 2019. [Online].
- [21] "What is shear locking?," [Online]. Available: https://femds.com/FEM_Guidelines/Prevent_Shear_Locking#:~:text=Shear%20locking%20is%20an%20error,a%20shear%20stress%20is%20introduced..
- [22] D. Hordijk, "Local approach to fatigue of concrete," 1991.
- [23] Vecchio, F.J., Collins, M.P., "Compression response of cracked reinforced concrete," *Str. Eng., ASCE* 119, 1993.
- [24] Selby, R.G., Vecchio, F.J., "Three-dimensional constitutive relations for reinforced concrete," University of Toronto, Toronto, 1993.
- [25] "Diana User's Manual 6.6.1 Rots' Element Based Method," 2017. [Online]. Available: <https://manuals.dianafea.com/d101/MatLib/node103.html#crack:bw:rots>.
- [26] "Diana User's Manual 6.6.2 Govindjee's Projection Method," 2017. [Online]. Available: <https://manuals.dianafea.com/d101/MatLib/node104.html#crack:bw:govind>.
- [27] fib, "fib Model Code for Concrete Structures 2010 Final draft," *fédération internationale du béton/International Federation for Structural Concrete*, 2012.
- [28] H. Shima, L.-L. Chou and H. Okamura, "Micro and macro models for bond in reinforced concrete," Tokyo, 1987.
- [29] Morelli, F., Amico, C., Salvatore, W., Squeglia, N., & Stacul, S., "Influence of Tension Stiffening on the Flexural Stiffness of Reinforced Concrete Circular Sections," *Materials*, Basel, Switzerland, 2017.
- [30] K. Dörr, "Ein Beitrag zur Berechnung von Stahlbetonscheiben unter besonderer Berücksichtigung des Verbundverhaltens," Darmstadt, 1980.
- [31] P. Evangeliou, "Probabilistic nonlinear finite element analysis of reinforced concrete beams without shear reinforcement," Delft, 2016.
- [32] C. Hartsuijker, J.W. Welleman, *Engineering Mechanics Volume 2: Stresses, Strains, Displacements*, Springer, 2007.
- [33] "CTB3335 Concrete Structures 2, Reader Torsion," 2020.
- [34] W. Peter, "The significance of warping torsion in the design of straight concrete box-girder bridges.," *Canadian Journal of Civil Engineering*, 2011.

- [35] StructurePoint, "FINITE ELEMENT ASPECT RATIO INFLUENCE IN CONCRETE FOUNDATION MODELS," StructurePoint, 2017.
- [36] T. T. Teshome, "Model uncertainty of non-linear finite element analysis of reinforced concrete beams without shear reinforcement," 2019.
- [37] Engen, M., Hendriks, M. A. N., Monti, G., & Allaix, D. L., "Treatment of modelling uncertainty of," *Structural Concrete*, 22(6), 3202-3212, 2021.
- [38] Rijkswaterstaat, "Richtlijnen Beoordeling Kunstwerken 1.1," 2013.
- [39] "faq tangent normal stiffness," [Online]. Available: <https://dianafea.com/faq-tangent-normal-stiffness>.
- [40] Rijkswaterstaat, "Wegen - Wegbeheer - Bruggen," [Online]. Available: <https://www.rijkswaterstaat.nl/wegen/wegbeheer/bruggen>. [Accessed 3 March 2022].
- [41] V.P. Barros, A.T. Beck, T.N. Bittencout, "Shear failure in reinforced concrete members without," IBRACON, 2020.
- [42] H. v. d. Ham, "CTB2220 B5 2019-2020 Dwarskracht 1," 2019.

Appendix A Schramm's experiments [2]: properties and results

Appendix A.1 includes an overview of the geometrical and material properties of Schramm's test beams R2, R4 and R10 [2]. Appendix A.2 shows all relevant figures used for the comparison with the finite element models. This includes the original force-displacement diagrams, crack plots at different load levels and strain in stirrups plots at different load levels. All information provided here directly follows from Schramm [2].

A.1 Geometrical and material properties

Table A.1: Geometrical properties of the concrete beam

Length	L	3500	mm
Length test area	L _{test}	2600	mm
Length support areas	L _{sup}	900	mm
Height	h	800	mm
Width test area	b	250	mm
Width at supports	b _{sup}	500	mm
Concrete cover (w.r.t. closed stirrups)	c	20	mm

Table A.2: Material properties of the test beams

		Test beam R2	Test beam R4	
<u>Concrete (target strength C30/37)</u>				
Mean Young's modulus	E _{cm}	33700	33130	N/mm ²
Mean cylindrical compressive strength	f _{cm,cyl}	47.0	37.6	N/mm ²
Mean cylindrical tensile strength	f _{ctm,cyl}	3.8	3.3	N/mm ²
<u>Longitudinal reinforcement</u>				
Diameter	∅ _{long}	25	25	mm
Young's modulus	E _{sm,long}	186700	186300	N/mm ²
Yield strength	f _{ym,long}	526.3	526.3	N/mm ²
Ultimate strength	f _{tm,long}	637.0	637.0	N/mm ²
<u>Stirrups</u>				
Diameter	∅ _{stirrup}	6	6	mm
Spacing	s	250	250	mm
Young's modulus	E _{sm,stirrup}	187900	186300	N/mm ²
Yield strength	f _{ym,stirrup}	588.2	583.5	N/mm ²
Ultimate strength	f _{tm,stirrup}	680.2	697.0	N/mm ²
<u>Stirrups ends of the beam</u>				
Diameter	∅ _{stirrupend}	12	12	mm
Spacing	s _{end}	80	80	mm
Young's modulus	E _{sm,stirrupend}	185200	181600	N/mm ²
Yield strength	f _{ym,stirrupend}	528.2	531.8	N/mm ²
Ultimate strength	f _{tm,stirrupend}	621.0	619.9	N/mm ²

Prestress tendons

Prestress on cross-section	σ_{pm}	2.5	2.5	N/mm ²
Prestress tendon area	A_{pm}	3x140	3x140	mm ²
Prestress force per tendon	P	250	250	kN
Young's modulus	E_{pm}	198100	198100	N/mm ²
0.1% fractile	$f_{pm0.1}$	1648	1648	N/mm ²
Ultimate strength	f_{pm}	1881	1881	N/mm ²

A.2 Results

The dashed lines in the force-displacement diagrams represent the initial elastic stage of a reference test.

A.2.1 Results R2 (closed stirrups)

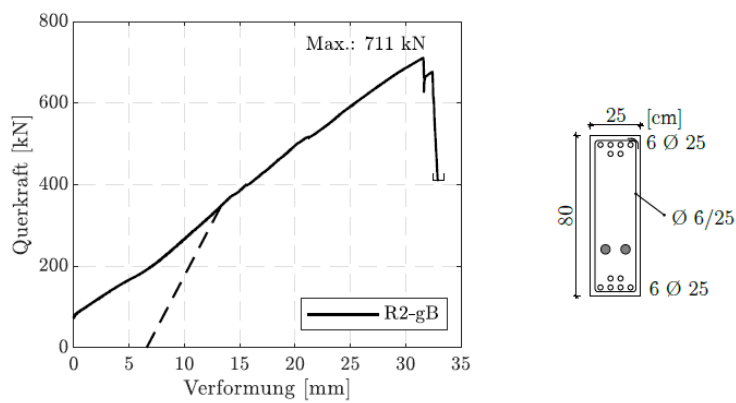


Figure A.1: Force-displacement diagram of test beam R2 [2]

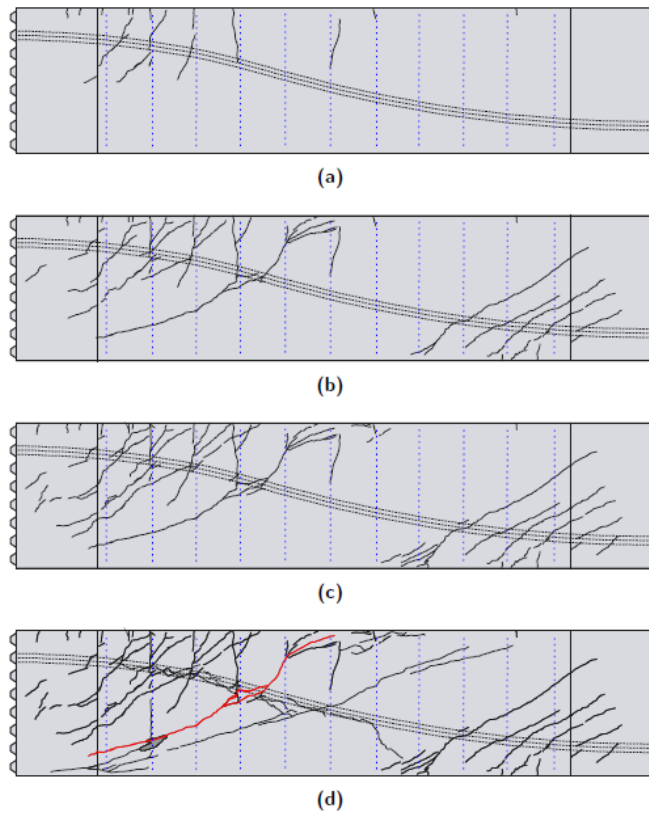


Abbildung A.5: Rissbilder, Versuch R2-gB

- (a) Rissbild für Laststufe 50 % · $V_{\max} = 356 \text{ kN}$
- (b) Rissbild für Laststufe 75 % · $V_{\max} = 533 \text{ kN}$
- (c) Rissbild für Laststufe 91 % · $V_{\max} = 647 \text{ kN}$
- (d) Rissbild nach Bruch

Figure A.2: Crack plots at different load levels of test beam R2 [2]

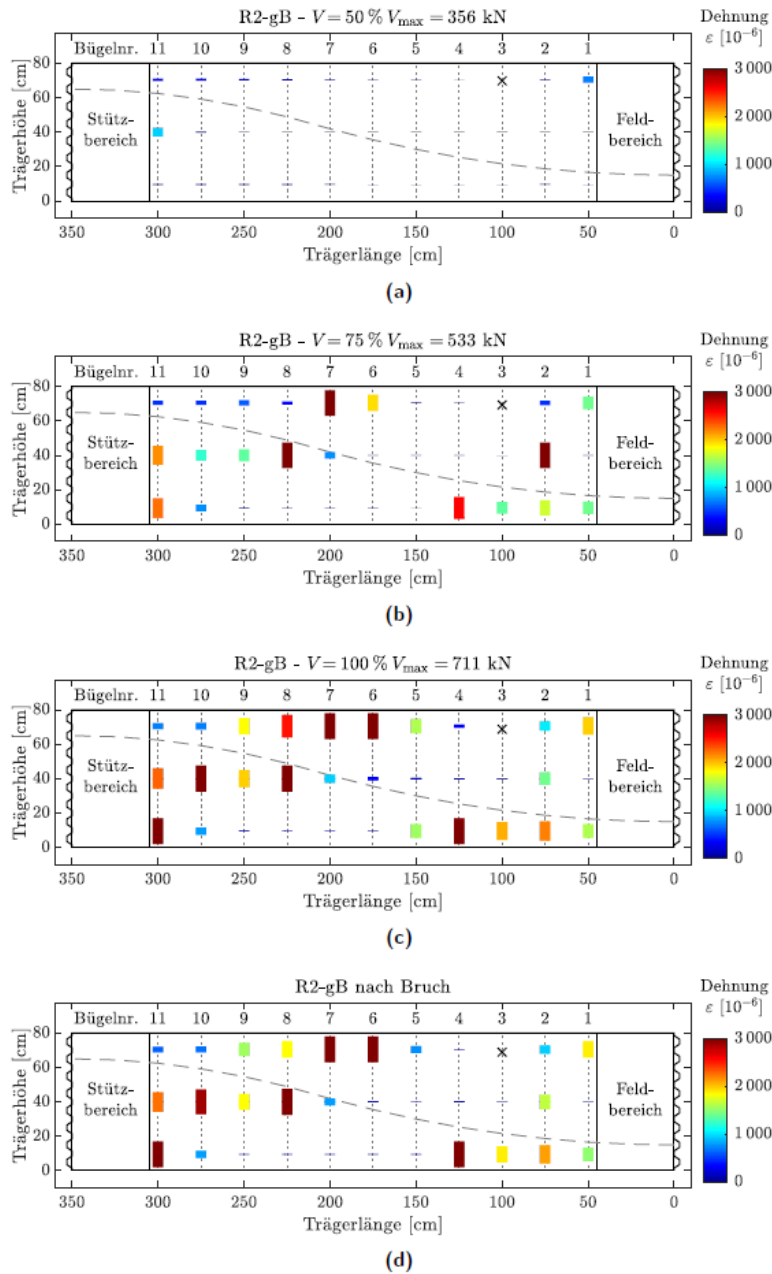


Abbildung A.6: Ergebnisse der Dehnungsmessungen an der Bügelbewehrung (Versuch R2-gB) mit DMS; DMS-Anordnung mittig sowie mit jeweils 7 cm Abstand vom Bauteilrand.

- (a) Dehnungen für Laststufe $50\% \cdot V_{\max} = 356 \text{ kN}$
- (b) Dehnungen für Laststufe $75\% \cdot V_{\max} = 533 \text{ kN}$
- (c) Dehnungen für Laststufe $100\% \cdot V_{\max} = 711 \text{ kN}$
- (d) Dehnungen nach Bruch

Figure A.3: Strain in stirrups plots at different load levels of test beam R2 [2]

A.2.2 Results R4 (open straight-legged stirrups)

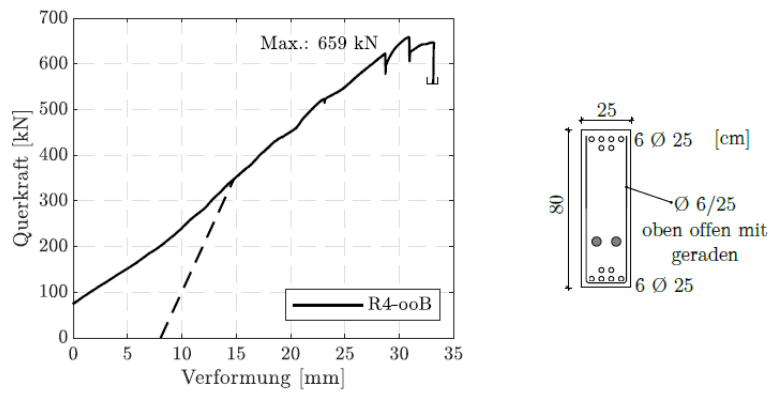


Figure A.4: Force-displacement diagram of test beam R4 [2]

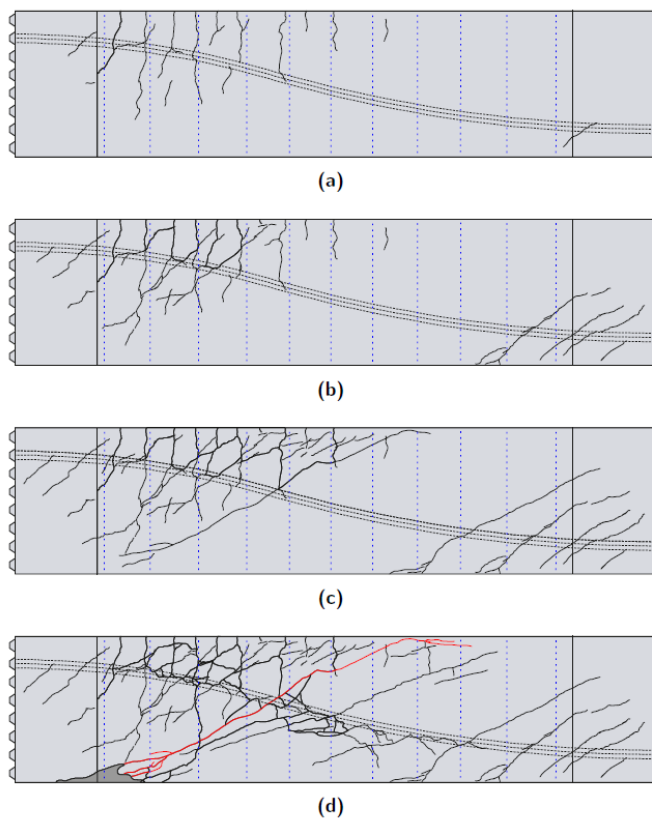


Abbildung A.13: Rissbilder, Versuch R4-ooB
 (a) Laststufe 50 % · $V_{\max} = 330 \text{ kN}$
 (b) Laststufe 75 % · $V_{\max} = 494 \text{ kN}$
 (c) Laststufe 94 % · $V_{\max} = 619 \text{ kN}$
 (d) Rissbild nach Bruch

Figure A.5: Crack plots at different load levels of test beam R4 [2]

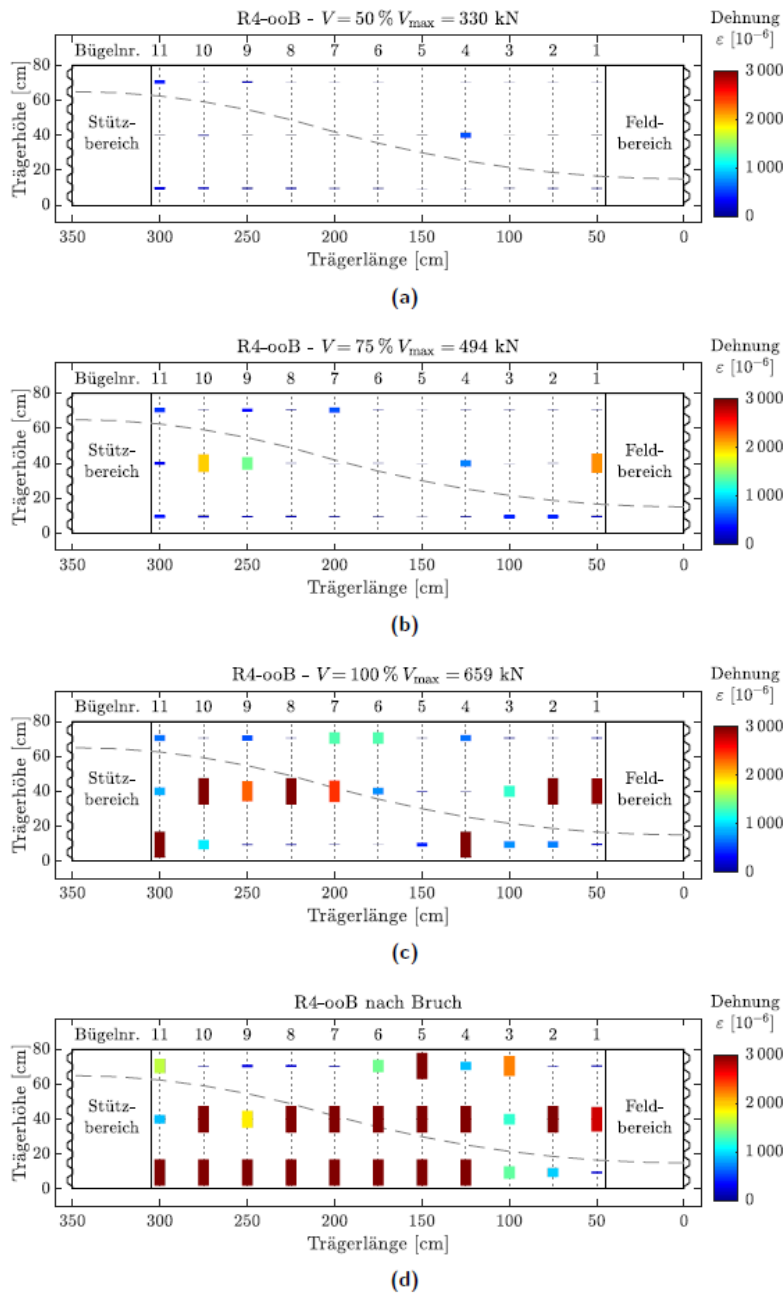


Abbildung A.14: Ergebnisse der Dehnungsmessungen an der Bügelbewehrung (Versuch R4-ooB) mit DMS; DMS-Anordnung mittig sowie mit jeweils 7 cm Abstand vom Bauteilrand.
 (a) Dehnungen für Laststufe $50\% \cdot V_{\max} = 330 \text{ kN}$
 (b) Dehnungen für Laststufe $75\% \cdot V_{\max} = 494 \text{ kN}$
 (c) Dehnungen für Laststufe $100\% \cdot V_{\max} = 659 \text{ kN}$
 (d) Dehnungen nach Bruch

Figure A.6: Strain in stirrups plots at different load levels of test beam R4 [2]

A.2.3 Results R10 (no stirrups)

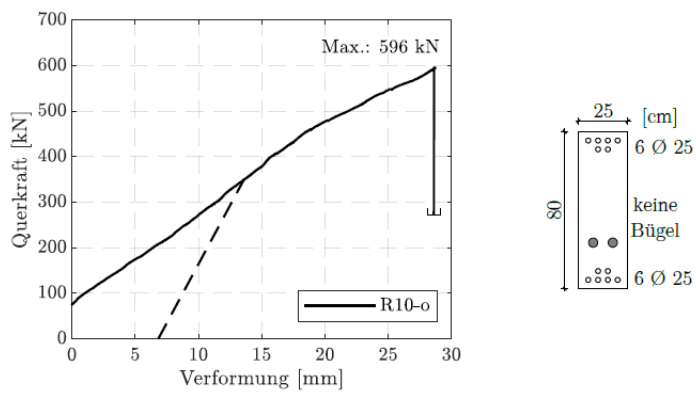


Figure A.7: Force-displacement diagram of test beam R10 [2]

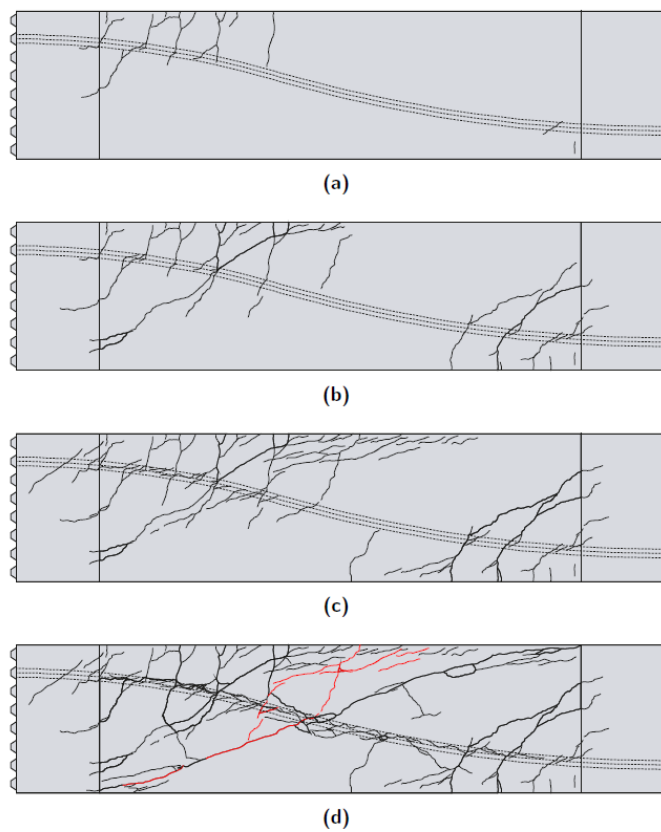


Abbildung A.37: Rissbilder, Versuch R10-o
 (a) Laststufe 50% · $V_{\max} = 295 \text{ kN}$
 (b) Laststufe 75% · $V_{\max} = 447 \text{ kN}$
 (c) Laststufe 99% · $V_{\max} = 590 \text{ kN}$
 (d) Rissbild nach Bruch

Figure A.8: Crack plots at different load levels of test beam R10 [2]

Appendix B Verification of the finite element model

In this appendix, multiple assumptions concerning the finite element model are validated. The topics discussed here are the boundary conditions, the stiffness of the steel plates and the interface between the steel plates and the concrete beam.

B.1 Boundary conditions: boundary springs vs. supports

To show that beams with supports result in a too-stiff response, models C1.1 and C1.2 are also modelled with the tops and bottoms of the plates restrained in the x-direction (instead of the boundary springs). These models are called C1.1sup and C1.2sup.

Figure B.1 shows the force-displacement curve of the models with boundary springs and supports. As expected, the models with supports behave much stiffer than the models with boundary springs. However, when comparing the models with the same element size, the ultimate failure load is approximately the same. The load-bearing mechanisms are also very much the same. Some proof for this is shown with strain plots at 75% at the ultimate load in Figure B.2 and Figure B.3.

The boundary springs seem to give sufficient flexibility to predict a more accurate approximation of the stiffness of Schramm's test beams [2], but also preserve the same failure load and mechanism. As a final check, the displacement in the x-direction for C1.2 is shown in Figure B.4. The maximum displacement at the top and bottom springs is indeed around 2 mm.

Based on this comparison, it can be stated that, in the case of an RC beam clamped on both sides, complete restraining in longitudinal direction results in a too-stiff response. By allowing a little rotational freedom in the form of boundary springs, the stiffness of the beam can be manipulated without changing the overall load-bearing behaviour. As a basic principle, a maximum longitudinal displacement of approximately 1-2 mm at the top and bottom springs can be assumed. Based on this, the required spring stiffnesses of the boundary springs can be iteratively determined.

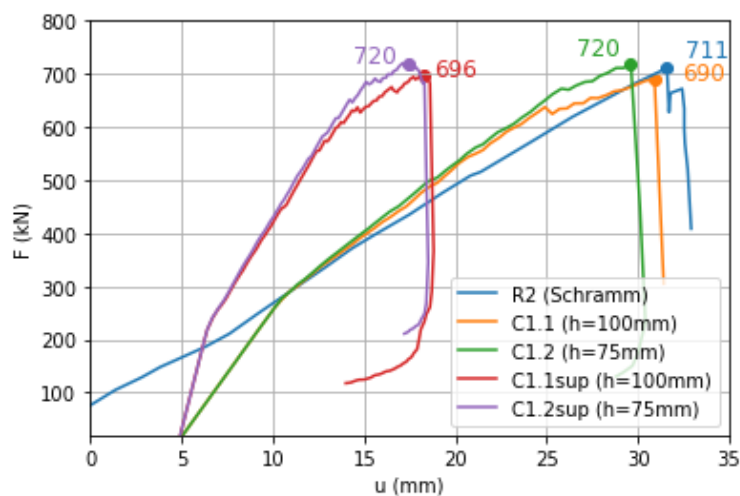


Figure B.1: Force-displacement curve boundary springs vs. supports

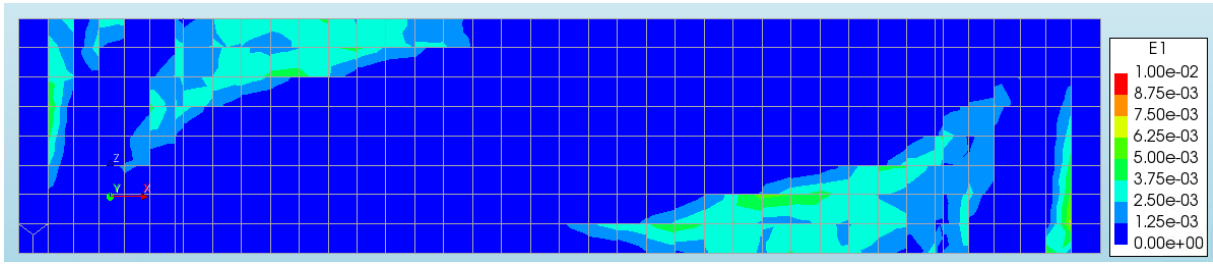


Figure B.2: Principal strain E1 at 75% F_{ult} of solution strategy C1.1

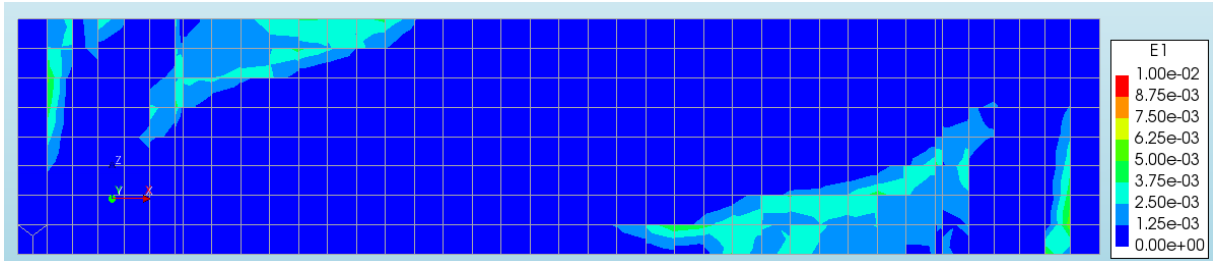


Figure B.3: Principal strain E1 at 75% F_{ult} of solution strategy C1.1sup

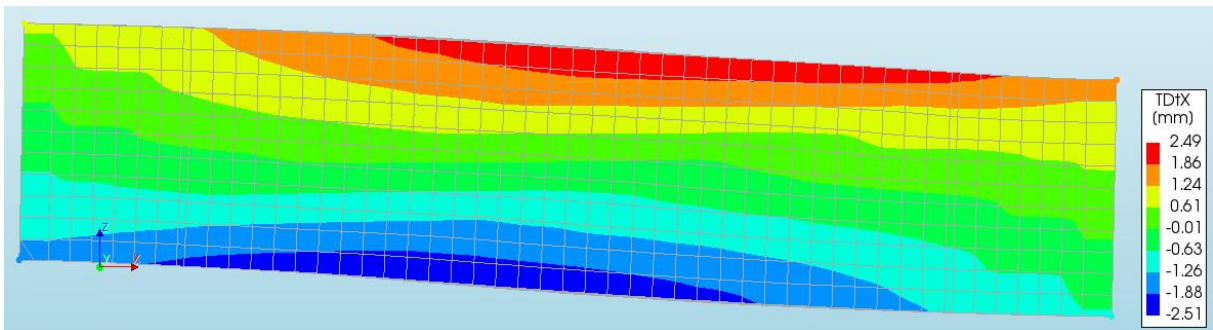


Figure B.4: Displacement TDtX at F_{ult} of solution strategy C1.2

B.2 Stiffness of the steel plates

Since the boundary conditions for the finite elements are modelled with boundary springs, small displacements are allowed at the edges. This allows the plate to deform more as well, which influences the stresses and strains transferred to the concrete beam. Here, two situations are investigated: solution strategy C1.1 with the original stiff plate with a Young's modulus of 1×10^8 N/mm² and solution strategy C1.1Emod with a realistic steel plate with a Young's modulus of 200.000 N/mm².

In Figure B.5, it can be seen that the ultimate shear strength and maximum displacement are approximately the same. However, the stiffnesses are different, especially at lower load levels. For C1.1Emod, it is difficult to determine the transition between the initial elastic stage and the cracking stage due to the smooth change in stiffness, where a 'kink' in the force-displacement curve is observed for C1.1.

At the very first load increment, the stresses close to the plates in the concrete beam for C1.1Emod are already equal to the tensile strength of the concrete (see Figure B.7). This means that the concrete cracks already at this load increment, which explains why there is no 'kink' in the force-displacement curve. The strains in the realistic plate are larger due to the interaction with the boundary springs, which also leads to larger strains in the concrete. This causes the early onset of cracking.

This is not observed for solution strategy C1.1 (see Figure B.6). The stiff plate behaves rigidly, causing smaller strains along the plate, resulting in the onset of cracking at a much higher load.

The influence of the plate modelling becomes less at a higher loading stage, where the stiffness and behaviour are almost entirely determined by concrete cracking and reinforcement interaction. The stiffnesses of C1.1 and C1.1Emod observed in Figure B.5 are as good as the same at displacements larger than 15 mm. Also, the failure mode of C1.1Emod (see Figure B.8) is the same as C1.1.

It can be therefore concluded that the stiffness of the plate is not very significant at higher loading levels and therefore both options suffice for this thesis. However, the stiff plate can describe the elastic behaviour of the concrete, which is more realistic according to the literature study. Therefore, it is preferred to use a stiff plate as used in solution strategy C1.1.

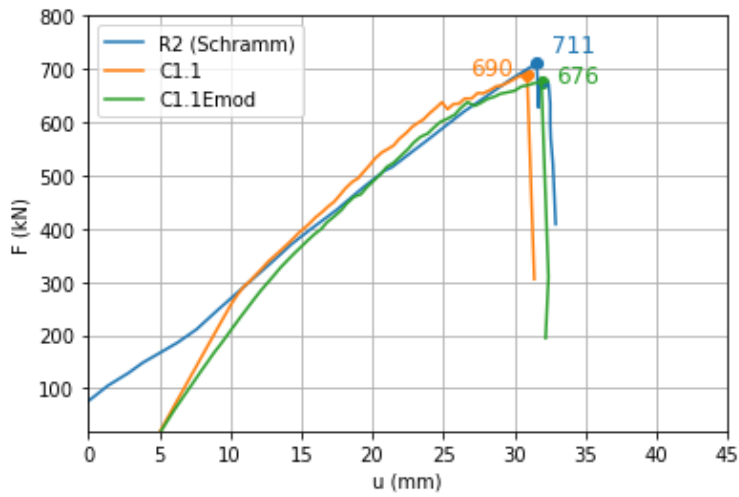


Figure B.5: Force-displacement curve stiffness of the steel plates

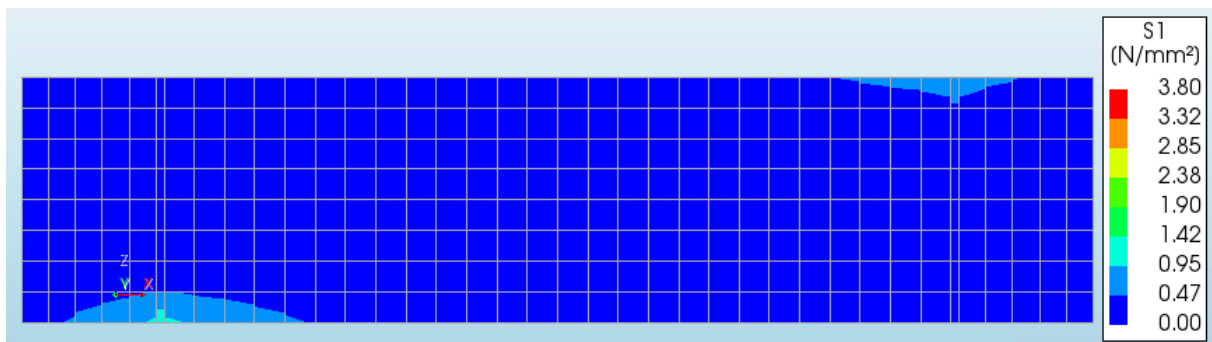


Figure B.6: Principal stresses S_1 at the first load increment ($V=40$ kN) for solution strategy C1.1

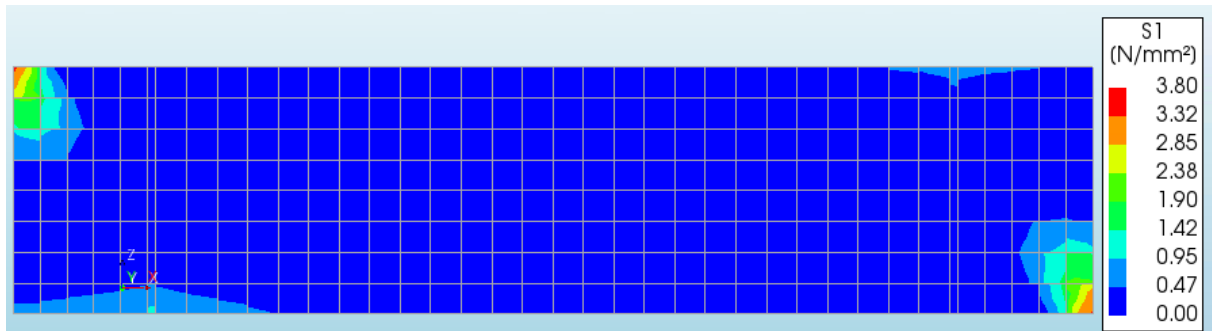


Figure B.7: Principal stresses S_1 at the first load increment ($V=40$ kN) for solution strategy C1.1Emod

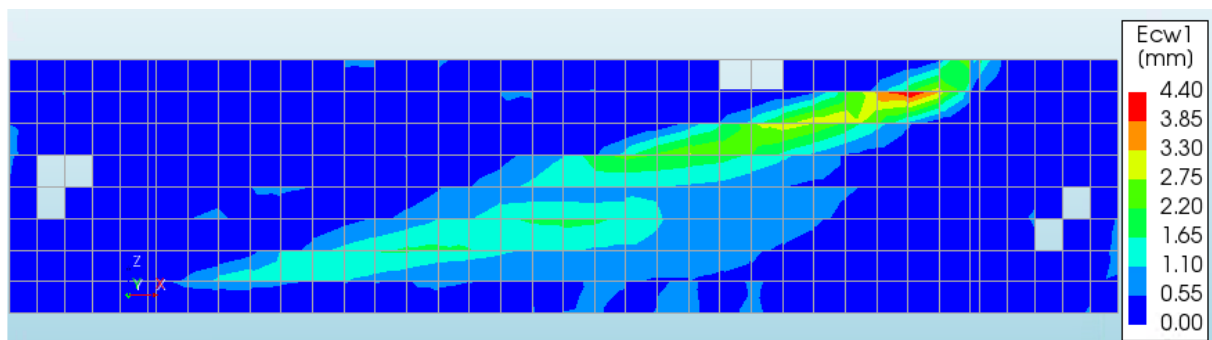


Figure B.8: Crack width at ultimate loading for solution strategy C1.1Emod

B.3 The interface between steel plates and concrete beam

To validate the assumption that it is not necessary to use interface elements between the steel plates and the concrete beam, solution strategy C1.1 is modelled with interface elements. Two variants are made varying in the assumptions around the nonlinear behaviour of the interface elements. The parameters of the variants are shown in Table B.1: Interface parameters of the two variants.

For the linear elastic stiffness moduli, the following rule of thumb is used [39]:

$$K_n = 100 \frac{E_c}{h} \quad (B.1)$$

$$K_t = \frac{K_n}{10} \quad (B.2)$$

According to the experimental setup of Schramm's tests [2], the interface between the steel plates and concrete beam should have a large shear stiffness due to the ribbed faces of the plates and beams. This is necessary to transfer the vertical forces between the plates and the beam since the beam is clamped. Since concrete has a very small tensile strength, the normal stiffness in tension should be very small. When no interface is defined, a crack along the plate develops, causing this decrease in stiffness. However, this is also able to model with interface elements.

Considering these properties, this nonlinear behaviour is modelled with tension and shear reduction models. A critical interface opening is defined at which the stiffness is reduced. With this, a relatively large opening is defined for the shear stiffness reduction. This means that the shear stiffness is not reduced in the tension zone until a large opening is formed. The influence on the behaviour of the beam of the critical tension opening is investigated, so two different values are defined here. When the critical tension opening is reached, the normal stiffness is reduced to zero.

Table B.1: Interface parameters of the two variants

	K_n (N/mm ³)	K_t (N/mm ³)	Critical tension opening (mm)	Tension stiffness reduction factor	Critical shear opening (mm)	Shear stiffness reduction factor
C1.1int1	33777	3377.7	0.01	0	0.1	0
C1.1int2	33777	3377.7	0.001	0	0.1	0

Figure B.9 shows the force-displacement curves for the different solution strategies. It can be seen that the loading paths for C1.1, C1.1int1 and C1.1int2 are very similar. The opening between the plates and beam is resisted by the longitudinal reinforcement and prestressing tendons. It results in the same effect of a crack along the plate, namely a decrease in the transfer of forces in the tension zone. The similarity in results is also shown in Figure B.10, Figure B.11 and Figure B.12, where the principal strains at 75% of the ultimate load are shown.

From these results, it can be concluded that it is unnecessary to define an interface between the steel plates and the concrete beam. Solution strategies without interface elements are able to sufficiently estimate the load transfer between the plates and beam by developing a crack along the plate in the tension zone, where the capacity of the small tension strength of the concrete before cracking is negligible compared to the 'immediate' opening of the interface.

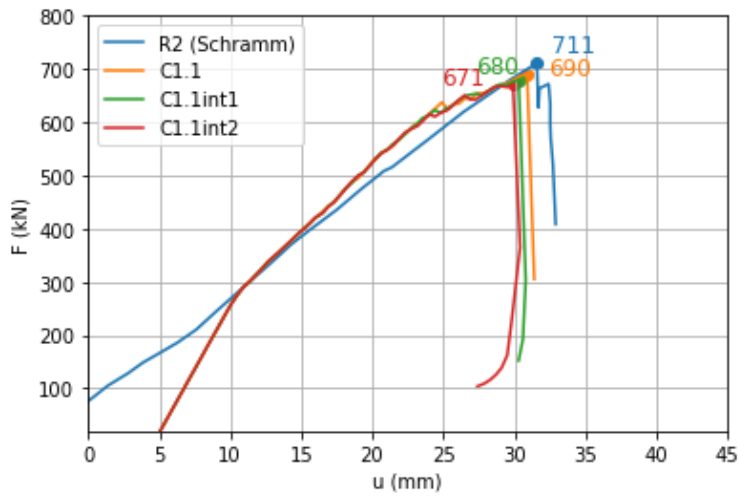


Figure B.9: Force-displacement curve interface elements

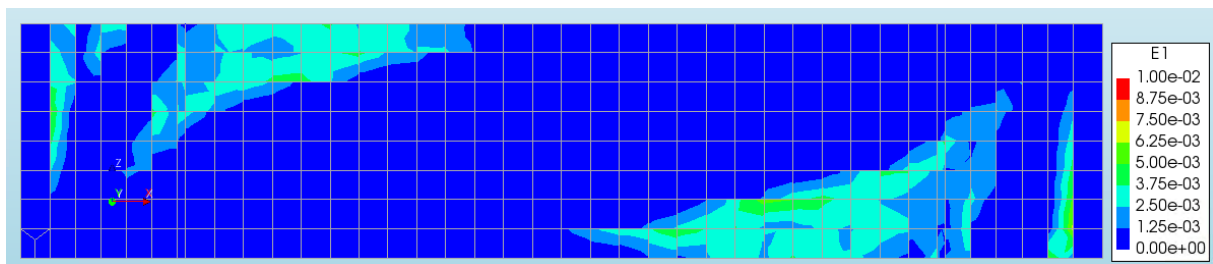


Figure B.10: Principal strain E1 at 75% F_{ult} of solution strategy C1.1

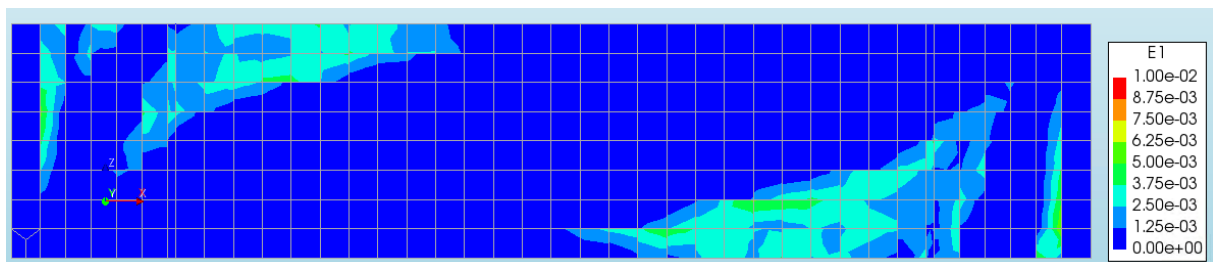


Figure B.11: Principal strain E1 at 75% F_{ult} of solution strategy C1.1.int1

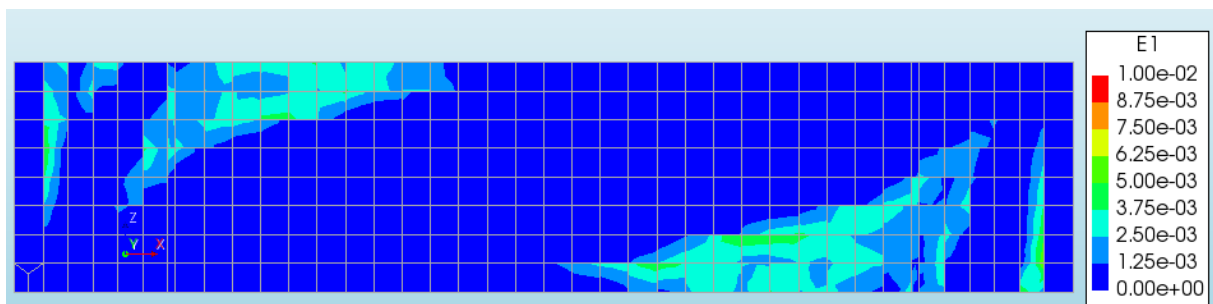


Figure B.12: : Principal strain E1 at 75% F_{ult} of solution strategy C1.1.int2

Appendix C Convergence plots

C.1 Group 1

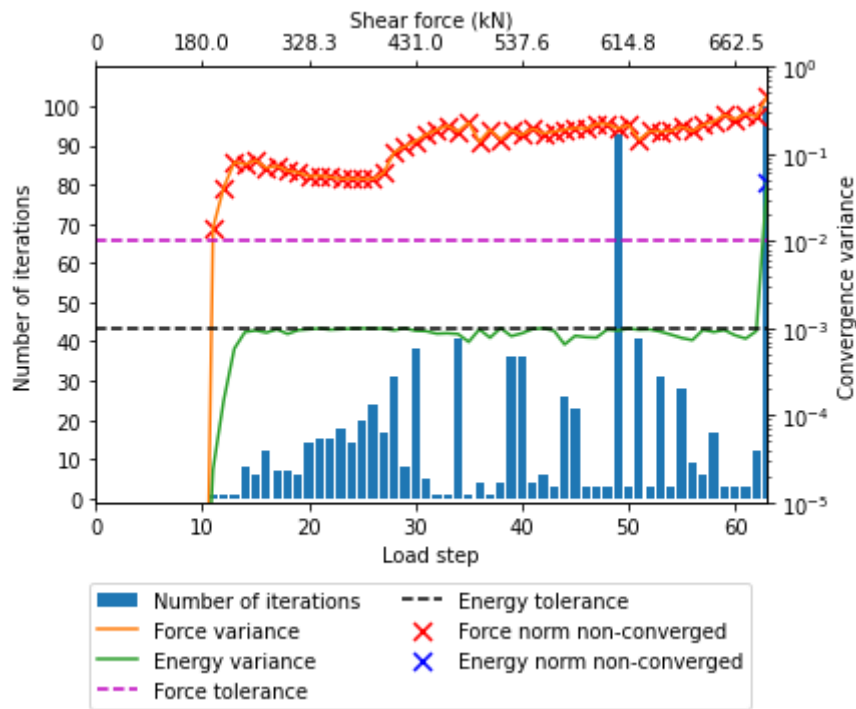


Figure C.1: Convergence behaviour solution strategy C1.1

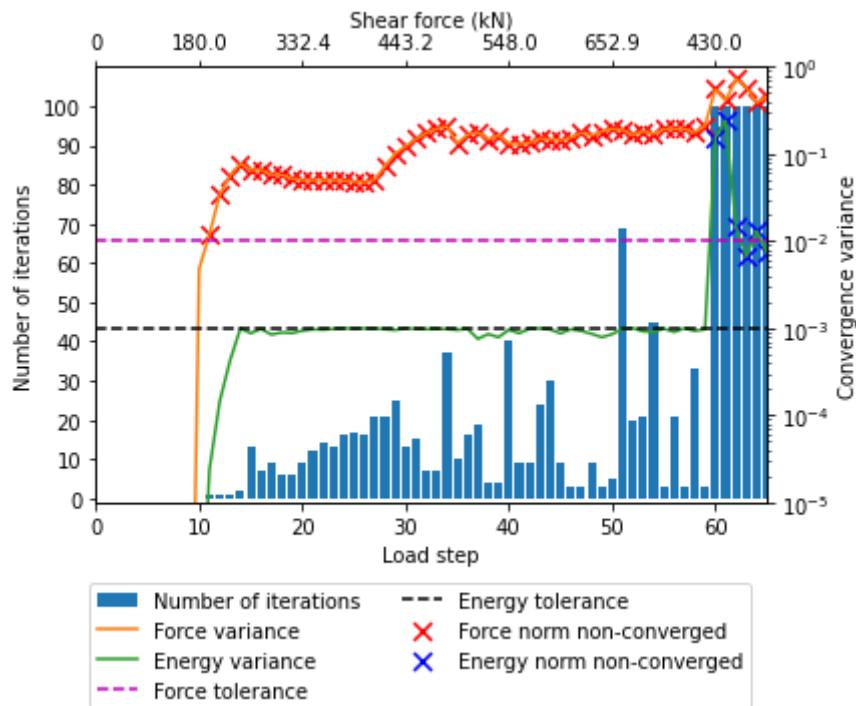


Figure C.2: Convergence behaviour solution strategy C1.2

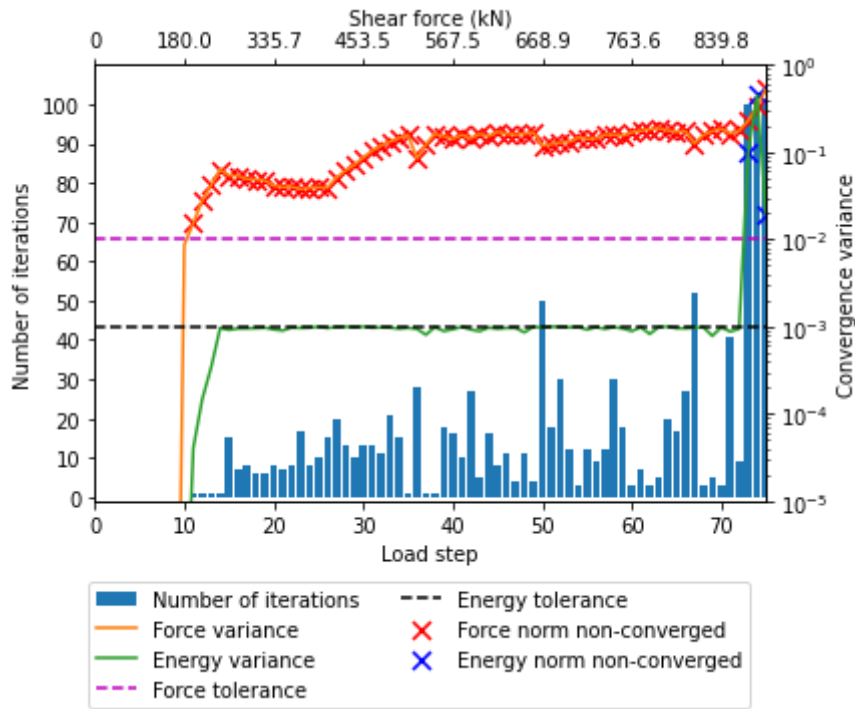


Figure C.3: Convergence behaviour solution strategy C1.3

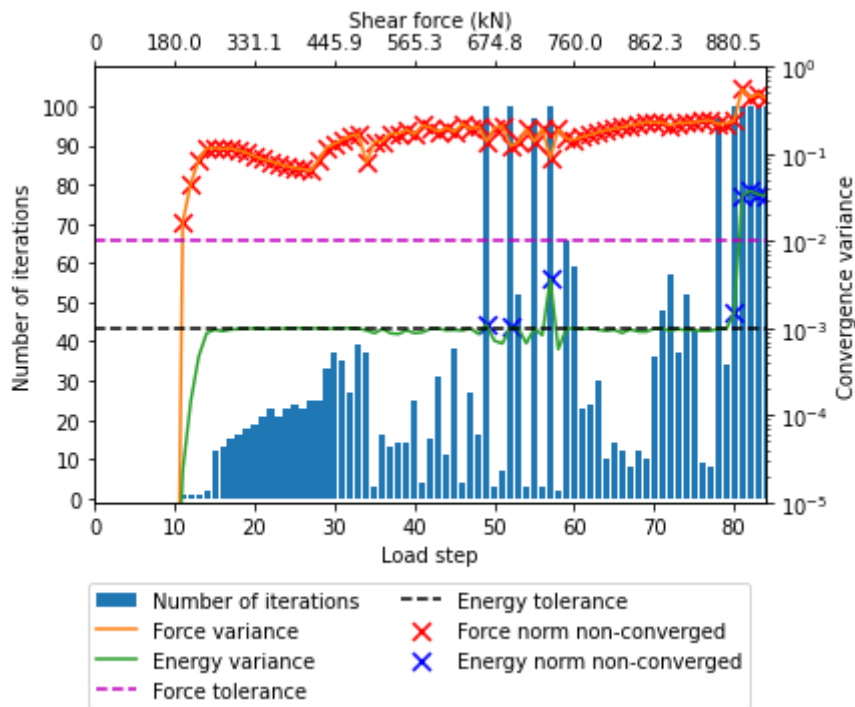


Figure C.4: Convergence behaviour solution strategy C1.4

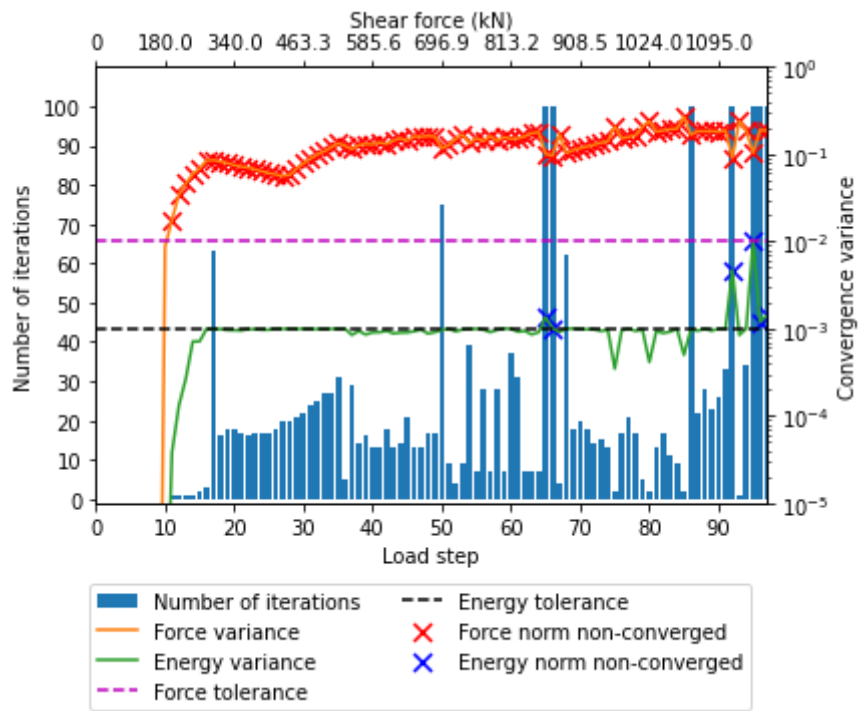


Figure C.5: Convergence behaviour solution strategy C1.5

C.2 Group 2

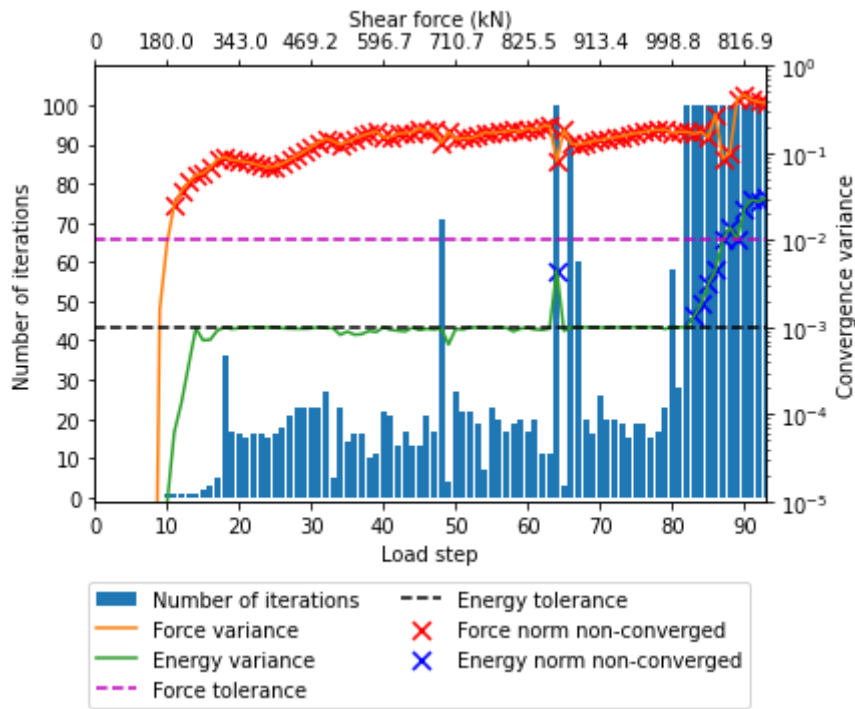


Figure C.6: Convergence behaviour solution strategy O2.1

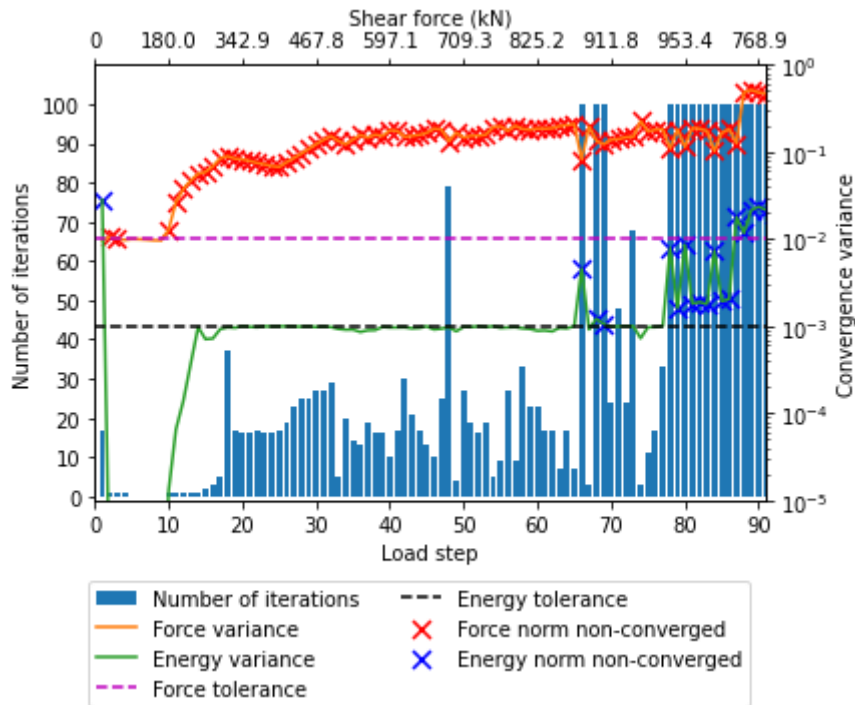


Figure C.7: Convergence behaviour solution strategy O2.2

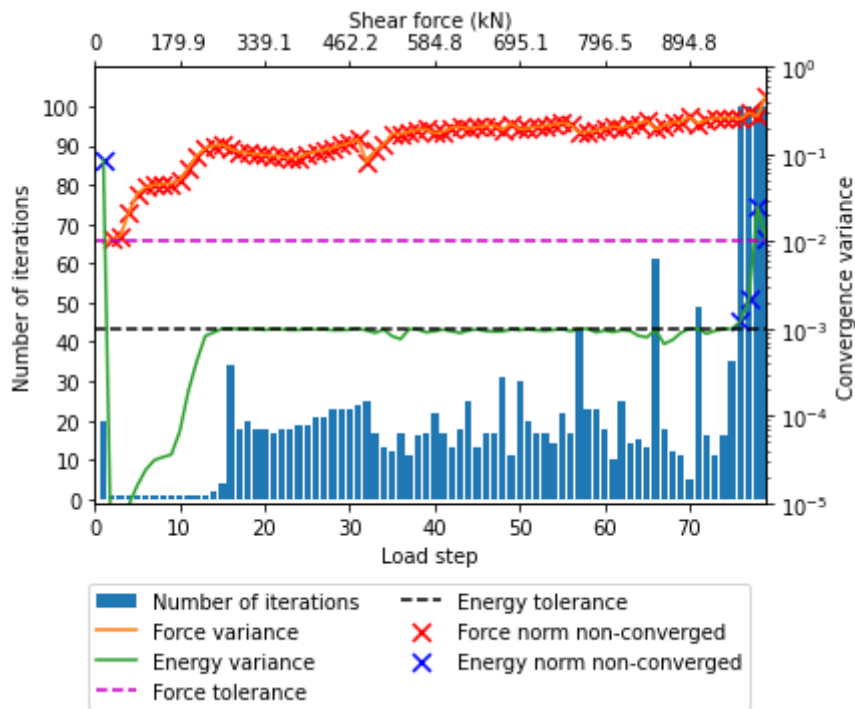


Figure C.8: Convergence behaviour solution strategy O2.3

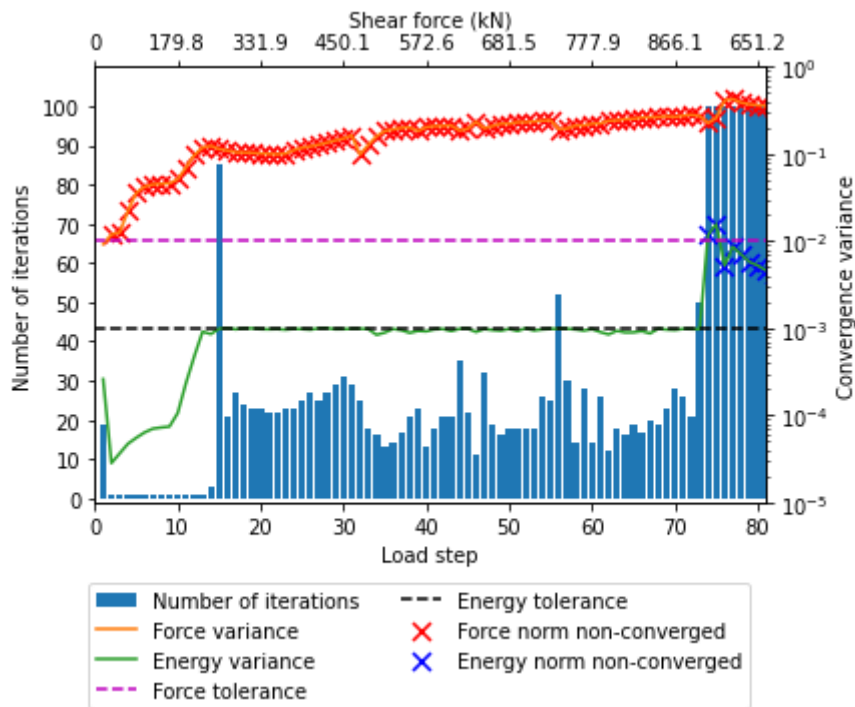


Figure C.9: Convergence behaviour solution strategy O2.4

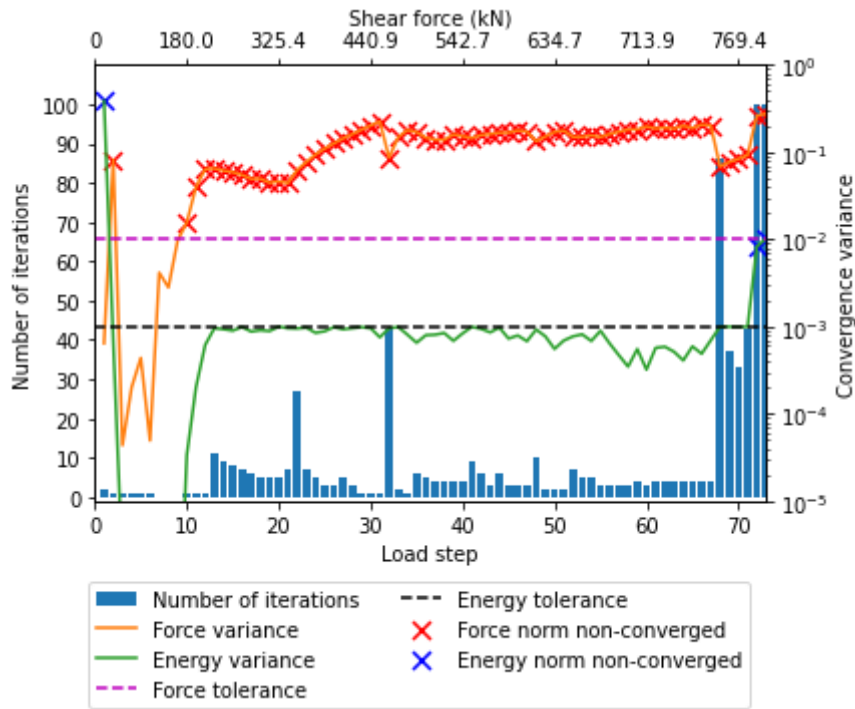


Figure C.10: Convergence behaviour solution strategy O2.5

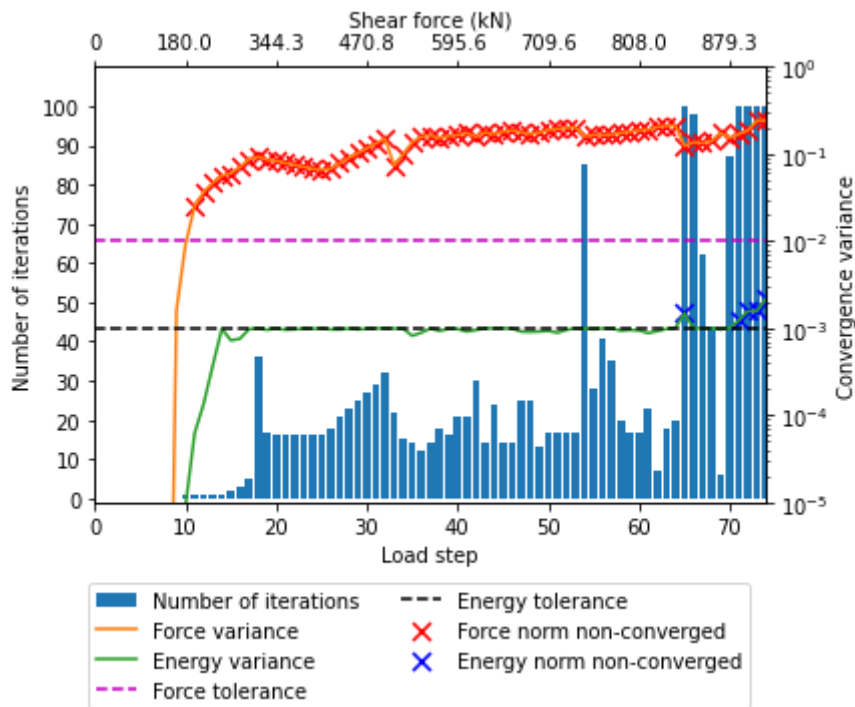


Figure C.11: Convergence behaviour solution strategy O2.6

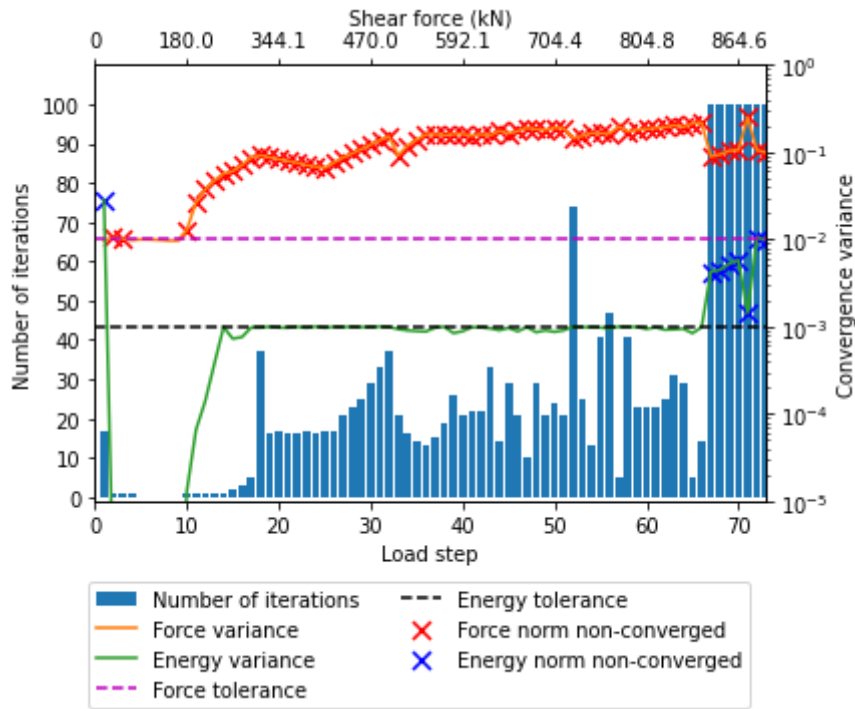


Figure C.12: Convergence behaviour solution strategy O2.7

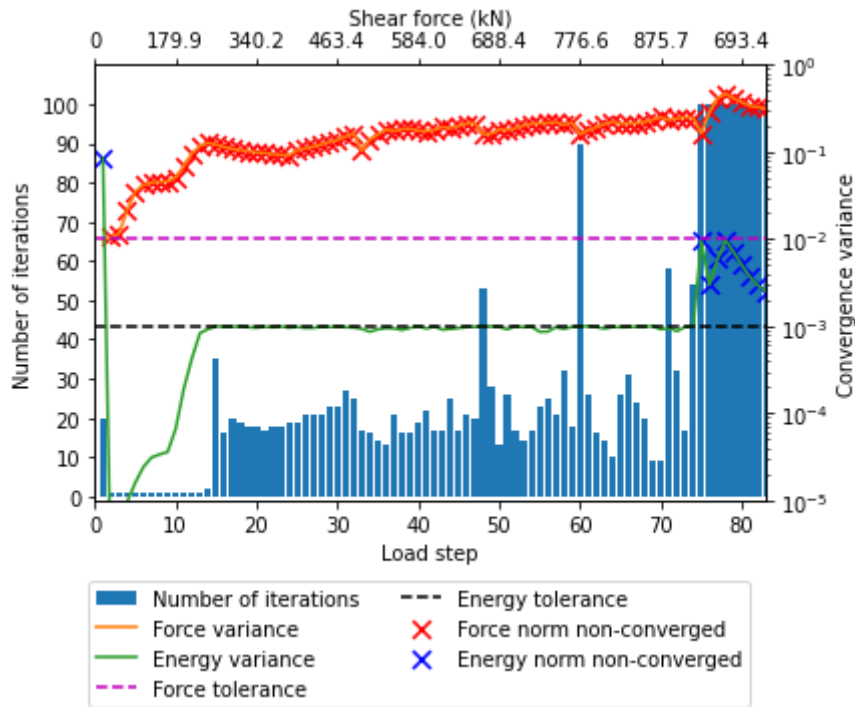


Figure C.13: Convergence behaviour solution strategy O2.8

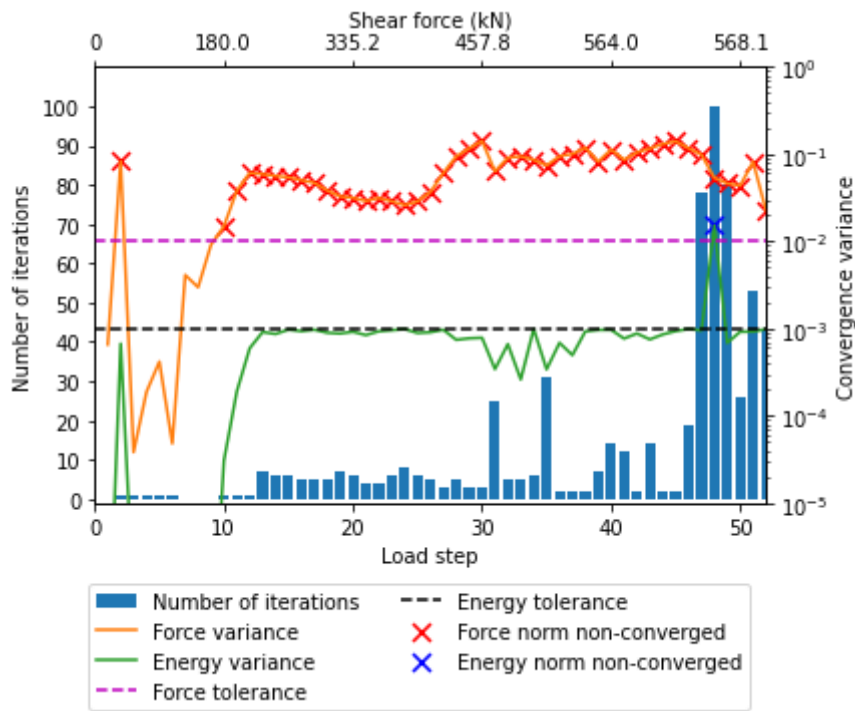


Figure C.14: Convergence behaviour solution strategy O2.9

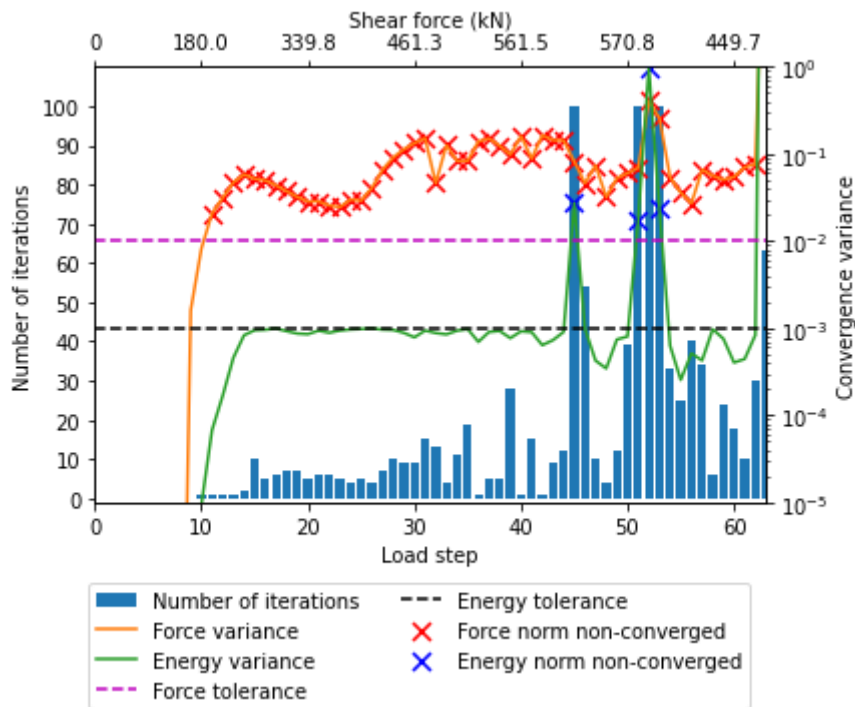


Figure C.15: Convergence behaviour solution strategy O2.10 (Divergence in final load step)